Karlsruher Institut für Technologie

Incorporation of Additional Radicals into Bis(phthalocyaninato)-Mononuclear and Bis(porphyrinato)(phthalocyaninato)-Dinuclear Rare-earth Complexes

Zur Erlangung des akademischen Grades eines

DOKTORS DER NATURWISSENSCHAFTEN

(Dr. rer. nat.)

von der KIT-Fakultät für Chemie und Biowissenschaften

des Karlsruher Instituts für Technologie (KIT)

genehmigte

DISSERTATION

von

M. Sc., Jo Komeda

1. Referent: Prof. Dr. Mario Ruben

2. Referent: Prof. Dr. Manfred Kappes

Tag der mündlichen Prüfung: 10. Februar 2025

Declaration

According to §13 paragraph 2 number 3 of the doctoral degree regulations of the Karlsruhe Institute of Technology for the KIT Faculty of Chemistry and Biosciences:

1. The submitted dissertation titled “Incorporation of Additional Radicals into Bis(phthalocyaninato)-Mononuclear and Bis(porphyrinato)(phthalocyaninato)-Dinuclear Rare-earth Complexes” is my own independent work.
2. I have only used the sources and aids indicated and have not made use of any unauthorized help from third parties. In particular, I have marked content taken literally or analogously from other works as such.
3. I have not previously submitted the thesis or parts thereof to a university in Germany or abroad as part of an examination or qualification.
4. I confirm the accuracy of the above declaration.
5. I am aware of the significance of the affidavit and the consequences under criminal law of an incorrect or incomplete affidavit.

I declare on oath that I have stated the absolute truth to the best of my knowledge and have not concealed anything.

....

Eidesstattliche Erklärung

Eidesstattliche Versicherung gemäß§13 Absatz 2 Ziffer 3 der Promotionsordnung des Karlsruher Instituts für Technologie für die KIT-Fakultät für Chemie und Biowissenschaften:

1. Bei der eingereichten Dissertation zu dem Thema “ Incorporation of Additional Radicals into Bis(phthalocyaninato)-Mononuclear and Bis(porphyrinato)(phthalocyaninato)-Dinuclear Rare-earth Complexes“ handelt es sich um meine eigenständig erbrachte Leistung.
2. Ich habe nur die angegebenen Quellen und Hilfsmittel benutzt und mich keiner unzulässigen Hilfe Dritter bedient. Insbesondere habe ich wörtlich oder sinngemäß aus anderen Werken übernommene Inhalte als solche kenntlich gemacht.
3. Die Arbeit oder Teile davon habe ich bislang nicht an einer Hochschule des In- oder Auslands als Bestandteil einer Prüfungs- oder Qualifikationsleistung vorgelegt.
4. Die Richtigkeit der vorstehenden Erklärung bestätige ich.
5. Die Bedeutung der eidesstattlichen Versicherung und die strafrechtlichen Folgen einer unrichtigen oder unvollständigen eidesstattlichen Versicherung sind mir bekannt.

Ich versichere an Eides statt, dass ich nach bestem Wissen die reine Wahrheit erklärt und nichts verschwiegen habe.

....

Abstract

In order to satisfy the growing demand for information technology, it is necessary to develop processors and storage that surpass Moore's Law. The former would be achieved by the development of quantum computers, while the latter would be realized by magnets working on the molecular scale. Bis(phthalocyaninato)-rare-earth(III) molecules have been intensively studied for their novelty of being both quantum bits and single molecule magnets.

In this thesis, aiming at the improvement of those properties, bis(phthalocyaninato)-rare-earth(III)-mononuclear and bis(porphyrinato)(phthalocyaninato)-dinuclear rare-earth(III) molecules with an additional radical were designed. Three projects were dedicated to this end, summarized in Chapter 2, 3, and 4, respectively.

Chapter 2 features the study of a bis(phthalocyaninato) yttrium (III) molecule functionalized by an isoindoline-based nitroxide radical. A diradical with *g*-asymmetry was designed and synthesized by introducing a nitroxide radical onto the $[YPc_2]^0$ platform. Various spectroscopic techniques and computational studies revealed that the electronic structures of the two spin systems within the diradical system were only minimally affected. Electron paramagnetic resonance (EPR) experiments in liquid solution clarified a weak exchange coupling with $|J| \sim 0.014\ \mathrm{cm}^{-1}$, which was subsequently rationalized by CAS-SCF calculations. EPR experiments in frozen solution with continuous wave (CW) exhibited a complicated and power-dependent spectrum that eluded analysis using the point-dipole model. Pulsed EPR manipulations with varying microwave powers or under varying magnetic fields showed that different resonances can be selectively enhanced or suppressed, based on their different tipping angles. In particular, Field-Swept Echo-Detected (FSED) spectra showed absorptions of MW power-dependent intensities, while Field-Swept Spin Nutation (FSSN) experiments revealed two distinct Rabi frequencies. In this study, a method for the synthesis and characterization of *g*-asymmetric two-spin systems of interest for the implementation of spin-based CNOT gates is presented.

Chapter 3 explains the study of a bis(phthalocyaninato)terbium (III) molecule functionalized by an isoindoline-based nitroxide radical. $TbPc_2$ is one of the most widely studied platforms as a single molecule magnet (SMM). Introduction of a radical is a widely adopted strategy to improve SMM performance. Here, the effect of the additional radical in $TbPc_2$ on its SMM property was investigated. Various spectroscopic techniques unambiguously revealed that both radicals are intact. Static and dynamic magnetic measurements demonstrated the unchanged magnetic character of the target molecule from $TbPc_2$. The magnetic property, as well as the presence of two radicals, make this molecule an interesting target for STM-EPR studies, which is discussed in detail in the outlook part.

Chapter 4 introduces the study of bis(porphyrinato)(phthalocyaninato)-dinuclear rare-earth(III) molecules with a radical. Spin transport measurements on tris(phthalocyaninato)-dinuclear rare-earth(III) molecules are a promising platform for nuclear spin qudits with increased multiplicity. However, the absence of the radical in this molecule has prevented studies on the coupling between the lanthanide and the conduction electron. Here, bis(porphyrinato)(phthalocyaninato)-dinuclear rare-earth(III) molecules with thiomethyl groups were prepared. The designed molecules were oxidized to obtain radicals, which was achieved by adjusting the HOMO-LUMO gap of the neutral complexes. UV-vis-NIR absorption spectroscopy showed their stability in air at room temperature for one week. The combination of CASSCF calculations and static magnetic measurements revealed the nature of their coupling. Dynamic magnetic measurements revealed that the magnetic properties change upon oxidation, namely from field-induced SMM to zero field SMM. The results of this study, together with the strong bond between the thiomethyl group and the gold electrode, could provide a new material for quantum information processing.

Throughout the studies described in the three chapters, the impact of additional radicals was demonstrated in the field of quantum information processing and single-molecule magnets. Furthermore, these results indicated the potential of this strategy in quantum information processing. The outlook for future single-molecule studies is described at the end.

Zusammenfassung

Um die wachsende Nachfrage nach Informationstechnologie zu befriedigen, ist es notwendig, Prozessoren und Speicher zu entwickeln, die das Mooresche Gesetz übertreffen. Ersteres könnte durch die Entwicklung von Quantencomputern erreicht werden, letzteres durch Magnete, die auf dem molekularen Maßstab arbeiten. Bis(phthalocyaninato)-Seltene Erd(III)-Moleküle wurden aufgrund ihrer neuartigen Eigenschaft, sowohl als Quantenbit als auch als Einzelmolekülmagnet zu agieren, intensiv untersucht.

In dieser Arbeit wurden Bis(phthalocyaninato)-Seltene Erd(III)-Moleküle und Bis(porphyrinato)(phthalocyaninato)-Seltene Erd(III)-Moleküle mit zusätzlichen Radikalen entwickelt, um diese Eigenschaften zu verbessern. Zu diesem Zweck wurden drei Studien durchgeführt, die in den Kapiteln 2, 3 und 4 zusammengefasst sind.

Kapitel 2 befasst sich mit der Untersuchung eines Bis(phthalocyaninato)-Yttrium(III)-Moleküls, das durch ein Nitroxidradikal auf Isoindolinbasis funktionalisiert wurde. Ein Diradikal mit künstlicher g-Asymmetrie wurde durch Einführen eines Nitroxidradikals zur bestehenden $[YPc_2]^0$ Radikalplattform synthetisiert. Verschiedene spektroskopische Techniken und Berechnungen zeigten, dass die elektronischen Strukturen der beiden Spinsysteme innerhalb des Diradikalsystems nur minimal beeinflusst wurden. Experimente zur Elektronen-Paramagnetischen-Resonanz (EPR) in flüssiger Lösung ergaben eine schwache Austauschkopplung mit $|J| \sim 0{,}014\ \mathrm{cm}^{-1}$, die anschließend durch CAS-SCF-Berechnungen rationalisiert wurde. „Continous wave“ (CW) EPR-Experimente in gefrorener Lösung zeigten ein kompliziertes und leistungsabhängiges Spektrum, das nicht dem üblichen Punkt-Dipol-Modell entsprach. Gepulste EPR-Manipulationen mit variierenden Mikrowellenleistungen oder unter variierenden Magnetfeldern zeigten, dass verschiedene Resonanzen selektiv verstärkt oder unterdrückt werden können, basierend auf ihren unterschiedlichen Kippwinkeln. Insbesondere zeigten Field-Swept Echo-Detected (FSED)-Spektren Absorptionen von MW-leistungsabhängigen Intensitäten, während Field-Swept Spin Nutation (FSSN)-Experimente zwei unterschiedliche Rabi-Frequenzen aufzeigten. In dieser Studie wird eine Methode zur Synthese und Charakterisierung von g-asymmetrischen Zwei-Spin-Systemen vorgestellt, die für die Implementierung von spinbasierten CNOT-Gattern von Interesse sind.

Kapitel 3 beschreibt die Studie eines Bis(phthalocyaninato)-Terbium(III)-Moleküls, das durch ein Nitroxidradikal auf Isoindolinbasis funktionalisiert wurde. $TbPc_2$ ist eine der am meisten untersuchten Plattformen für Einzelmolekülmagnete (SMM). Die Einführung eines Radikals ist eine weit verbreitete Strategie zur Verbesserung des SMM-Charakters. Hier wurde die Wirkung des zusätzlichen Radikals in $TbPc_2$ auf die SMM-Eigenschaften untersucht. Verschiedene spektroskopische Techniken zeigten eindeutig, dass beide Radikale intakt sind. Statische und dynamische magnetische Messungen zeigten den unveränderten magnetischen Charakter des Zielmoleküls im Vergleich zu $TbPc_2$. Die magnetischen Eigenschaften sowie das Vorhandensein von zwei Radikalen machen dieses Molekül zu einem interessanten Ziel für STM-EPR-Studien, das im Ausblicksteil ausführlicher diskutiert wird.

In Kapitel 4 wird die Untersuchung von zweikernigen Bis(porphyrinato)(phthalocyaninato)-Molekülen der dreiwertigen seltenen Erdionen mit Radikalen vorgestellt. Spin-Transport-Messungen an tris(phthalocyaninato)-dinuklearen seltenen Erd(III)-Molekülen sind eine vielversprechende Plattform für Kernspin-Qudits mit erhöhter Multiplizität. Da dieses Molekül kein Radikal besitzt, sind jedoch Studien über die Kopplung zwischen Lanthanid und Leitungselektron nicht möglich. Hierfür wurden zweikernige Bis(porphyrinato)(phthalocyaninato)-Moleküle der seltenen Erden mit Thiomethylgruppen hergestellt. Die entworfenen Moleküle wurden oxidiert, um Radikale zu erhalten, was durch die Anpassung der HOMO-LUMO-Lücke der neutralen Komplexe erreicht wurde. Die UV-vis-NIR-Absorptionsspektroskopie zeigte ihre Stabilität an Luft bei Raumtemperatur für eine Woche. Die Kombination aus CASSCF-Berechnungen und statischen magnetischen Messungen erlaubt Aussagen über die Art ihrer Kopplung. Dynamische magnetische Messungen ergaben, dass sich die magnetischen Eigenschaften bei der Oxidation ändern, nämlich von einem feldinduzierten SMM zum feldfreien SMM. Die Ergebnisse dieser Studie, zusammen mit der starken Bindung zwischen der Thiomethylgruppe und der Goldelektrode, könnten ein neues Material für die Quanteninformationsverarbeitung darstellen.

In den in den drei Kapiteln beschriebenen Studien wurde der Einfluss zusätzlicher Radikale auf dem Gebiet der Quanteninformationsverarbeitung und der Einzelmolekülmagnete nachgewiesen. Darüber hinaus wiesen diese Ergebnisse auf das Potenzial dieser Strategie für die Quanteninformationsverarbeitung hin. Ein Ausblick auf zukünftige Einzelmolekülstudien wird abschließend präsentiert.

Acknowledgment

First of all, I would like to thank Prof. Mario Ruben for providing me the opportunity to conduct my Ph.D. work in his group and for his continuous support. I also highly appreciate Dr. Svetlana Klyatskaya, Dr. Athanassios K. Boudalis, and Dr. Asato Mizuno for their help and guidance in my Ph.D. I am also grateful to Dr. Senthil Kumar Kuppsamy for spending a lot of time with me and deepening my scientific knowledge. I would also like to thank Dr. Sören Schlittenhardt for allowing me to ask questions numerous times. I deeply appreciate Dr. Sujit Kamilya and Dr. Jordan Appleton for revising the manuscript. I would also like to thank all my labmates for providing a comfortable environment – Dr. Concepción Molina-Jirón, Dr. Shagor Chowdhury, Dr. Barbora Brachnaokva, Dr. Sujit Kamilya, Yaorong Chen, Zhaoyang Jing, Patrick Lawes, Dennis Janković, Jean-Gabriel Hartmann, Rihab Sayid, Lukas-David Hamm, and Nikoleta Malinová. I also thank alumni – Dr. Eufemio Moreno-Pineda, Shirin Shakouri, Ting-ting Ruan, Sai Prasanna Kumar, and Nithin Suryadevara. I would like to acknowledge Hagen Sparrenberger for helping with all the lab supplies.

I appreciate all the coauthors for their contribution to the paper related to Chapter 2; Dr. A. K. Boudalis, Dr. Nicolas Montenegro-Pohlhammer, Cyril Autheaume, Dr. A. Mizuno, Prof. Philippe Turek, and Prof. M. Ruben. I described their respective contribution in Chapter 2.

I am grateful to all the coauthors for their contribution to the working paper related to Chapter 4; Dr. S. Schlittenhardt, Dr. A. Mizuno, Dr. E. Moreno-Pineda, Y. Chen, Dr. Olaf Fuhr, Dr. J. Appleton, Dr. A. K. Boudalis, Dr. S. Klyatskaya, and Prof. M. Ruben. I described their respective contribution in Chapter 4.

Finally, I would like to dedicate a special thanks to my family for their support in all my life.

Abbreviations

Commonly used abbreviations

AC	Alternating current
CASSCF	Complete active space self-consistent field
$CHCl_3$	Chloroform
COF	Covalent organic framework
Cp	Cyclopentadienyl
CShM	Continuous shape measurement
CT	Charge transfer
CW	Continuous wave
DC	Direct current
DCM	Dichloromethane
DFT	Density functional theory
EISC	Enhanced intersystem crossing
EPR	Electron paramagnetic resonance
ESI	Electrosprary ionization
FSED	Field sweep echo decay
GNR	Graphene nanoribbon
HF	Hyperfine coupling
HOMO	Highest occupied molecular orbital
IR	Infrared
ISC	Intersystem crossing
LF	Ligand field
Ln	Lanthanide
LUMO	Lowest unoccupied molecular orbital
MeOH	Methanol
mnt	Maleonitrile
MOF	Metal-organic framework
MS	Mass spectra
MW	Microwave
NIR	Near IR
NMR	Nuclear magnetic resonance
Pc	Phthalocyanine
PDI	Perrylene diimide
Ph	Phenyl
Por	Porphyrin
PPh_4	Tetraphenylphosphoryum
PTM	Pentachlorotriphenylmethyl
RASSCF	Restricted active space self-consistent field
SAM	Self-assembled monolayer
SAP	Square antiprism
SMM	Single molecule magnet
SOC	Spin orbit coupling
SOMO	Singly occupied molecular orbital
SQUID	Superconducting quantum interference device

SWCNT	Single-wall carbon nanotube
TA-QTM	Thermally assisted quantum tunneling of magnetization
TEMPO	2,2,6,6,-Tetramethylpiperydine 1-oxyl
tof	Time of flight
TPP	Tetraphenylporphyrin
TTM	Tris-2,4,6-trichlorophenylmethyl
U_{eff}	Energy barrier
UV	Ultraviolet
vis	visible
WFT	Wave function theory
XRD	X-ray diffraction
ZFS	Zero field splitting

Abbreviations specifically used in this thesis

$\mathrm{LnPc_2}$	Bis(phthalocyaninato)lanthanide(III), in any redox state
Y	Yttrium
Tb	Terbium
Dy	Dysprosium
Er	Erbium
Ho	Holumium
Gd	Gadorimium
Ce	Cerium
$[\mathrm{LnPc_2}]^{0/+/-}$	$\mathrm{LnPc_2}$ in neutral/cationic/anionic state
[NO]	Isoindoline moiety
SMe	Thiomethyl group
LnPcPor	Phthalocyaninato porpyrinato lanthanide (III)
$\mathrm{Ln_2(TPP)_2(Pc)}$	(Phthalocyaninato)bis(tetraphenylporphyrinato)-dinuclear lanthanide(III)
$\mathrm{Ln_2(Por)_2(Pc)}$	Bis(porphyrinato)(phthalocyaninato)-dinuclear lanthanide(III)
multiple-decker	It refers to multi-nuclear complex sandwiched by plain ligands.
T_2, T_{m}	The abbreviation of spin decoherence time is described in Section 1.3.2.2.
T_{B}	The definition of blocking temperature is described in Section 1.4.2.

Table of Contents

Chapter 1. Introduction and Theory

1.1. Toward the Next Generation: Beyond Moore’s Law

The historical period from the mid-20th century to the present is defined as the Digital Age.[1] Since 1948, when Claude Shannon, known as the father of the information age, proposed the encoding of information by the combination of zero and one,[2] human history has been accompanied by the evolution of information technologies (IT) and characterized by a rapid shift to an IT-centered economy. As IT has increasingly become integral to our lives, several issues have emerged. One significant problem is the limitation of processor capabilities. Goordon E. Moore, the co-founder of Intel, proposed in 1965 that the complexity of the components (= the number of transistors) would double approximately every year. Today this estimation is known as **Moore’s law**, which is revised to indicate a doubling every two years.[3] Currently this trend is driven by advancements in die shrinkage enabled by precise lithography,[4] however, many researchers predict that Moore’s law will come to an end in the near future.[5,6]

Another issue arises in data storage. Human history has always been accompanied by the progress of recording media. One milestone is the hard disk drive (HDD), driven by the giant magnetoresistance effect, which was for the first time discovered by Fert and Günberg, the winners of the Nobel Prize in physics in 2007.[7] As of 2024, semiconductor-based solid-state drive (SSD), together with HDD, serves as the main-stream, and the use of data servers represented by Amazon Web Service (AWS) is becoming more common. Since data servers rely on SSDs or HDDs for data storage, improving data capacity requires a breakthrough in either of them. However, both of them face obstacles; SSDs, made of semiconductors, are approaching the end of Moore’s Law, while HDDs cannot be further miniaturized due to the limitations imposed by many-body effects from spin-spin interactions at microscopic scales. In summary, breakthroughs are needed in both processing and storage technologies.

1.2. Quantum Information Processing

One possible solution to break through the current issue of semiconductor-based processors is to build a processor that can work based on a different mechanism. In 1982, Richard Feynman, the Nobel laureate in physics in 1965, proposed a computer based on quantum mechanics.[8] The fundamental unit in this system is the “bit”; while classical computers treat information as the combination of 1 or 0 (so-called bits), quantum computers use the combination of two-level quantum states, $|1\rangle$ or $|0\rangle$ – **qubit** (named after **qu**antum **bit**). Qubits feature two characteristics, **coherence** and **entanglement**. Coherence refers to the state where a quantum state exists as the mixture of $|1\rangle$ and $|0\rangle$ ($|\psi\rangle = \alpha|0\rangle + \beta|1\rangle, (\alpha^2 + \beta^2 = 1)$), which is often explained by Schrödinger’s cat. Since α and β can take any value under a normalization condition, qubits can treat more diverse information than conventional bits. On the other hand, entanglement represents the state where two qubits are correlated in a way that their states cannot be explained as a simple product of them. For instance, two coupled qubits result in the following four states:

$$|S\rangle = \frac{1}{\sqrt{2}}(|10\rangle - |01\rangle) \tag{1.1}$$

$$|T_0\rangle = \frac{1}{\sqrt{2}}(|10\rangle + |01\rangle) \tag{1.2}$$

$$|T_1\rangle = |11\rangle \tag{1.3}$$

$$|T_{-1}\rangle = |00\rangle \tag{1.4}$$

The first two states (equations 1.1 and 1.2) are known as Bell states, which cannot be expressed as $(\alpha|1\rangle + \beta|0\rangle)(\gamma|1\rangle + \delta|0\rangle)$. This means that altering the state of one spin will inevitably affect the other, leading to an entanglement of the two states. Together with algorithms that can efficiently utilize those features, quantum computers will exceed the power limitation of conventional computers.

Consequently, a question arises: what kind of systems or materials may serve as qubits? In 2000, DiVincenzo proposed some requirements, today known as **DiVincenzo's criteria**.[9]

1. A scalable physical system with well-characterized qubits (i.e., qubits with a defined Hamiltonian)

2. The ability to initialize the state of the qubit to a simple fiducial state, such as $|000\,...\rangle$

3. Long relevant decoherence times, much longer than the gate operation time

4. A "universal" set of quantum gates ("universal" stands for any coherent states, which can be achieved by the combination of simple quantum gates such as the CNOT gate (*vide infra*))

5. A qubit-specific measurement capability

Many qubit candidate systems satisfy the criteria above,[10] such as superconductors,[11,12] trapped ions,[13,14] neutral atoms,[15,16] photons,[17] and so on. Spin, a fundamental physical property with two states (up and down), is thus ideal for use as a qubit. Hence, many qubit systems are based on spin levels. Amongst candidates, molecular spin qubits are extensively studied.[18–21] Since their monodispersity and structural tunability satisfy Divincezo's criteria, various molecular systems have been explored. In the next section, starting from the explanation of the nature of spin from a quantum mechanical perspective, molecular spin qubits are explained regarding electronic spin qubit specific measurements, EPR, and qubit candidate molecules including metal complexes and organic radicals.

1.3. Molecular electron-spin qubits

1.3.1. Spin

The equations used in this section were created using the following references.[22,23]

The nature of spin and Bloch sphere

Even before the dawn of quantum mechanics, it was already known that electrons reside in doubly degenerated states, as demonstrated experimentally by Stern and Gerlach in 1922, known as Stern-Gerlach's experiment.[24] They used an Ag atom beam passing through collimating slits, which is after passing through a magnetic field from a permanent magnet projected on a screen. The projected pattern showed field-dependent splitting (**Zeeman splitting**), which evidenced the electron's two states. Today, this property of an electron is explained by its spin angular momentum (S_z). To grasp the image of spin, let's consider an electron under a magnetic field. XYZ cartesian can be drawn to represent real space, taking the z axis to be along a magnetic field ($\boldsymbol{B_0}$) (Figure 1.1.1a). Like in the case of classical mechanics where the energy of a magnet (with magnetic momentum of $\boldsymbol{M}$) under a magnetic field ($\boldsymbol{B}$) can be represented as $E = -\frac{1}{\mu_0}\boldsymbol{B}\cdot\boldsymbol{M}$, the spin Hamiltonian can be written as follows:

$$H_{spin} = \left(\frac{g\beta}{\hbar}\right)\boldsymbol{B}_0\boldsymbol{S_z} \tag{1.5}$$

g: g-Factor, which is in the case of free electron $g_e = 2.0023$.[25]
β: Bohr magneton
$\hbar$: Dirac constant

$\boldsymbol{S_z}$ is spin angular momentum expressed as follows:

$$\boldsymbol{S_z} = \frac{\hbar}{2}\begin{pmatrix}1 & 0\\ 0 & -1\end{pmatrix} \tag{1.6}$$

It has two eigenvectors $|\uparrow\rangle = \binom{1}{0}$ and $|\downarrow\rangle = \binom{0}{1}$ having two eigenvalues; $+\hbar/2$ and $-\hbar/2$, respectively. The Hamiltonian gives two states in the energy $E_{spin} = \mp\frac{1}{2}g\beta B_0$, which are parallel/antiparallel to the external magnetic field (and z axis), respectively. For simplicity, two spin states will be represented as up ($|\uparrow\rangle$) and down ($|\downarrow\rangle$), represented in Figure 1.1.1 a. Under a magnetic field with a certain strength, the spin resides in a coherent state of the two Zeeman-split states, namely the spin-up and spin-down levels:

$$\begin{aligned} |\psi\rangle &= \alpha|\uparrow\rangle + \beta|\downarrow\rangle \\ &= (\alpha_1 + i\alpha_2)|\uparrow\rangle + (\beta_1 + i\beta_2)|\downarrow\rangle \end{aligned} \tag{1.7}$$

where $|\alpha|^2 + |\beta|^2 = 1$, α, β are complex numbers, $\alpha_1^2 + \alpha_2^2 + \beta_1^2 + \beta_2^2 = 1$, $\alpha_1, \alpha_2, \beta_1, \beta_2$ are real numbers.

The parameters $(\alpha_1, \alpha_2, \beta_1, \beta_2)$ can be converted into polar coordinates as follows:

$$|\psi\rangle = \cos\frac{\theta}{2}|\uparrow\rangle + \sin\frac{\theta}{2}e^{i\phi}|\downarrow\rangle \tag{1.8}$$

where the angles are restricted as $0 \leq \theta \leq \pi$ and $0 \leq \varphi \leq 2\pi$. This is represented in a spherical coordinate system (Figure 1.1.1 b.). The coherent state can take whatever value on the surface of the sphere. The sphere is called **Bloch sphere**.

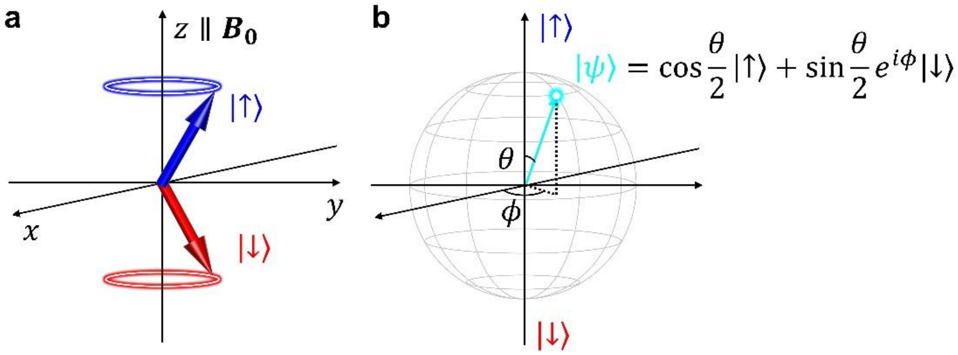

Figure 1.1.1. Schematic representation of (a) spin in XYZ coordinate and (b) spin in Bloch sphere.

Larmor precession

Then, let's consider the behavior of an electron under a static magnetic field more carefully. Schrödinger equation can be written as follows:

$$i\hbar\frac{\partial}{\partial t}\psi(x,t) = \hat{H}\psi(x,t) \tag{1.9}$$

Suppose that variational methods are applicable ($\psi(x,t) = (\alpha(t)|\uparrow\rangle + \beta(t)|\downarrow\rangle)\psi'(x)$), and suppose that ψ'(x) remains in a stationary state, it can be rewritten by using the spin Hamiltonian (eq. 1.5):

$$\begin{aligned} i\hbar\frac{\partial}{\partial t}\begin{pmatrix}\alpha\\ \beta\end{pmatrix} &= \hat{H}\begin{pmatrix}\alpha\\ \beta\end{pmatrix} \\ &= \begin{pmatrix}\frac{1}{2}g\beta B_0 & 0 \\ 0 & -\frac{1}{2}g\beta B_0\end{pmatrix}\begin{pmatrix}\alpha\\ \beta\end{pmatrix} \end{aligned} \tag{1.10}$$

This differential equation can be solved to give the solution as follows:

$$\alpha(t) = \alpha(0)e^{-i\left(\frac{g\beta B_0}{2\hbar}\right)t} \tag{1.11}$$

$$\beta(t) = \beta(0)e^{i\left(\frac{g\beta B_0}{2\hbar}\right)t} \tag{1.12}$$

The value $\omega_L = \frac{g\beta B_0}{\hbar}$ is called **Larmor angular frequency**. This represents the behavior of spin, where it aligns parallel/antiparallel to the external magnetic field, while it rotates in the XY-plane perpendicular to the magnetic field (represented as the rings in Figure 1.1.2). In the case when $\alpha(0) = \beta(0) = 1/\sqrt{2}$, $\begin{pmatrix}\alpha(t)\\ \beta(t)\end{pmatrix} = \frac{1}{\sqrt{2}}\begin{pmatrix}e^{-2i\omega_L t}\\ e^{2i\omega_L t}\end{pmatrix}$ is obtained. This can be further rewritten as follows:

$$|\psi\rangle = e^{-\frac{i\omega_L t}{2}}\left(\cos\frac{\pi/2}{2}|\uparrow\rangle + \sin\frac{\pi/2}{2}e^{i\omega_L t}|\downarrow\rangle\right) \tag{1.13}$$

Compared with the points on Bloch's sphere, the combination of $(\theta,\phi) = (\pi/2, \omega_L t)$ represents the point rotating along the equator with an angular momentum of ω_L (see the dot and the arrow in Figure 1.1.2, cyan). It is noteworthy that the product of Larmor angular frequency and Dirac constant is equal to the energy gap of two states, which is clear from the equation 1.10.

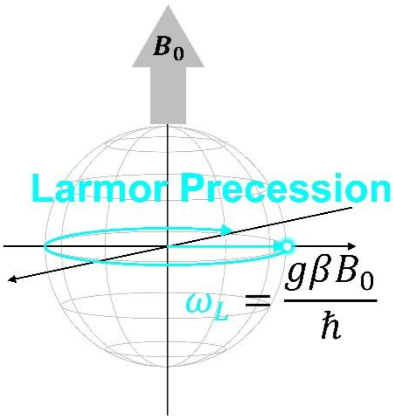

Figure 1.1.2. Schematic illustration of Larmor precession. Under static magnetic field (grey arrow), the spin in $\alpha(0) = \beta(0) = 1/\sqrt{2}$ (cyan straight arrow) rotates alongside the equator (cyan ellipse arrow).

Rabi oscillation

Finally, let's consider the behavior of an electron in the stationary magnetic field (B_0) alongside the z axis and a rotating magnetic field in a XY-plane (B_r with angular frequency ω_{MW}). The total magnetic field can be represented as follows:

$$\begin{aligned}\boldsymbol{B} &= \boldsymbol{B_0} + \boldsymbol{B_r} \\ &= (B_r \cos(\omega_{MW} t)\,, B_r \sin(\omega_{MW}\ t)\,, B_0)\end{aligned} \tag{1.14}$$

By taking into consideration that

$$S_z = \frac{\hbar}{2}\begin{pmatrix} 0 & 1 \\ 1 & 0 \end{pmatrix}, \qquad S_y = \frac{\hbar}{2}\begin{pmatrix} 0 & -i \\ i & 0 \end{pmatrix} \tag{1.15}$$

the spin Hamiltonian (eq. 1.5) can be written as follows.

$$\begin{aligned} H_{spin} &= \left(\frac{g\beta}{\hbar}\right)\boldsymbol{B}_0\boldsymbol{S_z} \\ &= \frac{g\beta}{2}\begin{pmatrix} B_0 & B_r e_r^{-i\omega_{MW} t} \\ B_r e_r^{i\omega_{MW} t} & -B_0 \end{pmatrix} \end{aligned} \tag{1.16}$$

By combining eq. 1.9 and eq. 1.16, Schrödinger equation can be written as follows:

$$i\hbar\frac{\partial}{\partial t}\begin{pmatrix} \alpha \\ \beta \end{pmatrix} = \frac{g\beta}{2}\begin{pmatrix} B_0 & B_r e_r^{-i\omega_{MW} t} \\ B_r e_r^{i\omega_{MW} t} & -B_0 \end{pmatrix}\begin{pmatrix} \alpha \\ \beta \end{pmatrix} \tag{1.17}$$

This derivation equation can be solved, and the solutions for ($\alpha(0)$, $\beta(0)$) = (1, 0) are as follows:

$$\alpha(t) = e^{-i\frac{\omega_{MW}}{2}t}\left(\cos\Omega t + i\frac{\omega_{MW} - \omega_L}{2\Omega}\sin\Omega t\right) \tag{1.18}$$

$$\beta(t) = -ie^{i\frac{\omega_{MW}}{2}t}\,\frac{\omega_r}{\Omega}\sin\Omega t \tag{1.19}$$

Ω: Defined by $\Omega = \sqrt{\omega_r^2 + \frac{(\omega_{MW} - \omega_L)^2}{4}}$

ω_r: Defined by $\omega_r = \frac{1}{2\hbar}g\beta B_r$

The probability of the up and down states are given as follows:

$$|\alpha|^2 = 1 - \frac{\omega_r^2}{\Omega^2}\sin^2\Omega t \tag{1.20}$$

$$|\beta|^2 = \frac{\omega_r^2}{\Omega^2}\sin^2\Omega t \tag{1.21}$$

The above discussion matches with the following situation: At the initial state (t = 0), where an external magnetic field $\boldsymbol{B}_0$ is applied alongside the z-axis, the spin will reside up. Now, the rotating magnetic field $\boldsymbol{B}_r$ starts to be applied, which is enabled by the application of an electromagnetic wave, specifically microwave irradiation. When the microwave angular frequency coincides with the Larmor angular frequency (=energy gap of up and down divided by Dirac constant), oscillation between up and down takes place with the frequency of Ω (Figure 1.1.3). This phenomenon is called **Rabi oscillation**, while Ω is called **Rabi angular**

frequency. On the other hand, when the microwave frequency does not precisely match $\omega_{MW} \neq \omega_L$, incomplete oscillation occur, which is governed by the ratio of ω_r and Ω. Notably, Rabi oscillation is a fundamental mechanism of magnetic resonance, as it correlates electromagnetic wave to spin behavior. In addition, it plays a key role in quantum information processing (QIP). As explained in Section 1.2, QIP requires the control of coherent two-level quantum states; in other words, the accessibility of the arbitrary point on the Bloch sphere is needed. Rabi oscillation presents a transition between these states throughout Bloch sphere, thus it works as a criterion of manipulability.

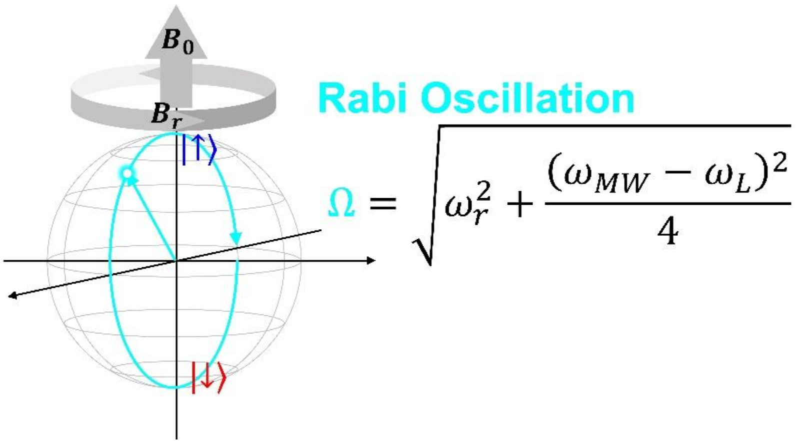

Figure 1.1.3. Schematic illustration of Rabi oscillation. Under a static and rotating magnetic field (grey arrow and grey ellipse, respectively), when the microwave angular frequency coincides with the Larmor angular frequency, the spin oscillates between up and down states (cyan arrows). Note that the ellipse is a simplified representation of the Rabi oscillation and is not precise.

1.3.2. Electron Paramagnetic Resonance (EPR)

Electron Paramagnetic Resonance (EPR) was explained in detail in the references.[26,27] Here, it was described in a simplified way, to highlight qubit-oriented measurements.

1.3.2.1. Continuous Wave EPR

Zeeman diagram and EPR spectrum of an electronic spin *S* = 1/2

In Section 1.3.1, the behavior of spin under static and rotating magnetic field was explained. Here, the experimental technique to characterize/manipulate spins is explained. The spin Hamiltonian $H_{spin} = g\beta \boldsymbol{B}_0/\hbar \boldsymbol{S_z}$ (**Zeeman term**) gives two states in $\pm\frac{1}{2}g\beta B_0$. The energy diagram of the two states is shown in Figure 1.2a, which is called **Zeeman diagram**. As explained in the last section, the resonance between up and down states can be driven by microwave when the frequency satisfies $\nu = g\beta \boldsymbol{B_0}/h$. The spectroscopic technique to scan an external field in order to observe resonance of paramagnetic specimen is called continuous wave electron paramagnetic resonance (cw-EPR), a widely used technique for paramagnetic molecules. In the case of a free electron, g-factor is isotropic and thus can be treated as constant along all three axes. On the other hand, for many paramagnetic molecules, the internal field mediated by spin-orbit coupling not only deviates the g value from g_e but also introduces anisotropy, typically expressed by a 3×3 matrix. Therefore, EPR is a powerful tool to identify different species. Commercially available EPR spectrometers are equipped with microwave sources of certain frequencies such as ν = 9.5 GHz (X Band), 34 GHz (Q band) and so on. Instead of ν, the external magnetic field B_0 is scanned, while the signal is detected by the induced current on the neighboring coil. The x-axis of the spectrum typically represents either B_0 or g (calculated by $g = h\nu/\beta B_0$), as depicted in Figure 1.2 a.

EPR spectrum of *S* = 1/2 with hyperfine coupling (when nuclear spin *I* = 1)

Many molecules bear nuclear spins which are hyperfine-coupled to electron spins. In such cases, the spin Hamiltonian can be written as $H_{el\&nuc\,spin} = \frac{g\beta \boldsymbol{B_0}}{h}\boldsymbol{S_z} + AS_zI_z$, where the second term is the nuclear spin term, and A is the hyperfine tensor. Figure 1.2b. represents the case of S = 1/2, I = 1. It results in six states, which allow three transitions governed by selection rules $\Delta\mathrm{M_S} = \pm 1, \Delta\mathrm{M_I} = 0$. Therefore, the EPR spectrum shows three peaks, each of which is energetically separated in ±A.

EPR spectrum of two coupled *S* = 1/2 system.

Finally, in the case of multi-electronic spins, we have to consider interactions between spins; exchange interaction (J) or dipolar interaction (D). Let's take an example of a two-spin system with different g values (g_1 and g_2) with isotropic exchange interaction. Its spin Hamiltonian can be written as $H_{two\,spin} = \frac{g_1\beta \boldsymbol{B}_0}{\hbar}\boldsymbol{S_1} + \frac{g_2\beta \boldsymbol{B}_0}{\hbar}\boldsymbol{S_2} + J\boldsymbol{S_1}\boldsymbol{S_2} + \boldsymbol{S_1}\mathbf{D}\boldsymbol{S_2}$, where D is dipole-dipole coupling tensor. In the case where the exchange coupling is strong enough, it results in four states;

$$|S\rangle = \frac{1}{\sqrt{2}}(|\uparrow\downarrow\rangle - |\downarrow\uparrow\rangle) \tag{1.22}$$

$$|T_0\rangle = \frac{1}{\sqrt{2}}(|\uparrow\downarrow\rangle + |\downarrow\uparrow\rangle) \tag{1.23}$$

$$|T_1\rangle = |\uparrow\uparrow\rangle \tag{1.24}$$

$$|T_{-1}\rangle = |\downarrow\downarrow\rangle \tag{1.25}$$

where the first one has spin total angular momentum $S = 0$, while the others have $S = 1$. Following the selection rule $\Delta S = 0$, it allows three transitions. On the other hand, the weak coupling regime splits it into four states; $|\uparrow\uparrow\rangle$, $|\downarrow\downarrow\rangle$, $|\uparrow\downarrow\rangle$, and $|\downarrow\uparrow\rangle$. It allows four transitions under the selection rule of $\Delta\mathrm{M_S} = \pm 1$. The four transitions are attributed to the flip of one spin in each spin state, which is useful when considering the CNOT gate (see Section 1.3.3).

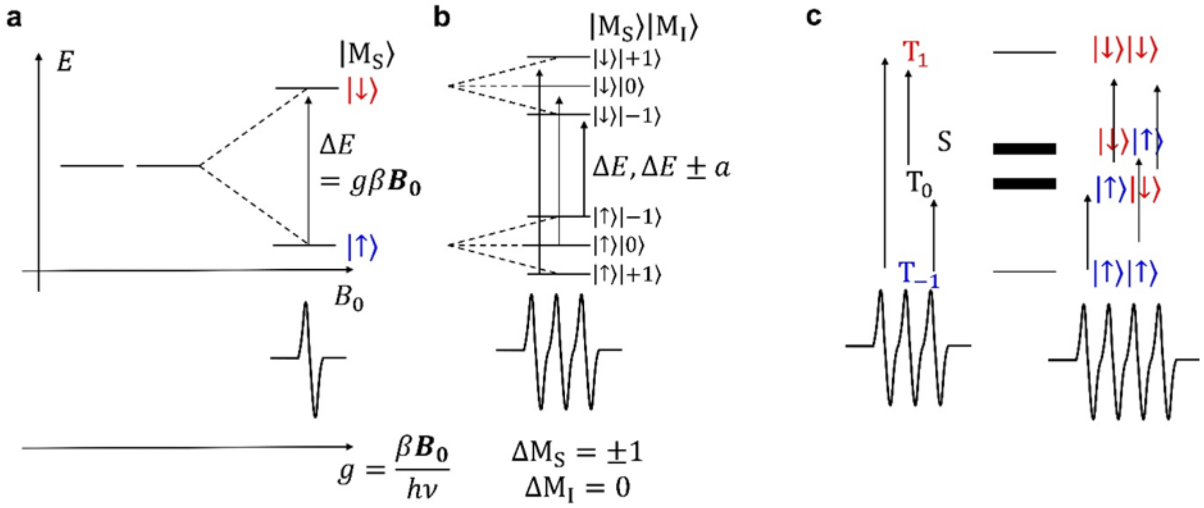

Figure 1.2. Zeeman diagrams of (a) S =1/2, (b) S = 1/2 hyperfine coupled to I = 1, and (c) two S = 1/2 with different g values, which are weakly (left) / strongly (right) exchange coupled each other. The corresponding EPR spectra were shown at the bottom of each diagram.

1.3.2.2. Fourier Transform (FT) Pulsed EPR

Spin-lattice relaxation time (T_1), decoherence time (T_2), and free induction decay (FID)

In a similar manner as FT-NMR,[28] EPR can be also performed with Fourier transform spectroscopy using a pulsed microwave. Unlike FT-NMR, where one pulse can cover the whole spectra during a short measurement period, FT-pulsed EPR often requires multiple pulses to achieve full spectral coverage. Nevertheless, FT-pulsed EPR is indispensable since it can determine some critical parameters for molecule-based QIP, as well proving the ability to arbitrarily control of the spin state.

As explained in Section 1.3.1, the initial state is prepared by applying the stationary external magnetic field, where most of the spins are aligned up. Manipulation of the spin on the Bloch sphere is achieved by applying pulse sequences. Here, let's consider the case to excite to the state $\alpha(0) = \beta(0) = 1/\sqrt{2}$ (Figure 1.3.1 a). This is achievable when $\Omega = \sqrt{2}, t = \frac{\pi}{2}\Omega$ (see eq. 1.18 and 1.19 in Section 1.2), and the pulse that satisfies this is called π/2 pulse. Over time, the excited state loses energy and relaxes to the ground state (Figure 1.3.1 a), described by the function $\left[1 - \exp\left(-\frac{t}{T_1}\right)\right]$, where T_1 is the **spin-lattice relaxation time**. This process is governed by the exchange of phonon with surroundings, namely Raman, Orbach, and Direct processes (see Section 1.4.2).

On the other hand, within a much shorter period before spin-lattice relaxation, Larmor precession of electron spin takes place (Figure 1.3.1 b), as explained in Section 1.3.1. The Larmor angular frequency (ω_L) is derived as half of the Zeeman splitting divided by the Dirac constant, $\omega_L = g\beta B_0/\hbar$. In practice, ω_L owns some fluctuation ($\omega_L \pm \Delta\omega$) due to inhomogeneity of the external magnetic field, difference of ligand fields, or coupling to spins in the environment, causing inhomogeneous broadening of $g\beta B_0$. Over time, this leads to coherent state variation, known as **decoherence**, expressed by the function $\exp\left(-\frac{t}{T_2}\right)$, where T_2 is the **spin-spin relaxation time**, or **spin decoherence time**. In many cases, stronger modulation is needed using the function: $\exp\left[\left(-\frac{t}{T_m}\right)^{\beta}\right](1 + k\sin(\omega_N t + \phi))$, where β is the stretch factor, k is the modulation depth, ω_N is the Larmor frequency of the nuclear spin, ϕ is the phase correction and T_m is called **phase-memory time**. Though T_2 and T_m are distinguished as explained above, they are often used interchangeably in the literature.[21] From the next section, the abbreviation will be unified as follows: T_m will be used for the one from a Hahn-echo-decay in pulsed EPR, while T_2 will be used for the one obtained in single-molecule measurement. The coherent state will be maintained only with decoherence time; thus, all the quantum computations must be operated during that time. Therefore, the decoherence time must be sufficiently long compared to quantum operations, as described in DiVincenzo's criteria. Typically, quantum gate operations take tens of nanoseconds.[29,30] Although T_1 is not directly connected to decoherence, from the definition, it is always true that $T_1 > T_m$. Therefore, T_1 can serve as the upper limit of T_m.

Larmor precession can be detected by the coil placed in XY-plane as an oscillating signal. The oscillation is driven by both the Larmor and microwave frequencies, represented by the product: $\cos 2\omega_L t \cos \omega_{MW} t = 1/2[\cos(2\omega_L + \omega_{MW})t + \cos(\omega_{MW} - 2\omega_L)t]$, whose first term is deleted with the use of a low-pass filters.[28] In the meantime, the amplitude of the oscillation decreases due to decoherence. In total, the signal is proportional to $\exp[i(2\omega_L - \omega)t] \exp\left[\left(-\frac{t}{T_m}\right)^{\beta}\right](1 + k\sin(\omega_N t + \phi))$, (the shape of the spectra is shown in Figure 1.3.1 b). This is called **free induction decay** (**FID**), which is one of the read-out techniques of spin state in pulsed EPR. Fourier transformation of FID gives the Larmor angular frequency $2\omega_L$, while the linewidth represents T_m.

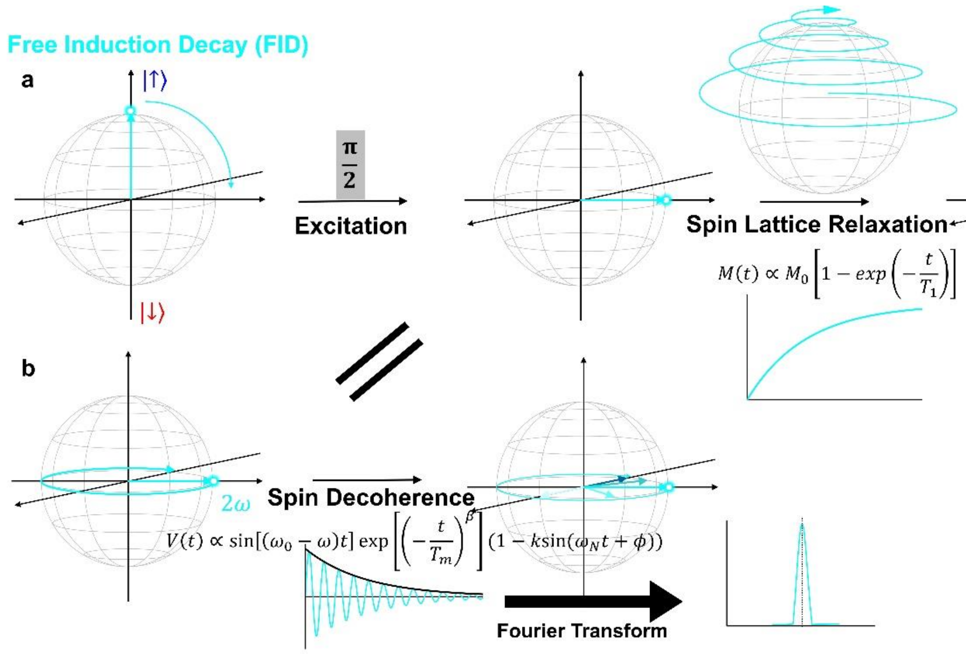

Figure1.3.1. Schematic illustration of two relaxation processes (spin-lattice relaxation (a) and spin decoherence (b)), and pulse sequences of free induction decay (FID).

Hahn-echo

Although T_m can be obtained from FID, it is often measured with another technique called **Hahn-echo**. In 1950, Erwin Hahn discovered that the applying of a π pulse enables to refocus of the spin in decoherence, giving a strong signal so-called echo. Figure 1.3.2 illustrates the procedure of a Hahn-echo measurement. It consists of the following sequence:

(1) Initially, spins are aligned up.

(2) A π/2 pulse rotates the spins to $\theta = \pi/2$.

(3) Decoherence happens during some period (τ), resulting in not aligned spin direction.

(4) Spins are flipped by the application of π pulse.

(5) Spin refocuses since the slower spins come first, and the faster ones come later.

(6) After the same time interval τ, all spins gather to give a strong signal, which is called an **echo**.

The signal strength of the echo is expressed as a function of t $\exp\left(-\frac{t}{T_2}\right)$, thus T_2 is obtained from Hahn-echo by varying τ.

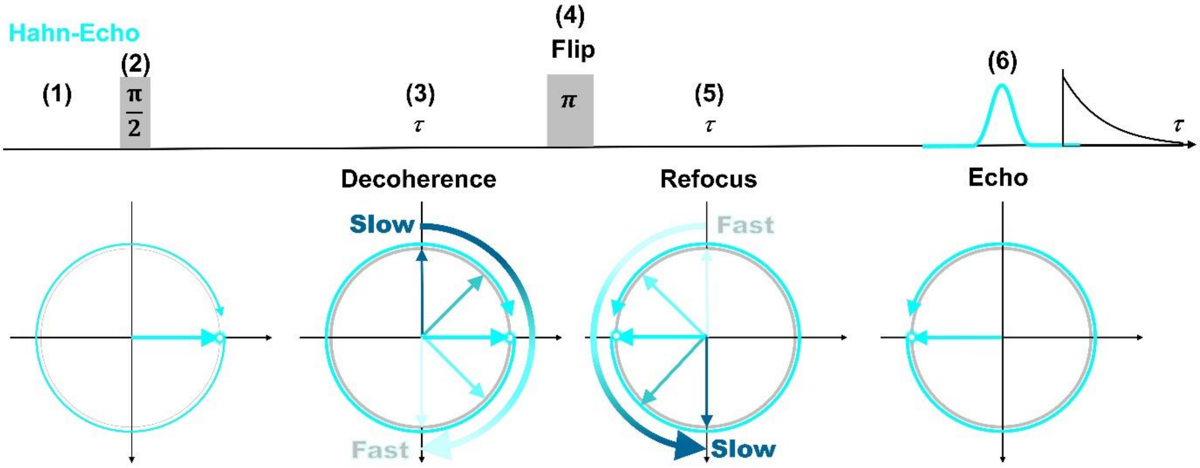

Figure1.3.2. Schematic illustration of pulse sequences of Hahn-echo. The numbers in brackets correspond to the sequence described in the text. The bottom represents the cross section (alongside the equator) of the Bloch sphere at the corresponding moment in the sequence.

Saturation recovery

Hahn-echo is a powerful tool for reading out the spin states, thus it is utilized to detect other parameters. For instance, T_1 is measured using the **Saturation recovery** technique. The sequence is depicted in Figure 1.3.3, explained as follows:

(1) The initial spin state is up.

(2) A π/2 pulse is applied.

(3) Spin-lattice relaxation takes place during some period.

(4) Another π/2 pulse will be applied after a waiting time T_R before the spin has fully relaxed to up. This process is repeated several times to enhance the echo intensity.

(5) After a waiting time T after the n^{th} pulse, a normal Hahn-echo sequence is applied.

Importantly, with short T, spins cannot recover to the initial state, therefore the echo is weak. Echo intensity versus T is governed by the function $1 - \exp(-t/T_1)$, hence saturation recovery gives information about T_1.

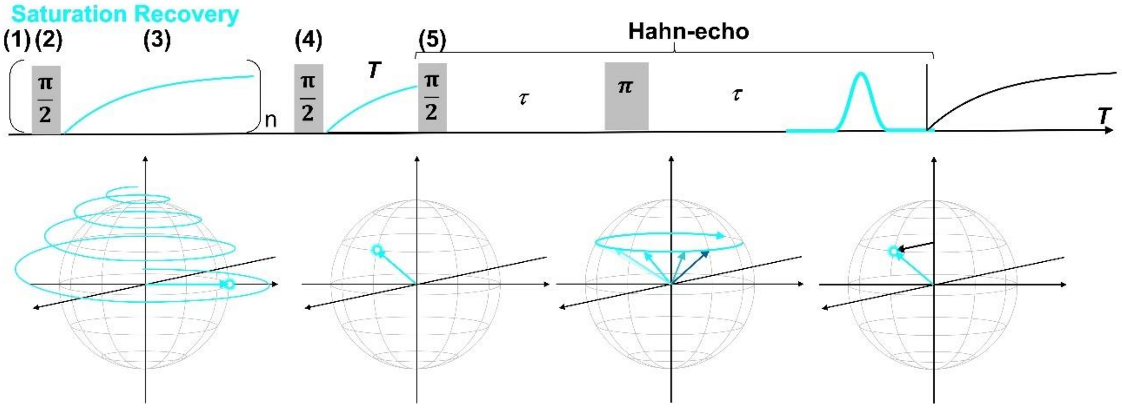

Figure1.3.3. Schematic illustration of pulse sequences of saturation recovery. The numbers in brackets correspond to the sequence described in the manuscript. The bottom represents the Bloch sphere at the corresponding moment in the sequence.

Spin nutation

As explained in Section 1.3.2, Rabi oscillation serves as a criterion of whether the system is capable of being manipulated coherently. It can be detected as echoes using the technique of so-called spin nutation (Figure 1.3.4). The sequence is as follows:

(1) The initial state is up.

(2) The nutation pulse is applied. While the pulse is applied, Rabi oscillation takes place, as explained in Section 1.2.

(3) After T_p, the irradiation of the pulse is stopped, and then left for T.

(4) A Hahn-echo sequence is performed.

Note that the tipping angle of spin depends on T_p, resulting in different echo strengths. T_p versus echo intensity reflects Rabi oscillation. Practically, this spectrum is used as a proof that the system can work as a qubit.

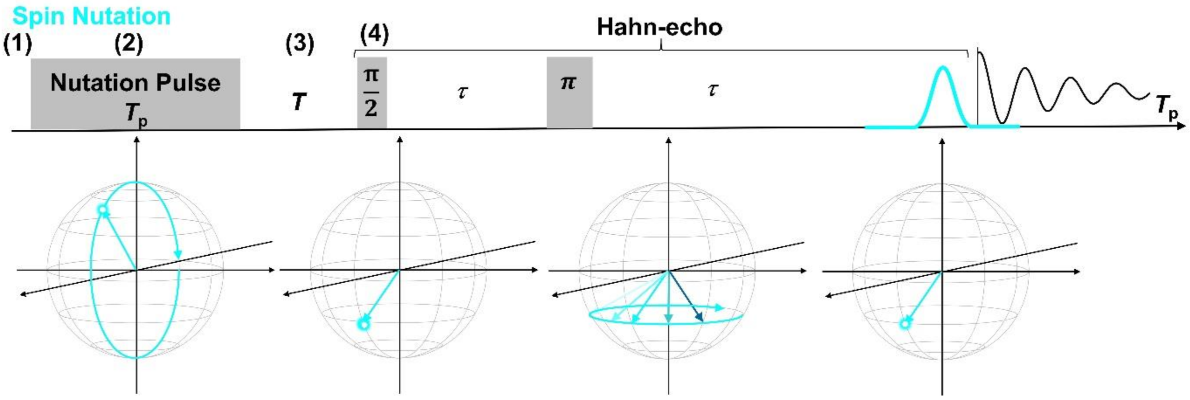

Figure 1.3.4. Schematic illustration of pulse sequences of spin nutation. The numbers in the brackets correspond to the sequence described in the manuscript. The bottom represents the Bloch sphere at the corresponding moment in the sequence.

Summary

The pulsed EPR, including initialization, manipulation, and read-out of spin-state was introduced. Two techniques for readout were explained: FID and Hahn-echo. As explained at the beginning of this section, the sequences presented above are basic ones: more complicated sequences using more pulses have been and are being reported.[26,27] Nevertheless, T_1, T_m, and Rabi oscillation are fundamental requirements for qubits. In the next chapter, some examples of molecular qubits will be described. Notably, those parameters play roles.

1.3.3. Metal Complex-Based Electron Spin Qubit

As discussed above, an electron spin has two coherent spin states under a non-zero magnetic field, which can be operated and/or measured using the EPR technique. Therefore, electron spin qualifies as a qubit. Among candidates, molecular spin qubits have been gaining a huge interest owing to their monodispersity and structural tunability.[18–21] The simplest yet essential example are molecules with a spin of $S = 1/2$, such as specific kinds of metal complexes and organic radicals.

Single qubits with long decoherence time

As described in Section 1.2, the performance of qubits is assessed based on DiVincenzo's five criteria. Among these criteria, decoherence time is paramount, as it can pose a significant obstacle to the development of multi-qubit arrays. As explained in Section 1.3.2.2, the spin-lattice relaxation time determines the upper limit of decoherence time, therefore both T_1 and T_m need to be considered. Again, as explained above, T_1 is caused by the absorption/emission of phonons from the environment, while T_m is derived from the perturbation of either g, β, or B. Consequently, numerous studies have focused on extending both the spin-lattice relaxation time and the decoherence time. Some examples are shown in Figure 1.4.1, which clearly shows the dependence on chemical families.

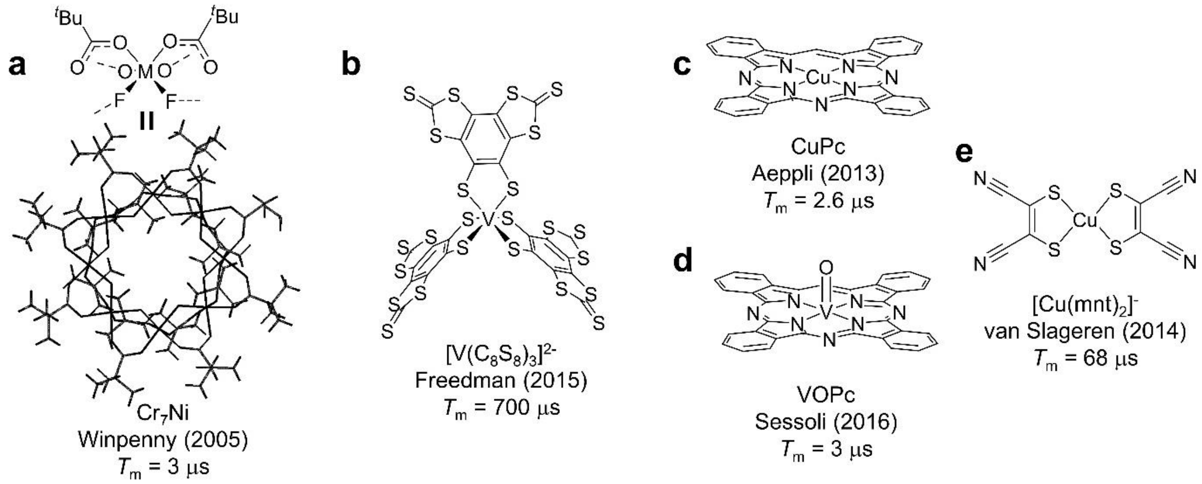

Figure 1.4.1. The structure of molecules with long decoherent times. (a) Cr_7Ni,[31,32] (b) $[V(C_8S_8)_3]^{2-}$,[33] (c) CuPc,[34] (d) VOPc, [35] (e) $[Cu(mnt)_2]^-$.[36]

An early example was demonstrated by Winpenny and coworkers in a Cr_7Ni cluster (Figure 1.4.1 a).[31,32] The cluster has seven Cr^{3+} ($S = 3/2$) and one Ni^{2+} ($S = 1$) antiferromagnetically coupled, resulting in $S = 1/2$.The influence of the ligand is also studied in Cr_7Ni, where the change of the central cation and peripheral functional group induces improvement of T_m from the original ($T_m = 3$ μs)[31] to the improved one ($T_m = 15$ μs)[37]. This improvement was particularly notable when the peripherals were deuterated, and the central cation was free from the rotary methyl group, both of which might cause an inhomogeneous magnetic field.

As of 2024, $[V(C_8S_8)_3]^{2-}$, reported by Freedman and coworkers in 2015, exhibited the longest T_m (700 μs) (Figure 1.4.1 b).[33] The study reported the impact of both structural modifications and environmental factors, namely the solvent. Various nuclear-spin-free ligands were investigated, showing slightly varied T_m values (1-4 μs at 80 K). In addition, the importance of deuteration was revealed when removing hyperfine interaction to have the highest T_m. Furthermore, they investigated the influence of the solvent as well, resulting in T_m of $[V(C_8S_8)_3]^{2-}$ varied from 1.5 μs in butyronitrile (PrCN) to 675 μs in carbon disulfide (CS_2). These results indicate that not only the nuclear spin inside of the molecule but also that of solvents plays a significant role in improving T_m.

Another aspect is the temperature dependence of T_m. In 2013, Aeppli and coworkers reported an EPR study on a thin layer of CuPc (Figure 1.4.1 c).[34] Although the longest spin decoherence time they observed (T_m = 2.6 μs) is not very long, it remains unchanged even at 80 K. Later in 2016, Sessoli and coworkers reported an EPR study on VOPc diluted in a crystal matrix of TiOPc (Figure 1.4.1 d).[35] They expanded the temperature range up to room temperature (T_m ~ 1 μs at 300 K). In both cases, the structural rigidity of phthalocyanine ligands may help with long coherence lifetime. Apart from phthalocyanine, in 2014, van Slageren and coworkers reported room-temperature coherence in the dithiolene complex $(PPh_4)_2[Cu(mnt)_2]$ in DMF (Figure 1.4.1 e).[36] The absence of nuclear spin, as well as rigid structure, enabled room temperature coherence (T_m ~ 1 μs at 300 K).

The correlation between phonon modes and spin-lattice/spin decoherence time has been intensively studied. For example, in 2023, Carretta and coworkers demonstrated inelastic X-ray scattering (IXS) together with DFT calculations. Earlier studies from Lunghi clarified that spin-phonon relaxation at temperatures above 10-20 K is due to a spin-phonon Raman mechanism (see Section 1.4.2, relaxation mechanism of SMM).[38,39] Therefore, they achieved simulated T_1 assuming this mechanism, which matched well with the experimental data. Notably, they achieved better T_1 results from simulation by excluding low-energy phonons (1-2 meV). Their IXS results revealed that the phonon mode at 1.5 meV is attributed to the distortion of the phenyl rings and the bending of the porphyrin ring. They simulated T_m as well, which also matched well with experimental results.

Overall, various molecules have been studied in pursuit of elongated T_1 and T_m. Several strategies have been pointed out to improve T_1 / T_m, such as removing nuclear spin, avoiding the use of rotary groups (e.g. methyl group), choosing an appropriate solvent such as CS_2, employing rigid structure and removing low-energy phonon modes.

Qubits with scalability

According to DiVincenzo’s criteria, qubit scalability is essential because the implementation of a quantum computer requires not just one, but many qubits. Most of the single qubit studies mentioned above are conducted on solution samples, thus a more densely packed systems are needed. Metal-organic frameworks (MOFs) are suitable for this purpose. Derived from the single qubits mentioned above and their structural derivatives, porphyrin-based MOFs (Por-MOFs) are a good choice due to their accessibility.[40] There are some porphyrin MOF-based qubits, three of which are listed in Figure 1.4.2. In 2017, Freedman and coworkers reported a Por-MOF based on 7% of low-spin Co(II)（S=1/2）in Zn (II) (S=0) (Figure 1.4.2 a).[41] The strong hyperfine coupling of M_S and M_I causes non-degeneracy (so-called avoided level crossing), which gives longer T_m = 14 μs. In 2018, Yamashita and coworkers reported a Por-MOF based on 2% of VO in TiO porphyrins (Figure 1.4.2 b).[42] They highlighted the extended T_1 compared to single molecules, attributing it to the suppression of distortion vibrations by the rigid structure of the MOF. Those two above mentioned studies are diluted ones, therefore there is still some space for scalability. In 2020, Freedman and coworkers reported a CuPor-MOF with Zr linker (Figure 1.4.2 c).[43] Rather good separation (one qubit per every 13.6 Å) enabled coherent manipulation even without dilution. This MOF features high qubits density, leading to scalability.

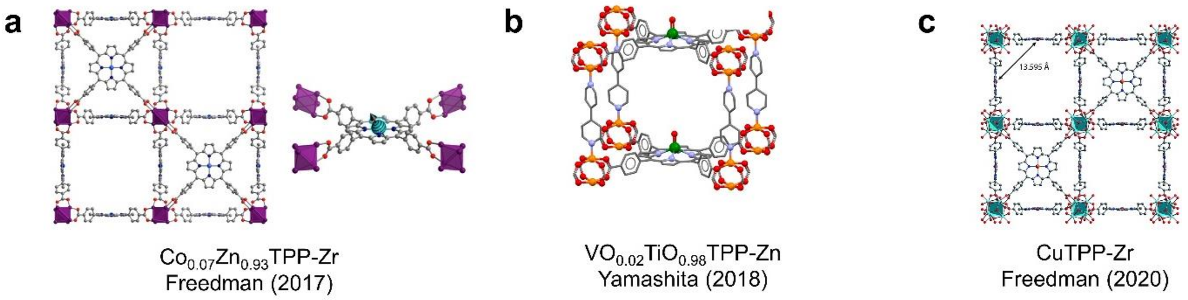

$Co_{0.07}Zn_{0.93}$TPP-Zr
Freedman (2017)

$VO_{0.02}TiO_{0.98}$TPP-Zn
Yamashita (2018)

CuTPP-Zr
Freedman (2020)

Figure 1.4.2. MOF qubits with larger scalability. Figure are reproduced from ref[41], ref[42], and ref[43] for a-c, respectively.

Multi-qubit gates

Classical computers rely on a combination of logic gates. Similarly, the implementation of a quantum computer requires a universal qubit gate. The “Controlled NOT” (**CNOT**) gate is the fundamental qubit gates, which is a quantum counterpart of the classic NOT gate. In classical computing, a NOT gate outputs the opposite of the input, as shown in Table 1.1.

Table 1. 1. Truth table of a classical NOT gate.

input	output
1	0
0	1

A CNOT gate consists of two qubits, where one qubit (target) is inverted similar to the NOT gate, only when the imput 1 (control qubit) is is in the state |1⟩, as represented in Table 1.2.

Table 1. 2. Truth table of quantum CNOT gate.

input 1	input 2	output 1	output 2
|0>	|0>	|0>	|0>
|0>	|1>	|0>	|1>
|1>	|0>	|1>	|1>
|1>	|1>	|1>	|0>

In electron spin qubits, weakly coupled two-spin systems with *g* asymmetry satisfy the above conditions. As described in Section 1.3.2.1, the EPR spectra of two weakly coupled $S = 1/2$ systems show four transitions that are attributed to the flip of two spins, which are split into two depending on the state of the other spin. In other words, by selectively controlling these transitions, a CNOT gate can be implemented. This was evidenced by Aromi and coworkers in 2017 using a Cerium - Erbium complex (CeEr, Figure 1.4.3 a).[44] They first prepared the La-Er and Ce-Y complexes, each of them having quasi $S = 1/2$ with $g_z = 10.00, 2.67$ owing to the Er and Ce centers, respectively. They also prepared the Ce-Er complex having two $S = 1/2$, which are exchange-coupled with $J_{\mathrm{Ce\text{-}Er}} = -0.015$ K. The weak exchange coupling enables four states with four transitions. They performed spin-echo measurements for the transition $|00\rangle \rightarrow |01\rangle$, presenting $T_m = 410$ ns. Overall, the use of two different metals is an effective approach to obtain a g-asymmetric two-spin system.

Another strategy is to employ dinuclear complexes with distortion angles. In 2023, Sessoli and coworkers demonstrated VOPor dimer, which consists of two oxovanadyl porphyrins linked at their meso positions (Figure 1.4.3 b).[45] The distortion between two porphyrin planes causes weak coupling $J \sim 10^{-2}$ cm^{-1} and strong anisotropy of the hyperfine tensor, as determined by frozen solution EPR. The relationship between the distortion angle and the observed EPR transition was further examined using angle-dependent CW EPR on two single-crystals of the VO-Por, one with a distortion angle of 64°, and the other with 72°. T_1 and T_m were measured for the VOPor dimer, showing its similar behavior to the monomer. They also reported the simulation of four states, revealing its potential for four independent transitions. Later, the same group reported a VOPor-CuPor dimer (Figure 1.4.3 c).[46] In this case, the transition of two spins is distinguished not only by hyperfine anisotropy but also by *g* asymmetry, making the energy separation of spin states angle-independent. Weak exchange coupling and unchanged relaxation behavior (T_1, T_m) from the monomers were also observed in VOPor-CuPor. Combining these results, they demonstrated that VOPor is a candidate for the construction of a CNOT gate.

Another approach involves linking two qubits with a switchable (paramagnetic/diamagnetic) linker. In 2016, Winpenny and coworkers reported metal clusters containing two Cr_7Ni (Cr_7Ni-$Co(SCN)_2$- Cr_7Ni, Figure 1.4.3 c), one with terpyridine and the other with pyridine, both of them coordinated to the Co ion, which is redox-switchable from Co(II) (diamagnetic) to Co(III) (LS paramagnetic, S = 1/2).[47] Utilizing different linkers, such as terpyridine and pyridine, allows for orthogonal alignments of two Cr_7Ni units. Two semi-isotropic Cr_7Ni were weakly exchange-coupled to anisotropic Co, resulting in eight addressable spin states.

To summarize, for CNOT gates, individual addressing of two weakly coupled spins is necessary. Some strategies have been utilized, such as the use of different metals with *g*-asymmetry, the introduction of a distortion angle for *g*-anisotropy, and the introduction of the third spin coupled to two spins with different strengths.

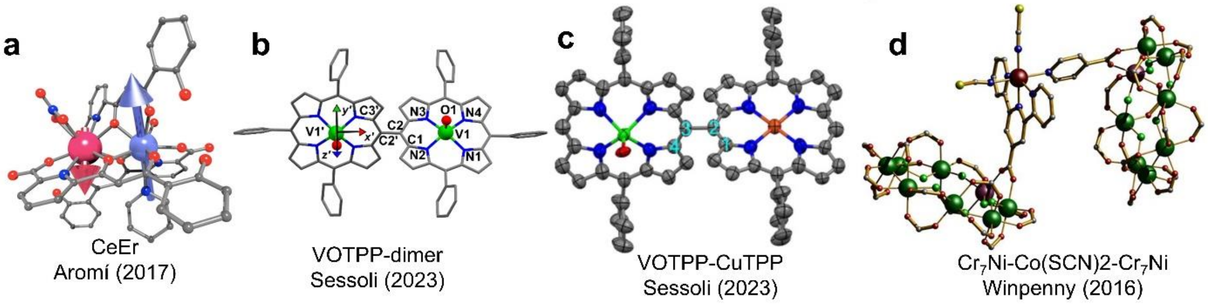

Figure 1.4.3. Di- or Multi-nuclear metal complexes studied as CNOT gate. Figures are reproduced with modification from ref.[44], ref.[45], ref.[46], and ref.[47] for a-d, respectively.

Summary

In this chapter, molecular qubits were introduced, to highlight the congruity of complexes as molecular qubit, as well as the accessibility of scalability and quantum gates. QTM-based qubits were excluded to an independent Section 1.4.4, since it is closely related to single-molecule magnets, therefore, better to explain after its introduction. In the next section, apart from metal complexes, organic radicals will now be explained.

1.3.4. Organic Radicals as Electron Spin Qubits

Organic radicals are organic molecules that have an unpaired electron (or multiple unpaired electrons). Odd-numbered valence electrons typically do not satisfy the octet rule, making the vast majority of organic radicals unstable. However, after the first discovery of a stable radical, the triphenylmethyl (trityl) radical by Gomberg in 1900,[48] various types of stable radicals have been found, as summarized in the book "*Stable Radicals: Fundamentals and Applied Aspects of Odd-Electron Compounds* (2010)".[49] As the variety of structures has extended, so has the field of application, including optics,[50] electronics,[51] and so on. This expansion led to the publication of a special issue of Chemical Reviews named "*Persistent and Stable Organic Radicals*" which was published recently in 2024.[52] Like metal complexes, organic radicals can be utilized for QIP. In fact, there are quite a few studies on radical-based quantum bits, summarized in a recent review from Sun and coworkers.[53] This chapter will summarize not only the studies discussed in this review but also those involving radical-chromophore qubits and excited state multiplet-based qudits.

Monoradicals for single qubits

In the realm of radical-based QIP, monoradicals correspond to the role of a single qubit. A key distinction between radicals and metal complexes lies in the absence of spin-orbital coupling in radicals, which is expected to elongate T_1. Although their spin relaxation times are not as extensively studied for qubits as those of metal complexes, there are quite a few reports of T_1 and T_m on radicals.[53] Some examples of organic radicals exhibiting long decoherence time are represented in Figure 1.5.1.

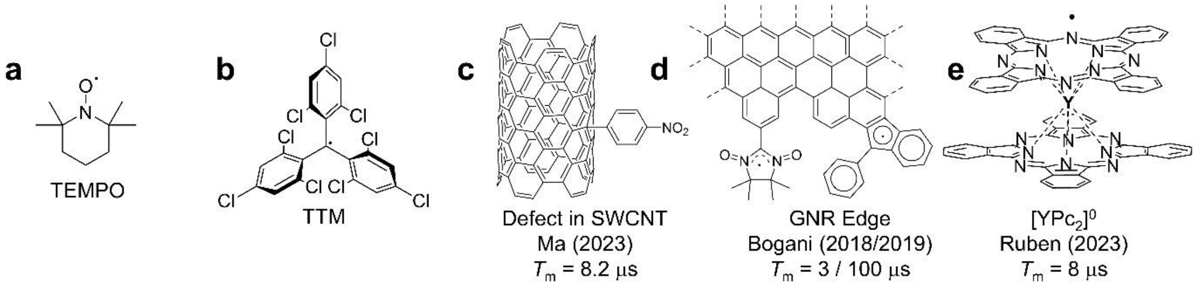

Figure 1.5.1. Monoradicals with long decoherence time. Note that TEMPO and TTM have not been studied for their single-qubit performance, though they are frequently used as qubit motif. SWCNT, GNR, and $[\mathrm{YPc}_2]^0$ are reported in ref. 54, [55] and [56], and [57], respectively.

In 2023, Ma and coworkers reported the decoherence time of the defects in single-wall carbon nanotube (SWCNT) (Figure 1.5.1 c).[54] It is known that SWCNT reacts with diazonium salts to give a defect, having $S = 1/2$.[58,59] In the study, they performed Hahn-echo and saturation recovery on the defect of SWCNT to obtain T_1 = 13 ms and T_m = 8.2 μs at 5 K. They claimed that T_1>> T_m means T_m can be elongated; this was supported by simulation results for the effects of different environmental spins such as ^1H, ^2H, and ^{13}C in the solvent/molecule.

Other carbon allotropes have been studied as qubit candidates as well. In 2018, Bogani and coworkers reported coherent spin manipulation of graphene nanoribbons (GNR) (Figure 1.5.1 d).[55] They have prepared GNR edge-functionalized with a nitronyl nitroxide (NIT) radical in a bottom-up synthetic approach. EPR studies revealed that its decoherence is T_m = 3 μs at room temperature even without optimization (such as deuteration, isotope enrichment with ^{15}N, etc.). Later in 2019, Bogani and coworkers reported 11,11′ - dibromo-5,5′ -bichrysene functionalized GNR.[56] By changing the solvent from toluene to CS_2, and by using the nuclear decoupling techniques, the decoherence time could be elongated up to T_m = 240 μs at 120 K.

On the other hand, the use of neutral bis(phthalocyaninato)yttrium(III) $[YPc_2]^0$ was reported in 2021 by Boudalis *et al*., conducting EPR studies on crystalline powder of $[YPc_2]^0$ (Figure 1.5.1 e).[60] The study highlighted strong anti-ferromagnetic intermolecular interaction due to close intermolecular π-π distances (3.2 Å). This result matched with the prior study of solid state ^1H-NMR on $[YPc_2]^0$.[61] Later in 2023, Suryadevara *et al*. reported a solution-based EPR study on $[YPc_2]^0$ and a porphrinato-phthalocyaninato yttrium(III)complex ($[YPcPor]^0$).[57] $[YPc_2]^0$ showed high T_1 (1 s at 10 K), and comparable T_m (8 μs at 40 K). $[YPcPor]^0$ also exhibited a long T_1 (0.9 s at 10 K), which proves that long spin-lattice relaxation time is the nature of bis(phthalocyanine)yttrium(III) complexes. Note that no optimization (deutration, use of CS_2, *etc*.) was adopted, suggesting potential for further improvement. Overall, organic radicals exhibit long T_1 due to their negligible spin-orbit coupling. On the other hand, the longest T_m is still not as long as those observed in $[V(C_8S_8)_3]^{2-}$, likely due to the limited optimization and fewer studies on radicals.

Radical-bearing assembly / polymers for scalability

As in the case of metal complexes, Por-MOF helps to construct densely packed qubit arrays, leading to scalability. In the case of radicals, not only MOFs, but also covalent organic frameworks (COFs), block chain copolymers, and self-assembled monolayers (SAM) have been reported (Figure 1.5.2).

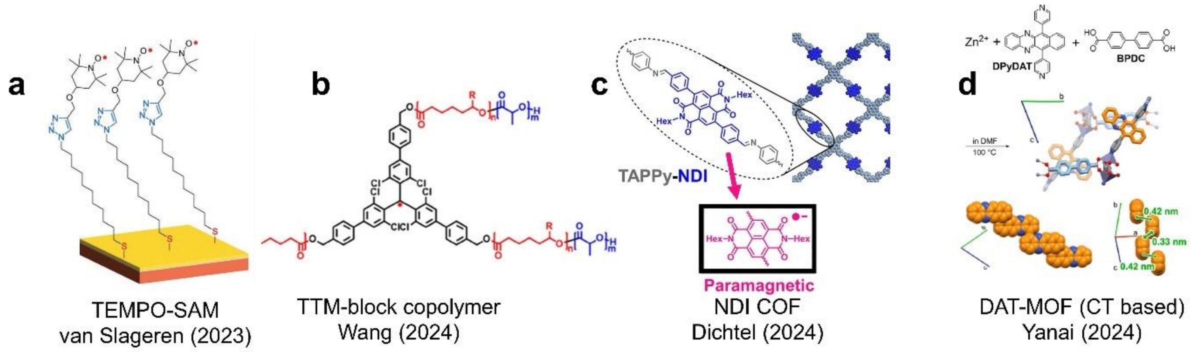

TEMPO-SAM
van Slageren (2023)

TTM-block copolymer
Wang (2024)

Paramagnetic
NDI COF
Dichtel (2024)

DAT-MOF (CT based)
Yanai (2024)

Figure 1.5.2. Radicals aiming at larger scalability with different approaches. Figures are reproduced with modification from ref 62, 63, 64, and 65 for a-d, respectively.

In 2023, van Slageren and coworkers reported a TEMPO-based SAM on a gold substrate (Figure 1.5.2 a).[62] Acetylene-tethered TEMPO was reacted with a pre-formed SAM having azide at the terminal position to form TEMPO monolayer. The TEMPO SAM presented improved T_m compared with the monomer in solution, even without dilution (T_m = 13.5 μs for SAM, while T_m = 3.2 μs for monomer, both were measured at 10 K).

In 2024, Wang and coworkers reported block copolymer incorporating trichloro triphenyl methyl (TTM) radicals (Figure 1.5.2 b).[63] Since TTM is known for its doublet-based luminescence,[50] they performed a combined study of polymer morphology/coherence time/luminescence. Note that even in the best case, the performance is not as good as other radicals shown in Figure 1.5.1 (T_m = 0.3 μs at 30 K).

COFs are also unique in radical chemistry. In 2024, Dichtel *et al*. reported a COF constructed from redox-active naphthalene diimide (NDI) (Figure 1.5.2 c).[64] The radical was introduced via the reduction of NDI by adding a controlled amount of cobaltocene. The use of COFs is advantageous since ions and neutral molecules typically cannot be co-crystalized. The relaxation times (T_1 = 164 ms, T_m = 2.36 μs) were obtained at 10 K. They noted that higher concentrations lead to shorter T_m, which they attributed to either dipolar interaction between radicals, or nuclear spins of countercations.

The use of a radical generated through charge separation was demonstrated by Yanai and coworkers in 2023 (Figure 1.5.2 d).[65] They prepared a MOF constructed with Zn^{2+}, 4,4’-biphenyl-dicarboxylic acid, and 5,12-diazatetracene (DAT). Despite the absence of a radical in the original MOF, it undergoes conversion into a radical through the following process: under photo-irradiation at a wavelength of λ = 532 nm, DAT is excited and undergoes intersystem crossing (ISC). The triplet is then converted into a radical via charge separation, which has a lifetime of a few hours. Both the triplet states and the radical were characterized using transient

EPR (tr-EPR) and EPR respectively. The authors emphasized that the generated radical is spin-polarized: the radical in the thermal equilibrium of $|\uparrow\rangle$ and $|\downarrow\rangle$ is polarized into $|\downarrow\rangle$ via polarization from triplet (T_0 — ↑ to T_1 — ↓, the representation is shown in eq.1.23 — 1.25), which is originally polarized. The polarization of the radical spin state enables room temperature coherent manipulation, with T_1 = 214 μs and T_m = 0.98 μs.

Diradicals for quantum gates

There are some reports utilizing diradicals as multiqubit gates. In 2012, Takui and coworkers. reported a prototypical diradical CNOT gate using a TEMPO dimer (Figure 1.5.3 a).[66] It has two TEMPO motifs isolated in ~2 nm, resulting in a weak exchange coupling. They used deuterated and ^{15}N enriched TEMPO to obtain spectra with narrow linewidths, which enable independent addressing of spin states of two spins. Furthermore, the non-linear alignment of the two TEMPO moieties enabled a non-co-linear g-tensor. Owing to these factors, the compound showed well-characterized signals in EPR measurements on a diluted single crystal. They demonstrated spin nutation on one of the transitions, clearly showing Rabi oscillation with a duration time of 200 ns.

Later in 2023, Winpenny and coworkers further investigated TEMPO dimers employing the same strategy to what has been done for NMR-based qubit studies (Figure 1.5.3 b).[67] They designed TEMPO-linkers so that the exchange coupling would be $\frac{h}{T_m} < J < \frac{h}{T_{manip.}}$ ($T_{manip.}$ is the single-qubit operation time, determined to be 22 – 32 ns). By using different pulesd EPR protocols, entanglement and read-out of the spin states could be achieved. Most importantly, using multi-frequency pulse sequences such as double electron-electron resonance (DEER), they demonstrated quantum tomography, which describes quantum states. With the obtained tomography, they determined a pseudo fidelity of 0.78, which measures how closely a quantum operation approximates an ideal operation. Although these two studies have little similarity (the former is an EPR study on a diluted crystal aiming at individual spin addressing, while the latter being an EPR study on a solution sample to demonstrate multi-frequency pulse sequence), they clearly evidenced the utility of TEMPO.

Another system is pentachloro(triphenyl)methyl (PTM) dimer. In 2023, van Slageren and coworkers reported EPR studies on a PTM radical and a PTM dimer (Figure 1.5.3 c).[68] Although it has nuclear spin-rich chlorine substituents (^{35}Cl, I = 3/2), the absence of protons, as well as its solubility in CS_2, enables long decoherence times (T_m = 148 μs up to 100 K). DEER, as well as the single-frequency technique for refocusing (SIFTER) and double quantum coherence (DQC), prevent exchange coupling, thus enabling independent addressing of two spins. They also emphasized that chemical functionalization would lead to photo-emissive PTM dimers.

The diradicals mentioned above, except for Takui's system, are not applicable as CNOT gates, since two identical spins cannot be identified as control/read-out bits. In 2020, Wasielewski and coworkers reported a CNOT gate candidate using an excited state diradical (Figure 1.5.3 d).[69] They used the molecule functionalized with tetrathiafulvalene (TTF), 8-aminonaphthalene-1,8-dicarboximide (ANI), and pyromellitimide (PI), aiming at photoexcitation of TTF (TTF*-ANI-PI) followed by charge transfer (TTF•-ANI-PI•). The resulting diradical (TTF•-ANI-PI•) has two spins with different *g*-tensors, owing to the different environments of TTF and PI. Both TTF and PI have T_m ~ 1 ms. They emphasized that their system has initial pure states (singlet) due to the spin selection rule. By comparing to ground-state diradicals the initial state was defined as pseudo-pure, depending on the Boltzmann distribution.

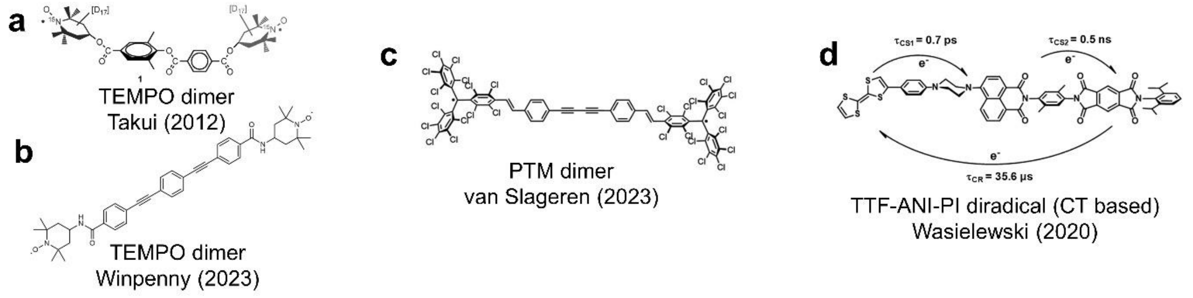

Figure 1.5.3. Chemical structures of diradicals for quantum gates. Figures are reproduced with modification from ref. 66, 67, 68, and 69 for a-d, respectively.

Multiplet-based qudits

A variety of studies using excited multiplets for QIP have been carried out. Multiplets (triplet, quartet, quintet, etc.) offer a higher multiplicity than two, therefore it is typically referred to as qu***d***it (d represents multiplicity). As two-level states can be represented by the surface of the Bloch sphere, which is a two-dimensional Euclidean plane, d-level states are represented in d dimensional Hilbert space. The challenge in using closed-shell chromophores as triplet qubits lies in their low triplet yield, since singlet (S = 0) to triplet (S = 1) transitions are spin-forbidden. One solution is to attach a radical to a chromophore. Radical-chromophore molecules allow enhanced intersystem crossing (EISC) due to either spin-allowed electron exchange or large spin-orbit coupling with the radical, meaning that ISC of the chromophore is no longer spin-forbidden.[70] Varieties of chromophore-radical systems have been studied.[71] Among those molecules, the TEMPO-PDI system is the most widely studied as of 2024 (Figure 1.5.4 a).[72–76] The intermediate interaction between TEMPO and PDI enabled high triplet yields. Because of the relaxation to the ground state that is spin-forbidden, the excited trip-quartet state has a long lifetime. Coherent manipulation of trip-quartet state with long decoherence time has been achieved through chemical modification, resulting in T_m = 4.2 μs at 85 K.[76] In this case, the excited states lose energy through non-radiative paths, making optical readout of spin states impossible.

On the other hand, there is an example of the optical readout of an excited multiplet. In 2023, Evans and coworkers reported a TTM-anthracene (An) monoradical and a TTM-An-TTM diradical (Figure 1.5.4 b).[77] They designed molecules so that the energy levels between the excited triplet of An and the excited doublet level of TTM would match. TTM was attached to carbazole due to its high quantum yield.[78] Transient spectroscopy measurements (absorption, emission, EPR) revealed that the excitation of the doublet ($^2[D_1\text{-}S_0]$) immediately yields (in picosecond order) a triplet state in An ($^2[D_0\text{-}T_1]$), which is converted to a quartet ($^4[D_0\text{-}T_1]$) through ISC in tens of nanoseconds. Transient spin nutation was also performed, demonstrating coherent manipulation of quartet states. The low energy gap between $^2[D_1\text{-}S_0]$ and $^2[D_0\text{-}T_1]$ enables back transfer, resulting in doublet-based emission with high quantum yield. Owing to these properties, they demonstrated optical readout of spin states using the technique of optically detected magnetic resonance (ODMR), commonly adopted in NV centers in diamond. Furthermore, they investigated a TTM-An-TTM diradical. The diradical, which is in its ground state weakly or negligibly exchange coupled, results in a strongly correlated quintet state $^5[D_0\text{-}T_1\text{-}D_0]$. The quintet state can be coherently manipulated at room temperature, with a lifetime of 20 μs.

As explained above, typically, closed-shell organic compounds do not undergo ISC; however, there are some exceptions. One of them is fullerene C_{70}, which undergoes ISC with a 90% yield.[79] In 2021, Gao and coworkers reported the coherent manipulation of the excited triplet state of C_{70}, which they call qutrit (Figure 1.5.4 c).[80] They performed tr-EPR to reveal T_1 = 3-5 ms and T_m = 13-20 μs, respectively. Their coherent state was presented in tomography, while the operation was demonstrated by quantum interference.

Another candidate molecule is pentacene, known for its singlet fission properties. Singlet fission is a phenomenon where a photogenerated singlet exciton is coupled to a neighboring chromophore, resulting in a pair of triplet excitons.[81,82] In 2024, Yanai and coworkers demonstrated the use of a triplet pair of pentacene as a qudit (Figure 1.5.4 d).[83] They first prepared the MOF from 4,4′ -(pentacene- 6,13- diyl)dibenzoic acid (PDBA) and $ZrCl_4$, ensuring a regulated distance of 0.35 nm between the nearest pentacene pairs. Transient absorption spectra and tr-EPR clarified that the MOF can successfully produce triplet-pairs, which can further be converted into a quintet state. They performed tr-pulsed EPR on the quintet state, revealing T_1 = 3.8 μs, T_m = 150 ns at room temperature, and demonstrated spin nutation to show Rabi oscillation. This comprehensive understanding of multiplet excitons facilitates the realization of qudits.

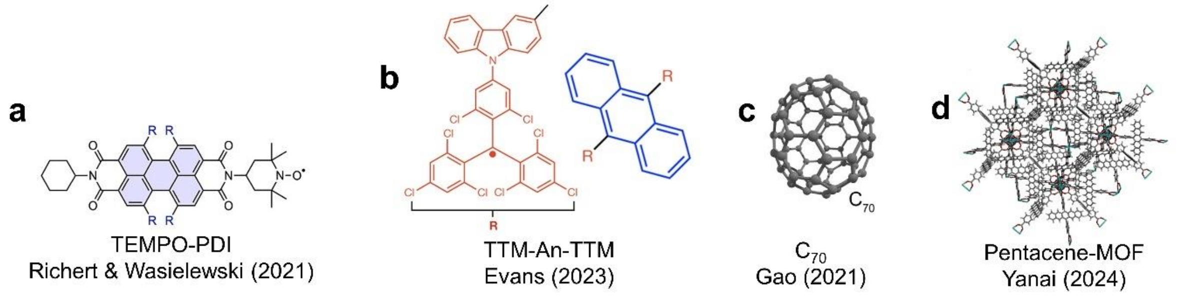

Figure 1.5.4. Molecules studied as qudits using their multiplet. Figure a-d are reproduced with modification from ref.71, 77, 80, and 83, respectively.

Summary

In Section 1.3.4, the studies on radicals for QIP were summarized. One notable feature of organic radicals is their lack of SOC, which contributes to their long T_1. Although efforts to enhance decoherence time are limited, some studies suggest that strategies effective for transition metals, such as deuteration and the use of CS_2, may also be applicable to radicals. For scalability, different strategies have been adopted, which might be also applied in transition metal complexes.

The simplest strategy to construct a CNOT gate is using different metals such as Ce-Er, though this approach does not apply to radicals. Nevertheless, various strategies have been reported, such as designing a diradical with different tipping angles and nuclear spin anisotropy or generating *g*-asymmetric diradicals through photo-irradiation. In addition, various useful pulse techniques such as DEER have been demonstrated.

Importantly, many of the studies on radical-based QIP derive from different fields of science. For example, defects in SWCNT have been studied for their photoluminescence,[58] while peripheric spins on GNRs are strongly correlated with edge effects in graphene electronics.[55] TTM radicals have been studied for their unique doublet emission,[50,84] which was utilized for optical readout of the spin state. I believe that as more radical species from other fields are explored, the domain of radical-based QIP will continue to expand. QTM-based qubits were omitted despite radicals taking an important role, which will be explained in Section 1.4.4.

Spin is one of the most fundamental physical properties, having two levels that can be coherently manipulated via the EPR technique. Molecules, including metal complexes and organic radicals, are suitable for electron spin qubits due to their monodispersity and structural tunability. Although a wide variety of molecules have been investigated, further studies are needed for practical implementation. In the next section, single molecule magnets (SMMs) will be explained. While most research efforts have focused on memory applications at the nano scale, some studies are exploring the use of SMMs for QIP.

1.4. Single Molecule Magnet (SMM)

1.4.1. What is SMM?

According to "*A Dictionary of Physical Science* (1976)", the word "magnetism" is defined as:[85] "*The phenomenon produced by magnetic fields, involving interaction at a distance caused by the motion or spin of charged particles. ...*" Depending on the interactions, magnetism can be categorized into several groups, including ferromagnetism, antiferromagnetism, and paramagnetism. In particular, ferromagnetism, characterized by strong interaction with a non-zero total magnetic moment, allows materials to function as permanent magnets. However, these materials lose their permanent magnet properties as the domain size becomes smaller than a few nanometers, as many-body effects due to spin-spin interactions do not hold at the nanoscopic scale. As explained in Section 1.1, this hampers the development of Magnetoresistive Random-Access Memory (MRAM) with smaller sizes and larger capacities. To achieve further improvements, a permanent magnet driven by alternative mechanisms becomes necessary.

Single-molecule magnets (SMM) are molecules that can retain their magnetization for long period, independent of intermolecular interactions. The magnetism of SMMs is due to a doubly degenerate ground state with either an up or down spin, separated by an energy barrier known as U_{eff}.[86,87] The first example, discovered by Sessoli *et al.* in 1993, was a Mn_{12} cluster (Figure 1.6 a).[88] To illustrate the origin and criteria of SMMs, let's consider the Mn_{12} molecule. It consists of four Mn^{4+} having S = 3/2 and eight Mn^{3+} having S = 2, which are anti-ferromagnetically coupled resulting in the total spin of S = 10. As shown in Figure 1.6 a, the energy associated with the SMM property is attributed to ligand field (LF), exchange, and zero field splitting (ZFS). Consequently, the effective spin Hamiltonian can be described as follows:

$$H_{eff} = DS_z^2 + E\left(S_x^2 - S_y^2\right) \tag{1.26}$$

where D is the axial anisotropy parameter, and E is the rhombic anisotropy parameter, which is zero in axial symmetry. In the case of Mn_{12}, eq. 1.27 gives the energy:

$$E(M_S) = DM_S^2 \tag{1.27}$$

This is known as zero-field splitting. Therefore, when $D < 0$, the ground states are at the largest M_S (= S), and the energy barrier (shown in a grey arrow in Figure 1.6 a) is expressed as $\Delta = E(M_{Smax}) - E(M_{Smin}) = DS^2$. In the case of Mn_{12}, a negative D and a large total spin S leads to SMM behaviour.

In 2003, Ishikawa reported SMM behavior in $TbPc_2$, marking the first instance of a lanthanide-based single-ion magnet (Figure 1.6 b).[89] Since the orbital angular momentum L is retained for f electrons, the ground-state multiplets are characterized by a total angular momentum J arising from the spin–orbit coupling (SOC). As shown in Figure 1.6 b, in the case of lanthanide SMMs, the energy is attributed to SOC and LF. In this case, the effective spin Hamiltonian can be written as follows.

$$H_{eff} = \sum_{k=2}^{6} \sum_{q=-k}^{k} B_k^q \hat{O}_k^q \tag{1.28}$$

where B_k^q are the ligand field parameters, while $\hat{O}_k^q$ are the Steven's operators. In the case of $TbPc_2$, which has a Tb(III) ion surrounded by eight nitrogen atoms in a square-antiprism (SAP) configuration, it has a double-well energy potential with a high-spin ground state ($J = \pm 6$) and a large energy barrier $U_{\mathrm{eff}} = 400$ cm^{-1}. Since the spin Hamiltonian is highly dependent on the coordination environment, the choice of an appropriate chemical system is essential to achieve a high U_{eff}. In Section 1.4.3, the comparison of chemical species will be summarized.

SQUID magnetometry is a powerful tool to experimentally ascertain whether a molecule qualifies as a Single-Molecule Magnet (SMM), and determine the parameters such as U_{eff}, H_{c} and T_{B}. This will be described in the next section.

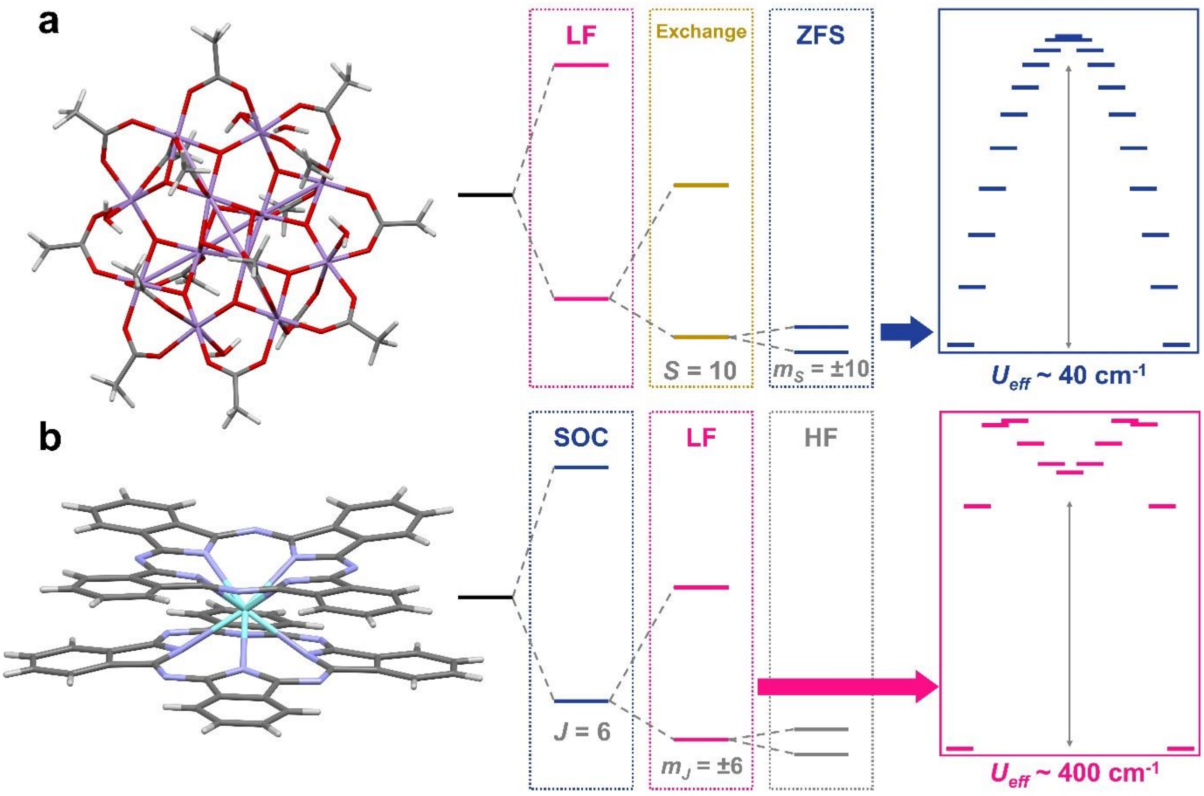

Figure 1.6. Molecular structure of Mn_{12} cluster (a) and $TbPc_2$ molecule (b), , along with their respective energy splitting diagrams (middle), and the diagrams determining their SMM property (right). The molecular structures are recreated using the reported structures (CCDC 1103442 and ref [90], respectively). The diagrams are inspired by ref [91] and ref [92].

1.4.2. Bulk magnetometry using a superconducting quantum interference device (SQUID)

Magnetometry is a technique employed to measure the magnetization M or the magnetic moment μ of a sample.[93] The Superconducting QUantum Interference Device (SQUID) is an electronic element composed of a superconductor circuit with either one or two Josephson junctions.[93] These Josephson junctions, which occur between two superconductors, allow tunneling (known as the Josephson effect). SQUIDs are exceptionally sensitive to changes in magnetization, making them valuable for magnetometry applications. One of the most common uses of a SQUID magnetometer is DC susceptibility measurement. In this method, the sample's magnetic susceptibility (χ) is measured under a DC magnetic field. The observed magnetization is converted into χ under the following approximation.

$$\chi = \frac{\partial M}{\partial H} \cong \frac{M}{H} \tag{1.29}$$

H : External magnetic field

Temperature-dependence of χ provides important informations. For example, at the high-temperature region, Curie-Weiss law is known to be true for χ.[94]

$$\chi = \frac{C}{T - \theta} \tag{1.30}$$

C : Curie constant
θ : Curie-Weiss temperature
T : temperature

At high temperatures where $T \gg \theta$, the product of $\chi_M = \chi/mol$ and T is approximated as follows.

$$\chi_M T \cong C = \frac{N_A g^2 \mu_B^2}{3k_B} \cdot S(S+1) \tag{1.31}$$

where
N_A : Avogadro's number;
g : Lande's g value;
μ_B : Bohr's magneton;
k_B : Boltzmann constant;
S : spin quantum number.

As explained in the previous section, in the case of lanthanides, due to non-negligible SOC, total angular momenta should be taken into account:

$$\chi_M T = \frac{N_A g_J^2 \mu_B^2}{3k_B} \cdot J(J+1) \tag{1.32}$$

Since this value is consistent for each lanthanide ion, the high temperature (or room temperature) value of $\chi_M T$ serves as a powerful magnetic characterization tool. For example, in the case of a complex with Tb(III) ion (g_J = 3/2), the room temperature value should be $\chi_M T = 11.82$.[95]

On the other hand, at low temperatures, $\chi_M T$ values give information about the interaction between spins (Figure 7a). In the case of antiferromagnetic (AFM) coupling, where spins mutually cancel each other's magnetization, the $\chi_M T$ values decrease upon cooling. Conversely, in the case of ferromagnetic coupling, the $\chi_M T$ values increase as the system cools.

Although DC magnetometry provides valuable data, it doesn't give any information about SMM properties. Instead, two techniques are commonly used to characterize SMMs; AC in-phase/out-of-phase susceptibility measurements and hysteresis measurements. The AC susceptibility measurement involves the determination of the sample's magnetization under oscillating external magnetic fields. The magnetization obtained here can be expressed as follows.

$$M(t) = M_0 + (\chi' - i\chi")h \tag{1.33}$$

When the AC frequency (ω) is fast enough, there is no time to relax, resulting in adiabatic susceptibility χ_S. On the other hand, when ω is slow enough, the susceptibility will match with the isothermal one, χ_T. The intermediate state is fitted by the generalized Debye model:

$$\chi(\omega) = \chi_S + \frac{\chi_T - \chi_S}{1 + (i\omega\tau)^{1-\alpha}} \tag{1.34}$$

where alpha represents the distribution of the relaxation time. The real and imaginary parts of this expression can be written as:

$$\chi'(\omega) = \chi_S + (\chi_T - \chi_S)\frac{1 + (\omega\tau)^{1-\alpha}\sin\left(\frac{\pi\alpha}{2}\right)}{1 + 2(\omega\tau)^{1-\alpha}\sin\left(\frac{\pi\alpha}{2}\right) + (\omega\tau)^{2-2\alpha}} \tag{1.35}$$

$$\chi"(\omega) = (\chi_T - \chi_S)\frac{(\omega\tau)^{1-\alpha}\cos\left(\frac{\pi\alpha}{2}\right)}{1 + 2(\omega\tau)^{1-\alpha}\sin\left(\frac{\pi\alpha}{2}\right) + (\omega\tau)^{2-2\alpha}} \tag{1.36}$$

From AC susceptibility measurements, the frequency dependence of χ' and χ'' is obtained (Figure 1.7b). The peak in χ'' is a characteristic feature arising from the slow relaxation of magnetization in single-molecule magnets (SMMs). This relaxation occurs only when specific mechanisms are triggered, which will be mentioned later. The parameters α and τ can be extracted from a Cole-Cole plot of the experimental data, as shown in Figure 1.7c. The obtained lifetime can be fitted with the following equation.

$$\tau^{-1} = \tau_{QTM}^{-1} + AT + BT^{n} + \tau_0^{-1} \exp\left(-\frac{U_{eff}}{k_B T}\right) \tag{1.37}$$

where the first term represents quantum tunneling of magnetization (QTM), the second is the Direct term, the third is the Raman term, and the last is the Orbach term. Each term represents different processes of the relaxation of magnetization as shown in Figure 1.7d,e.[96]

1. QTM: This process involves tunneling between degenerate magnetic states. It occurs between sublevel states such as m_S or m_I, and is explained in more detail in Section 1.4.4. QTM is dominant at low temperatures, as it is temperature-independent while other mechanisms are activated with rising temperatures.

2. Direct process: In this one-phonon process, energy exchange occurs between spin and the lattice. This process is typically pronounced under external field: Zeeman splitting lifts the degeneracy of $|\uparrow\rangle$ and $|\downarrow\rangle$, and the relaxation emits a phonon corresponding to $h\nu$.

3. Raman process: This two-phonon relaxation process involves a virtual excited state. The virtual state originates from the inelastic dispersion of a phonon or simply of a molecular vibration.

4. Orbach process: The Orbach process also involves two-phonon relaxation but via a real excited state. In the case of an SMM, this requires it to overcome the energy barrier (U_{eff}) dominated by Boltzmann distribution. As a result, this process becomes dominant at high temperatures.

QTM can be suppressed by applying an external field, as two magnetic states are no longer degenerated. On the other hand, the direct process is particularly observed under a magnetic field (Figure 1.7e). The energy barrier U_{eff} is a crucial parameter when discussing SMM properties, whose definition is described in the last section. Researchers have explored strategies to enhance U_{eff}, which will be explained in the upcoming section.

The other technique to evaluate SMMs is the field dependence of the magnetization at various temperatures (Figure 1.7f). Hysteresis loops are observed in many SMMs, although not all of them exhibit this behavior.

One crucial parameter is the blocking temperature (T_B). It can be determined by three definitions: (i) the temperature at which the field-cooled and zero-field-cooled magnetic susceptibilities diverge,[97] (ii) the temperature at which the relaxation time τ is equal to 100 s,[98,99] and (iii) the maximum temperature at which hysteresis is observed.[98,99] While the second one is considered as the "golden standard" for quantitatively comparing different molecules,[98] a large portion of articles only discussed the last one despite its dependence on arbitrarily chosen parameters, such as the scanning rate.[99] Since the next section deals with the literature survey, the abbreviation T_B refers to the last one, which is commonly used in articles. Additionally, in Chapter 3, blocking temperatures with different definitions are distinguished using terms like "blocking temperature (τ = 100 s)" or abbreviations like "$T_{B(\tau\ =\ 100\ s)}$". In practical applications, the blocking temperature aligns with the device's operating temperature, making it significantly important. As of 2024, the highest reported T_B is 80 K (*vide infra*), surpassing liquid nitrogen temperature (77 K) but still falling short of room temperature. The correlation between U_{eff} and T_B has been investigated previously,[100,101] however, the recent report from Gaita-Ariño and coworkers concluded that the correlation is not universally applicable: the strategy suitable for one is not suitable for another.[99]

Another important parameter is the coercive field (H_c), which is defined as the hysteresis opening at which M is equal zero (see Figure 1.7f). Similar to permanent magnets, where a large H_c is desired, achieving a larger H_c is also a goal for single-molecule magnets (SMMs). In many cases of SMM, the hysteresis loop is butterfly-shaped, with magnetization relaxation occurring near-zero field due to quantum tunneling of magnetization (QTM). As mentioned above, suppression of QTM is achieved by the application of an external field. Thereby, the coupling to radicals is a good strategy, as it introduces an inner field. In the next section some examples of adopting this strategy will be explained.

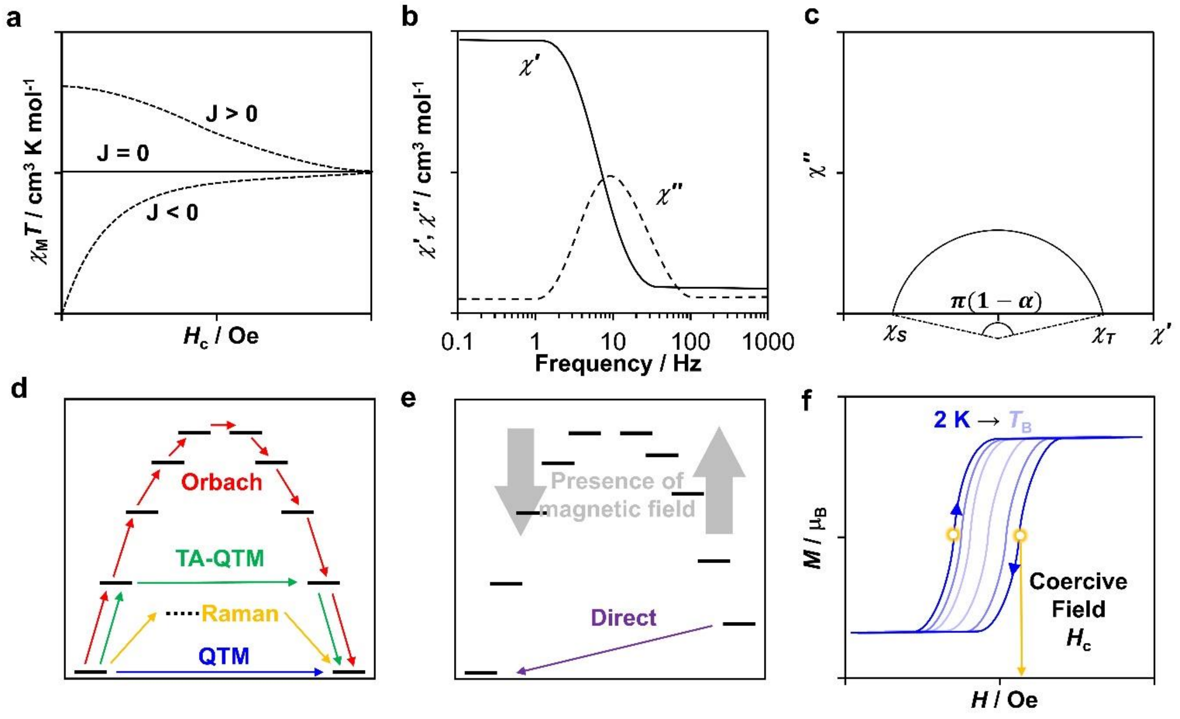

Figure 1.7. (a) Schematic illustration of $\chi_M T$ versus T plot. The ones for FM (J > 0) and AFM (J < 0) are represented as dotted lines. (b) Schematic illustration of frequency dependence of AC in-phase (solid line) / out-of-phase (dotted line) susceptibility. (c) Schematic illustration of Cole-Cole plot. Figures b and c are created with inspiration from ref[86]. (d and e) Energy diagram

and representation of several relaxation mechanisms. (f) Hysteresis loops under various temperatures. Coercive field at 2 K is represented in the yellow arrow and the dots.

1.4.3. Lanthanide SMMs – from single-ion magnets to radical-bridged dinuclear Ln-SMM

In the last section, the technique for evaluating SMM properties was explained. In this section, the strategies for obtaining SMMs with high performance will be discussed. First of all, the choice of metal ion plays a crucial role. Most SMMs are based on Kramers ions such as dysprosium(III) or erbium(III), where half-integer spins yield bi-stable ground states regardless of the ligand field symmetry. However, there are some examples of SMMs with non-Kramers ions such as holmium (III) or terbium(III). In these cases, the ligand field with an axial symmetry is required.[102]

As explained in Section 1.4.1, in the case of Ln-SMM, the ligand field dominantly affects the relaxation barrier U_{eff}. In 2022, Duan *et al*. analyzed over 1400 reported single-ion magnets and summarized their trends.[99] They claimed the complexes with oblate lanthanide ions sandwiched between planar ligands are one promising strategy to obtain a large energy barrier. This holds true for $\mathrm{TbPc_2}$. For those complexes with certain symmetries ($D_{4\mathrm{d}}$, $D_{5\mathrm{h}}$, C_{∞}), the transverse crystal field arising from $B_k^{q\neq 0}$ in the crystal field Hamiltonian has a negligible effect, which is favorable to retain magnetic anisotropy. This was most clearly evidenced by Layfield and coworkers in 2018.[103] They prepared $(\mathrm{Cp}^{i\mathrm{Pr}5})\mathrm{Dy}(\mathrm{Cp}^*)$, where a dysprosium ion is sandwiched between two cyclopentadienyls; one is tethered with five isopropyl group while the other has with five methyl groups (Figure 1.8 top left). Remarkably, they reported an ultra-high energy barrier $U_{\mathrm{eff}} = 1541\ \mathrm{cm^{-1}}$, as well as record-high $T_{\mathrm{B}} = 80$ K for this compound.

As an alternative approach, the addition of organic radicals in Ln-SMMs has been employed in various studies.[104,105] An early example is a neutral bis(phthalocyaninato)terbium(III) ($[\mathrm{TbPc_2}]^0$), which contains an organic radical delocalized over the ligand (**π radical**).[106] This species showed improved SMM property compared to its anionic counterpart $[\mathrm{TbPc_2}]^-$ regarding both U_{eff} and H_{c}. In 2004, Ishikawa *et al*. reported that $[\mathrm{TbPc_2}]^0$ exhibited an increased energy barrier ($U_{\mathrm{eff}} = 590$ K) compared to $[\mathrm{TbPc_2}]^-$ ($U_{\mathrm{eff}} = 331$ K)[89] (Figure 1.8 top middle).[106] Later, in 2008, Ishikawa and coworkers reported the comparison of the magnetic properties of $[\mathrm{Tb(PcOEt_8)_2}]^+$ and $[\mathrm{Tb(PcOEt_8)_2}]^-$.[107] The cation showed larger U_{eff} than the anion (790 K vs 734 K), which they attributed to the change in the LF. The same group previously reported that the HOMO of $[\mathrm{TbPc_2}]^-$ has antibonding nature.[108,109] Therefore, it can be concluded that oxidation of $[\mathrm{TbPc_2}]^-$ leads to the contraction between Pc-Pc distance, resulting in the improvement of U_{eff}. On the other hand, as explained in the previous section, the presence of radicals in Ln-SMM is expected to lead to exchange-bias. It was demonstrated by Veciana and coworkers in 2011. They performed magnetic dichroism (MCD) measurements on the solution samples of $[\mathrm{TbPc_2}]^+$, $[\mathrm{TbPc_2}]^0$ and $[\mathrm{TbPc_2}]^-$. With MCD, hysteresis loop analogue to a SQUID measurement can be measured, but only in a diluted sample. While the two non-radical species ($[TbPc_2]^+$, $[TbPc_2]^-$) show butterfly-shaped hysteresis, the radical species ($[TbPc_2]^0$) showed box-shaped hysteresis. The larger coercive field of the neutral species clearly evidences the suppression of QTM, owing to the exchange coupling between the Tb(III) ion and the π radical (exchange-bias). Later, the interaction between the Tb(III) ion and the π radical was experimentally determined. In 2018, Hill and coworkers reported the EPR study on $[TbPc_2]^0$. Angular-dependent high-frequency EPR on a single-crystalline sample revealed a weak anti-ferromagnetic coupling nature ($J_{\mathrm{Rad\text{-}Tb}}$ = -0.15 cm^{-1}). Overall, the presence of a π radical in $[TbPc_2]^0$, weakly interacting with Tb, improves the SMM property of $[TbPc_2]^0$, due to the improvement in LF and the exchange-bias.

On the other hand, there are further radical-containing Ln-SMMs, such as nitronyl-nitroxide, TEMPO, bipyridine, etc.[104] They typically exhibit stronger $J_{\mathrm{Rad\text{-}Ln}}$ than $TbPc_2$. However, as Duan *et al*. summarized,[99] such complexes are less valuable for further studies, since the maximum energy barrier U_{eff} is limited to 58.75 K.[110]

Another strategy is to bridge dinuclear Ln complexes by an organic radical. The key is strong exchange coupling between Ln and radical ($J_{\mathrm{Ln\text{-}Rad}}$), which is achieved by the radical's diffused spin density penetrating the deeply buried 4f orbitals of Ln centers. The strong $J_{\mathrm{Ln\text{-}Rad}}$ leads to either/both "giant spin" effect[111–113] or/and exchange-bias[104]. An early but prominent example was showcased by Long and coworkers in 2011,[111,114] with dinuclear Ln (= Tb, Ho, Er, Gd, Dy) complexes having a $N_2^{3-\cdot}$ radical as a bridging ligand ($\{[(Me_3Si)_2N]_2(THF)Ln\}_2(\mu\text{-}\eta^2\text{:}\eta^2\text{-}N_2)$, Figure 1.8 top right). It revealed a large $J_{\mathrm{Gd\text{-}Rad}}$ = -27 cm^{-1}, and a relatively high blocking temperature (8 K for Dy and 14 K for Tb) and large H_c (1.2 T for Dy and 4.7 T for Tb, both at 11 K). Although the obtained energy barrier was moderate (U_{eff} = 123 cm^{-1} for Dy and 227 cm^{-1} for Tb), this strategy serves as a milestone of improvement of SMM performance using a radical-bearing bridging ligand. Later in 2017, Demir *et al*. reported dinuclear Ln complexes with a $N_2^{3-\cdot}$ bridge and axial Cp ligands.[115] It was expected that the combination of two successful strategies; (i) Cp sandwich and (ii) a $N_2^{3-\cdot}$ bridge, would bring an improved SMM performance. This is true, particularly for Tb resulting in an improved energy barrier, blocking temperature, and coercive field (U_{eff} = 276 cm^{-1}, T_B = 20 K, and H_c = 7.9 T at 10 K, respectively). Different kinds of radical-bearing bridging ligands have also been employed, for example, in 2012, Demir *et al*. reported dinuclear Ln complexes with bipyrimidyl-bridging ligand ($(Cp^*{}_2Ln)_2(\mu\text{-bpym}^{\bullet})$, Figure 1.8 bottom left).[116] This system shows the opposite trend, where the complex with Dy ions showed better performance (U_{eff} = 87.3 cm^{-1}, T_B = 6.5 K, and H_c = 0.6 T at 3 K for Dy, while U_{eff} = 44 cm^{-1}, T_B and H_c was hard to discuss due to narrow opening of hysteresis even at 1.8 K for Tb). One notable advantage of organic radicals is their tunability, unlike for the $N_2^{3-\cdot}$ radical. In 2020, Long and coworkers demonstrated structure-dependence of SMM properties by comparing electron-withdrawing/donating substituents on a bipyrimidyl radical of $[(Cp^*{}_2Ln)_2(\mu\text{-bpym}^{\bullet})]^+$.[117] They revealed the tendency of stronger coupling with electron-withdrawing groups ($J_{\mathrm{Gd\text{-}Rad}}$ = –11.1 cm^{-1} for —F while $J_{\mathrm{Gd\text{-}Rad}}$ = –2.7 cm^{-1} for —

NMe_2). Interestingly, there is a linear relationship between $|J_{\mathrm{Gd\text{-}Rad}}|$ and U_{eff}, where U_{eff} can be tuned up to 93 $\mathrm{cm^{-1}}$ with F.

Although bipyrimidyl radicals allow tuning of $J_{\mathrm{Gd\text{-}Rad}}$, their SMM performance is inferior to that of $N_2^{3-\cdot}$ radicals, probably due to the longer Ln-Ln distance. Therefore, the ideal situation is predicted to be when two lanthanides are placed in the closest distance bridged with a single-electron bond. This was showcased in 2022 by Long and coworkers.[118] They presented dinuclear Ln complex with three iodide anionic bridge ($(\mathrm{Cp}^{i\mathrm{Pr}5})_2\mathrm{Dy}_2\mathrm{I}_3$, Figure 1.8 bottom middle). Instead of bridging ligand, an electron resides in $5d_{z^2}$ orbital of two lanthanbides, resulting in σ bond formation. It resulted in a significant improvement of exchange coupling ($J_{4\mathrm{f}\text{-}5\sigma}$ = +387 $\mathrm{cm^{-1}}$ obtained from the fitting of Gd), which led the record-breaking coercive field of H_c = 14 T even at 60 K, as well as extraordinarily high blocking temperature and energy barrier (T_B = 77 K, U_{eff} = 1631 $\mathrm{cm^{-1}}$).

Contrary to the prediction, there is one example showing enhanced SMM property even with a long Ln-Ln distance. In 2018, Yamashita and coworkers reported $[\mathrm{TbPc_2}]^0$ dimer, which has two $[\mathrm{TbPc_2}]^0$ units linked by one benzene ring (Figure 1.8 bottom right).[119] From DFT calculation, they anticipated that the two radicals originating from each $[\mathrm{TbPc_2}]^0$ cores are strongly coupled (J = 200 $\mathrm{cm^{-1}}$), which resulted in better SMM performance than the original $[\mathrm{TbPc_2}]^0$ (U_{eff} = 588 $\mathrm{cm^{-1}}$, T_B = 16 K, and H_c = –0.06 T at 0.5 K).

In conclusion, single molecule magnets, showing slow relaxation of magnetization, can be characterized by SQUID magnetometry as the most powerful technique, in particular, AC susceptibility and hysteresis loop measurements, which gives the important criteria U_{eff}, T_B, and H_c. To achieve improved values, many attempts have been made. One strategy is to engineer the ligand field, which is represented in $(\mathrm{Cp}^{i\mathrm{Pr}5})\mathrm{Dy}(\mathrm{Cp}^*)$. Another strategy is to add a radical at a close proximity to the lanthanide in dinuclear Ln complexes, which has been experimentally demonstrated by $(\mathrm{Cp}^{i\mathrm{Pr}5})_2\mathrm{Dy}_2\mathrm{I}_3$. It is notable that even though researchers have achieved T_B = 80 K, which is higher than liquid nitrogen temperature, but still much lower than room temperature, implementation of a device based on SMMs remains difficult. Nevertheless, considering the fact that T_B increased significantly from liquid helium temperature to liquid nitrogen temperature in 30 years, the future of SMM is still promising. Another fact to be considered is stability. Unfortunately, both $(\mathrm{Cp}^{i\mathrm{Pr}5})\mathrm{Dy}(\mathrm{Cp}^*)$ and $(\mathrm{Cp}^{i\mathrm{Pr}5})_2\mathrm{Dy}_2\mathrm{I}_3$ are highly air-sensitive. For memory device implementation, an air-stable molecule would be advantageous.

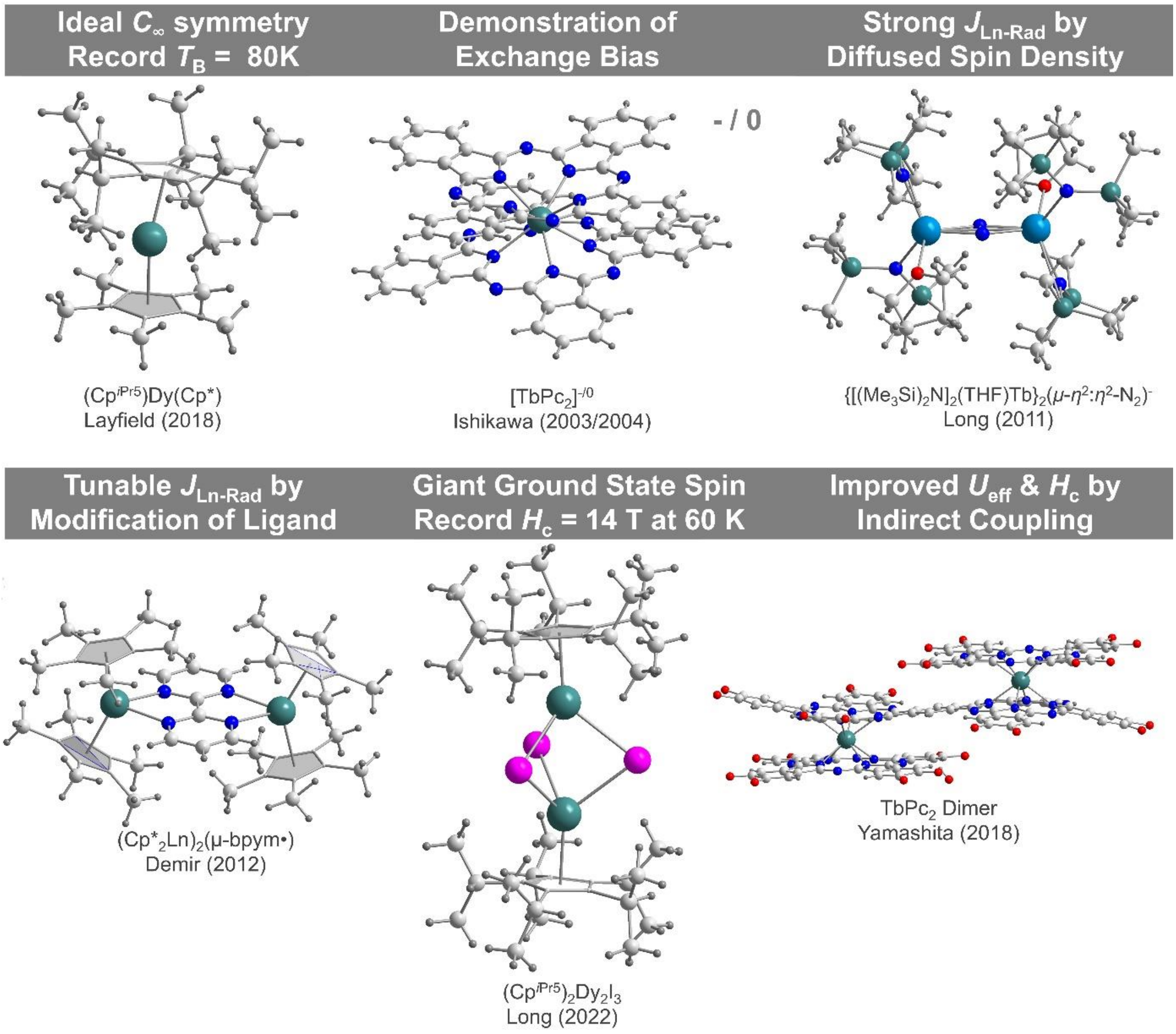

Figure 1.8. Crystallographic structures of Ln-SMMs. Crystal structures are from ref.[90,116] for $[\mathrm{TbPc_2}]^{0/-}$ and $(\mathrm{Cp^*_2Ln})_2(\mu\text{-bpym}^{\bullet})$, and for the others from CCDC (1854468, 802816, 2097928, and 1450136), respectively.

1.4.4. QTM for quantum information processing

μ-SQUID –addressing nuclear spin states via QTM

Three years after the first report of an SMM $\mathrm{Mn_{12}}$,[88] Sessoli and coworkers discovered staircase-like steps in the hysteresis loop of a single-crystal of $\mathrm{Mn_{12}}$.[120] The steps were observed at the magnetic field where the energies of different substates matched, revealing quantum tunneling of magnetization (QTM). Inspired by this phenomenon, QIP based on SMM's spin state was proposed.[121] In 2003, Hill *et al*. demonstrated EPR on SMMs, using two $\mathrm{Mn_4}$ clusters dimerized by supramolecular interaction.[122] They asserted that their findings evidence the utility of their system as a qubit.

Like Mn_{12}, $TbPc_2$ also exhibits a staircase in the hysteresis loop. In 2005, Ishikawa and Wernsdorfer reported low-temperature (0.04 K) μ-SQUID measurements on 2% of $[TbPc_2]^-TBA^+$ diluted in a single-crystal of $[YPc_2]^-TBA^+$.[123] The respective hysteresis loops exhibited a staircase-like structure (Figure 1.9.1). In this case, the field matches with the crossing point of the Zeeman diagram considering the hyperfine coupling of the total angular momentum of Tb (J = 6) and its nuclear spin (I = 3/2). The crossing points are avoided level crossing, thus preferable for QIP (*vide infra*). They also tried diluted $[DyPc_2]^-TBA^+$, though no clear step appeared unlike for $[TbPc_2]^-TBA^+$. One significant difference is their isotopic abundance. Terbium resides as ^{159}Tb (I = 3/2) in a natural abundance of 100%, while dysprosium has seven naturally abundant isotopes; ^{156}Dy (I = 0, 0.06%), ^{158}Dy (I = 0, 0.01%), ^{160}Dy (I = 0, 2.34%), ^{161}Dy (I = 5/2, 18.91%), ^{162}Dy (I = 0, 25.51 %), ^{163}Dy (I = 5/2, 24.90%), ^{164}Dy (I = 0, 28.18%). Later in 2017, Moreno-Pineda *et al*. reported isotope-enriched $DyPc_2$ ($^{163}DyPc_2$ and $^{164}DyPc_2$) and their μ-SQUID measurements.[124] A clear difference was illustrated where $^{164}DyPc_2$ showed hysteresis with no staircase feature, while $^{163}DyPc_2$ showed some steps attributed to the avoided level crossing of the transition between $|\pm J_z\rangle|I_z\rangle$ and $|\mp J_z\rangle|I_z\rangle$. In short, the hyperfine coupling enables to readout nuclear spin states of a lanthanide center via μ-SQUID measurement.

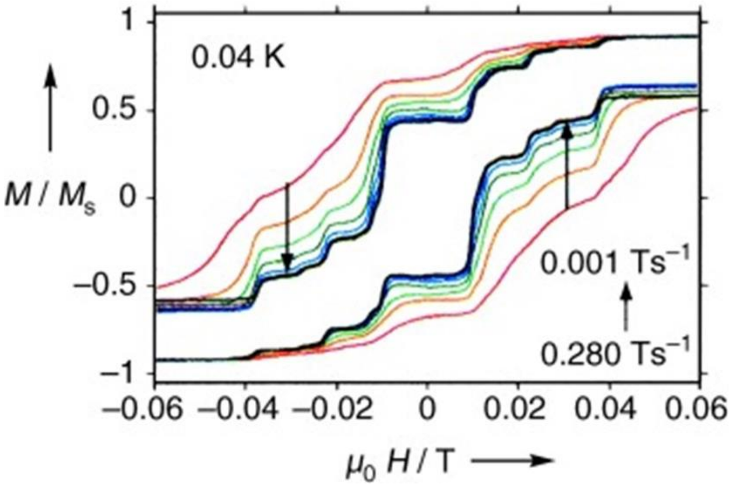

Figure 1.9.1. Magnetic hysteresis loop of $TbPc_2$ measured via μ-SQUID measurement. Reproduced from ref[123].

Spin transport on $TbPc_2$ – the implementation of a quantum algorithm with a nuclear spin qudit

Nuclear spin is an ideal candidate as a qubit due to its inherent shielding, which reduces environmental interference.[125] Nevertheless, its shielded nature also makes it challenging to read out the nuclear-spin state. As discussed above, $TbPc_2$ functions as an SMM, because of its high-spin ground state and strong uniaxial magnetic anisotropy. In addition, hyperfine interaction facilitates the relaxation of magnetization *via* QTM, allowing the readout of nuclear spin states. These features encouraged researchers to utilize $TbPc_2$ for QIP, similar to Mn_{12}. In 2013, 2014, and 2017, Ruben, Wernsdorfer and coworkers reported a series of studies on the read-out and operation of the nuclear-spin state of $TbPc_2$, as well as the implementation of the quantum algorithm, using the single-molecule junction technique shown in Figure 1.9.2 a.[126–128]

In 2014, by using two of the four spin states, they demonstrated a nuclear spin qubit.[127] They performed the following steps:

(1) Readout: Unlike the other steps, readout was reported earlier in 2012.[126] The nuclear spin readout was conducted electronically through a **spin cascade** (Figure 1.9.2 b). This involves three spins (the π radical (S = 1/2, in this context also called read-out dot), the total angular momentum of Tb (J = 6), and the nuclear spin of Tb (I = 3/2)) and two types of interactions (hyperfine and exchange).

- Hyperfine coupling: As explained in the last section, at low temperatures, the magnetic relaxation is mostly due to the avoided level crossing of $|\pm J\rangle|I\rangle$ and $|\mp J\rangle|I\rangle$. $|I\rangle$ can be selectively readout using the magnetic field where QTM is observed.

- Exchange coupling: The previously discussed weak yet significant exchange coupling between the π radical and the magnetic moment of Tb^{3+} is essential for spin transport measurements.[129]

Overall, nuclear spin read-outs are performed as follows. First, the $TbPc_2$ molecule, connected to the gate, source, and drain electrodes, functions as a single-molecule transistor due to its rich redox properties. The presence of a SOMO makes it possible to observe the Kondo peak (*vide infra*) in the differential conductance versus field plot. Second, the exchange coupling generates a local effective magnetic field. This results in a change in the chemical potential when the magnetization of the terbium reverses, causing a jump in conductance (Figure 1.9.2 b right).[126] Finally, this jump is triggered by a change in the magnetic moment of Tb^{3+}, due to QTM at specific magnetic fields.

(2) Initialization: At low temperatures, the energy ground state is populated following the Boltzmann distribution. To initialize any desired state, the magnetic field is swept and the

nuclear spin state detected by the external field position by the transition is monitored through process (1). Once the transition is detected, the magnetic field is held constant.

(3) Manipulation: The hyperfine splitting between the four nuclear-spin states can be electrically controlled due to the hyperfine Stark effect. In addition, these four states are unevenly split because of quadrupolar coupling. As a result, it is possible to manipulate any desired state by applying an appropriate radiofrequency pulse. Indeed, Rabi oscillations were demonstrated, which proves the potential as a qubit (Figure 1.9.2 c).

(4) Storage: Likewise, electronic spin qubits mentioned in Section 1.3, T_1 and T_2 are crucial criteria for nuclear spin qubits. T_1 is determined by statistically analyzing the duration the nuclear spin state persists: T_1 ~ 17 s for $|m_I\rangle = |\pm 1/2\rangle$ while T_1 ~ 34 s for $|m_I\rangle = |\pm 3/2\rangle$. On the other hand, T_2 is derived using the Ramsey fringe technique, which involves two $\pi/2$ pulses. The maximum T_2 observed is about 0.32 milliseconds, with potential for extension.

Later in 2017, a qudit was realized by following similar steps and introducing multi-frequency pulses.[128] One potential application of qudits is in Grover's algorithm, which offers a polynomial speedup for database searches compared to classical algorithms.[23] This algorithm has been demonstrated experimentally through the following steps (Figure 1.9.2 d):

(1) Readout and initialization: Same as above.

(2) Hadamard gate: After initialization, a coherent superposition of all the states is created via a multi-frequency pulse.

(3) Grover gate: The population of the researched state was amplified using a second pulse. The researched state can be tagged by either phase or energy.

(4) Readout of the resulting state: Same as above.

As a result, by using quantum amplitudes to evaluate event probabilities, the likelihood of finding the desired research state significantly increases.

To the best of my knowledge, these results are the first and only studies demonstrating a molecule-based quantum algorithm. Nevertheless, they have led many other researches, such as the study on the superiority of $TbPc_2$ qudits fidelity, the invention of qudit-based processors, and the discovery of fault-tolerant qudit operation.[130–132]

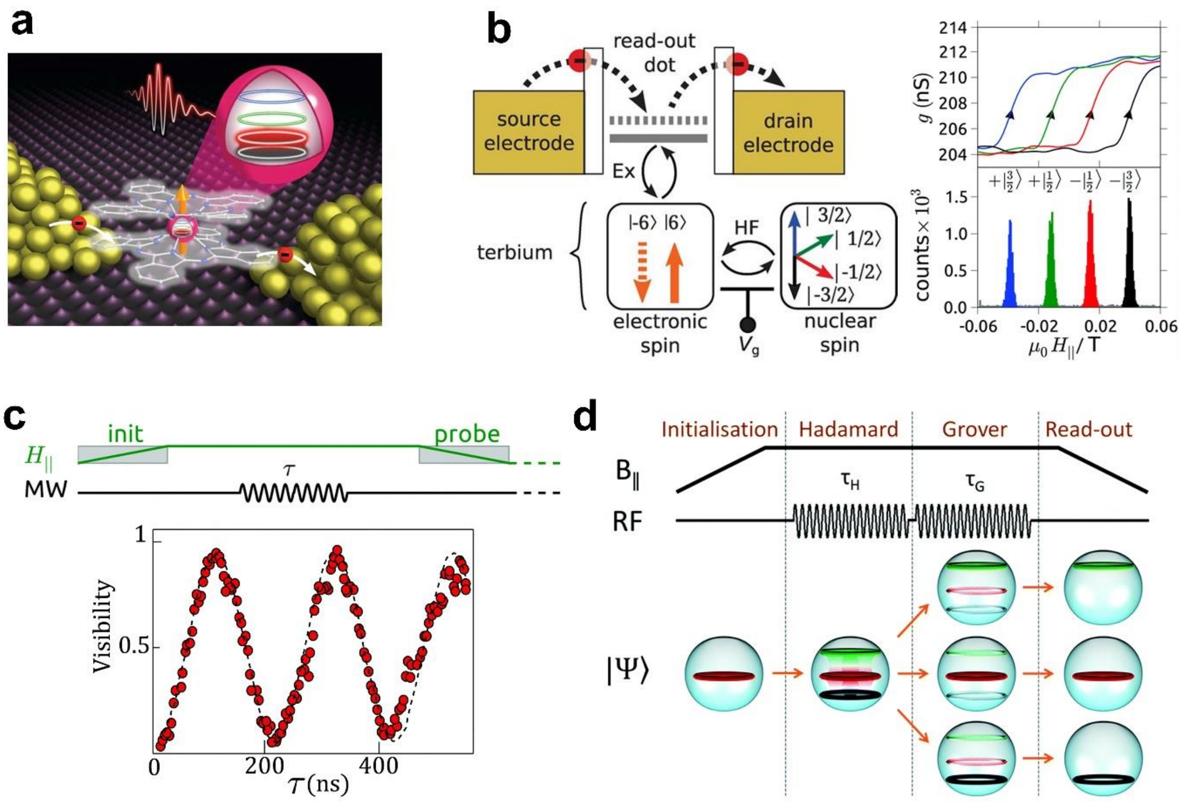

Figure 1.9.2. (a) Schematic illustration of the setup for spin transport measurements of $TbPc_2$. (b) Spin cascade enabling nuclear-spin readout (left), alongside conductance jumps and histograms correlating to each spin state (right). (c) Nuclear spin manipulation: sequence scheme (top) and Rabi oscillations (bottom). Reproduced from ref.[127] (d) Schematic illustration of the sequence for Grover algorithm. Reproduced from ref.[128]

STM Kondo measurement – alternative approach toward qudit operation

An alternative method to access nuclear spin involves scanning tunneling microscopy (STM). This technique has been widely used to study the $[TbPc_2]^0$ molecule owing to its high thermal stability and sublimation capability. STM measurements on these molecules were performed on different substrates such as Cu(111), graphene, and Au(111).[90,133–135] In 2011, Komeda *et al*. reported the first observation of the Kondo effect in the $[TbPc_2]^0$ molecule on Au(111).[136] The Kondo effect, in which the resistance increased due to the formation of a Kondo–Yoshida singlet between conductive electrons and magnetic impurities, is observed as a sharp peak at the Fermi level in scanning tunneling spectroscopy (STS). Notably, this peak was only seen when the STM tip was positioned over the phthalocyanine ligand, suggesting that the Kondo peak originates from an interaction between the current electron and the π radical. Due to the low reduction/oxidation potential of $[TbPc_2]^0$, the π radical is easily quenched, resulting in a limited number of materials where the Kondo peak is visible.

As described above, the Kondo effect was used for nuclear-spin readout in spin-transport measurements. Therefore, researchers are now trying to replicate these spin transport results with STM/STS. For instance, in 2021, Wulfhekel and coworkers reported the detection of the total angular momenta of the dysprosium ion in bis(phthalocyaninato)dysprosium(III) in spin-polarized STS at milli-Kelvin.[137] Initially, non-spin-polarized STS under an external magnetic field was measured, observing a splitting of the Kondo peak, which was attributed to the exchange interaction between the π radical and the magnetic moment of Dy. Subsequently, the spectra were measured under varied external magnetic fields, showing a gradual increase in the splitting with increasing field strength. The split Kondo peaks were well-fitted by considering the SOMO as a spin ½ system and the exchange interaction as an effective exchange field, defined as B_{ex}. Furthermore, using a spin-polarized tip, they observed enhancement or suppression of either one of the split peaks, which was also fitted well using the same model but with a spin polarization of the Cr tip. The obtained B_{ex} versus normalized peak asymmetry was simulated better when considering that the Dy magnetic moment is not stable near zero magnetic fields. Overall, the Dy magnetic moment was read out as a function of the applied magnetic field.

Although the current read-out extends up to total angular momenta as of 2024, ongoing efforts aim to utilize this method for nuclear spin readout. It is notable that the use of ^{163}Dy leads to an increased Hilbert space compared to ^{159}Tb, since ^{163}Dy has a larger nuclear spin ($I = 5/2$) than ^{159}Tb ($I = 3/2$).

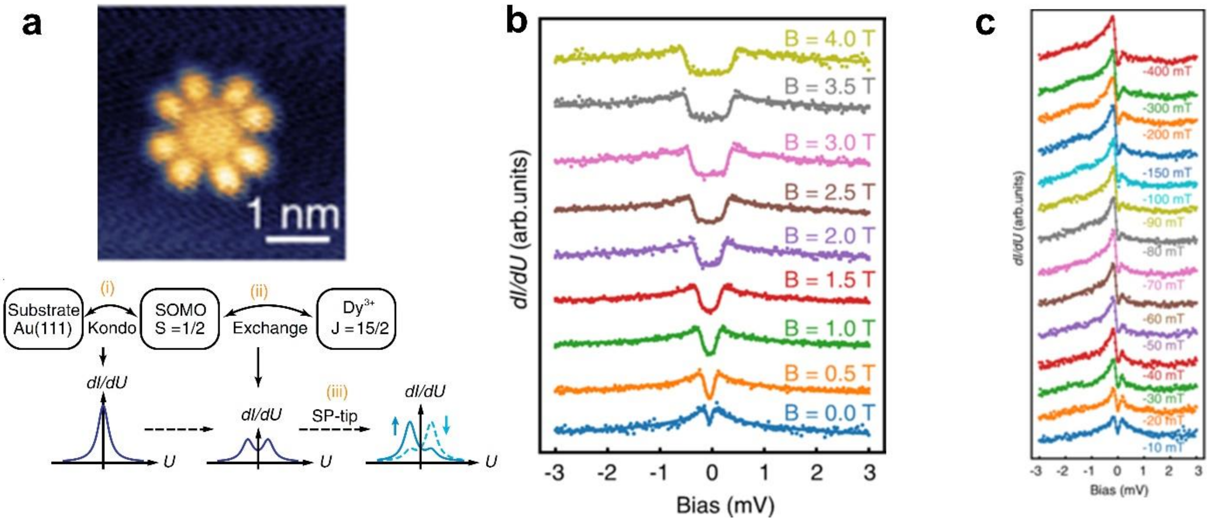

Figure 1.9.3 (a) STM image of DyPc$_2$ (top) and spin-polarized STS curve under magnetic field (bottom), and related spin cascade (bottom). (b) Magnetic field dependence of the splitting of the Kondo peaks. (c) Spin-polarized scanning tunneling spectra of DyPc$_2$ as a function of applied magnetic field. Reproduced from ref[137].

Studies on Tb_2Pc_3 – toward increased Hilbert spaces

An alternative approach is the use of multinuclear lanthanide complexes. In 2018, Wernsdorfer and Ruben proposed that multi-nuclear phthalocyanine complexes (Ln_nPc_{n+1}) are potentially applicable as nuclear spin qudits (Figure 1.9.4 a), as they satisfy the following criteria: (i) SMM character, (ii) the hyperfine coupling between electron spin and nuclear spin, and (iii) the exchange coupling between electron spins of lanthanides ($J_{\mathrm{Ln-Ln}}$). Importantly, they predicted that the multiplicity (d) would increase exponentially: $d = (2I+1)^n$.

The concept proposed here was later demonstrated experimentally. Before the spin-transport study, in 2018, Moreno-Pineda *et al*. reported a μ-SQUID study on a tris(phthalocyaninato) dinuclear terbium(III) complex (Tb_2Pc_3).[138] Using Tb_2Pc_3 diluted in a single crystal of Y_2Pc_3, hysteresis loops were observed at 30 mK, accompanied with staircase-like steps. The simulation of the Zeeman diagram predicted that only 10 out of 100 level crossings have large tunneling splitting, and 3 of them occur at the same field. Indeed, only seven steps were observed in the hysteresis loops, whereas the resonance field matched well with the simulation.

Later in 2021, the same group demonstrated the spin transport measurements on Tb_2Pc_3 molecule.[139] The detail of the experiment was discussed at "(1) Readout" in the two previous subsections. Unlike $TbPc_2$, Tb_2Pc_3 doesn't have a π radical (*vide infra*). Instead, a read-out dot is injected from electrodes by controlling a gate voltage, which participates in the spin-cascade. In the differential conductance trace measurement, conductance jumps were observed at seven different fields, which was confirmed by the histogram constructed by the repetition of the measurement. The fields where the conductance jumps were observed didn't match with the simulation, which they attributed to the miss-alignment of the easy axis of the Tb_2Pc_3 molecule with the magnetic field.

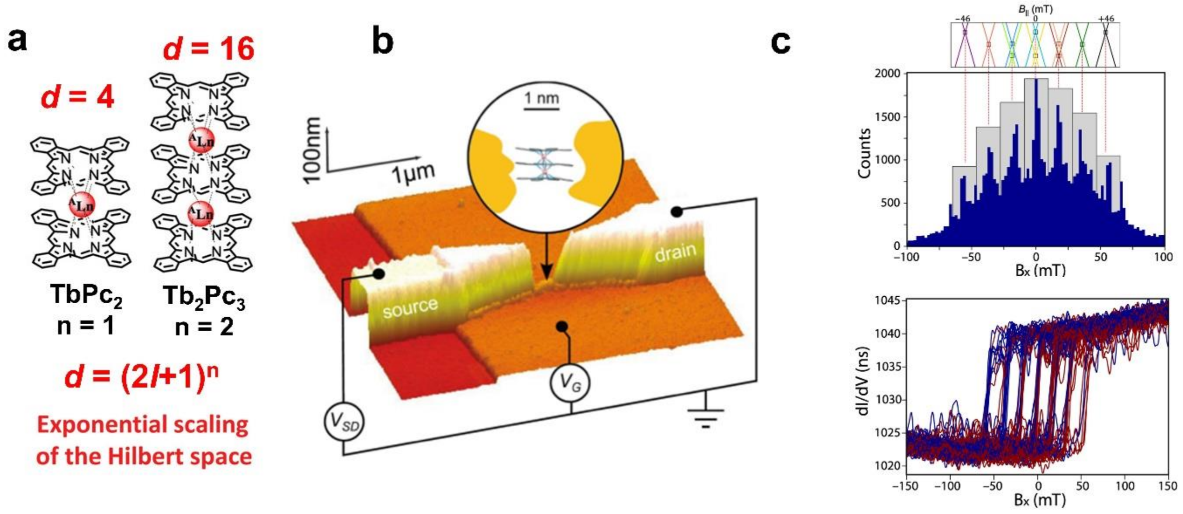

Figure 1.9.4. (a) Schematic illustration of the expansion of Hilbert space by multi-nuclear complexes (Tb_nPc_{n+1}). Reproduced from ref.[138] (b) AFM image of the setup of spin transport

measurements of Tb_2Pc_3. (c) Conductance jumps and their histograms with corresponding level crossings (bottom and top, respectively). Reproduced from ref.[139]

In conclusion, this section reviewed the historical studies on nuclear spin addressment. In this context, $TbPc_2$ is the most extensively studied molecule. To increase Hilbert space, two approaches have been explored: the use of ^{163}Dy and the expansion to multiple-decker Ln_nPc_{n+1}. The latter enables more drastic change; however, to date, the reported maximum value of *n* is two. To my best knowledge, quadruple and quintuple decker have only been reported in lanthanide/cadmium mixed-metal system.[140]

1.5. Bis(phthalocyaninato)lanthanide(III) / Tris(phthalocyaninato)dilanthanide(III) Complexes

In the previous sections, bis(phthalocyaninato)yttrium(III)/terbium(III) complexes ($LnPc_2$) were discussed for their potential as molecular qubits and/or single-molecule magnets (SMMs). This section will summarize those studies, and also introduce tris(phthalocyaninato) bis(yttrium(III)/terbium(III)) complexes. A key focus of this section is to highlight the role of π radicals, which will become evident through a comparison between $LnPc_2$ and Ln_2Pc_3.

As previously noted, $LnPc_2$ complexes consist of a lanthanide (III) ion sandwiched between two phthalocyanine ligands (Figure 1.10a left). The charge imbalance (Ln^{3+} and $Pc^{2-} \times 2 = -4$, resulting in a total charge of -1) leads to the formation of a π radical ($\boldsymbol{S} = 1/2$) in their neutral species. Meanwhile, the terbium ion possesses both a total angular momentum ($\boldsymbol{J} = 6$) and a nuclear spin ($\boldsymbol{I} = 3/2$), as described below. Studies on molecular qubits and SMMs have leveraged these characteristics, as shown in Figure 1.10b-d left.

One notable property of $LnPc_2$ is its SMM property (Figure 1.10b left). As elaborated in section 1.4, $[TbPc_2]^-$ is the first lanthanide SMM reported in 2003 with $U_{\mathrm{eff}} = 331$ K.[89] Later, it was found that radical-bearing $[TbPc_2]^0$ showed improved SMM behavior ($U_{\mathrm{eff}} = 590$ K), due to improved LF and exchange-bias.[106,141] At low temperatures, $[TbPc_2]^-$ exhibits relaxation of magnetization driven by QTM between hyperfine states, which appears as a staircase-like structure in the hysteresis loop (Figure 1.10c left).[123] As discussed in Section 1.4.4, this effect has been applied to implement Grover's algorithm using nuclear spin qudits.[126–128] The key lies in readout, which is enabled by a spin cascade involving *S*, *J*, and *I*. In contrast, $[YPc_2]^0$ serves as an electron spin qubit (Figure 1.10d).[57,60] As explained in Section 1.3.4, similar to other radicals, the absence of SOC contributes to long T_1. $[YPcPor]^0$ and its dimers were studied as well, which showed the same tendencies as $[YPc_2]^0$.

On the other hand, Ln_2Pc_3 are complexes having two lanthanide (III) ions sandwiched by three phthalocyanine ligands (Figure 1.10a right). Unlike $[LnPc_2]^0$, $[Ln_2Pc_3]^0$ has no π radical, because of the charge balance (Ln^{3+} × 2 = +6 and Pc^{2-} × 3 = -6, leading to a net charge of 0)). To date, a stable radical of Ln_2Pc_3 (such as $[Ln_2Pc_3]^{+/-}$) has not been isolated, probably due to their instability. This lack of π radicals limits the scope of investigation, as shown below.

Similar to $TbPc_2$, Tb_2Pc_3 also exhibits SMM properties (Figure 1.10b right). In 2005, Ishikawa *et al*. observed slow relaxation of magnetization in Tb_2Pc_3,[142] noting two peaks in χ'' *vs* T, which indicated that two terbium ions are in different ligand fields (LF) and weakly coupled. Later, in 2016, Yamashita and coworkers reported the magnetic study on three types of complexes: Tb_2Pc_3, Tb_2Pc_2Por, and Tb_2PcPor_2.[143] They found that Tb_2Pc_3 behaves as zero-field SMM, while Tb_2Pc_2Por and Tb_2PcPor_2 exhibit field-induced SMM properties. They also found that only Tb_2Pc_2Por showed two peaks in χ'' *vs* T, while the others showed a single peak. These differences were attributed to their unique LF symmetries around the terbium ions: square antiprism between Pcs and square prism between Pc and Por. Although the Tb dinuclear complex has prompted researchers to introduce a radical-bridging ligand (as explained in Section 1.4.3), the absence of a radical in this molecule has hindered such an approach. On the other hand, similarly to $TbPc_2$, the relaxation of magnetization of Tb_2Pc_3 via QTM also reflects its nuclear spin state (Figure 1.10c right). As explained in Section 1.4.4, in 2018, Moreno-Pineda *et al*. reported a μ-SQUID study on a Tb_2Pc_3 molecule, observing seven steps in the hysteresis loop. [138] Later, in 2021, spin transport measurements on Tb_2Pc_3 revealed nuclear spin readout at the single-molecule level, where an injected electron participates in the spin cascade as a read-out dot. Nevertheless, the nature of the exchange coupling remains uncertain (*e.g.*, the strength of coupling and whether the radical couples to both terbium ions symmetrically). On the other hand, the lack of the π radical consequently prevents Ln_2Pc_3 from being used as an electron spin qubit.

In summary, in this section, $LnPc_2$ and Ln_2Pc_3 were reviewed in terms of three research objectives: SMM, electron-spin qubit, and nuclear spin qudit. By contrasting $LnPc_2$ owning a π radical and Ln_2Pc_3 without π radical, the role of the π radical was highlighted.

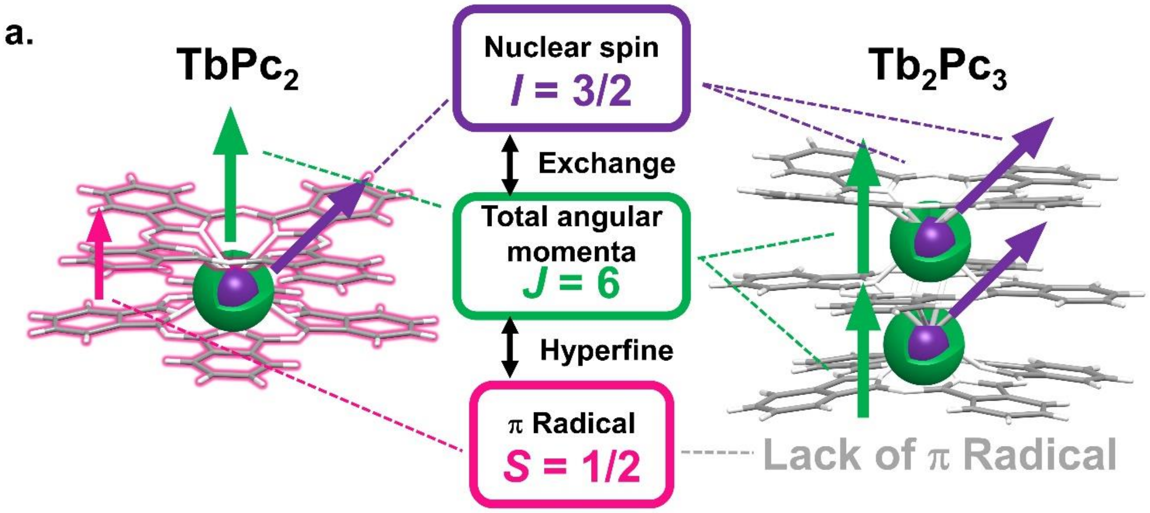

b. Single-Molecule Magnet (Section 1.4.3)

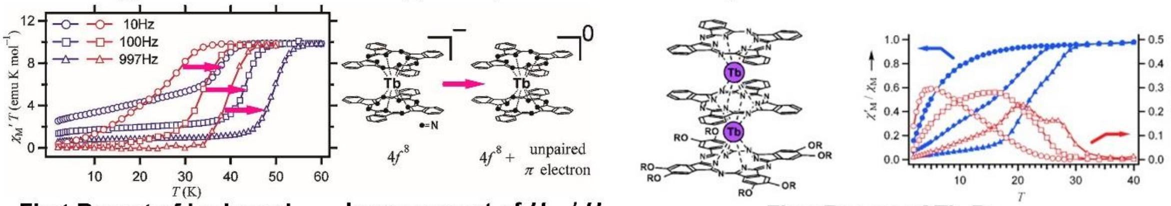

First Report of Ln-based SMM
Ishikawa (2003)

Improvement of U_{eff} / H_c by π radical
Ishikawa (2004) / Veciana (2011, 2013)

First Report of Tb$_2$Pc$_3$-based SMM
Ishikawa (2005)

c. QTM for Quantum Information Processing (Section 1.4.4)

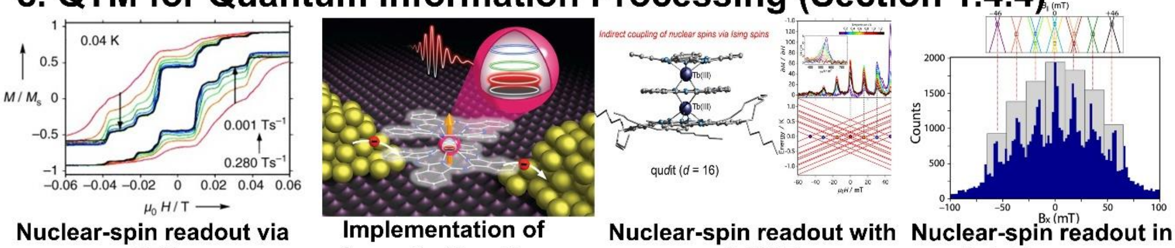

Nuclear-spin readout via QTM
Ishikawa, Wernsdorfer (2005)

Implementation of Grover's Algorithm
Ruben, Wernsdorfer (2012, 2014, 2017)

Nuclear-spin readout with μ-SQUID
Ruben, Wernsdorfer (2017)

Nuclear-spin readout in Spin Transport
Ruben, Wernsdorfer (2017)

d. Yttrium analogues of Spin Qubits (Section 1.3.4)

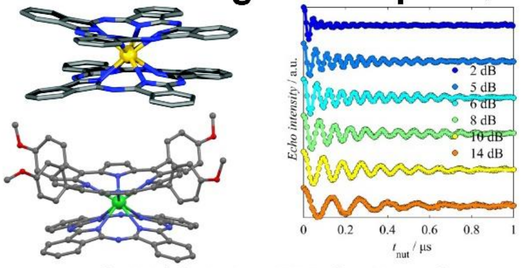

Solid / Solution EPR Studies of [YPc$_2$]^0 and [YPcPor]^0
Ruben (2021, 2023)

Figure 1.10. Overview of previous studies of $TbPc_2$ and Tb_2Pc_3. (a). The molecular structure of $TbPc_2$ (left) and Tb_2Pc_3 (right), with a schematic illustration of the spin cascade (middle). Arrows represent the spins, with colors matching the spin cascade scheme. Each molecule is painted in the corresponding color to clearly show where the spins are located, while the absence of the π radical in the Tb_2Pc_3 molecule is shown in grey. Cross sections of ions are also shown to display the nuclear spins. (b-d) Research on $TbPc_2$ and Tb_2Pc_3 molecules. Studies are arranged on the left and right sides clearly indicate their respective molecules, with related section numbers provided in brackets. Note that the right bottom is kept blank due to the lack of a π radical in Y_2Pc_3.

1.6. Aim of the thesis

Throughout this chapter, the growing demands for quantum information processors and atomic-scale memory devices have been overviewed, which are essential for advancing the digital age as it continues to adhere to Moore’s law. Section 1.5 highlighted that these requirements can be effectively addressed by bis(phthalocyaninato)lanthanide(III) complexes. The π radical plays an important role in these systems by: (i) functioning as an electron spin qubits, (ii) improving SMM properties, and (iii) contributing to spin cascade, which enables the readout of nuclear spin states. This was further elucidated through comparisons with tris(phthalocyaninato)dilanthanide(III) complexes, which lack a π radical. Therefore, the incorporation of an additional radical represents an effective strategy to enhance or compensate the function of the existing π radical.

The aim of this thesis is to expand the properties of bis(phthalocyaninato)lanthanide(III) and bis(porphyrinato)(phthalocyaninato)dilanthanide(III) complexes by introducing an additional radical. To this end, bis(phthalocyaninato)lanthanide(III) complexes having an additional radical on the periphery of phthalocyanine, and bis(porphyrinato)(phthalocyaninato)-dilanthanide(III) complexes containing a π radical have been designed. Specifically, three systems were investigated, as listed below.

$[YPc_2]^0$ with isoindoline-based nitroxide radical

Aiming at CNOT gate implementation using $[YPc_2]^0$ platforms, a newly designed diradical was synthesized and studied with various EPR techniques.

$[TbPc_2]^0$ with isoindoline-based nitroxide radical

Magnetic measurements were carried out on its terbium analogue to reveal the effect of additional radicals on the SMM properties of $[TbPc_2]^0$.

Bis(porphyritnato)(phthalocyaninato)diterbium(III) complex with π radical

A radical-bearing bis(porphyritnato)(phthalocyaninato)diterbium(III) complex was studied for the first time in bulk state, whose magnetic study was conducted thoroughly.

These studies are described in Chapter 2, 3, and 4, respectively. The conclusions and outlook are described in conclusive remark.

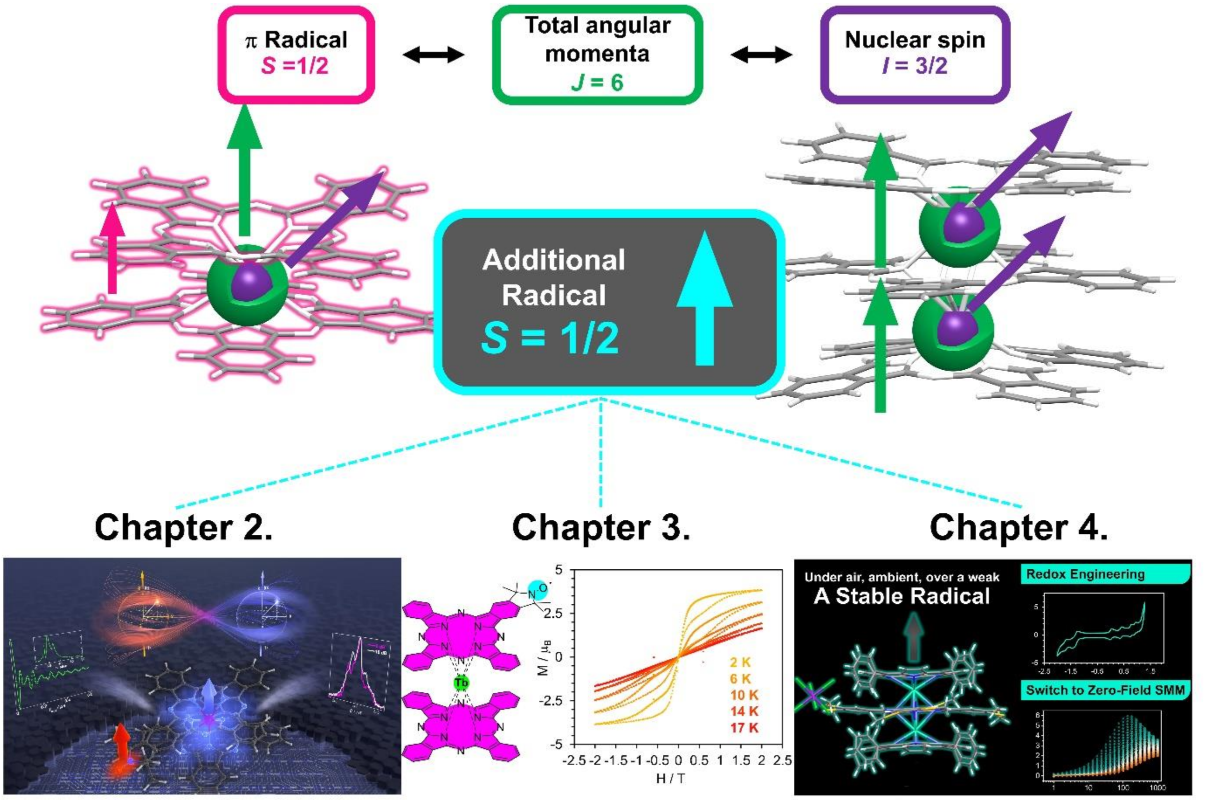

$[YPc_2]^0$ with isoindoline-based nitroxide radical

$[TbPc_2]^0$ with isoindoline-based nitroxide radical

Bis(porphyritnato)phthalocyaninato-diterbium(III) complex with π radical

Figure 1.11. Schematic illustration of the aim of the thesis: the incorporation of an additional radical in bis(phthalocyaninato)-mononuclear and tris(phthalocyaninato)-dinuclear terbium(III) complex. At the bottom, three projects are shown with illustrations, while the corresponding chapter numbers are shown on the top.

Chapter 2. Selective Transition Enhancement in a *g*-Engineered Diradical

This chapter is based on the published paper[144]: "J. Komeda, A. K. Boudalis, N. Montenegro-Pohlhammer, C. Antheaume, A. Mizuno, P. Turek, M. Ruben. Selective Transition Enhancement in a g-Engineered Diradical. *Chem. Eur. J.* **2024**, *202400420*. https://doi.org/10.1002/chem.202400420." The figures and tables represented in this chapter are reproduced from the original paper under the terms of the CC BY-NC-ND 4.0 license (https://creativecommons.org/licenses/by-nc-nd/4.0/). I sincerely appreciate the other authors' contribution: A. K. B. co-initiallized the project and carried out the EPR studies, N. M-P. performed DFT and CASSCF calculation, C. A. performed ESI-MS on the EPR specimen, A. M. supervised synthesis and characterization, P. T. gave guidance on EPR measurement, and M. R. directed the entire research. In this research, I conceived the idea together with A. K. B. and performed synthesis, characterization, and electrochemical study. The original manuscript was mainly written by myself and A. K. B., and edited by all the authors. I also acknowledge Sandra and Gareth Eaton, University of Denver, for performing the analysis of the fluid solution spectrum, as well as for several insightful discussions. I also acknowledge Dr. Sylvain Bertaina, Institut Matériaux Microélectronique et Nanoscience de Provence, for helpful discussions on the Rabi frequencies of weakly coupled systems.

2.1. Introduction

As explained in Chapter 1 Section 1.3.3, molecular spin qubits have garnered increasing interest due to their structural flexibility and uniformity. These qubits exhibit decoherence times that are long enough to allow quantum gate operations, typically in the range of tens of nanoseconds, as seen in $[V(C_8S_8)_3]^{2-}$.[33] Among the candidate molecules, organic radicals are drawing particular attention due to their extended spin-lattice relaxation times, attributed to their small spin-orbit coupling (SOC) (see Chapter 1 Section 1.3.4). I have also addressed the application of diradicals for multi-qubit gates. In particular, two spin systems that can be individually manipulated via pulsed electron paramagnetic resonance (pEPR) are suitable for implementing CNOT gates, as they enable selective flipping of one spin while leaving the other unchanged. This was proposed by Volkov and Salikohv in 2011,[145] and demonstrated experimentally by Takui and coworkers in 2012.[66] Additionally, Winpenny and coworkers recently reported a protocol for evaluating entanglement between two spins.[67]

The utility of bis(phthalocyaninato)lanthanide(III) complexes are described exclusively in Chapter 1 Section 1.5. These complexes have received attention as nuclear spin qudits for over a decade. However, recently, our group has explored the use of π radicals as an electron spin qubit.[57,60] So far, two types of compounds have been investigated; $[YPc_2]^0$ and $[YPcPor]^0$, both of which gave long T_1 and T_m. Though the relaxation nature remained unchanged in YPcPor dimers, however, their symmetric and isotropic *g* value prevents them from being used to implement CNOT gates. As explained in Chapter 1 Section 1.3.3 and 1.3.4, a CNOT gate is determined as follows: two spins coupled weakly, both of them are either *g* asymmetric (e.g. CeEr)[44] or with non-colinear and anisotropic g (e.g. VOTPP-dimer)[45]. Therefore, diradicals with engineered *g*-asymmetry based on YPc_2 platform is desirable.

In this chapter, I present the design, synthesis, characterization, and EPR studies on a $[YPc_2]^0$ derivative functionalized with isoindoline-based nitroxide radical, compound **1** (see Figure 2.1). One challenge encountered was the limited understanding of the delocalized radical. As shown in the end of the chapter, the distance between spins and the strength of exchange coupling are the critical parameters in QIP. The weak coupling regime is suitable for CNOT gate, while the strong coupling regime may serve as triplet-based qubits (e.g. qutrit based on C_{70}) [80]. With the series of EPR studies, the nature of the coupling in **1** was clearly determined.

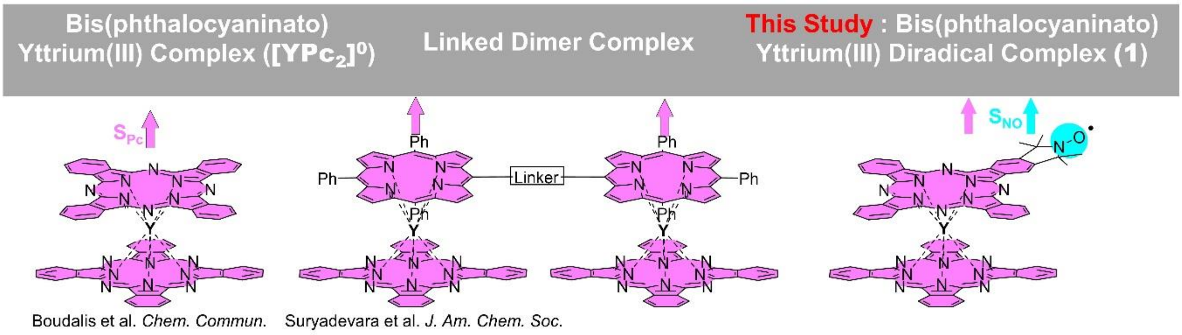

Boudalis et al. *Chem. Commun.* Suryadevara et al. *J. Am. Chem. Soc.*

Figure 2.1. Overview of the studies on bis(phthalocyaninato)- or (porphyirinato)(phthalocyaninato)- yttrium(III) complexes. **S_{Pc}**, which is delocalized over phthalocyanine rings, is depicted in magenta; **S_{NO}**, which is localized at [NO]·, is represented as a cyan circle.

2.2. Results

2.2.1. Synthesis and Characterization

Synthesis

Isoindoline-based nitroxide radical was selected as the peripheral radical group due to its stability against the high-temperature conditions of the phthalocyanine formation reaction.[146] Moreover, its rigid structure is advantageous for preserving a fixed orientation and distance between the two radicals (**S_{pc}** and **S_{NO}**), which will prevent any unwanted rotation of the radical moiety in the solution.

Previously, it was reported that mono-, di-, tri- substituted $LnPc_2$ analogues could be obtained in higher yields when synthesizing from reactions between phthalonitrile derivatives and lanthanide mono-phthalocyanine complexes compared to other traditional methods for $LnPc_2$ analogs.[147–149] Employing this method, compound **1** was synthesized using yttrium(III) phthalocyaninato acetate complex (YPcOAc) as a template. 5,6-Dicyano-1,1,3,3-tetramethylisoindolin-2-yloxyl (**[NO]$^{\cdot}$PN**) and YPcOAc were prepared following the literature methods,[146,150–152] which are further described in Chapter 5. The reaction of **[NO]$^{\cdot}$PN** with a slight excess of phthalonitrile and YPcOAc in the presence of 1,8-diazabicyclo- [5.4.0]undec-7-ene (DBU) yielded a mixture containing $[YPc_2]^0$, **1**, di-substituted $[YPc_2]^0$, along with other unidentified by-products (Figure 2.2).

The obtained crude material was purified by silica gel column chromatography (eluent; $CHCl_3$ with 1% of Et_3N). This process was repeated several times until only one green spot appeared in thin-layer chromatography (TLC). After reprecipitation from a $CHCl_3$/MeOH mixture yielded a diradical **1** as a green powder. Unfortunately, the material didn't crystalize in any combination of conventionally used solvents such as CH_2Cl_2, hexane, etc. This is attributed to the low symmetry of this molecule. Indeed, to my best knowledge, no single-crystal structure has been reported for monosubstituted $LnPc_2$ derivatives.

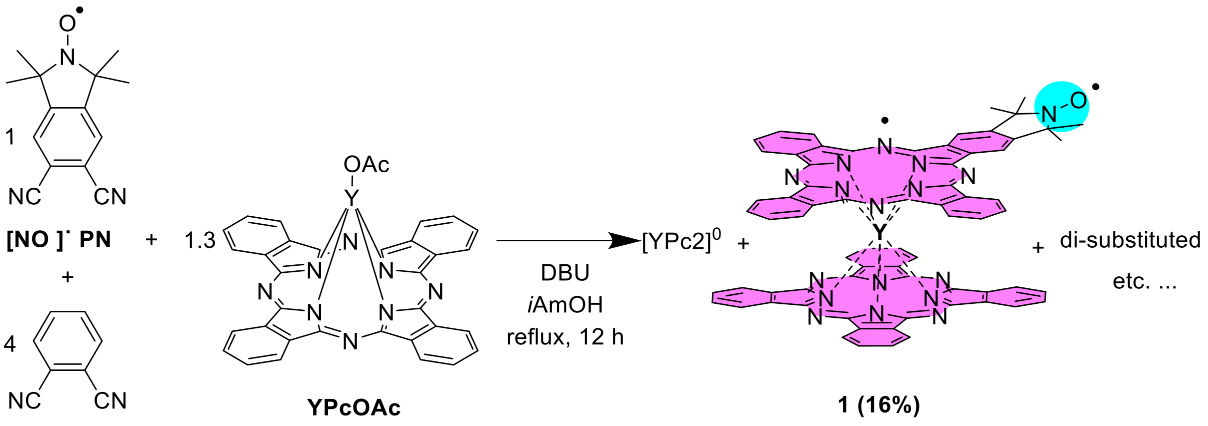

Figure 2.2. Reaction scheme of the synthesis of **1**. Reproduced from ref.[144]

UV-vis-NIR absorption spectroscopy

First, the obtained material **1** was characterized with UV-vis-NIR abs. spectroscopy. Figure 2.2. represents the UV-vis-NIR absorption spectra of $[YPc_2]^0$, **1**, and **[NO]$^{\cdot}$PN**. The spectrum of **1** is almost identical to that of $[YPc_2]^0$, represented by a Soret band around 350 nm and a Q band at around 750 nm, both of which are known as characteristic of neutral bis-(phthalocyaninato) complexes.[149] Absorption bands that represent $\mathbf{S_{Pc}}$ were detected for both of them as well; a blue valence (BV) band (ca. 450 nm), a red valence (RV) band (ca. 900 nm), and an intervalence (IV) band at the NIR.

The absence of the characteristic peak of the $[NO]^{\cdot}$ moiety in the spectrum of **1** was explained by the comparison of $[YPc_2]^0$, **1**, and **[NO]$^{\cdot}$PN** and TD-DFT calculation. First, in the UV-vis spectrum, no peak with absorption coefficients (ϵ) of higher than 0.5 $M^{-1}cm^{-1}$ was observed in the region λ>300 nm (Figure 2.2.d grey line). In comparison with $[YPc_2]^0$ and **1** (Figure 2.2b), it is clear that the peak top is apart from the region of interest.

Furthermore, TD-DFT calculation predicted that the [NO]· moiety exhibited absorption peaks at λ = 484.72 nm and 401.81 nm, with significantly weaker oscillation strengths compared to the UV region peaks. Therefore, the UV-vis absorption spectrum and TD-DFT calculation for **[NO]$^{\cdot}$PN** suggest that the absorption bands associated with the $[NO]^{\cdot}$ moiety are significantly weaker (ϵ<0.5 $M^{-1}cm^{-1}$) than the Q band of $[LnPc_2]^0$ (ϵ ~2×10^5 $M^{-1}cm^{-1}$)[152]). As a result, the absorption features associated with $LnPc_2$ dominate the spectrum of compound **1**.

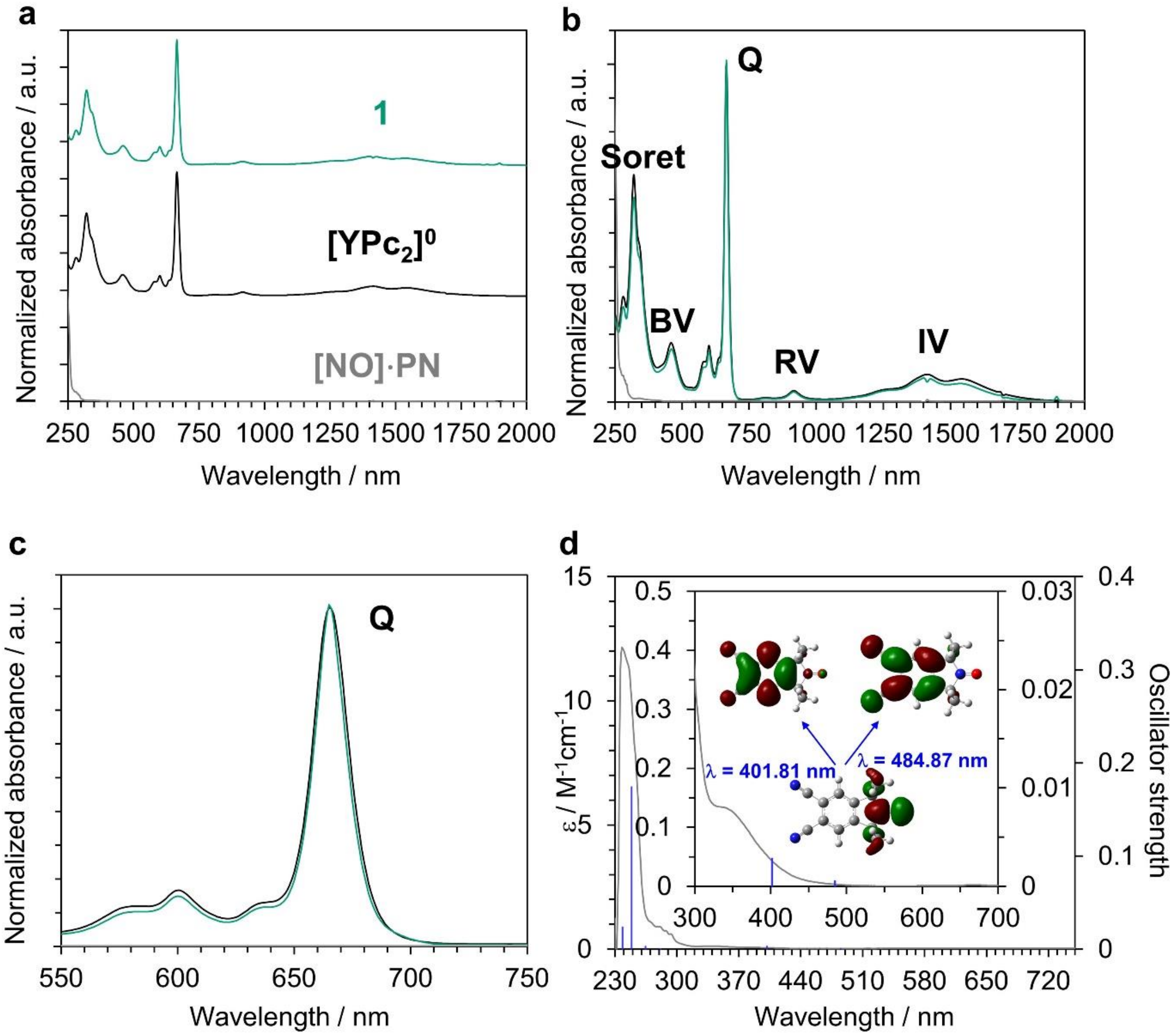

Figure 2.3. (a-c) UV-vis-NIR absorption spectra of **1** (green), [YPc$_2$]^0 (black), and **[NO]˙PN** (grey) in CHCl$_3$ in stacking (a) and overlaid (b) configuration, and the expansion of (b) in 550 – 750 nm (c). (d) Comparison of UV-vis-NIR absorption spectrum of **[NO]˙PN** (grey) and TD-DFT calculation result (blue). Inset represents the spectrum measured for the condensed sample (cf. the sample in 1.07 M used, while the other spectrum is taken with the sample in 8.6 × 10^{-2} M) and calculated peaks (λ = 401.81nm and 484.87 nm). The molecular orbitals shown in the middle are the ones related to each absorption peak. Reproduced from ref.[144]

IR spectroscopy

Figure 2.4 represents the IR spectra of $[\mathrm{YPc_2}]^0$, **1**, and **[NO]$^{\cdot}$PN**. In the fingerprint region (500–1000 cm^{-1}), similar peaks were observed for **1** and **[NO]$^{\cdot}$PN**. Additionally, around 1500 cm^{-1}, similar peaks were seen for **1** and $[\mathrm{YPc_2}]^0$. The distinctive peak for isoindoline nitroxide at 1700 cm^{-1} was present in both **1** and **[NO]$^{\cdot}$PN**.[146] Importantly, no peak was observed around 3500 cm^{-1} for **1**, which certifies the absence of NO−H bonds made from the reduction of nitroxide radical.

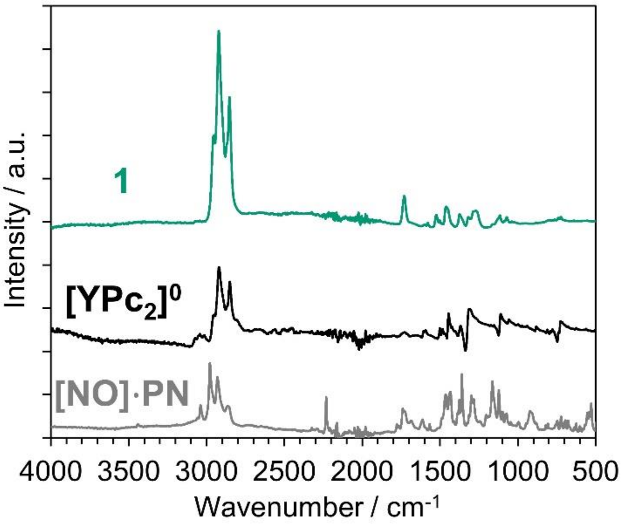

Figure 2.4. IR spectra for **1** (green), $[\mathrm{YPc_2}]^0$ (black), and **[NO]$^{\cdot}$PN** (grey). Reproduced from ref.[144]

ESI-mass spectrometry

High-resolution Electrospray Ionization Mass Spectrometry (ESI-HRMS) was performed for compound **1** (Figure 2.5a). The spectrum displayed a signal from one ion, whose isotopic pattern matched well with the simulation. The purity of the material was confirmed by the absence of the signals corresponding to $[YPc_2]^0$ and di-substituted one (Figure 2.5b,c). The findings were in complete agreement with ESI-HRMS investigations conducted on the EPR sample (Figure 2.6a).

To further investigate the stability of compound **1** against protonation, an ESI-HRMS spectrum was measured with the addition of 0.1% (v/v) acetic acid in MeOH. Notably, this analysis revealed a +1 m/z peak shift for a portion of the sample (Figure 2.6b), consistent with the nitroxide moieties undergoing disproportionation into hydroxide and oxoammonium species under acidic conditions. Remarkably, a significant portion of the sample remained resistant to protonation even under these conditions, further confirming the stability of the [NO]· radical in compound **1**.

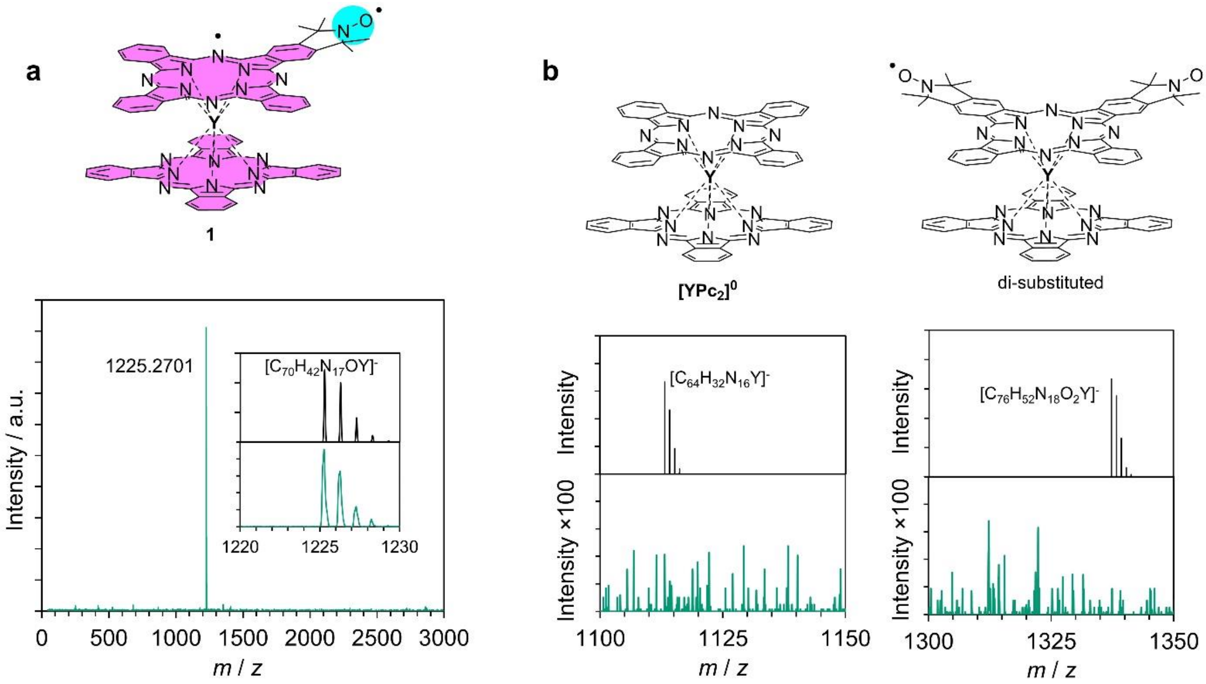

Figure 2.5. ESI-MS spectrum of **1**. The inset compares the experimental (green) and simulated (black) isotopic patterns. Reproduced from ref.[144]

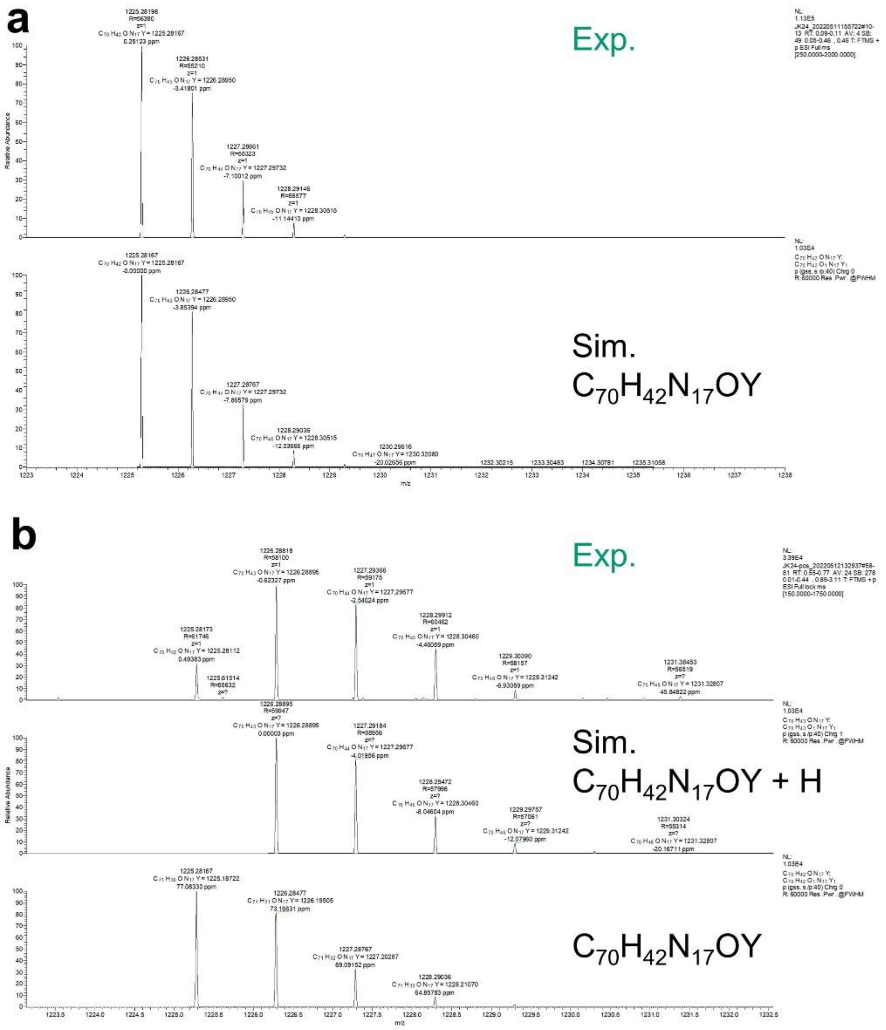

Figure 2.6. (a) HRMS (ESI+-Orbitrap) spectra of **2** after EPR measurement (top) and simulated spectra calculated for $C_{70}H_{42}ON_{17}Y$ m/z: $[M]^{+\cdot}$ = 1225.28167 (bottom); Found 1225.28198 (0.25ppm). (b) HRMS (ESI+-Orbitrap) spectra of **2** with an addition of 0.1%v/v acetic acid (top), and simulated spectra calculated for $C_{70}H_{43}ON_{17}Y$ m/z: $[M+H]^{+}$: 1226.28895; Found 1226.28818 (-0.62 ppm) (middle) and calculated for $C_{70}H_{42}ON_{17}Y$ m/z: $[M]^{+\cdot}$; Found 1225.28167 (0.49 ppm) (bottom). Reproduced from ref.[144]

Characterization of the Adduct in EPR Sample – Investigation of the Stability of the Sample

As will be mentioned later, a minor (~10 %) nitroxyl-radical component was detected in EPR measurement. To identify the possible nitroxide-radical, the UV-Vis-NIR absorption spectrum was measured on the $CHCl_3$ solution of the sample used for fluid EPR measurement. It exhibited a shoulder peak at 700 nm on the longer wavelength side of the Q band (at 665 nm). Given that a redshift of a Q band is typically observed in cationic $[LnPc_2]^+$ derivatives, the observed shoulder peak likely corresponds to an adduct formed by the oxidation of **1**, comprising $[YPc_2]^+$ and $[NO]^{\cdot}$ moieties ($[Y(Pc)(PcNO)]^{\cdot +}$ (**1’**)), possibly due to air oxidation of **1** during the sample storage and/or preparation. The intensity ratio of the shoulder peak to the Q band peak is 0.028. Considering the molar absorption coefficients (ε) for Q bands of $[LnPc_2]^0$ ($\varepsilon = 1.9 \times 10^5$ M^{-1} cm^{-1}) and $[LnPc_2]^+$ ($\varepsilon = 0.5 \times 105$ M^{-1} cm^{-1}),[149] the composition of **1’** in the EPR sample is estimated to be 9.7%. To the best of my knowledge, molar absorption coefficients have only been reported for $[LuPc_2]^+$ derivatives in the series of cationic $LnPc_2$, probably due to their poor solubility in any organic solvent. To sum up, the adduct was determined to be the oxidation product of **1**, designated as **1’**.

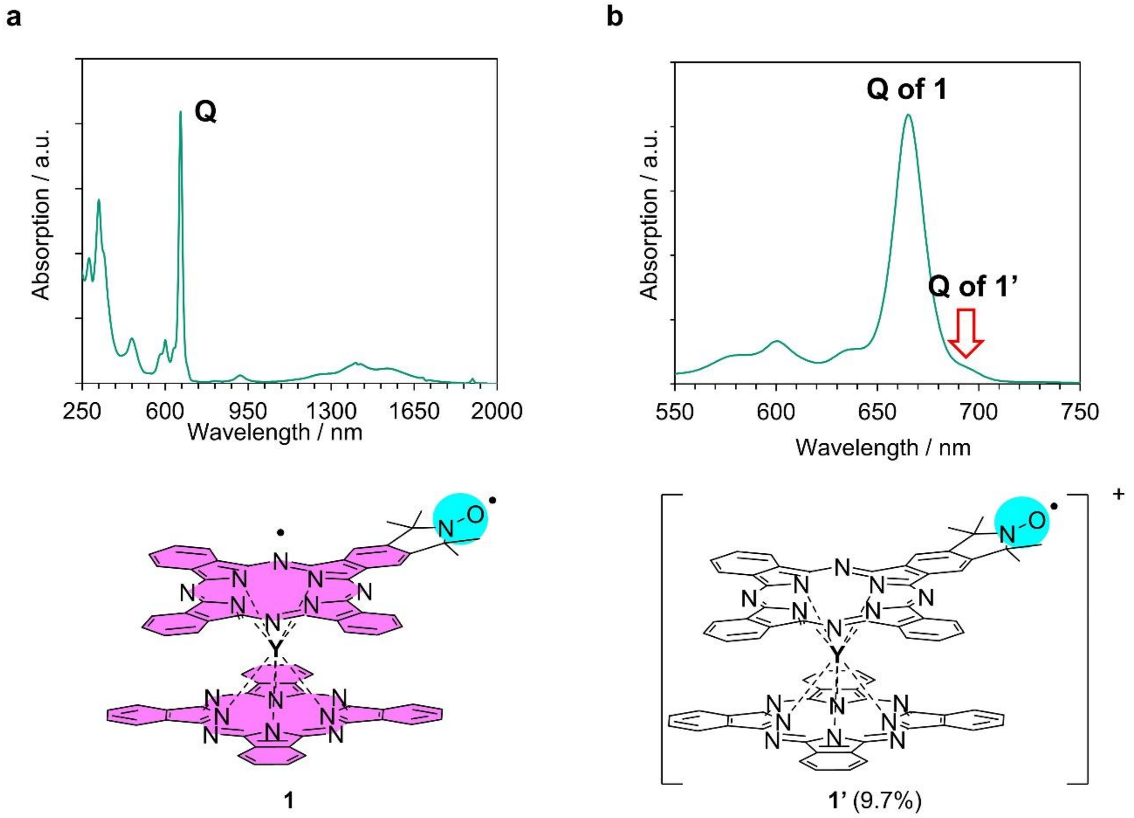

Figure 2.7. UV-Vis-NIR absorption spectrum of the $CHCl_3$ solution of **1** used for EPR measurement (a), and the expansion of Q band (b). The bottom line represents molecular structures of **2** and **2’**. **S$_{Pc}$** and **S$_{NO}$** are represented in magenta and cyan, respectively. Reproduced from ref.[144]

2.2.2. Computational and Electrochemical Study

Energy Calculation

To explore the molecular and electronic structure of compound **1**, Density Functional Theory (DFT) and Wave Function Theory (WFT) based calculations were performed. In addition, the magnetic coupling between the unpaired electron localized at [NO]· group and the one on the Pc rings was investigated. First of all, the initial molecular structure of **1** was optimized through the DFT methodology, using the Perdew–Burke–Ernzerhof (PBE) exchange correlation. Dispersion interactions were treated with the DFT-D3 atom-pairwise correction.

Energy calculations revealed that the molecular orbitals (MOs) of compound **1** closely resemble those of compound $[YPc_2]^0$, with one notable exception: SOMO-1 in compound **1** is localized at the [NO]· moiety (Figure 2.8). This result aligns with data of UV-Vis-NIR absorption spectroscopy and cyclic voltammetry studies (see Section 2.2.1 and the latter part of this section, respectively).

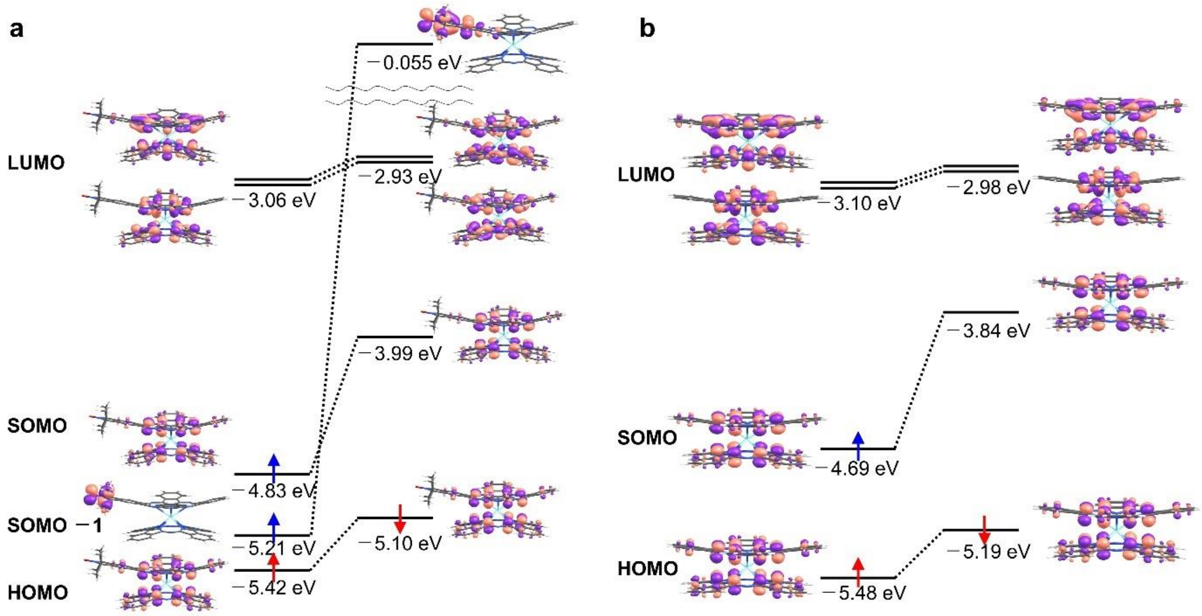

Figure 2.8. Molecular orbitals of **1** (a) and $[YPc_2]^0$ (b) calculated with UB3LYP/TZVP. Note that β MOs of **1** between β SOMO − 1 and β LUMOs are omitted for clarity. The energy level of β SOMO − 1 and β LUMO is 305β and 302/301β, respectively. The isosurface value for **1** and $[YPc_2]^0$ is both 0.03. Reproduced from ref.[144]

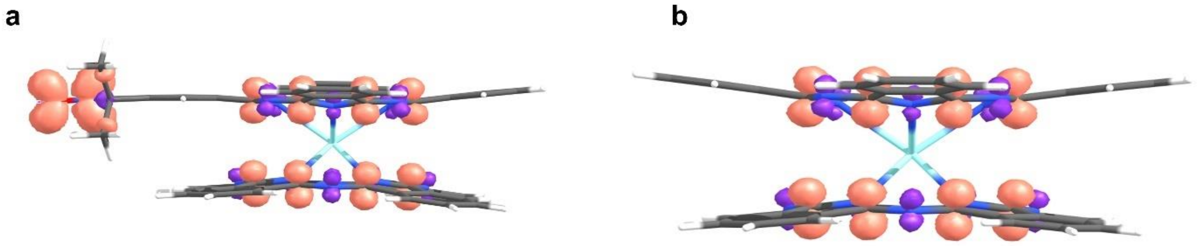

Figure 2.9. Spin densities of **1** (a) and $[YPc_2]^0$ (b). The isosurface value for **1** and $[YPc_2]^0$ is both 0.003. Reproduced from ref.[144]

Calculation of the coupling constant J

The coupling constant *J* was calculated to be 4.24 cm^{-1} (127 GHz) using a broken symmetry (BS) methodology, indicating weak ferromagnetic coupling between both centers. The magnetic orbitals (Single Occupied Molecular Orbitals, SOMOs) and spin density of the high-spin (HS) and BS states are depicted in Figure 2.10. Analysis of this figure suggests that the weak ferromagnetic behavior of the coupling mainly results from insufficient overlap between the orbitals. This reduced 'kinetic exchange' contribution favors antiparallel alignment (antiferromagnetic) and reflects the ability of magnetic electrons to transition between sites in the singlet state.

To further refine the energy calculations of both the singlet and triplet states for compound **1**, the multireference CASSCF/NEVPT2 methodology was employed. An active space of two electrons in two orbitals was used, with an average of the singlet and triplet ground states (Figure 2.9 and 2.11). The results of this study are shown in Table 2.1. As expected, the *J* value obtained through the CASSF/NEVPT2 methodology (-0.04 cm^{-1}) is considerably lower than the one calculated using the DFT, as it is known that BS methodology tends to overestimate the magnitude of the J values, and also, strongly depending on the employed exchange-correlation (XC) functional.[153–156] In addition, in this case, the CASSCF/NEVPT2 calculations also predict a different coupling nature, i,e, antiferromagnetic. However, given the small magnitude of *J*, determining the exact nature of the coupling (ferro- or antiferromagnetic) is challenging, especially since the experimental molecular structure is unavailable, and even slight structural variations could alter spin state energies within this computed *J* range. Nevertheless, the magnitude of the *J* from CASSCF aligns well with the experimental value obtained from fits of fluid solution CW EPR spectra (see Section 2.2.3).

Table 2.1. Calculated coupling constant *J* by the DFT and WFT methods performed on **1**.

	BS (B3LYP)	CASSCF(2,2)/NEVPT2
J (cm^{-1})	4.24	-0.04

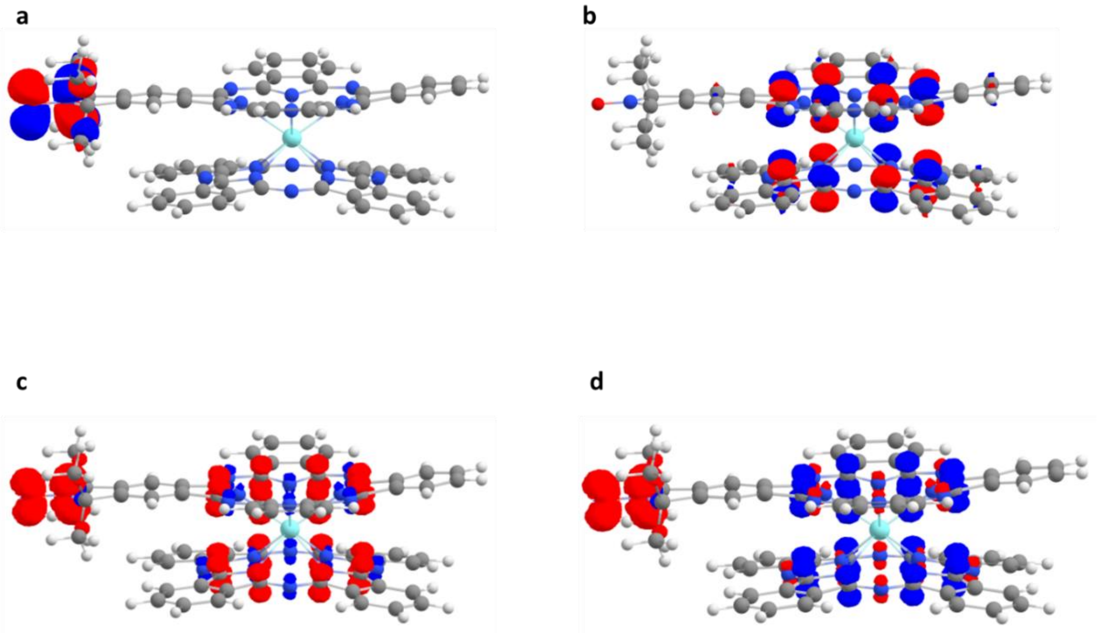

Figure 2.10. **a, b:** Singly-occupied orbitals obtained from the high (HS) state ($S = 1$) for the **1**, employing the B3LYP functional. The spin density of the HS state (c) and broken symmetry (BS) state (d). In (c) and (d), red represents spin up, and blue spin down densities. Reproduced from ref.[144]

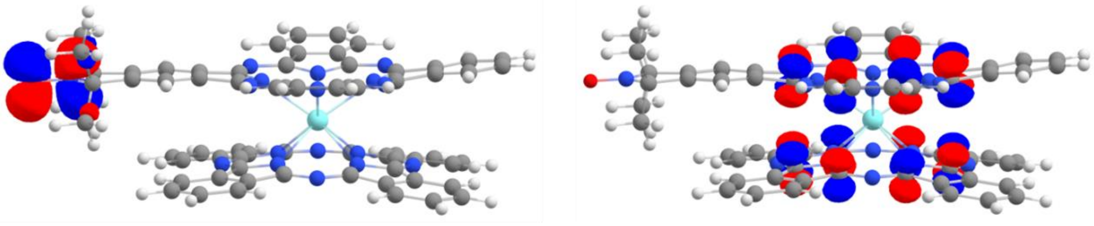

Occ=1.000

Occ=1.000

Figure 2.11. Active orbitals and their corresponding electronic occupations (occ), employed in the CASSCF/NEVPT2 calculations for the **1**. Reproduced from ref.[144]

Electrochemical Study

To investigate the redox properties of compound **1**, cyclic voltammetry was performed on both $[YPc_2]^0$ and **1**. The cyclic voltammogram of **1** closely resembled that of $[YPc_2]^0$, except for additional peaks attributed to the nitroxide moiety. Specifically, **1** exhibited seven redox couples similar to those observed for $[YPc_2]^0$. These redox events correspond to the oxidation (E_o’ = 1.04 and -0.07 V vs. ferrocenium/ferrocene (Fc^+/Fc)) and reduction (E_o’ = -0.53, -1.69, -2.01, -2.29, and -2.44 V) of the Pc ligands (Table 2.2). However, in contrast to $\mathbf{[YPc_2]^0}$, an irreversible oxidation wave at 1.25 V and a redox couple at E_o’ = 0.43 V were observed in **1**.

To identify these features, cyclic voltammetry was also performed on [NO]· dibromobenzene (**SM3**, Figure 2.12b and Table 2.3). The results showed an irreversible wave at 1.53 V and a redox couple at E_o’ = 0.53 V, consistent with previously reported values. Given that redox potentials vary with different functional groups (0.37–0.53 V) [157], these waves were assigned to oxidations centered at the [NO]· moiety. Overall, the redox characteristics of compound **1** reflect the combined redox properties of $[Y(Pc)_2]$· and [NO]· moieties. This conclusion aligns with DFT calculations, which reveal separate molecular orbitals (MOs) for **1**—one localized on the $[Y(Pc)_2]^{\cdot}$ moiety (similar to MOs of 1) and the other localized on the $[NO]^{\cdot}$ moiety (Figure 2.8).

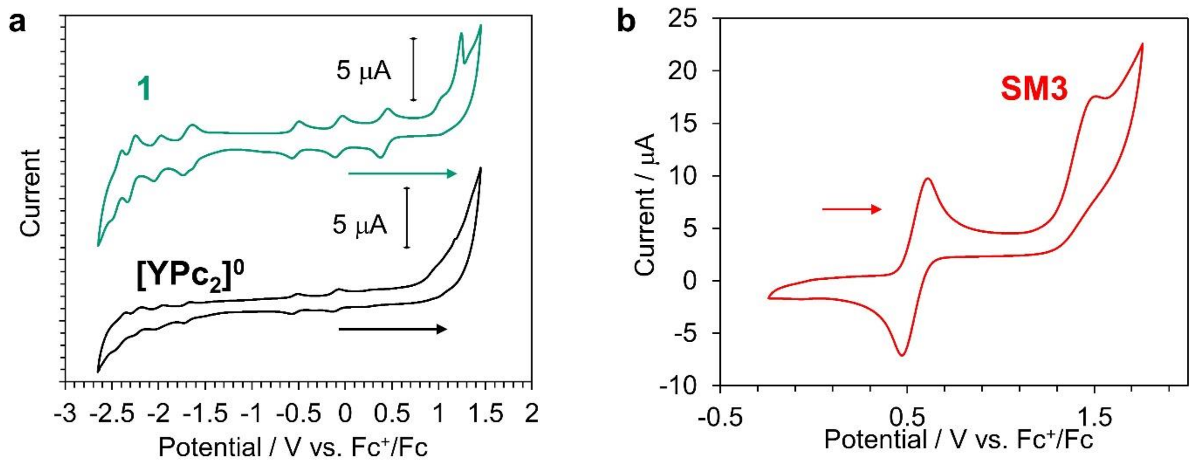

Figure 2.12. (a) Cyclic voltammogram of **1** (green) and $[YPc_2]^0$ (black) at a scan rate of 100 mVs^{-1}. (b) Cyclic voltammogram of **SM3** at a scan rate of 100 mVs^{-1}. The directions were shown by arrows. Reproduced from ref.[144]

Table 2.2. Redox potentials of seven redox couples observed in both **1** and $\mathbf{[YPc_2]^0}$ (V vs. Fc^+/Fc).

	$[YPc_2]^{2+/+}$	$[YPc_2]^{+/0}$	$[YPc_2]^{0/-}$	$[YPc_2]^{-/2-}$	$[YPc_2]^{2-/3-}$	$[YPc_2]^{3-/4-}$	$[YPc_2]^{4-/5-}$
1	1.04	-0.07	-0.53	-1.69	-2.01	-2.29	-2.44
$\mathbf{[YPc_2]^0}$	1.11[a]	-0.10	-0.54	-1.70	-2.00	-2.23	-2.40

[a]The value is used from the literature.[158]

Table 2.3. Potentials of a redox couple and an irreversible oxidation wave observed in **1**, **SM3**, and general value for molecules with $[NO]^{\cdot}$ (V vs. Fc^+/Fc).

	$[NO]^{\cdot}/[NO]^+$	2nd Oxd

1	0.43	1.25
SM3	0.53	1.53
General [NO]$^{\cdot}$	0.37-0.53^{a}	-

^{a}The value is used from the literature.[157]

2.2.3. CW EPR - Determination of the J-Coupling (in coll. with Dr. A. Boudalis)

CW EPR in fluid solution

Continuous-wave (CW) spectra in a fluid solution were measured at room temperature to reveal the isotropic component of hyperfine interactions. The spectra exhibit two distinct components, each featuring triplet signals—a common characteristic of hyperfine coupling to ^{14}N(I = 1). The results are illustrated in Figure 2.13.

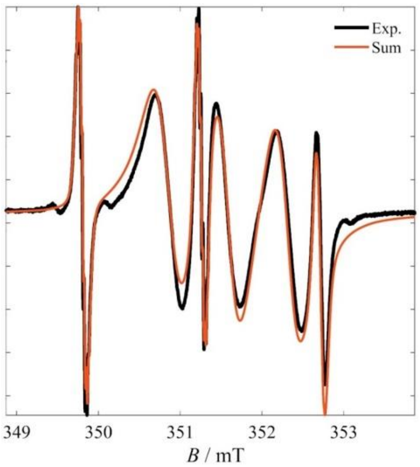

Figure 2. 13. X-band fluid solution spectrum (black) in 4 : 1 CD_2Cl_2:$CHCl_3$ at ambient temperature and simulation (red) as the mixture of non-interacting nitroxide adduct **1’** (see Section 2.2.1) (~10 %) and spin-coupled complex **1** with J=15 mT (~90 %). Experimental conditions: f_{EPR}=9.8620 GHz, ΔB_{mod}=0.0098 mT$_{\mathrm{pp}}$, P_{MW}=0.51 mW. Reproduced from ref.[144]

During preliminary fitting, each of spectral components were analyzed separately and modeled using Easyspin’s garlic function. One component, later attributed to the diradical system **1** (as explained below), showed broad line widths. In contrast, the other component (assigned to a **1’** monoradical, as described later) displayed narrow lines with additional features arising from ^{1}H and ^{13}C hyperfine couplings.

The best-fit parameters included g_{dirad} = 2.0041, σ_{G} = 0.201 mT, σ_{L} = 0.203 mT, A_{Ndirad} = 20.47 MHz, with a relative weight of 92% and g_{NO} = 2.0060, σ_{G} = 0.013 mT, σ_{L} = 0.020 mT, $A_{\mathrm{N(NO)}}$ = 40.96 MHz, $A_{\mathrm{H(NO)}}$ = 0.69 MHz, $A_{\mathrm{C(NO)}}$ = 17.88 MHz, (with a relative weight of 8 %), where g represents isotropic g values, σ represents half width at half maximum of Gaussian (σ_{G}) or

Lorentzian (σ_L), and A represents hyperfine coupling constant. Remarkably, the spin Hamiltonian parameters for the nitroxide radical closely resemble those previously determined for the parent 1,1,3,3-tetramethylisoindolin-2-yloxy radical in a 218 K fluid toluene solution (specifically, g_{NO} = 2.0054, $A_{N(NO)}$ = 39.52 MHz, $A_{H(NO)}$ = 0.68 MHz, $A_{C(NO)}$ = 17.9 MHz).[159] The fitting results are depicted in Figure 2.14.

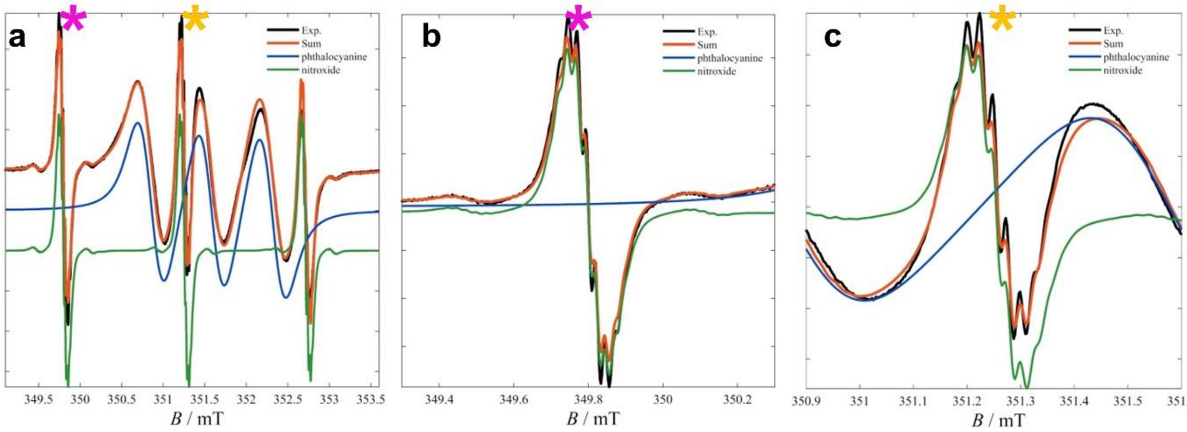

Figure 2.14. (a) Fluid solution spectrum of **1** in a $CD_2Cl_2/CDCl_3$ 4:1 solvent mixture (black) and fits to two spin systems (red) assigned to phthalocyaninato (blue) and nitroxo (green) radicals. (b,c) Expansions of the low-field (b) and central resonances (c) of the NO-radical triplet demonstrating the hyperfine couplings to ^{1}H nuclei. Corresponding peak locations are indicated by asterisks in pink and yellow, respectively. Reproduced from ref.[144]

An interesting feature of these spectra lies in the hyperfine splittings, which were absent in both the powder and frozen solution spectra of the parent compound $[YPc_2]^0$.[57,60] These splittings were also not predicted by DFT calculations. To confirm whether this absence of hyperfine splitting holds true in fluid solution spectra of the parent molecule, additional studies were conducted on compound $[YPc_2]^0$. These investigations revealed a straightforward singlet signal without any hyperfine splitting. The best-fit parameters for this signal were g_{pc} = 2.0022, σ_G = 0.462 mT, σ_L = 0.027 mT (as shown in Figure 2.15).

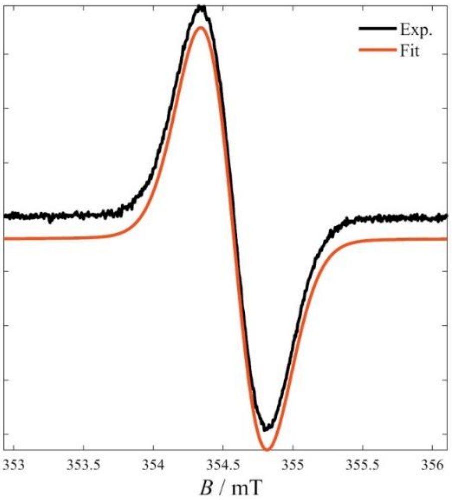

Figure 2.15. X-band fluid solution spectrum of $[YPc_2]^0$ in 4 : 1 CD_2Cl_2:$CHCl_3$ at ambient temperature (black) and simulation (red). Reproduced from ref.[144]

While one of these peak sets closely resembled that of the free nitroxide radical, the other exhibited distinct differences compared to the spectra of $[YPc_2]^0$. This led to a hypothesis that the broad triplet corresponds to the diradical **1**, whereas the narrow triplet belongs to a minority monoradical species **1'**, with the radical localized solely on the nitroxide moiety. Although this species would appear indistinguishable from the ESI-MS spectra of the diradical, the UV-vis-NIR absorption spectrum of **1** used for EPR indicated the presence of a small amount (9.7%) of the oxidized species of **1** (see Section 2.2.2).

Analysis of the fluid CW EPR spectrum

The fluid-solution EPR spectra of the phthalocyanine-nitroxide diradical **1** (Figure 2.13) were analyzed by summing AB splitting patterns, similar to previous studies on copper-nitroxide complexes[160,161], dinitroxides[162] and trityl-nitroxides[163]. The Hamiltonian can be expressed[161] as:

$$\hat{H} = g_1\beta_e B\hat{S}_1 + g_2\beta_e B\hat{S}_2 + hA_1\hat{S}_1\hat{I}_1 + hJ\hat{S}_1\hat{S}_2 \qquad (2.1)$$

Here, g_1 and g_2 represent the g-values for nitroxide and phthalocyanine radicals, A_1 is the nitroxide nitrogen hyperfine coupling in Hz, J is the electron-electron exchange interaction in Hz, β_e is the electron Bohr magneton, and h is Planck's constant. The first three terms describe the spectra for non-interacting nitroxide and phthalocyanine. The Kivelson model accounts for incomplete motional averaging of the g and A anisotropy of the nitroxide. [164]

$$\Delta B_{pp} = A + Bm_I + Cm_I{}^2 \qquad (2.2)$$

where ΔB_{pp} is the peak-to-peak linewidth, m_I is the nitrogen nuclear spin state, and A, B, and C are adjustable parameters. While this model fits nitroxide linewidths well in the absence of spin-spin interaction, it does not fully describe the impact of incomplete motional averaging in spin-coupled complexes.

The interaction between the unpaired electrons of phthalocyanine and nitroxide ($hJ\hat{S}_1\hat{S}_2$) causes each line in the spectrum for each paramagnetic center to split into a doublet. Using the AB splitting formalism familiar from NMR spectroscopy of *J*-coupled nuclei[165], the impact of this spin-spin interaction was analyzed on the fluid solution spectrum of **1**. The positions and relative intensities of the four lines in an AB pattern are summarized in Table 2.4. Here, B_{avg} represents the average resonance fields for the two spins in the absence of interaction, and Δ is the separation of the resonance fields without spin-spin interaction. Additionally, $C = 0.5(J^2 + \Delta^2)^{1/2}$, and $\sin 2\theta = J/2C$.[164]

As J increases, two lines move toward B_{avg} increasing in intensity, while two lines move away from B_{avg}, decreasing in intensity. In the discussion below for the spectrum of **1**, the focus is on the lines moving toward B_{avg}, as these dominate the spectrum.

Table 2.4. Positions and relative intensities of the four lines in an AB splitting pattern[a].

Line	Offset from B_{avg}[b]	Relative Intensity
a'	$-J/2 - C$	$1 - \sin(2\theta_{\mathrm{AB}})$
a	$J/2 - C$	$1 + \sin(2\theta_{\mathrm{AB}})$
b	$-J/2 + C$	$1 + \sin(2\theta_{\mathrm{AB}})$
b’	$J/2 + C$	$1 - \sin(2\theta_{\mathrm{AB}})$

[a] Equations taken from Ref. 6. B_{avg}, J, C, Δ are in magnetic field units, which are mT in this chapter. The designations a', b' refer to the lower intensity lines and a, b refer to higher intensity lines. When applied to phthalocyanine-nitroxides the designations a and b are replaced by N and P that refer to nitroxide and phthalocyanine, respectively. Δ is the separation between resonance fields for the phthalocyanine and nitrogen m_I lines in the absence of spin-spin interaction. $C = 0.5*(J^2 + \Delta^2)^{1/2}$ and $\sin(2\theta_{\mathrm{AB}}) = J/2C$.[165]

[b] B_{avg} is the average of the resonance fields for the two spins in the absence of interaction and is different for each of the three nitrogen m_I lines of the nitroxide-phthalocyanines.

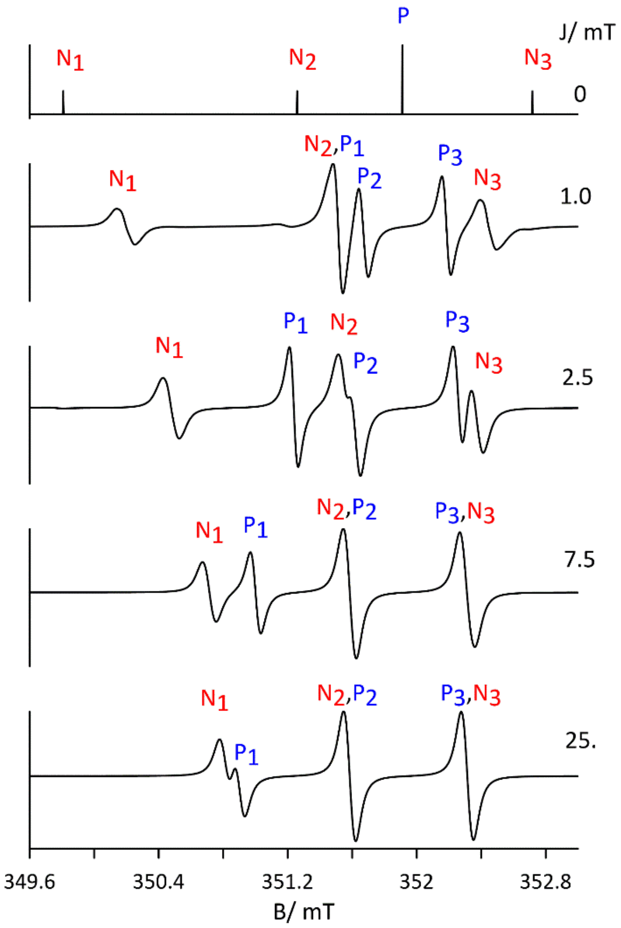

Figure 2. 16. Simulations of the AB splitting patterns for a phthalocyanine-nitroxide diradical using the parameters given in the text for a series of *J* values, in mT. Phthalocyanine and nitroxide lines are labeled as P_I and N_I with the subscript designating the nitrogen hyperfine line. Reproduced from ref.[144]

The spectra shown in Figure 2.16 were calculated using the program CUNO, designed to simulate fluid solution EPR spectra of spin-coupled copper-nitroxide complexes.[161] The mathematical framework applies to any pair of interacting S = ½ centers. These simulations, based on a microwave frequency of 9.862 GHz (matching the data acquisition frequency for **1** in Fig. 2.12), utilized the following nitroxide parameters: $g_{NO} = 2.0060$, $A_N = 40.74$ MHz, A_H (12 equivalent protons) = 0.67 MHz, phthalocyanine $g_{Pc} = 2.0023$, and a series of *J* values. Lorentzian linewidths were 0.1 mT for lines moving toward the center of the AB pattern and 0.5 mT for lines moving away from the center.

In the stick spectrum for $J = 0$ (Figure 2.16), three nitroxide lines are present (N_1, N_2, and N_3) due to nitrogen hyperfine coupling and one phthalocyanine line in the absence of electron spin-

spin interaction are observed. When J ranges from 1.0 to 25 mT, the spectra include both nitroxide proton hyperfine coupling and nitrogen hyperfine coupling. The phthalocyanine lines in the AB patterns are labeled with subscripts corresponding to the nitrogen hyperfine lines (P_1, P_2 and P_3). Without interaction, resonances N_1, N_2, and N_3 occur at 349.81, 351.26, and 352.72 mT, while the phthalocyanine resonance is at 351.91 mT, resulting in Δ values of 2.1, 0.65, and 0.81 mT for the three AB patterns.

As J increases, N_1 and P_1 move closer together, as do N_2 and P_2, and N_3 and P_3. A J value of 7.5 mT is sufficient to make N_2 and P_2 positions coincide, and similarly for N_3 and P_3. However, even at J = 15 mT, the positions for N_1 and P_1 are not fully averaged. The larger J required for N_1 and P_1 averaging, compared to other AB patterns, aligns with the larger Δ value. When positions are fully averaged for all three AB patterns, the nitrogen hyperfine coupling and proton hyperfine couplings are half of the values for isolated nitroxide.

Although the same linewidths were used for all six lines, overall linewidths for N_1, N_2, and N_3 decrease with increasing J due to the effective proton hyperfine decreasing from A_H to $A_H/2$. Conversely, the overall linewidths for P_1, P_2, and P_3 increase with increasing J because the effective A_H increases from 0 to half of the nitroxide value. In experimental data, variations in J values may cause linewidths for all lines to increase with increasing J.

In short, using the CUNO program, the fluid solution spectrum of compound **1** was simulated, accounting for electron spin-spin coupling between two inequivalent $S = 1/2$ centers. The Kivelson model, originally developed for nitroxide radicals, approximated incomplete motional averaging. Sharp lines at 349.81, 351.26, and 352.72 mT, with partially resolved proton hyperfine coupling, were assigned to **1'**, where the Pc ring system is diamagnetic. Parameters for the non-interacting nitroxide (g_{NO} = 2.0060, A_N = 40.74 MHz, A_H (12 protons) = 0.67 MHz, Kivelson linewidth parameters A = 0.028 mT, B = 0.006 mT) aligned well with fits for the structurally related free radical. The broad lines corresponded to the spin-coupled diradical **1**, simulated with g_{NO} = 2.0060, A_N = 40.74 MHz, A_H (12 protons) = 0.67 MHz, g_{pc} = 2.0023, J = 0.014 cm^{-1} (420 MHz), and Kivelson linewidth parameters A = 0.33 mT, C = 0.001 mT. These parameters matched expectations for two paramagnetic centers without spin-spin interaction. The computed J value closely resembled the one from WFT calculations ($|J|$ = 0.04 cm^{-1}, see Section 2.2.2). The simulation did not include natural abundance ^{13}C hyperfine lines.

CW EPR in frozen solution

These results were utilized in the analysis of continuous wave (CW) electron paramagnetic resonance (EPR) spectra in frozen solutions of the diradical. To investigate the magnetic anisotropies within the diradical system, CW EPR spectra were measured in frozen solution at X and Q-bands. These spectra exhibited a complex pattern, reflecting the contribution of multiple spin Hamiltonian terms (as shown in Figure 2.17).

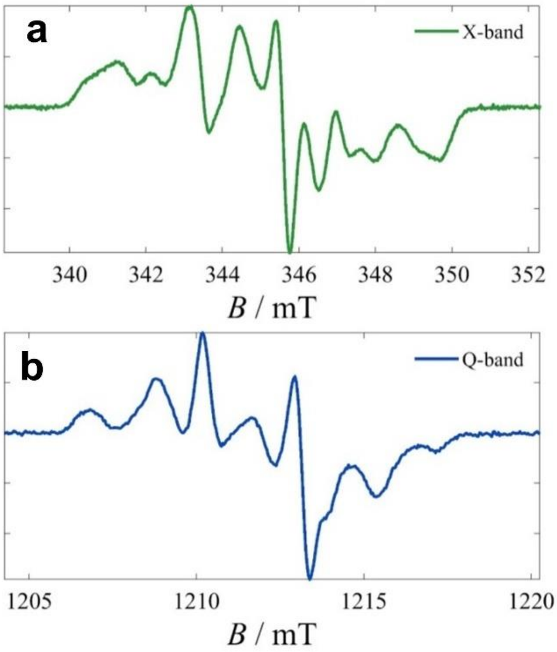

Figure 2.17. X- and Q-band (a and b, respectively) CW EPR spectra on a frozen solution of **1**. Experimental conditions: X-band. T=90 K, f_{EPR}=9.67629 GHz, ΔB_{mod}=0.1 mT$_{pp}$., P_{MW}=0.52 μW. Q-band. T=85 K, f_{EPR}=34.0002 GHz, ΔB_{mod}=0.1 mT$_{pp}$, P_{MW}=1.12 μW. Reproduced from ref.[144]

At 90 K, variable-power studies revealed distinct changes in the intensities of various resonances. Specifically, the high-field resonances (with g<2.002) exhibited greater intensity enhancement compared to those at lower fields as microwave power increased. This significant alteration in the spectrum shape introduced uncertainties during fitting attempts. Additionally, the entire spectrum displayed saturation effects even at very low microwave powers, as evident from plots scaled to √PMW (see Figure 2.18).

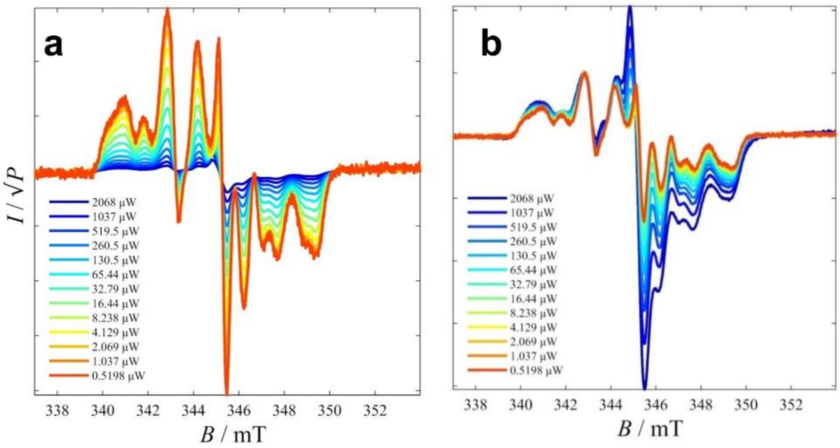

Figure 2.18. X-band EPR spectra of a frozen solution of **1** (90 K) scaled to $\sqrt{P_{MW}}$ (left), and normalized to the intensity of the resonance at $g \sim 2.016$ (right). Experimental parameters: $T = 90$ K, $f_{EPR} = 9.67629$ GHz, $\Delta B_{mod} = 0.1$ $\mathrm{mT_{pp}}$.

Efforts were made to fit these spectra using a model involving two S=1/2 spins interacting through the previously derived exchange interaction and a dipolar interaction based on a point-dipole approximation. Unfortunately, these attempts were unsuccessful due to the inadequacy of the point-dipole model in capturing the behavior of closely spaced spins, especially when one of them is strongly delocalized.

2.2.4. Pulse-EPR – Selective Resonance Enhancement (in coll. with Dr. A. Boudalis)

Field-sweep echo-detected (FSED) EPR

Initially, the behavior of CW spectra was attributed to distinct relaxation characteristics of the two spin centers. To address the potential effects of slow spin-lattice relaxation, field-sweep echo-detected (FSED) pulsed EPR experiments were conducted. These experiments enabled to select appropriate Shot Repetition Times (SRT) based on prior measurements of T_1 (where SRT>$5T_1$).

Significant differences were observed in the FSED and CW spectra (Figure 2.19). To investigate their origins, field-dependent saturation-recovery and echo-decay experiments were conducted, to analyze the spin dynamics of each resonance (Figures 2.20 and 2.21). Specifically, it was focused on whether T_1 and T_m displayed anisotropies and whether the spins S_{pc} and S_{NO} exhibited distinct relaxation profiles or functioned as a single magnetic system.

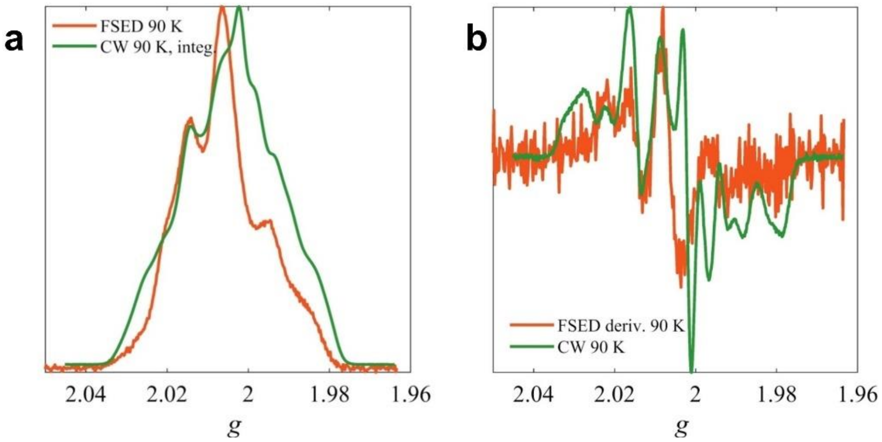

Figure 2.19. Comparisons of CW and FSED spectra of **1** at 90 K (a). Comparison of the FSED spectrum to the integral of the CW spectrum (b). Comparison of the CW spectrum to the derivative of the FSED spectrum. *Experimental parameters.* CW spectrum: f_{EPR} = 9.68389 GHz, P_{MW} = 0.207 μW, ΔB_{mod} = 0.1 mT$_{pp}$. FSED spectrum: f_{EPR} = 9.73089 GHz, $\pi/2$ pulse = 16 ns, τ = 454 ns. Reproduced from ref.[144]

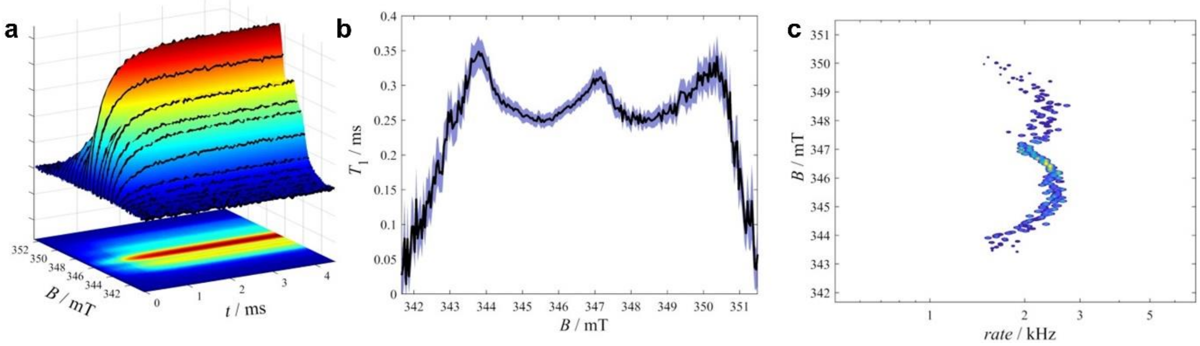

Figure 2.20. (a) Variable-field saturation-recovery experiments at 90 K on **1**. (b) Best-fit T_1 times to a monoexponential law. The blue patch indicates the limits of the 95% confidence intervals. (c) Contour plot of the intensities of the relaxation rates.

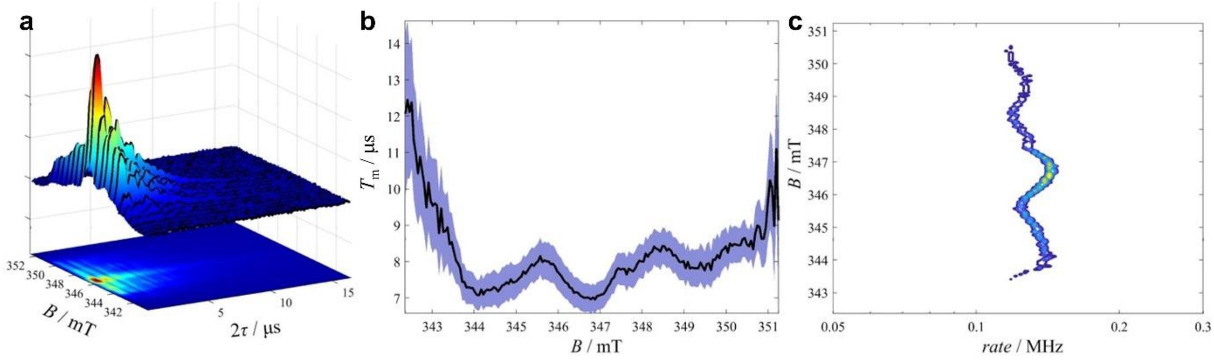

Figure 2.21. (a) Variable-field echo decay experiments on **1** at 90 K. (b) Best-fit T_m times to a monoexponential law. The blue patch indicates the limits of the 95% confidence intervals. (c) Contour plot of the intensities of the relaxation rates.

Determination of T_1 and T_m, and their anisotropy

Two approaches were adopted to analyze these experiments. First, the saturation-recovery (or echo decay) trace was fitted with a monoexponential recovery (or decay) to assess T_1 (or T_m) field dependencies. Second, inverse Laplace transforms (LT^{-1}) were performed at each field to determine whether unique relaxation times adequately describe the experimental time traces. This mathematical treatment has been previously applied in REFINE spectroscopies.[166,167]

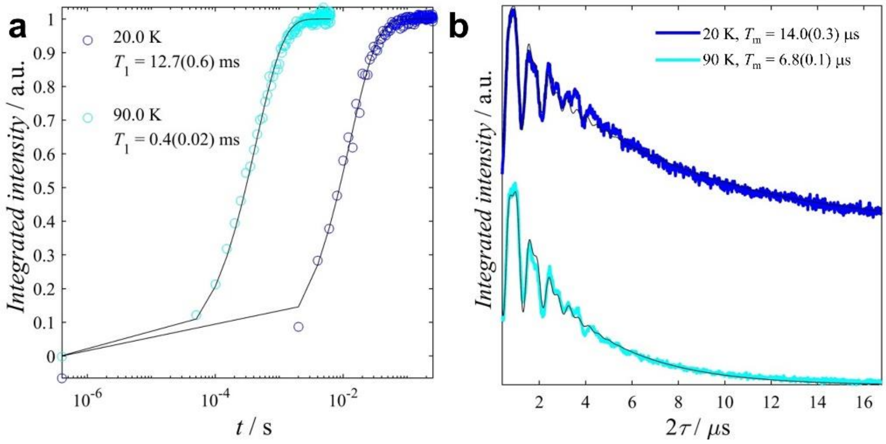

Figure 2.22. Saturation recovery (a) and echo decay (b) traces at 20 and 90 K, and fits to monoexponential processes. Reproduced from ref.[144]

The inverse Laplace transform provides a spectrum of exponential decay or recovery rates. This process is analogous to how the Fourier transform yields a spectrum of periodic oscillation frequencies. Both transforms operate on time-dependent functions ($I(t)$) and convert them into spectra with an independent variable in units of t^{-1}. The Fourier transform (FT) focuses on the periodic part of the dataset, resulting in a spectrum of frequencies. In contrast, the inverse

Laplace transform (LT^{-1}) emphasizes the exponential decay or recovery part, leading to a spectrum of relaxation rates.

To apply the LT^{-1} to saturation recovery (SR) or echo decay (ED) data, the first step involves calculating a spectrum of SR/ED traces while varying T_1 (or T_m) within a broad range to construct the decay rate spectrum. For the SR trace, a simple monoexponential decay law is used:

$$M(t) = M_0 e^{-\frac{t}{T_1}} \tag{2.3}$$

The ED trace requires additional consideration due to the presence of two peaks in their Fourier transform spectra, corresponding to ^{1}H and ^{2}H modulations. The relaxation law for the ED trace involves two modulations at frequencies ($f_{1,2}$), each decaying with characteristic times ($b_{1,2}$), represented as follows:

$$M(2\tau) = M_0 e^{-\frac{2\tau}{T_m}} \left(1 + \sum_{i=1}^{2} k_i \, e^{-\frac{2\tau}{b_i}} \cos\left(4\pi f_i \tau + \varphi_i\right)\right) \tag{2.4}$$

At each field, the SR/ED traces were fitted to the relaxation laws mentioned earlier. Subsequently, the decay rate spectra were computed by varying T_1 or T_m while maintaining all other variables at their best-fit values. In particular, for SR traces, the saturation value (M_0) remained fixed, whereas for ED traces, the magnetization at $2\tau = 0$ and the modulation parameters (M_0, f_i, φ_i) were held constant.

This procedure gave a family of traces, samples of which are given in Figure 2.23.

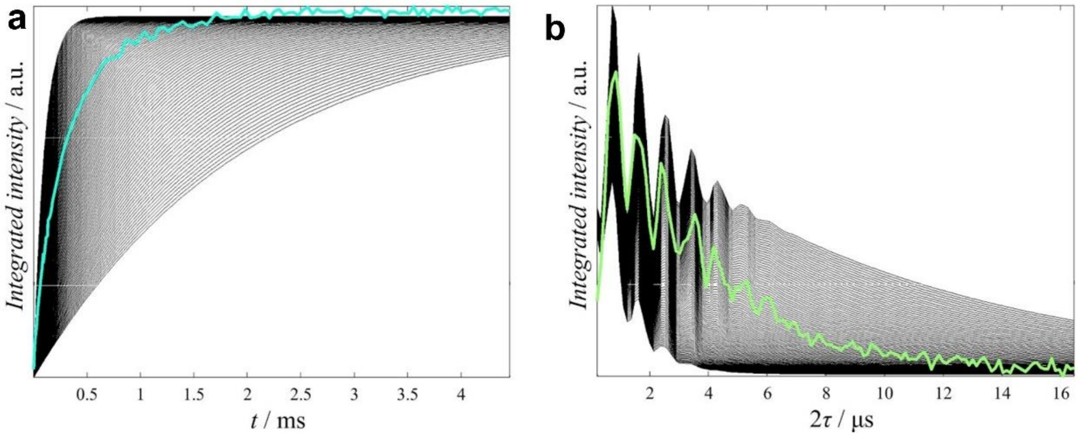

Figure 2.23. (a) SR trace at the spectrum maximum (blue line) and a family of curves calculated for varying T_1 times (black lines). (b) ED trace at the spectrum maximum (green line) and a family of curves calculated for varying T_m times (black lines). Reproduced from ref.[144]

After obtaining the calculated families of curves, the next step was computing the weight vector for each curve using a Nonnegative Linear Least Squares (NNLS) procedure. Specifically, this was accomplished using MATLAB's lsqnonneg function. The resulting weight vector represents a spectrum of rates that optimally fits the experimental SR/ED data. A typical spectrum is given in Figure 2.24.

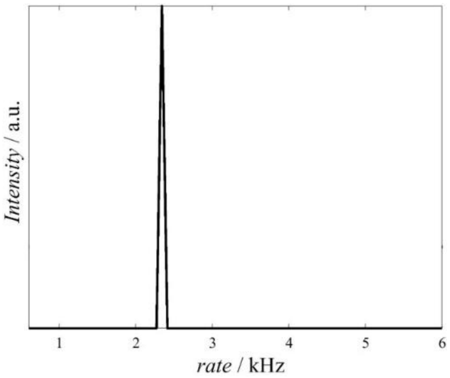

Figure 2.24. Spectrum of SR rates fitted to the family of curves shown in Figure 2.21.

Both methods confirmed distinct T_1 and T_m times for the spin dynamics of all resonances, along with subtle anisotropies. Notably, the T_1 field dependence resembles that observed in nitroxide radicals,[168] suggesting that the faster-relaxing component (the nitroxide radical in this case) influences the relaxation of the slower-relaxing component ($[YPc_2]^0$ radical) in the coupled diradical system. This phenomenon has been previously observed in nitroxide-trityl exchange-coupled diradicals,[163] where the faster-relaxing nitroxide becomes the rate-determining factor, accelerating the relaxation of the trityl component.

In summary, variable-field experiments revealed distinct relaxation rates, indicating the existence of a singular exchange-coupled system in compound **1**. The magnetic relaxation in this system is governed by its faster-relaxing nitroxide subcomponent, which also exhibits characteristic magnetic anisotropy. Note that the minority species **1'** remains undetectable in these experiments due to its small quantity and likely similar relaxation behavior to that of compound **1**.

FSED with varying pulse amplitude

These conclusions did not address the discrepancy between the CW and FSED spectra. To address this, it was hypothesized that different resonances corresponded to transitions within multiplets of varying total spin (S_T), resulting in distinct tipping angles. A previous study explicitly investigated this phenomenon in a copper(II)-nitroxyl radical complex, where FSED spectra collected with varying B_1 pulses exhibited different spectral profiles.[169] Indeed, within the spin system, singlet-triplet and triplet-triplet transitions displayed different tipping angles—

the former approaching an effective spin state of *S*=0, while the latter tended toward an *S*=1 state.

In FSED experiments using pulses of the same duration ($t_{\pi/2}$=16 ns) but varying powers, this effect was evident (see Figure 2.15). Notably, while the *g*=2.014 resonance remains dominant, a resonance at *g*=2.023 disappears as microwave (MW) powers increase, and a new resonance at *g*=2.028 emerges. Likewise, on the high-field side of the spectrum, a resonance at *g*=2.004 vanishes, replaced by one at *g*=2.000.

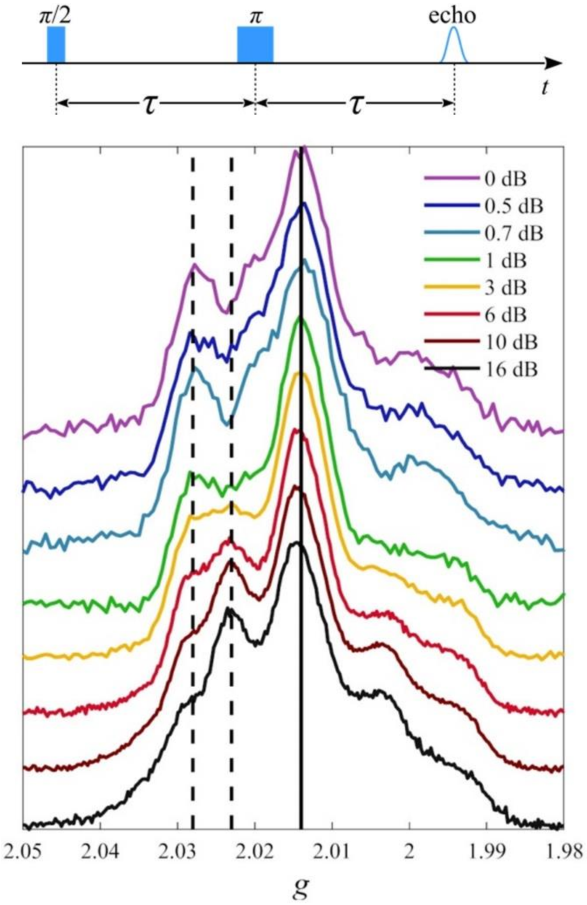

Figure 2.25. FSED spectra of **1** at 90 K and at different pulse intensities. The vertical continuous line shows the *g*=2.014 (345.1 mT) main absorption and the dashed ones the power-dependent absorptions at *g*=2.023 (343.7 mT) and *g*=2.028 (342.7 mT). Detailed nutation experiments were conducted on the *g*=2.014 and 2.028 absorptions (Figures 2.28 a and d, respectively). Experimental parameters: f_{EPR}=9.72721 GHz, π/2 pulse=16 ns, τ=454 ns. The 0 dB spectrum corresponds to a MW field B_1 of 1.1 mT. Reproduced from ref.[144]

To establish that the resonances at *g*=2.0023 and 2.0028 corresponded to transitions of distinct spin multiplicities, and thus different Rabi frequencies, nutation experiments were performed on compound **1** at 6 dB using the corresponding magnetic fields. The Fourier-transformed (FT) spectra revealed two peaks at 18.0 and 23.4 MHz, along with a low-frequency peak at 14.65

MHz attributed to ^{1}H ESEEM modulations (see below for details). The relative increase in the high-frequency component at lower magnetic fields indicated varying dominance of these resonances as a function of field.

To validate the peak assignments, variable-power studies were conducted at both the main peak (g=2.014) and one of the minor peaks (g=2.0023). These experiments (see Figure 2.26) unveiled two Rabi oscillations with frequencies dependent on the field strength (B_1), along with a third oscillation near 15 MHz that remained unaffected by power variations, whereas the third oscillation was attributed to ^{1}H ESEEM (see Figures 2.28)

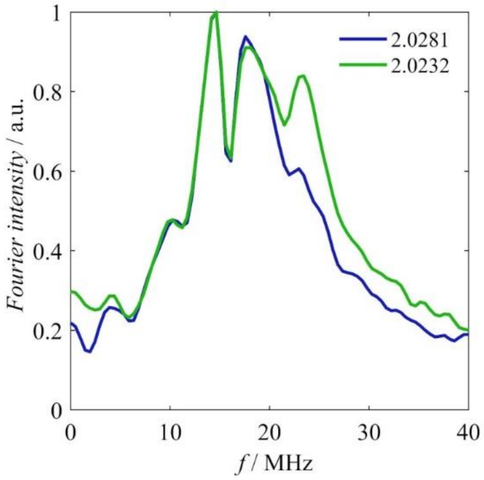

Figure 2.26. FT spectra of the nutation traces of **1** at the g = 2.0028 and 2.0023 resonances. Experimental conditions: T = 90 K, f_{EPR} = 9.72707 GHz, HPATT = 6 dB, $t_{\pi/2}$ = 16 ns, τ = 480 ns. Reproduced from ref.[144]

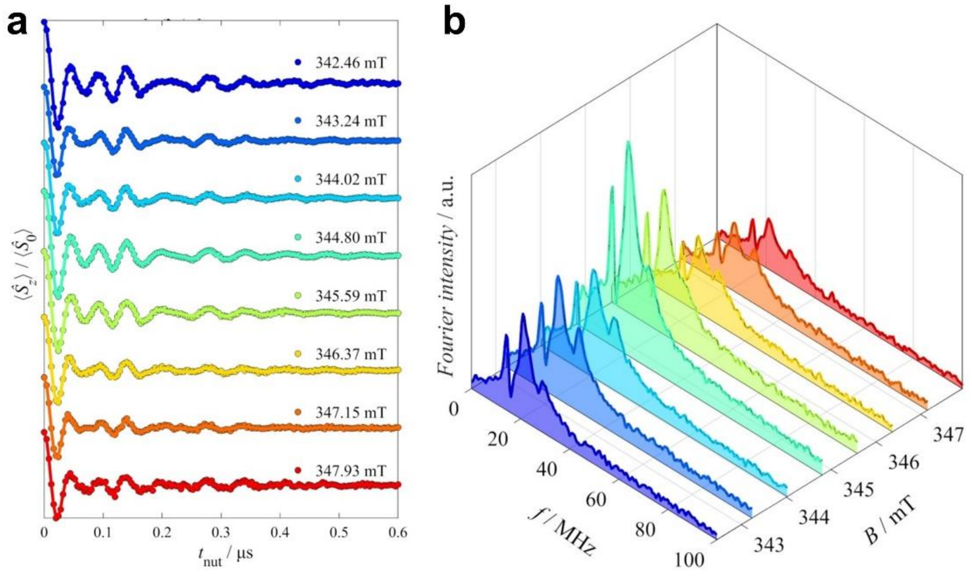

Figure 2.27. (a) Nutation traces of **1** at 20 K at indicated magnetic fields and their fits to three exponentially decaying oscillations. (b) FT spectra of these traces. Reproduced from ref.[144]

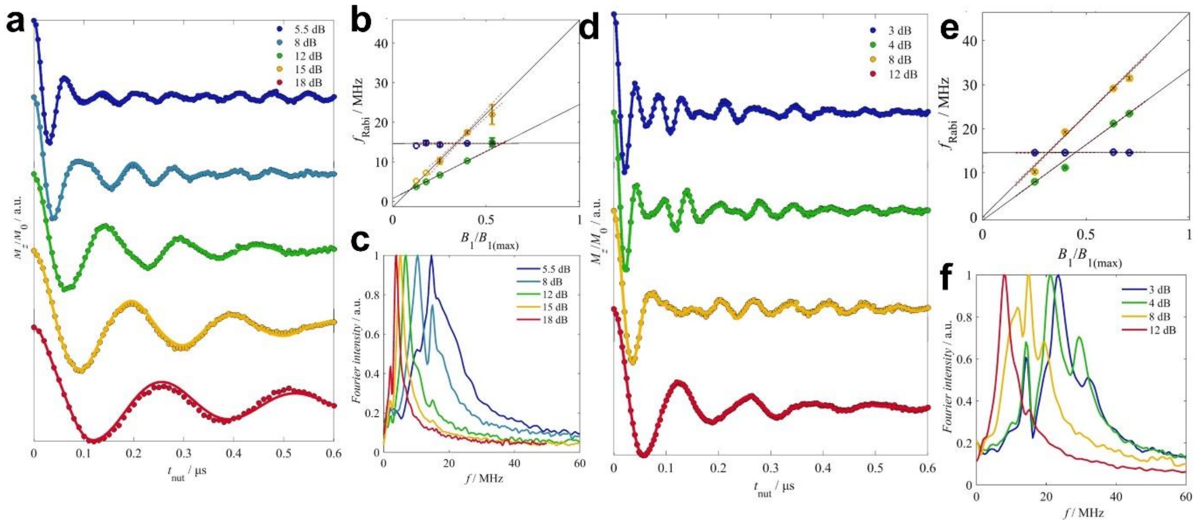

Figure 2.28. (a) Nutation traces of **1** at 345.0 mT (*g* = 2.014) and fits two three exponentially decaying oscillations. (b) Linear Deming fits of the derived oscillation frequencies as a function of the B_1 strength. These reveal one B_1-independent oscillation to be ^{1}H ESEEM (blue) and the other two, with frequencies varying linearly with B_1, to be Rabi oscillations. (c) FT spectra of the nutation traces at various power levels. (d) Nutation traces of **1** at 343.7 mT (*g* = 2.028) and fits two three exponentially decaying oscillations. (e) Linear Deming fits of the derived oscillation frequencies as a function of the B_1 strength. These reveal one B_1-independent oscillation to be ^{1}H ESEEM (blue) and the other two, with frequencies varying linearly with B_1,

to be Rabi oscillations. (f) FT spectra of the nutation traces at various power levels. Reproduced from ref.[144]

To investigate the spin states associated with various resonances, Field-Swept Spin Nutation (FSSN) experiments were conducted across the entire magnetic field range. Leveraging insights from prior variable-power experiments, a microwave (MW) power level was chosen that effectively separated Rabi oscillation frequencies from the ^{1}H ESEEM frequency—achieving satisfactory results with a 4 dB attenuation. Additionally, the pulse duration was set for the Hahn-echo detection block to $t_{\pi/2}$=12 ns.

Figure 2.29 (a) displays the nutation traces and their Fourier-transformed (FT) spectra. These data were fitted to a model involving three exponentially damped oscillations; a power-independent component around 15 MHz attributed to ^{1}H ESEEM, along with two power-dependent oscillations corresponding to Rabi oscillations. The fitting was done according to

$M_y(t) = M_0 \sum_{i=1}^{3} k_i e^{-\frac{t}{\tau_i}} \cos(2\pi f_{\mathrm{i}}(2\tau) + \varphi_i)$, where M_0 is the initial magnetization, f_{Ri} are the oscillation frequencies, k_i their relative amplitudes, τ_{Ri} their characteristic damping times and ϕ_i their phases. The field dependence of best-fit parameters is represented in Figure 2.29 (b).

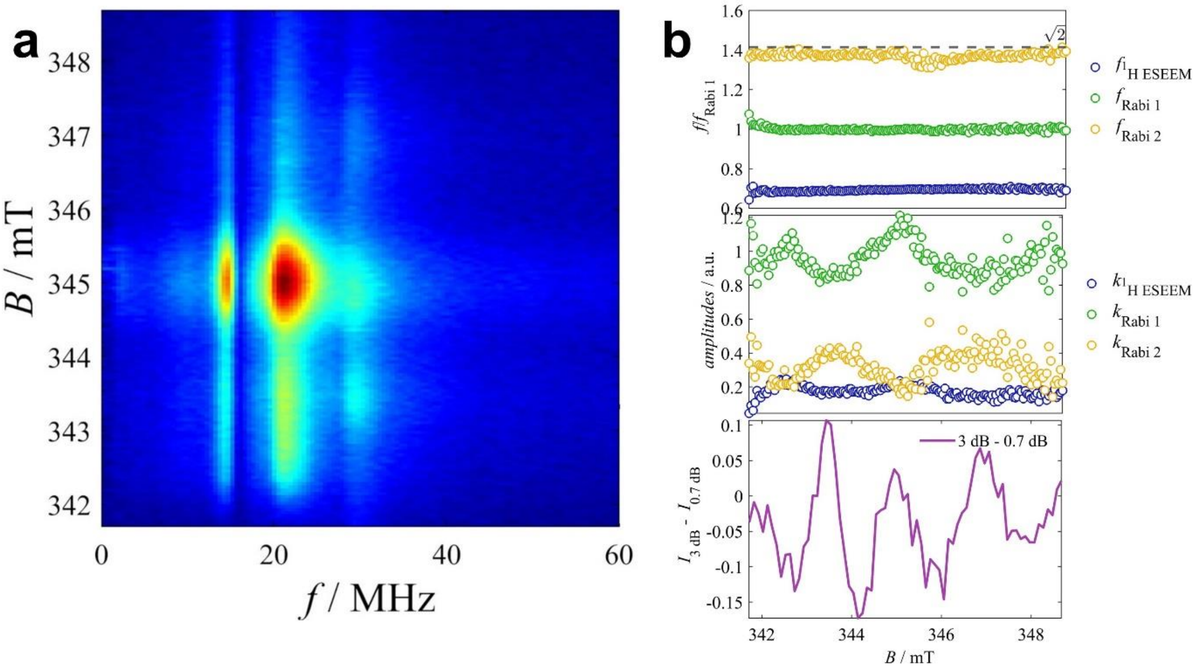

Figure 2.29. (a) Variable-field FT spectra of the nutation traces of **1** at 20 K. (b) Top and middle panels: Magnetic field dependence of the frequencies (relative to the "*S*=1/2" frequency) and relative amplitudes of the three oscillations. The horizontal dashed line in the top panel indicates the theoretical √2 frequency ratio between pure *S*=1 and *S*=1/2 spins. Bottom panel:

Difference between the 3 and 0.7 dB FSED spectra. Maxima show resonances whose flip angles are such that they become suppressed at higher MW powers. Reproduced from ref.[144]

It is noteworthy that there is a clear correlation between the oscillation amplitudes (k_i) and the FSED spectra. While the low-frequency oscillation dominates across all magnetic fields, exhibiting amplitude maxima at g-values of 2.028, 2.014, and 1.995, and minima at *g*-values of 2.023 and 2.003, the high-frequency oscillation behaves inversely with respect to the magnetic field, which aligns with the correlation of k_i amplitudes.

The MW power enhancements/suppressions in the FSED spectra align precisely and the subtraction of the 0.7 dB spectrum from the 3 dB spectrum yields the corresponding maxima at the resonances that are suppressed at higher powers and minima at the resonances suppressed at lower powers (Figure 2.22 b bottom). This direct correlation indicates a connection between the FSED spectra shape and the relative amplitudes of Rabi oscillations in FSSN experiments.

2.2.5. Distance Determinations from Nutation Spectroscopy (in coll. with Dr. A. Boudalis)

Based on the fitted data, the Rabi oscillation frequencies remained constant at 29.35(35) MHz and 21.35(19) MHz, indicating distinct spin characteristics. Particularly, their ratio was equal to 1.37, which is very close to, but not precisely equal to √2. The latter value theoretically corresponds to transitions within the “*S*=1” and “*S*=1/2” multiplets, respectively, as described by the relation:[27,170]

$$f_{nut} = \frac{\mu_B g_1 B_1}{h}\sqrt{S(S+1) - M_S(M_S+1)} \qquad (2.5)$$

where g_1 is the *g*-tensor element along the laboratory *x*-axis and B_1 is the strength of the excitation magnetic field. This relationship specifically applies to intramultiplet transitions within single-spin systems or multispin systems characterized by strong *J* couplings, where *S* and M_S are assumed to be good quantum numbers. However, in scenarios involving hyperfine interactions, admixtures of nuclear states, or diradicals with $J \sim \Delta g \mu_B B_0$,, these conditions no longer remain valid,[27] requiring additional refinements.[171]

In the intermediate case where $J \sim A_{HF}$ and $J \gg \Delta g \mu_B B_0$, the expected relation does not hold, which aligns with the observations. The analysis of Rabi frequencies in such systems serves as a valuable tool for investigating weak terms, including dipolar, hyperfine, exchange interactions, and *g*-asymmetries.

In the simplest case, where a symmetric ($\mathbf{g}_1 = \mathbf{g}_2$) diradical with $J \sim 0$, no hyperfine interactions and moderate dipolar interactions ($r_{12} \sim 16$ Å) is considered,[172] two Rabi frequencies are predicted above certain B_1 intensities. These frequencies correspond to on- and off-resonance excitations. However, field-swept nutation studies in this work revealed only one such frequency due to the weak interactions and symmetric *g* tensors. Additionally, the theory predicted that these frequencies would deviate from the expected values under the influence of dipolar-induced anisotropy. Furthermore, Δg effects were expected to amplify this deviation, especially in cases of *g*-asymmetry, where *J*-coupling also plays a role. This led to analyze the ratio of two Rabi frequencies within the context of a system experiencing dipole-induced zero-field splitting (zfs),[172] allowing to propose a rationalization for the observations.

In a dipole-dipole interaction in a spin system with isotropic S=1/2 spins, the dipolar interaction tensor $\mathbf{D}_{12}$ induces zfs in the ST=1 state, given by $D_{12(\mathrm{zfs})} = 3\mathbf{D}_{12(\mathrm{zz})}/2$. This zfs leads to an energy splitting of $\Delta E_{S=1}=D_{12(\mathrm{zfs})}/2$. Importantly, this energy splitting is related to the interspin distance through the empirical relation $\Delta \mathrm{E}_{\mathrm{S}=1} = \beta^2 g^2/r_{123}$, where β^2 is approximately 12980 MHz/Å^3 (or 0.43297 cm^{-1}/Å^3).

Considering the power attenuation in the experiment (4 dB corresponding to $B_1 \sim 0.66$ mT), curve of calculated Rabi frequency ratios as a function of $D_{12(\mathrm{zfs})}$ was constructed (Figure 2.30a). The observed ratio of 1.37 corresponds to a $D_{12(\mathrm{zfs})}$ value of approximately 53.7 MHz. Assuming the simplified point-dipole approximation relation $D_{12(\mathrm{zfs})} = \beta^2 g^2/2\mathrm{r}_{123}$, this energy corresponds to an interspin distance of $r_{12} \sim 7.85$ Å (Figure 8, right). Although the proposed model simplifications allow only qualitative analysis, it is noteworthy that the predicted distance falls within the middle of the range of interspin distances based on the calculated structure of the system (approximately 6.5–12.5 Å).

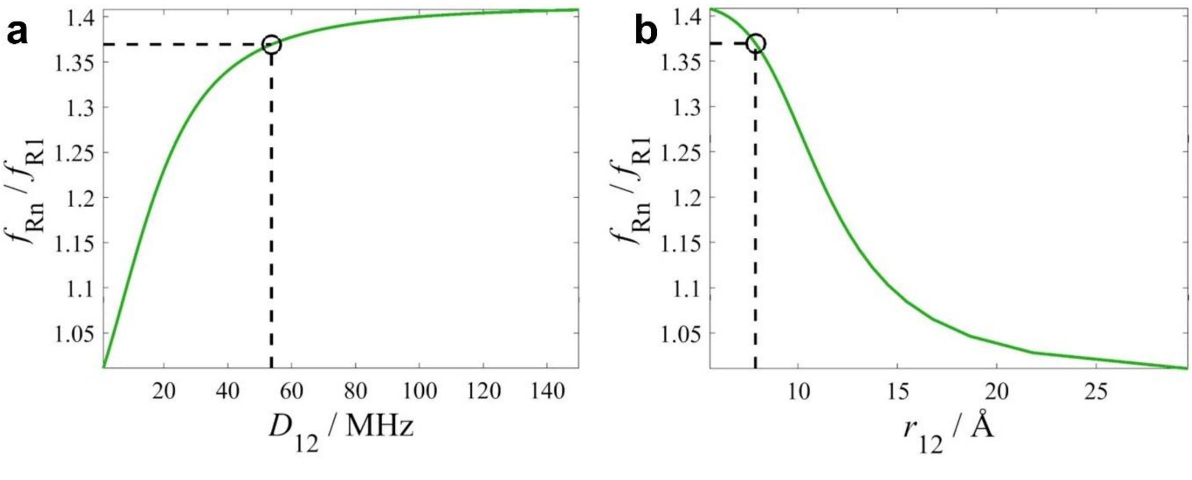

Figure 2.30. Ratio of the Rabi frequencies calculated for different dipolar interaction strengths (top) and the corresponding distances based on the point-dipole model (bottom). The dashed lines indicate the dipolar zfs and corresponding distance for the experimentally determined ratio of 1.37 (53.7 MHz, 7.85 Å). Reproduced from ref.[144]

2.3. Discussion and Conclusions

This work initially aimed to synthesize a weakly coupled diradical with an engineered g-asymmetry. This was achieved, resulting in a system containing two distinct spins characterized by weak superexchange coupling ($|J| \sim 420$ MHz/0.014 cm^{-1}). However, interpreting the frozen-solution CW EPR spectra posed challenges due to two factors. First, the coexistence of exchange and hyperfine couplings led to a closely-packed spin ladder with numerous closely spaced transitions. Second, strong spin delocalization over the phthalocyanine rings invalidated the point-dipole approximation.

Subsequent investigations revealed several key findings. First, the uniqueness of T_1 and T_m times was confirmed, indicating that **1** behaves as a collective spin system. Second, variable-power FSED spectra and FSSN studies showed resonances between states of different spin multiplicities, reflecting different tipping angles. While this phenomenon is known in g-asymmetric spin-coupled systems, variable-power FSED experiments have primarily been used for analytical purposes, such as deconvoluting multicomponent spectra. Similarly, FSSN experiments complement PELDOR in assessing dipolar interactions but remain rare, relying on visual inspection of the respective FT spectra.

With analytical goals in mind, the behavior of system **1** was further investigated. Careful analysis of nutation traces provided information on frequencies, amplitudes, and decay times, revealing that the "*S*=1" Rabi frequency is influenced by a dipolar-induced zfs of 53.7 MHz, corresponding to a distance of 7.85 Å.

Table 2.5. Overview of the spin Hamiltonian parameters of **1** determined by the experiments in this work.

Parameter	**Value**	**Experiment**
$g_{\mathrm{NO(iso)}}$	2.0060	Fluid solution EPR
$A_{\mathrm{N\text{-}NO(iso)}}$	40.74 MHz	
$A_{\mathrm{H\text{-}NO(iso)}}$	0.67 MHz	
$g_{\mathrm{pc(iso)}}$	2.0023	
J	420 MHz	
$D_{\mathrm{12(zfs)}}$	53.7 MHz	FSSN

Beyond their analytical purpose, these fits revealed two distinct Rabi frequencies (along with a ^{1}H ESEEM frequency). The relative amplitudes of these frequencies at a given microwave

(MW) power depended on the magnetic field. These findings directly correlated with variable-power FSED experiments, where resonances at specific fields could be selectively enhanced or suppressed by adjusting MW power.

Overall, the results showcased a system with two distinct transitions that could be controlled at desired amplitudes through proper magnetic field and MW power selection. In this context, diradical **1** resembles a spin qutrit (see Chapter 1. Section 1.3.4), although it might more accurately be described as a moderately coupled two-qubit system. Notably, the MW pulses used in the experiments had the same frequency. However, using two different frequencies—such as mixing the primary MW frequency with an Arbitrary Waveform Generator—could yield even more precise excitations and fine-tuned control of qutrit of **1**.

From the perspective of molecular spin qubits, this work demonstrated the versatility of molecular-engineered diradicals. In the weak-exchange limit, diradicals could be useful for individually addressable two-qubit gates, whether stable[67] or photogenerated transient ones[69]. In the strong-exchange limit, diradicals formed triplet states suitable for qutrit implementations. Transient triplet states generated through photoexcitation have already been proposed for qutrit implementation.[80]

While this work was not aiming at the optimization of the decoherence properties of diradical **1** (e.g., through ligand deuteration, very low temperatures, or dynamic decoupling sequences), it is notable that these properties compare favorably with those of other stable diradicals or photoexcited triplet systems, as indicated in Table 2.6.

Table 2. 6. T_1 and T_m times of indicative diradical or spin triplet systems (stable or photoexcited), compared with those of **1**.

System	**T_1 (ms)**	**T_m (μs)**	**Reference**
bis-TEMPO		6.89 (50 K)	Ref.[66]
PTEMPO [a]	57 (10 K)	3.2 (10 K)	Ref.[62]
$(\mathrm{TTF}^{+})^{\cdot}$-(pyromellitimide^{-})$^{\cdot}$ [b]		2.6 (5 K)	Ref.[69]
$[\mathrm{Y(Pc)_2}]^{\cdot}$	~10^3 (10 K)	8 (40 K)	Ref.[57]
$\mathrm{C_{70}}$ (S = 1) [b]	3-5 (5 K)	13-20 (5 K)	Ref.[80]
2	13 (20 K)	14 (20 K)	This work
	0.4 (90 K)	6.8 (90 K)	

[a]4-propargyl-2,2,6,6,-tetramthylpiperidine-1-oxyl.[62] [b]Photoexcited.

Based on the research, it was found that diradical **1** lies between certain limits, complicated by hyperfine interactions that create a closely-packed spin ladder. In light of this, specific design elements need to be revised to enhance system utility. Two directions in molecular design are being pursued. First, replacing the nitroxide with a spin carrier lacking hyperfine interactions would simplify addressing the two-spin system. Second, introducing a linker (such as an acetylene[57] or phenyl linker) between the radicals is crucial for experiments demonstrating the CNOT gate operation. Additionally, experimental protocols are under development for multifrequency control of the spin qutrits.

The future synthetic efforts will be based on the $LnPc_2$ motif, which facilitates single-molecule experiments like spin transport,[126–128] STM Kondo measurements, and STM EPR. These techniques will help to study individual molecules derived from this research.

Chapter 3. Radical-Functionalized Bis(phthalocyaninato)-Terbium(III) Exhibiting Slow Relaxation of Magnetization

3.1. Introduction

As explained in Chapter 1 molecule-based quantum devices offer the potential to overcome limitations imposed by Moore's law. Specifically, Chapter 1 Section 1.5 highlighted that the molecule bis(phthalocyaninato)terbium (III) ($[TbPc_2]^{0/+}$) shows promise as both a single-molecule magnet (SMM) and a molecular qubit.

As outlined in Chapter 1 Section 1.4, $TbPc_2$ exhibits SMM performance despite its non-Kramers nature, owing to its high-spin ground state and strong magnetic anisotropy. Since the first report on its anionic form ($[TbPc_2]^-$) by Ishikawa and colleagues in 2003,[89] researchers have attempted to improve its properties. One approach is to incorporate a π radical: the neutral form ($[TbPc_2]^0$) displays superior SMM properties than $[TbPc_2]^-$, owing to the improved ligand field and the exchange-bias.[106,141,173] Efforts have been made to further improve these properties. One approach involves $[TbPc_2]^0$ dimer, which demonstrates enhanced exchange-bias by the interaction between π radicals, linking two terbium centers.[119] Another approach involves substituents: various derivatives have been reported, as summarized in the literature.[91,99] Among these $[TbPc_2]^0$ derivatives, the one with an amino group currently demonstrates the best SMM performance as of 2024.[174] In particular, those with substituents on only one Pc (hetero-substituted) showed the best performance, indicating that the hetero-substitution with an electron-donating group is preferable.

On the other hand, in the field of quantum computational science, $[TbPc_2]$ has been explored as a nuclear spin qubit (see Chapter 1 Section 1.4.4). Alternatively, the radical delocalized over phthalocyanine rings of $[TbPc_2]^0$ (**S_{Pc}**) is a promising electron spin qubit candidate, as the radical is delocalized over the carbon atoms of the Pc rings, resulting in low spin-orbit coupling. As explained in Chapter 1 Section 1.3.4, its yttrium analogue ($[YPc_2]^0$) is reported for the long spin-lattice relaxation time (T_1 ~ 1 s at 10 K).[57] Attempts to incorporate $[YPc_2]^0$ into multi-qubit array have been made as well. For example, our group reported yttrium(III) phthalocyanine-porphyrin dimer tethered with ethynyl/phenyl bridge.[57] In addition, as described in Chapter 2, $[YPc_2]^0$ with peripheral isoindoline nitroxide group has been reported (**1**).[144] However, challenges remain for these complexes to function as qubit gates. In addition to those described in Chapter 1 Section 1.3, an example of a CNOT gate is found in the use of the STM-EPR technique for adatomsystems.[175] Here, the key is to create two weakly interacting Ti atoms with *g*-asymmetry by the local magnetic field produced by the neighboring Fe. STM-EPR can be also applied to molecules. The early example of the STM-EPR study on a molecule was on iron phthalocyanine (FePc) molecule. This technique was utilized to investigate the interaction between FePc and other spins (either another FePc of titanium adatom),[176] or to demonstrate the coherent manipulation.[177] Another example is $[TbPc_2]^0$ molecule. In 2022, Komeda and coworkers reported STM-EPR on $[TbPc_2]^0$ molecule on NaCl layer on the Cu(100) surface.[178] They conducted CW-EPR, where the clear peak was observed only when the tip was above ligands.

As described above, both incorporating an additional radical interacting with π radical and hetero-substitution of electron-donating groups are good strategies to improve SMM properties of $[TbPc_2]^0$. Meanwhile, systems with two electron spins and an Ising-like spin are interesting target for STM-EPR. Herein, bis(phthalocyaninato)terbium (III) incorporated with isoindoline nitroxide group (**2**) was synthesized, employing the same skeleton as **1**, aiming at bifunctionality; tuning of slow relaxation of magnetization and creating a two-qubit gate. This study will focus on the former objective, examining the effects of substituents containing weakly coupled radicals and nitroxide radicals through magnetic measurements. Based on the magnetic properties of **2** determined here, it was discussed how the magnetic properties of this molecule may function in future STM studies.

3.2. Results

3.2.1. Synthesis and characterization

Synthesis

Compound **2** was synthesized in the same manner as the method used for **1**, as represented in Figure 3.1. Detailed synthesis steps are provided in Chapter 5. Here, the mixed solvent ($CHCl_3$ / toluene mixture in the ratio of 9 to 1 with the addition of 0.5% acetone) was used as an eluent in silica gel column chromatography. This mixed solvent improved the separation (*e.g.* the repetition of the column reduced to 3 times from 5 times). However, challenges with recrystallization remained for compound **2**.

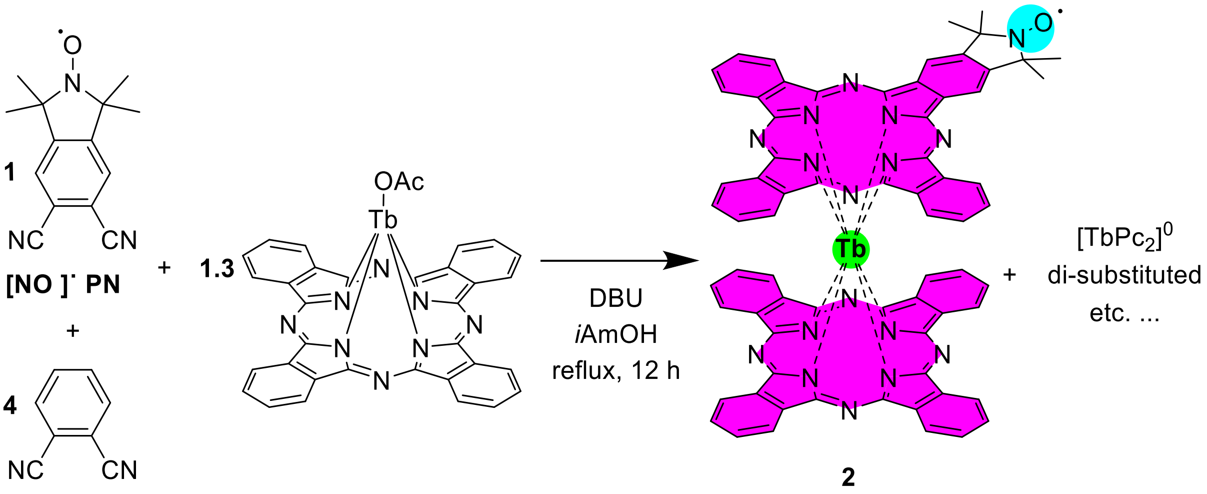

Figure 3.1. Reaction scheme for the preparation of **2**.

Characterization

In Chapter 2, I presented the full characterization of compound **1** using UV-vis-NIR spectroscopy, IR spectroscopy, high-resolution ESI mass spectrometry, cyclic voltammetry, and CW and pulsed EPR. Notably, **2** cannot be measured by our EPR equipment. As demonstrated previously,[179] $[TbPc_2]^0$ requires high-field EPR equipment, which is typically home-built, since the strong anisotropy of $\mathbf{J}_{Tb}$ is transferred to the radical. Nevertheless, as demonstrated in the case of **1**, the combination of spectroscopic techniques can detect the monoradical impurity. These results were quantitatively consistent with fluid solution EPR data. Therefore, in this section, I will discuss the purity of the sample with a series of spectroscopic techniques other than EPR.

UV-vis-NIR absorption spectroscopy

The UV-vis-absorption spectrum of **2** has similar characteristics to that of $[TbPc_2]^0$, characterized by a Soret band around 350 nm, a BV band around 450 nm, a Q band around 750 nm, an RV band around 900 nm, and a broadened IV band at the NIR region (cf. 1500 nm)

(Figure 3.2). These peaks are unique to $[LnPc_2]^0$ molecules, thus confirming the structure of the molecule.[90] The absence of nitroxide moiety features was attributed to the lower molar absorption coefficient of nitroxide absorption peaks compared to those of $LnPc_2$ moieties, as demonstrated in Chapter 2. Importantly, at a higher wavelength than Q band (Figure 3.2 b), no shoulder peak was observed. As discussed in Chapter 2, this peak is attributed to the cationic species $[LnPc_2]^+$. Therefore, the absence of this peak confirms the lack of cationic impurities.

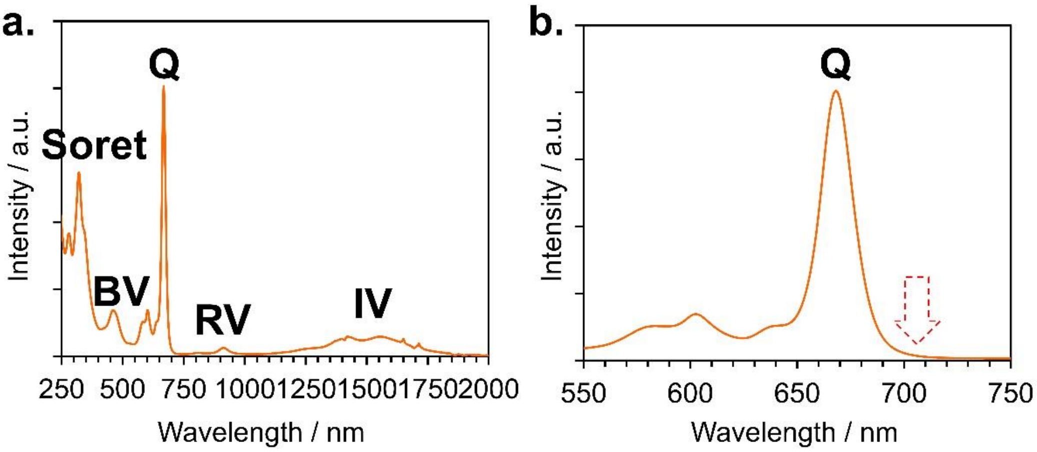

Figure 3.2. Normalized UV-vis-NIR spectra of **2** (a) and that with expansion to Q band (b). The absence of the shoulder peak is shown as a red arrow.

IR spectroscopy

The IR spectrum of compound **2** shows similar peaks as that of **1**, particularly in the fingerprint region assigned to nitroxide moiety and around 1500 cm^{-1} attributed to $LnPc_2$ structure (Figure 3.3). Here, the point to be focused in the peak at 1700 cm^{-1} and the broad peak around 3500 cm^{-1}. As discussed in Chapter 2, the former evidence $NO^{\cdot}$, while the latter presents NO-H, which is the common bi-product from a reduction of nitroxide radical. In Figure 3.3, the $NO^{\cdot}$ peak is clearly visible, while the NO-H peak is not seen. Overall, both of those factors evidenced that the peripheral radical was intact.

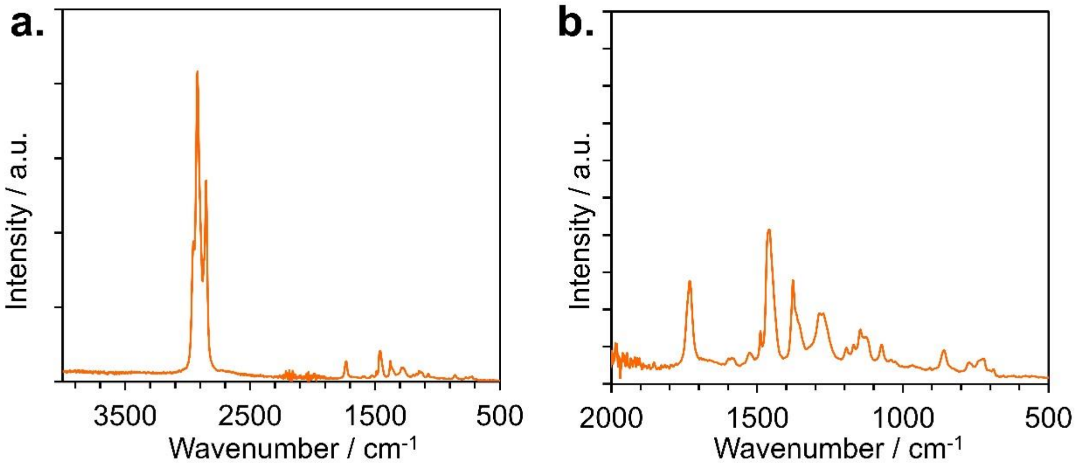

Figure 3.3. IR spectra of **2** (a) and its expansion in 500 – 2000 cm^{-1} (b).

ESI-mass spectrometry

The high-resolution electrospray ionization mass spectrum (ESI-MS) of **1** displayed a single peak corresponding to the targeting molecule. As discussed in Chapter 2, from this spectrum, two information can be derived: the accuracy of the purification and the extent of the decomposition. The former mentions the impurities such as $[TbPc_2]^0$, or di-substituted one. Figure 3.4 illustrates that such peaks were not observed, suggesting that the purification was accomplished. On the other hand, the decomposition of radicals can happen for both nitroxide and π radicals. In the case of **1**, the decomposition of nitroxide radical is typically observed as a shift of +1 in the m/z value, whereas the π-radical decomposition is not detectable by ESI-MS. In Figure 3.4 inset, such a signal was not observed. Overall, it was proved that the sample was free from oxidated species.

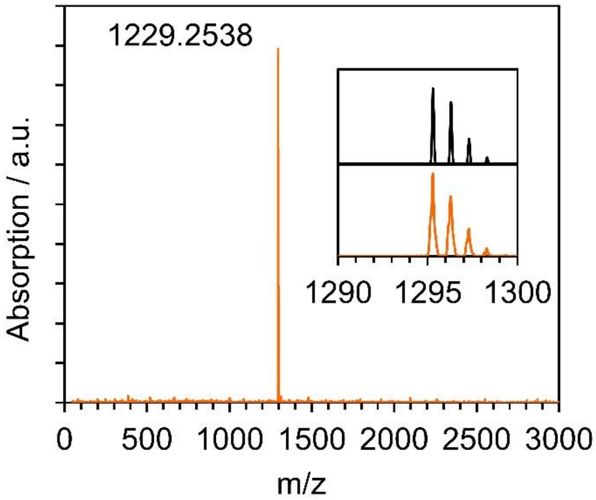

Figure 3.4. ESI mass spectrum of **2**. Inset represents the expansion of the signal (orange) and simulated spectrum of $C_{70}H_{42}N_{17}OTb$.

Electrochemical study

Cyclic voltammogram was performed on **2**, showing 7 redox couples and 1 irreversible oxidation peak (Figure 3.5). A comparison of the redox behavior of **1** and **2** showed peak positions of **2** matches quite well with that of **1** (Table 3.1). Judging from the fact that the redox properties of $[YPc_2]^0$ and $[TbPc_2]^0$ are quite similar,[158] this result indicates that the electronic structure of **2** is quite similar to that of **1**. Overall, the electronic structure of **2** is similar to **1**, which can be explained as the sum of $[TbPc_2]^0$ and $[NO]^{\cdot}$.

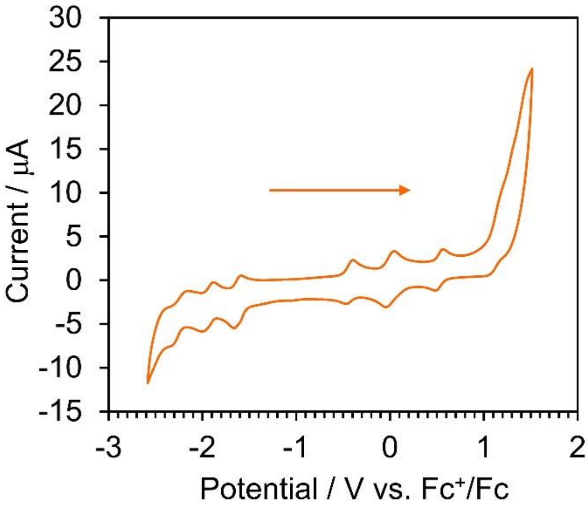

Figure 3.5. Cyclic voltammogram of **2** at a scan rate of 100 mVs^{-1}. The arrow represents the direction of the scan.

Table 3.1. The comparison of the redox peak positions of **1** and **2**.

	2nd Oxd	$[LnPc_2]^{2+/+}$	$[NO\ ]^{\cdot}/[NO]^{+}$	$[LnPc_2]^{+/0}$	$[LnPc_2]^{0/-}$	$[LnPc_2]^{-/2-}$	$[LnPc_2]^{2-/3-}$	$[LnPc_2]^{3-/4-}$
1	1.25	1.04	0.43	-0.07	-0.53	-1.69	-2.01	-2.29
2	1.45	1.13	0.54	-0.02	-0.43	-1.63	-1.94	-2.25

Conclusive remark of characterization

Compound **2** was thoroughly characterized using UV-vis-NIR spectroscopy, IR spectroscopy, ESI-mass spectrometry, and cyclic voltammetry. In addition, the purity of the compound was confirmed by UV-vis-NIR spectroscopy revealing the absence of oxidated form.

3.2.2. Magnetometry

Static magnetic properties

Magnetometry measurement were performed on a bulk powder sample of **2**. DC magnetic susceptibility of **2** is shown in Figure 3.6. χ_MT value at 300 K was 11.7 cm^{3}Kmol^{-1}, which is in good agreement with the expected for a terbium (III) ion along with two radicals (12.5 cm^{3}Kmol^{-1}) shown as the black line. As the temperature decreases, χ_MT value decreases, while at 30 K, it starts increasing. Similar behavior was found in unsubstituted TbPc$_2$, which was explained by inter-molecular ferromagnetic dipolar interaction.[180] Therefore, the behavior of **2** is attributed to intermolecular dipolar coupling or intramolecular exchange coupling.

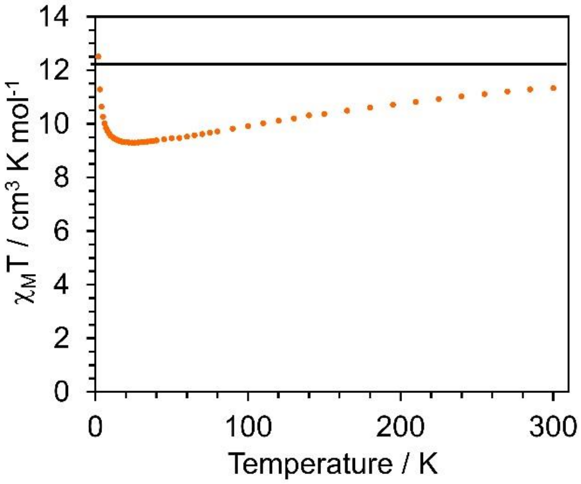

Figure 3. 6. χ_MT versus T plot for **2**. The black solid line represents the calculated value for Tb(III) and two radicals (12.5 cm^3 K mol^{-1}).

In addition, magnetic hysteresis measurement was performed for **2** with a sweep rate of 25 Oe/s. Compound **2** exhibited a butterfly-shaped hysteresis loop up to 17 K, while after 18 K the hysteresis opening was hardly observable (Figure 3.7, 3.8). As discussed in Chapter 1, the introduction of an exchange-bias is crucial for suppressing quantum tunneling of magnetization (QTM), which in turn can increase the coercive field (H_c). Such an effect was not observed in **2** even at 2 K, probably due to the weakness of the exchange coupling indicated by Chapter 2.

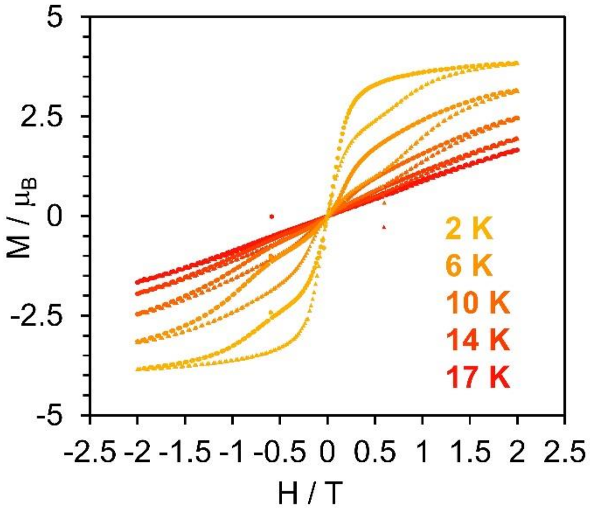

Figure 3.7. Magnetic hysteresis loop of **2**. Circle and triangle markers represent *M* - *H* plots while decreasing/increasing field, respectively.

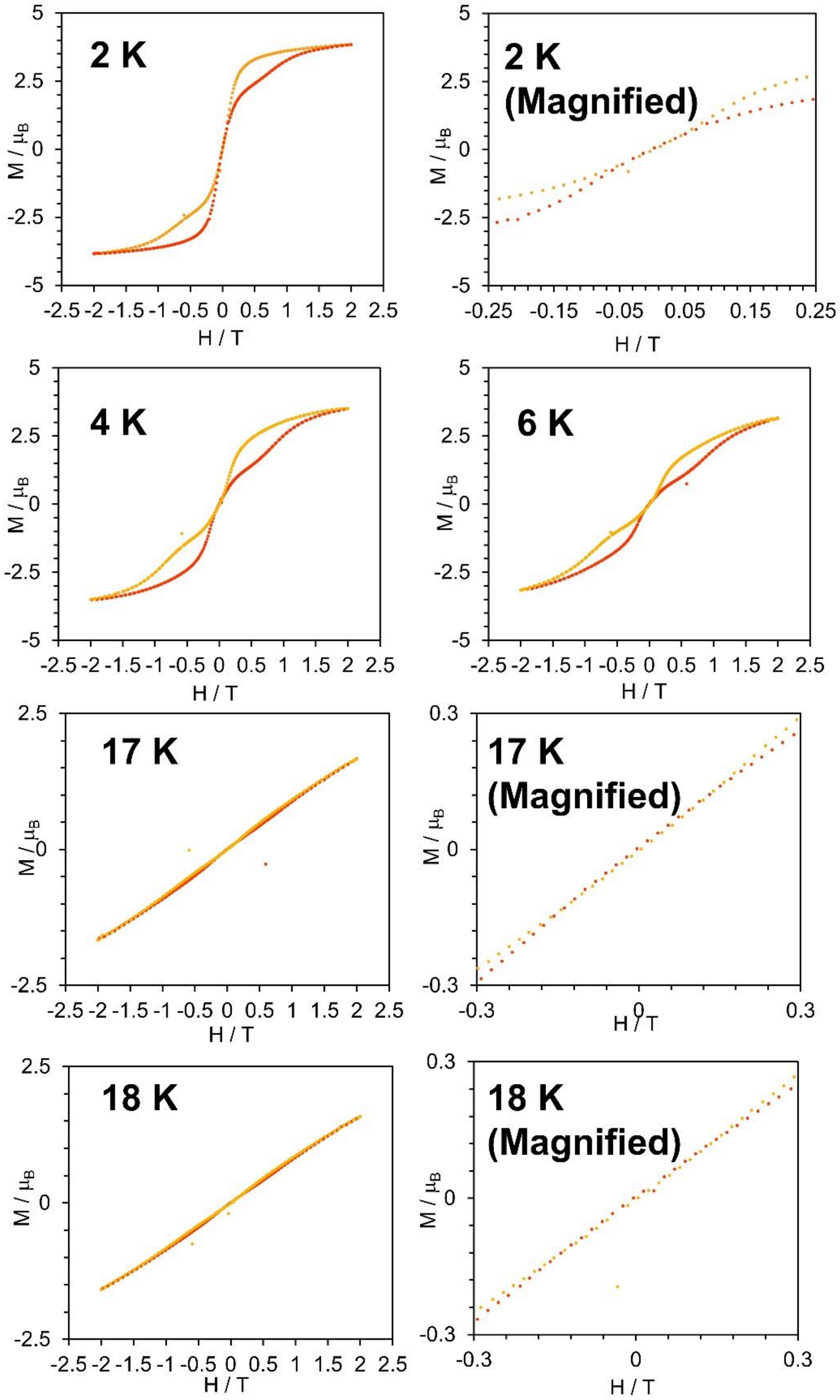

Figure 3.8. Magnetic hysteresis loop of **2** at presented temperatures. Red and yellow markers represent *M* - *H* plots while decreasing/increasing field, respectively.

Dynamic magnetic properties

To determine the magnetization relaxation behavior of **2**, measurements were conducted at zero field. χ_M' versus temperature and χ_M'' versus temperature are shown in Figure 3.9, while the Cole-Cole plot is presented in Figure 3.10. Within the frequency range of 1 – 1000 Hz, the peak was observed in χ_M'' versus temperature plot from 2.5 K up to 50 K.

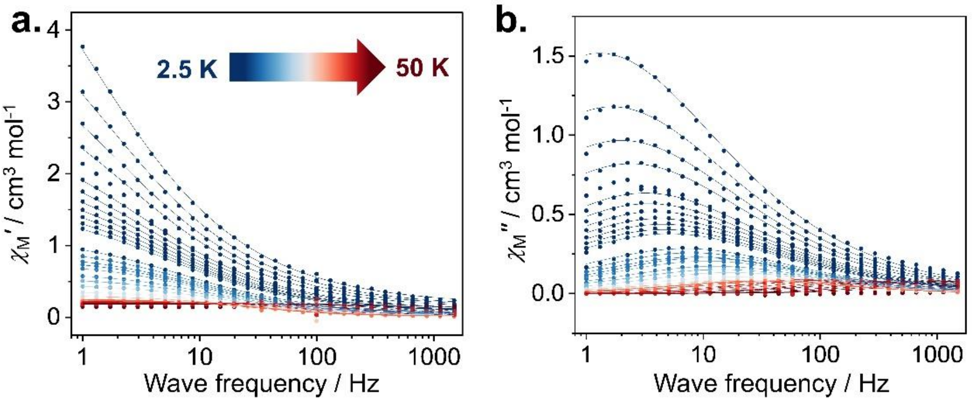

Figure 3.9. Frequency dependence of χ_M' and χ_M'' of **2** at each temperature under zero magnetic field. The solid line is the fitting.

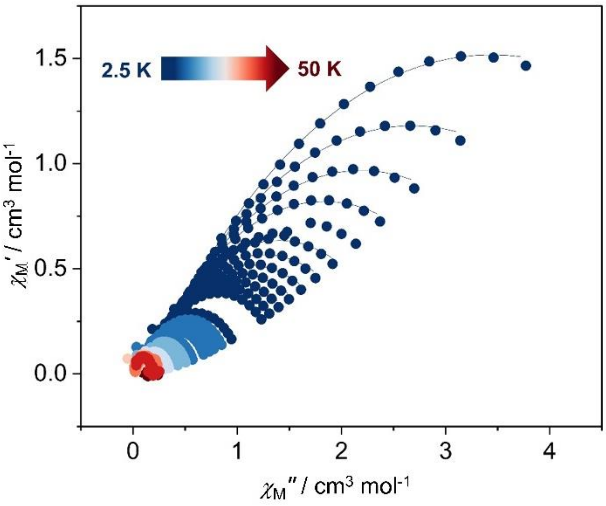

Figure 3.10. Cole-cole plot of **2**. The solid line represents fitting.

The obtained out-of-phase AC susceptibility was fitted with the generalized Debye model (Figure 3.9, 3.10 solid lines, and Table 5.1 in Chapter 5).[181,182] Figure 3.12 depicts the obtained lifetime (τ) versus temperature plot. The plot was well fitted with the following equation.

$$\tau^{-1} = \tau_0^{-1} \exp\left(-\frac{U_{eff}}{T}\right) + CT^n \qquad (3.1)$$

At higher temperature regions above 41 K, Orbach process is dominant (see Chapter 1 Section 1.4.2). It was fitted by using Arrhenius equation ($\tau^{-1} = \tau_0^{-1} \exp\left(-\frac{U_{eff}}{T}\right)$), which provided the parameters U_{eff} = 670 ± 15 K, τ_0 = (2.07 ± 0.66) × 10^{-10} s. On the other hand, the lower temperature region below 36 K was best fitted with Raman process which was fitted by this equation: $\tau^{-1} = CT^n$, yielding the parameters: C = 1.08 ± 0.05 s^{-1}, n = 1.18 ± 0.02. The overall spectrum appears as a curve, unlike that of $[TbPc_2]^0$.[180] Such behavior can also be found in functionalized $[TbPc_2]^0$ derivatives,[119,183,184] probably because of additional phonon mode introduced by functional groups.

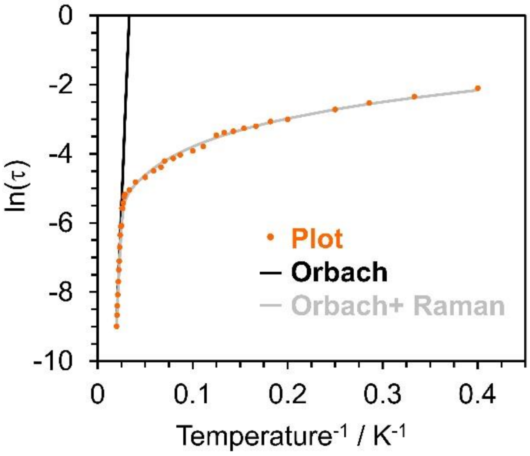

Figure 3.11. Plot of ln(τ) (natural logarithm of the relaxation time, in seconds) versus temperature inverse. Fittings are done with the equation: $\tau^{-1} = \tau_0^{-1} \exp\left(-\frac{U_{eff}}{T}\right) + CT^n$, where U_{eff} = 670 ± 15 K, τ_0 = (2.07 ± 0.66) × 10^{-10} s., C = 1.08 ± 0.05 s^{-1}, n = 1.18 ± 0.02. Orbach (black solid line) represents the first term while Orbach + Raman (grey solid line) represents the first and second term.

3.3. Discussion

As discussed in Chapter 1, SMM property is typically argued according to parameters such as U_{eff}, T_{B}, H_{c}, *etc*. Here, in order to evaluate the magnetic property of **2**, these values were compared to the literature values.

Hysteresis loop was observed for **2** up to 17 K in sweep rate of 25 Oe/s. It is higher than that of alkoxy-substituted $[\mathrm{TbPc}^{*}{}_2]^0$ (15 K in the sweep rate of 50 Oe/s),[185] whereas not as high as the highest one reported for amino-substituted $[\mathrm{TbPc}^{*}{}_2]^0$ (30 K in the sweep rate of 200 Oe/s).[174] It is notable that the scan speed significantly affects the hysteresis loop; the faster the scan is, the higher the maximum temperature will be. Therefore, although it can be concluded that the SMM property of **2** is not significantly diminished, it cannot be discussed quantitatively. As described in Chapter 1 Section 1.4.2, blocking temperature can be also defined as the temperature at which $\tau = 100$ s is observed. By extrapolating the Orbach term shown above, $T_{\mathrm{B}(\tau = 100\ \mathrm{s})} = 24.90$ K was obtained. In the same manner, $T_{\mathrm{B}(\tau = 100\ \mathrm{s})} = 24.94 – 29.83$ K were obtained for the $[\mathrm{TbPc}_2]^0$ derivatives, which is summarized in Table 3.2. Overall, in terms of the blocking temperature, the SMM property of **2** is unchanged from other $[\mathrm{TbPc}_2]^0$ derivatives.

Table 3.2. Comparison of T_{B} in two definitions to the literature values.

System	Blocking temperature Hysteresis[a]	 $\tau = 100$ s[b]	Reference
2	17	24.90	This work
amino, hetero	30	27.27	Jiang 2017[174]
alkoxy, homo	15	26.56	Sessoli 2014[185]
pristine (1)		24.94	Yamashita 2017[180]
pristine (2)		29.83	Yamashita 2017[180]

a. The maximum temperature at which the hysteresis loop is open. The conditions of these measurements are described in the main manuscript. b. The temperature at which $\tau = 100$ s is observed, which was obtained by extrapolating the Orbach term. U_{eff} and τ_0 are from literature noted in the column “Reference”.

The coercive field of **2** was observed to be zero, even at 2 K. The large H_{c} of $[\mathrm{TbPc}_2]^0$ was reported by Veciana and coworkers in solution phase MCD measurement. However, as demonstrated by Yamashita and coworkers in 2017, H_{c} was not observed in a crystalline sample of $[\mathrm{TbPc}_2]^0$ measured by SQUID.[180] Additionally, TbPc_2 dimer (Figure 1.8) showed a non-zero coercive field up to 16 K.[119] due to strong radical-radical exchange ($J_{\mathrm{Rad\text{-}Rad}} = 300\ \mathrm{cm}^{-1}$). Overall, the behavior of **2** is more similar to $[\mathrm{TbPc}_2]^0$ than the TbPc_2 dimer, probably because of the weak radical-radical exchange ($|J_{\mathrm{Rad\text{-}Rad}}| = 0.014\ \mathrm{cm}^{-1}$)

The energy barrier U_{eff} was determined to be $U_{eff} = 670$ K. The U_{eff} values reported for $[\mathrm{TbPc}_2]^0$ vary depending on the crystallinity. In 2004, Ishikawa and coworkers reported $U_{eff} = 590$ K for bulk powder sample of $[TbPc_2]^0$,[106] while in 2017, Yamashita and coworkers reported U_{eff} = 753 K and 801 K for crystalline samples of $[TbPc_2]^0$ without and with lattice solvent, respectively.[180] Electron-donating substituents on one of the two Pcs improve U_{eff}, as seen in hetero-substituted $[TbPc_2]^o$ with both alkoxide and amino substituents, which achieved high U_{eff} values of 938 K and 939 K, respectively (Figure 3.12).[174,186] In contrast, U_{eff} of **2** is in the range of those of $[TbPc_2]^0$ (Figure 3.12), implying the relaxation behavior of pristine $[TbPc2]^0$ is preserved in **2**.

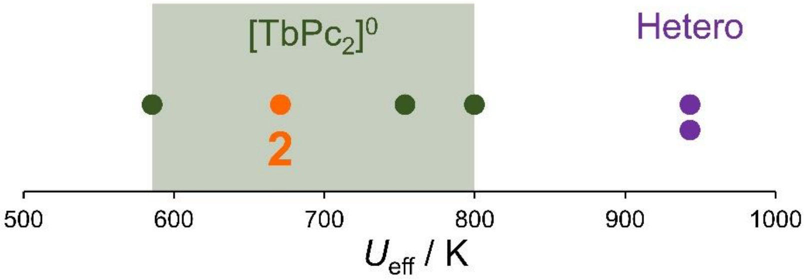

Figure 3.12. Schematic representation of U_{eff} values of $[TbPc_2]^0$ derivatives. Each example is mentioned in the manuscript.

DC magnetic susceptibility supported that the sample is magnetically pure. The hysteresis loop measurement revealed T_B =17 K (from hysteresis loop measurement) / 24.9 K (from AC data) while H_c = 0 Oe even at 2 K. In addition, AC susceptibility and its fitting revealed various parameters represented by U_{eff} = 670 K. These findings collectively suggest that the magnetic properties of **2** are similar to that of $[TbPc_2]^0$.

The discussion above concludes that the SMM property of $[TbPc_2]^0$ is preserved in **2**. In addition, spectroscopic characterization revealed that the diradicals remain intact, suggesting that compound **2** possesses the three-spin configuration comprising two radicals and one single-molecule magnet (SMM) center. As mentioned in the introduction section, CNOT gate was implemented by adatom systems containing three spins: two Ti (S = 1/2) adatoms and one Fe adatom, employing STM-EPR technique. Given the similarity of these two systems, STM-EPR studies on **2** are highly promising, in the perspective that the incorporation of SMM may effectively create *g* asymmetry. In this context, the applicability of electrospray on **2** is preferable, which is confirmed by ESI-MS on both **1** and **2**. As explained in Chapter 1. Section 1.4.4, $[LnPc_2]^o$ compounds can be sublimated, facilitating scanning tunneling microscopy (STM) studies. However, one challenge is that the thermal stability remains uncertain after the addition of functional groups: the sublimation temperature of $TbPc_2$ is 600 K[187], where most of the organic compounds decompose. Other than sublimation, electrospray ionization has been studied as a deposition method.[188] It is desired that STM-EPR will be performed against **2**, by applying this technique.

3.4. Conclusion

This chapter explored bis(phthalocyaninato) terbium (III) functionalized with an isoindoline nitroxide group, with the aim of tuning SMM property and QIP application. Compound **2** was synthesized, and characterization confirmed the preservation of both radicals, consistent with findings from Chapter 2. The blocking temperatures were obtained from both hysteresis loop measurement and AC susceptibility measurement, both of which are comparable with those of other $[TbPc_2]^0$ derivatives. Hysteresis loop measurement also clarified that the coercive field was zero even at 2 K, suggesting that exchange-bias was not sufficient enough to suppress QTM, unlike $[TbPc_2]^0$ dimer. AC susceptibility measurement and its fitting clarified that the relaxation of **2** can be expressed as a combination of the Orbach and Raman processes. Particularly, U_{eff} = 670 K is in the range of original $[TbPc_2]^0$, and not as high as those that possess electron donating groups on only one of Pc ligands. Overall, the magnetic behavior of **2** aligns closely with that of $[TbPc_2]^0$. The preserved SMM property and the presence of two radicals may cause *g*-asymmetry due to deviation of the local magnetic field, which makes this molecule an intriguing target for STM-EPR. In this context, the suitability of this molecule with the electron spray ionization technique might be preferable.

Chapter 4. Switchable Magnetic Properties in a Redox-Active Bis(porphyritnato)(phthalocyaninato)-diterbium(III) Single-Molecule Magnet

4.1. Introduction

In the field of information storage and quantum information processing (QIP), achieving molecule-based quantum devices has been a highly ambitious objective. As explained in section 1.5, amongst candidate molecules, bis(phthalocyaninato) terbium (III) ($TbPc_2$) has been intensively studied for its novelty of being both a single molecule magnet (SMM) and a molecular qubit.[91,189] In 2003, Ishikawa *et al.* reported that terbium(III) in the $TbPc_2$ complex owns a doubly degenerate ground state with high magnetic anisotropy, leading to its slow relaxation of magnetization.[89] Later, it was found that the nuclear spin states can be accessed via the magnetic relaxation of $TbPc_2$ via quantum tunneling of magnetization (QTM) in low temperature μ-SQUID measurements.[123] Nuclear spins are ideal for QIP due to their shielded nature, which allows long decoherence time.[125] Here, terbium is feasible, since its only natural abundant isotope ^{159}Tb bearing a nuclear spin $I = 3/2$ gives rise to a four-level system as multiplicity is defined as $d = 2I + 1 = 4$ (where d is the system's dimension). The series of studies demonstrated the implementation of Grover's quantum algorithm using three of the four nuclear spin states of $TbPc_2$ via single-molecule spin transport measurements.[126,128,190] Multi-level qubits with d > 2 are called qudits, which allow more information per unit for storage and manipulation.[191] Qudit-oriented quantum algorithms[128,189], as well as an evaluation method of fidelity[130] have been developed, leading to more robust quantum error correction and increased computational power of qudits. One major challenge in improving qudits is scaling up the dimension of d. As described in section 1.5, previously, Wernsdorfer and Ruben have proposed that exponential up-scaling of the multiplicity $d = (2I + 1)^n$ (where n is the number of nuclear spin bearing centers) can be achieved by using multiple-decker lanthanide complexes, in which multiple metal centers and ligands (phthalocyanine or porphyrin) are stacked like a sandwich.[191] Later in 2021, this concept was demonstrated experimentally in spin transport measurements on a tris(phthalocyaninato) dinuclear terbium(III) complex $Tb_2(Pc)_3$ (Figure 4.1. left).[139]

Whether multiple-decker complexes are qualified as qudits is determined by several factors, such as SMM character, the hyperfine coupling between electron spin and nuclear spin, and the exchange coupling between electron spins of lanthanides ($J_{\text{Ln-Ln}}$).[189,191] In the case of $Tb_2(Pc)_3$, the last one is particularly important, as several studies reported their weak $J_{\text{Ln-Ln}}$.[143,192,193] Particularly in spin transport, the exchange coupling between radical and lanthanide spin ($J_{\text{rad-Ln}}$) is crucial since nuclear-spin readout in spin transport is enabled by "spin cascade" between the nuclear spin of ^{159}Tb, the total angular momenta of ^{159}Tb, and the radical.[129] It is notable that, unlike the case of $[TbPc_2]^0$, where $J_{\text{rad-Tb}}$ was investigated in bulk sample using high-field EPR,[179] $J_{\text{rad-Tb}}$ remains unknown in $Tb_2(Pc)_3$. As described in Section 1.4.3, $J_{\text{rad-Ln}}$ and $J_{\text{Ln-Ln}}$ have been widely investigated in varieties of radical-bridged di-lanthanide complexes. Over the last decade, these complexes have been explored aiming at high-performance SMMs.[104,105] The radical coupled to a lanthanide or bridging two lanthanides induces either exchange-bias[104,119] or giant spin effect[112–114], thereby enhancing SMM performance. Indeed, the linear correlation between $J_{\text{rad-Ln}}$ and the energy barrier U_{eff} has been demonstrated.[117] However, a significant problem arises because, unlike $[\text{TbPc}_2]^0$, neutral $\text{Tb}_2(\text{Pc})_3$ does not have a radical (see Section 1.5). The presence of radical-bearing $\text{Tb}_2(\text{Pc})_3$ has been reported in previous studies, for instance through in situ UV-vis spectroscopy,[140,194] in situ Kondo measurements using scanning tunneling spectroscopy,[195,196] and by mixing with corrole ligands.[197–199] However, none of these approaches fully satisfy our demand, as the first two are not applicable to bulk magnetometry, and the latter, due to broken symmetry, does not qualify as an SMM,[199] which falls outside our area of interest. In short, for a more reliable qubit, a $\text{Tb}_2(\text{Pc})_3$ molecule is required possessing SMM properties and the capability of being converted into a radical suitable for magnetic measurements.

Here, bis(porphyrinato)phthalocyaninato dinuclear rare-earth(III) complexes functionalized with thiomethyl groups were designed (**3-Ln**, Figure 4.1 right). The thiomethyl group is preferable in two ways: (1) It forms a strong bond with the gold electrode, and (2) it functions as an electron donor. This work focused on the latter. Using its electron-donating property, two objectives were settled: (1) Tuning the redox level of the bis(porphyrinato)phthalocyaninato dinuclear rare-earth(III) complexes to enable conversion into a radical species, and (2) studying the magnetic properties of the radical, particularly the difference of SMM properties.

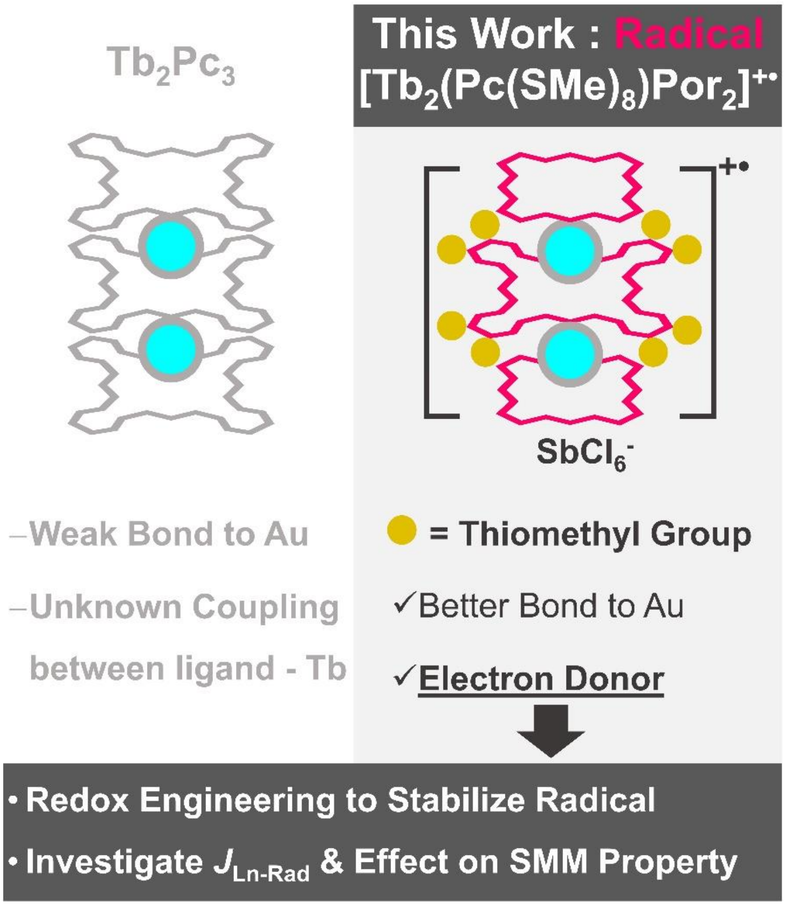

Figure 4.1. Schematic illustration of Tb_2Pc_3 (left) and bis(porphyrinato)((octathyomethyl)phthalocyaninato)diterbium(III) complex (**4-Tb**) (right). Research objectives are summarized below the scheme.

4.2. Results

4.2.1. Synthesis and characterization

Synthesis of starting material; $[LnPc_2(SMe)_{16}]^0$

Prior to the preparation of **3-Ln**, $[LnPc_2]^0$ (Ln = Tb, Y) with thiomethyl groups was prepared ($[LnPc_2(SMe)_{16}]^0$, as shown in Figure 4.4). The synthetic details are described in Chapter 5. In a similar manner as Chapter 2 and 3, $[LnPc_2(SMe)_{16}]^0$ was characterized with various spectroscopic techniques (see Figure 4.2, 4.3).

The UV-vis-NIR spectra of $[LnPc_2(SMe)_{16}]^0$ are similar to those of $[LnPc_2]^0$ with some minor differences: a Soret band (ca. 320 and 390 nm, with a clear split), a Q band (ca. 710 nm), a blue valence (BV) band (ca. 550 nm, redshifted in 100 nm), a red valence (RV) band (ca. 950 nm, redshifted in 50 nm), and an intervalence band at the NIR. These features are consistent with those of previously reported $[LnPc_2]^0$ derivatives with thioalkyl groups.[200] Those differences are probably because of the induction effect of the thiomethyl group. On the other hand, IR spectra of $[LnPc_2(SMe)_{16}]^0$ showed similar features with those of $[LnPc_2]^0$. It also showed additional features assigned to the thiomethyl group, such as the one at 1280 cm^{-1} (*Ph-S* stretching) and 1400 cm^{-1} (-CH_3 umbrella motion).[201] It matched with the previously reported IR spectra on alkoxy-substituted [LnPc$_2$]^0, where the characteristic vibrational bands of the Pc rings and those of the substituents can be separately identified. The ESI-mass spectra of [LnPc$_2$(SMe)$_{16}$]^0 showed one signal, whose isotropic pattern matched with those of the target materials. Overall, [LnPc$_2$(SMe)$_{16}$]^0 were well characterized, and were used for further reaction.

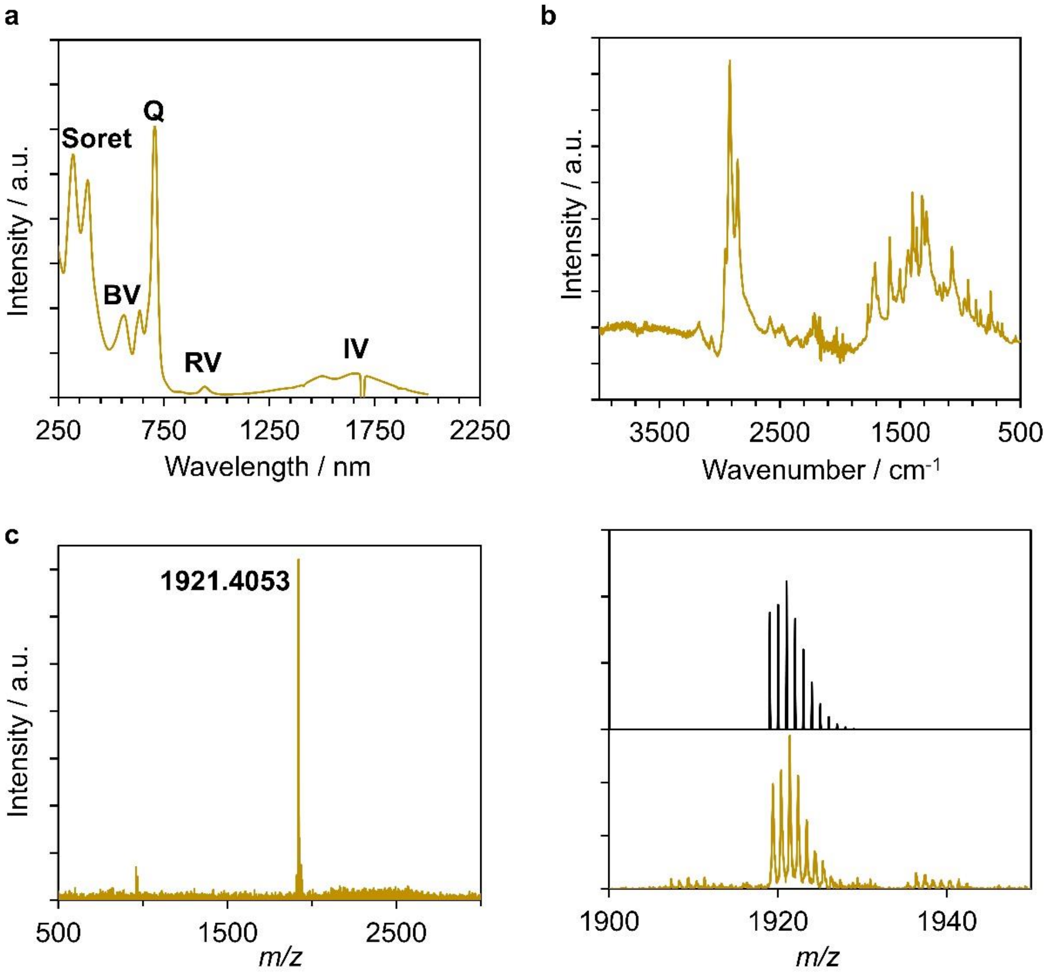

Figure 4.2. (a) UV–vis–NIR spectrum of **[TbPc$_2$(SMe)$_{16}$]^0**. (b) IR spectrum of **[TbPc$_2$(SMe)$_{16}$]^0**. (c) ESI-mass spectrum of **[TbPc$_2$(SMe)$_{16}$]^0** (left: the entire spectrum, right bottom: the expansion of the strongest peak, right top represents a simulated spectrum of $C_{88}H_{72}N_8S_{16}Tb$).

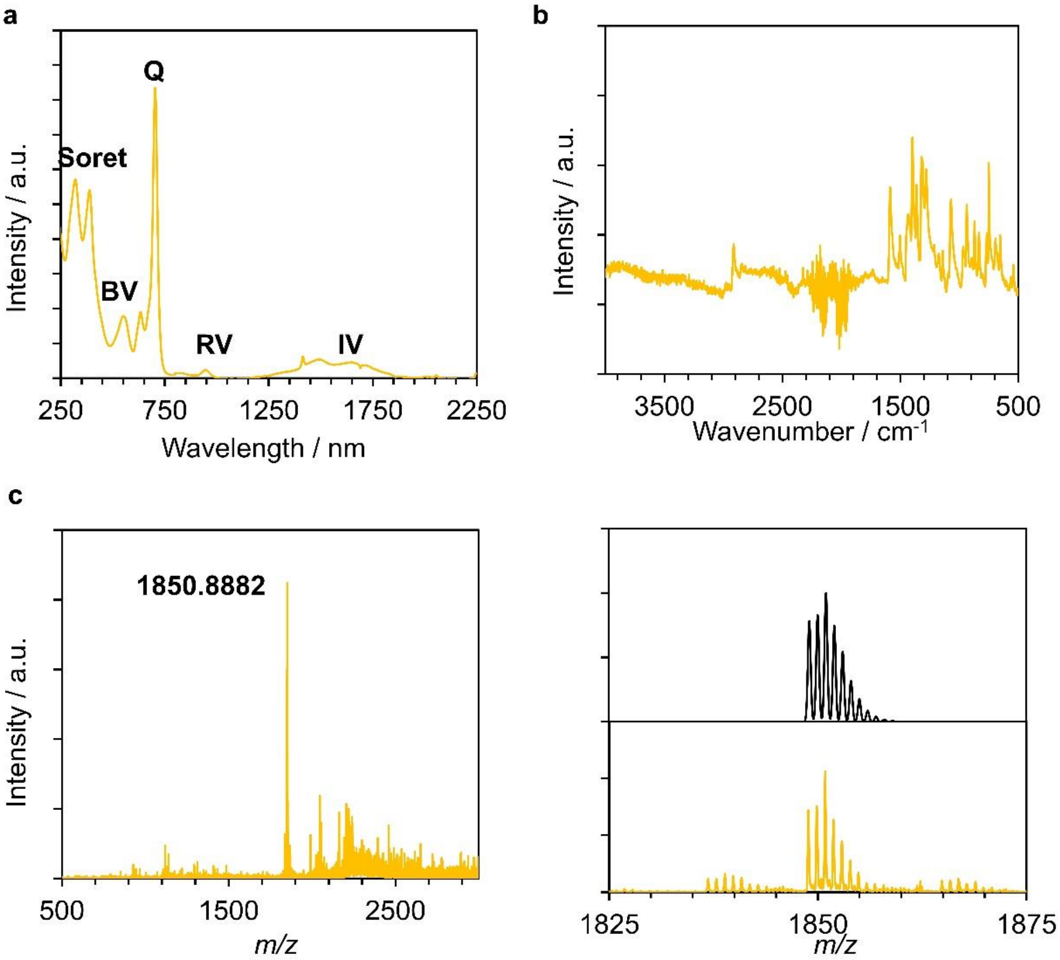

Figure 4.3. (a) UV–vis–NIR spectrum of **[YPc$_2$(SMe)$_{16}$]^0**. (b) IR spectrum of **[YPc$_2$(SMe)$_{16}$]^0**. (c) ESI-mass spectrum of **[YPc$_2$(SMe)$_{16}$]^0** (left: the entire spectrum, right bottom: the expansion of the strongest peak, right top represents a simulated spectrum of $C_{88}H_{72}N_8S_{16}Y$).

Synthesis of neutral Lanthanide(III) bis(porphyrinato)((octathiomethyl)-phthalocyaninato) complexes (3-Ln)

Lanthanide(III) bis(porphyrinato)((octathiomethyl)phthalocyaninato) complexes (**3-Ln**, **Ln** = **Tb**, **Y**) were synthesized in a two-step tandem one-pot reaction following a previously invented synthetic path (Figure 4.4).[202] The reaction proceeds in three steps: (1) In situ generation of monoporphyrinic species Ln(Por)(acac) for 4 h, which further acts as a template for the second step. This approach offers a solution for the instability of the intermediate lanthanide monoporphyrinates. (2) Addition of the pre-synthesized **[LnPc$_2$(SMe)$_{16}$]^0** complex. It undergoes in situ thermal splitting, followed by the reaction with Ln(Por)(acac). (3) Formation of **3-Ln** in 16 h reflux. Previously, the selectivity of such processes was explained in the way of quantum-chemical calculations, which is explained as follows:[203] First, the distribution of electronic density in the intermediate heteroleptic LnPcPor complex was asymmetric and shifted to the phthalocyanine ligand, along with the charge density. Moreover, in the presence of electron-donating alkoxy-groups, the distribution of HOMO achieve ca. 40% and 60% at porphyrin and phthalocyanine ligands, respectively. Consequently, the polarization of the molecule results in the selective interaction of the monoporphyrinate at the phthalocyanine site of the LnPcPor complex. Similarly, the electron-donating thiomethyl groups of the $LnPc_2$ complex triggered the process regioselectively. Overall, owing to the advantages of the method mentioned above, the crude material could be easily purified with silica gel column chromatography (eluent: $CHCl_3$/hexane = 2/1 at first, then 100% $CHCl_3$) to give green powder. It was further purified by recrystallization in $CHCl_3$/hexane to give crystalline particles suitable for single-crystal XRD (*vide infra*).

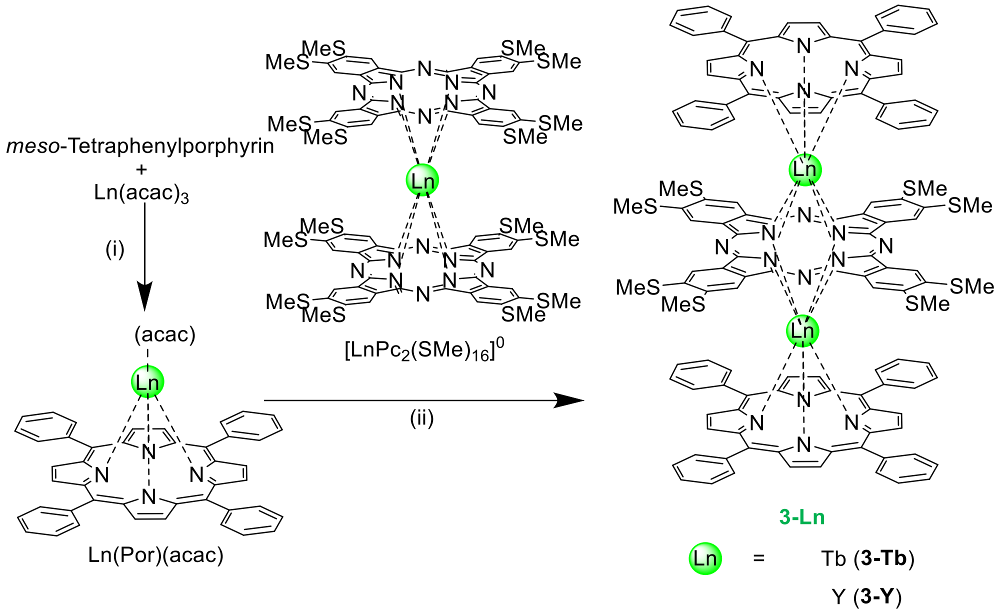

Figure 4.4. Synthetic pathway for the preparation of the bis(porphyrinato)(phthalocyaninato) lanthanide complexes (**3-Ln**). (i) in 1,2,4-trichlorobenzene/*n*-octanol, reflux, for 4h. (ii) same solvent, reflux, for 16 h.

UV-vis-NIR absorption spectroscopy of 3-Ln

Figure 4.5 depicts the UV-vis-NIR absorption spectrum of **3-Ln**. Since both of them exhibit similar character, the latter discussion will be based on **3-Tb**. Electronic absorption spectra are the most commonly used technique to characterize macrocyclic tetrapyrrolic compounds and their metal complexes.[143] As demonstrated previously,[202,204,205] the sets of bands in the spectrum are generally similar and are determined by the electronic transitions of each particular ligand. The Pc^{2-} and Por^{2-} Soret bands of **3-Tb** appear at 350 and 400 nm, respectively. The Q bands of Pc^{2-}, which also contain some contributions from the Por ligands, appear at 1000 nm. The absorption at 500 nm and 635 nm are assigned to the Q band mainly of Por^{2-}. Moreover, sulfur-containing chromophores tend to absorb light at lower energies than oxygen-containing analogs, thereby tuning the energy of transitions in the UV and visible regions. This allows for independent tuning in the spectral region between 250 and 300 nm. Thus, the presence of an electron-donating thiomethyl group in the phthalocyanine macrocycle of **3-Tb** is evidenced by the appearance of additional peaks at 380 nm and 712 nm, similar to what is observed for **[LnPc$_2$(SMe)$_{16}$]^0**.

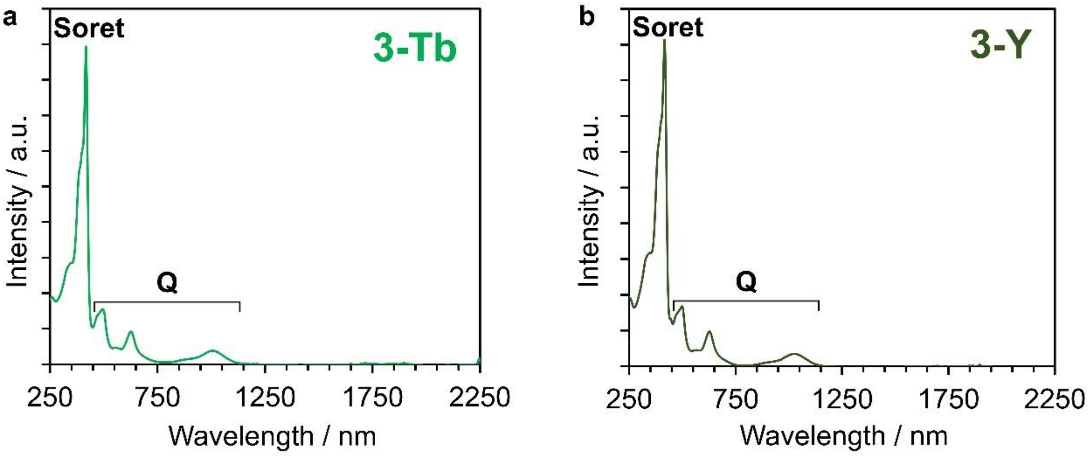

Figure 4.5. UV-vis-NIR spectrum of **3-Tb** (a) and **3-Y** (b) in CHCl$_3$.

IR spectroscopy of 3-Ln

The IR spectra for **3-Ln** are identical, therefore later only that of **3-Tb** is discussed. It is similar to those of Tb$_2$PcPor$_2$[143], confirming structural similarities. Additional peaks were observed as well, such as the one at 1200 cm^{-1} (*Ph-S* stretching) and 1400 cm^{-1} (-*CH$_3$* umbrella motion).[201] As is the case of **16SMe-LnPc$_2$**, these peaks are characteristics of -SMe groups, which is distinguished from the peaks of isoindole stretching.[206]

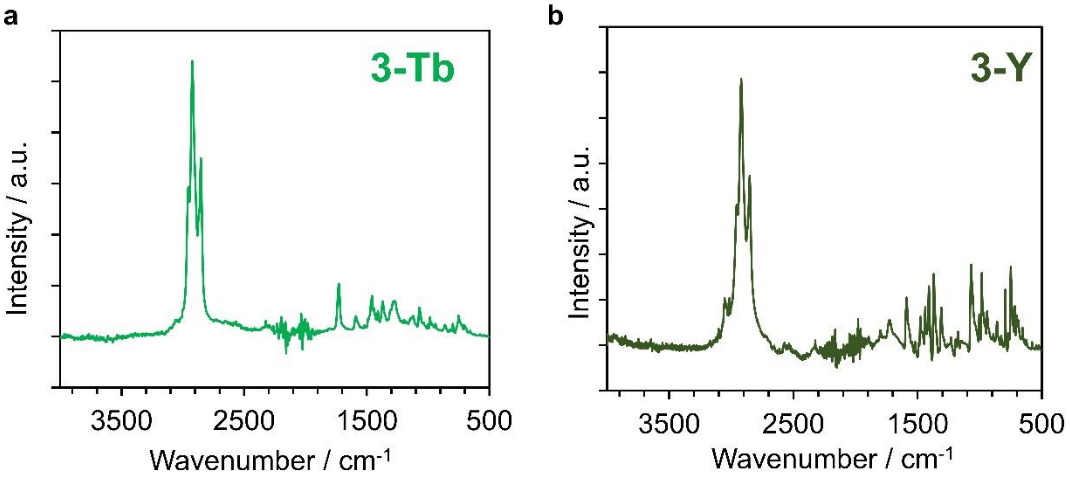

Figure 4.6. IR spectra of **3-Tb** (a) and **3-Y** (b).

ESI-mass spectrometry

High-resolution ESI-ToF-mass spectrometry was performed on both **3-Tb** and **3-Y**, showing signals from a single ion, whose isotope pattern matched the simulated one (Figure 4.7).

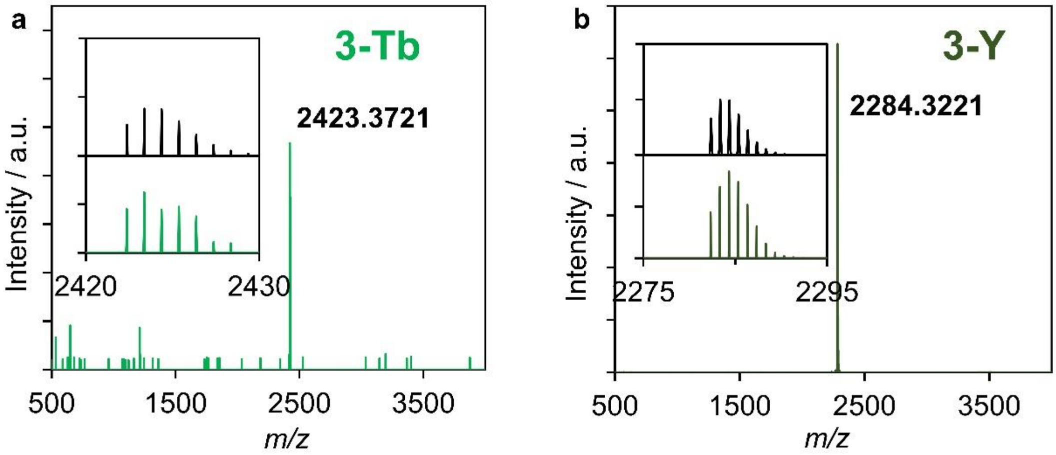

Figure 4.7. ESI-mass spectrum of **3-Tb** and **3-Y** (a and b, respectively. Insert bottom: the expansion of the strongest peak, insert top: simulated spectrum of $C_{128}H_{88}N_{16}S_8Tb_2$ and $C_{128}H_{88}N_{16}S_8Y_2$, respectively).

NMR spectroscopy

The molecular structure of the diamagnetic **3-Y** complex was demonstrated to be of the form (Por)Y(Pc)Y(Por) by its ^{1}H - and ^{13}C-NMR spectra recorded in CD_2Cl_2 (Figure 4.8 and 4.9). Peak assignment of ^{1}H-NMR was done based on the integral of H (SCH_3 and β position of porphyrin) or multiplet splitting (Pc and *o* / *m* / *p* of Por). Endo / exo protons were determined from NOESY, where the ones showing stronger peaks at the crossing points with Pc (red circle) were assigned to endo, while those showing weaker signals (light blue) were assigned to exo. The presence of peaks for exo-protons is likely due to possible rotation around the Ph-Por bond. On the other hand, the peaks in ^{13}C-NMR were assigned via HSQC- and HMBC-2D NMR. The only peak of aliphatic carbon at $\delta = 17.25$ ppm was assigned to carbon 10. The peak assignments for carbons 1, 2, 3, 4, 5, 9, and 12 were understood by HSQC-, while the rest were assigned by HMBC-NMR experiments. The correlation between ^{1}H-NMR and ^{13}C-NMR peaks is shown with yellow dashed lines.

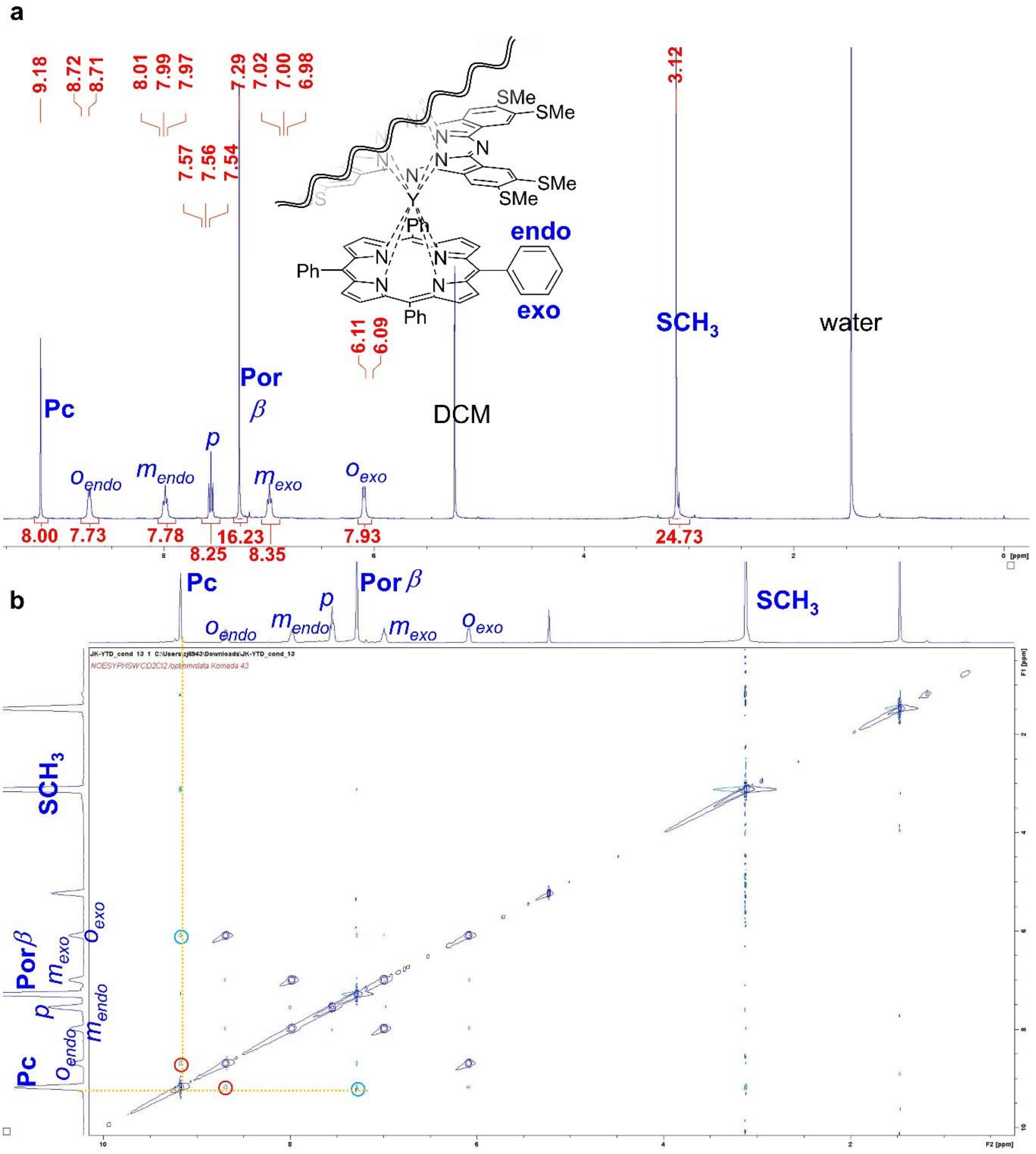

Figure 4.8. ^{1}H-NMR (b) and NOESY spectrum (a) of **3-Y**. The inset represents the bottom half of **3-Y**, where all protons are represented.

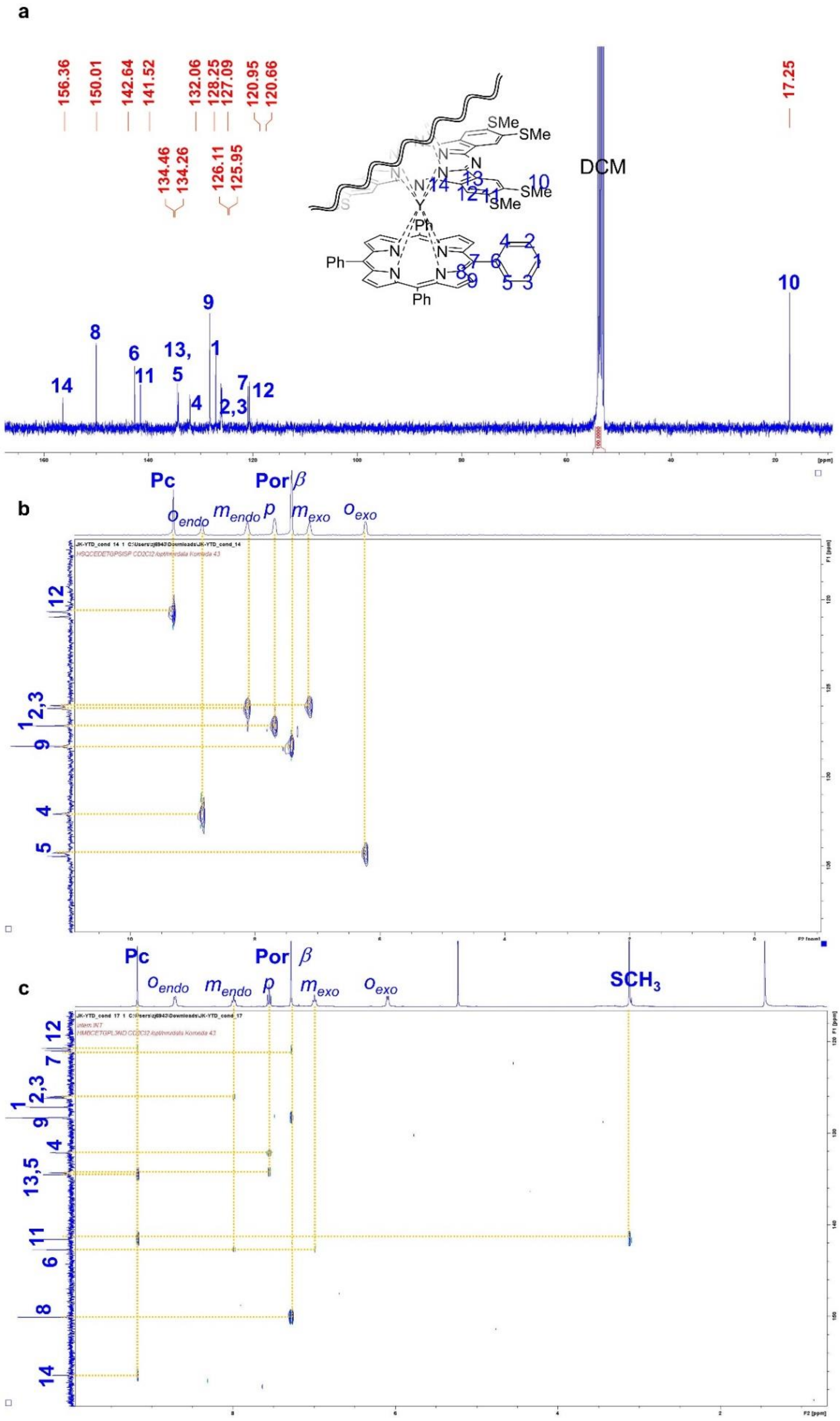

Figure 4.9. ^{13}C-NMR (a), HSQC (b), and HMBC (c) spectra of **3-Y**. The inset represents the bottom half of **3-Y**, where all carbons are represented.

Cyclic voltammetry

In order to study the redox properties of **3-Tb** and **3-Y**, cyclic voltammetry (CV) was performed in CH_2Cl_2 solution. **3-Tb** and **3-Y** showed redox properties typical of bis(porphyrinato)phthalocyaninato dinuclear rare-earth(III) molecules[204,207] (Figure 4.10 and Table 4.1). Six quasi-reversible redox waves were observed at $E_{1/2}$ at 0.94, 0.78, 0.40, 0.04, -1.33, -1.68 V vs. ferrocene/ferrocenium (Fc/Fc^+) for **3-Tb**, and at $E_{1/2}$ 0.95, 0.79, 0.39, 0.01 ,-1.31, -1.67 V for **3-Y**, respectively. As previously reported[204], such redox profiles are independent from the central metals, but related to the ligand-centered redox reactions ($[Ln_2(TPP)_2(Pc)]/[Ln_2(TPP)_2(Pc)]^+$, $[Ln_2(TPP)_2(Pc)]^+/[Ln_2(TPP)_2(Pc)]]^{2+}$, and $[Ln_2(TPP)_2(Pc)]/[Ln_2(TPP)_2(Pc)]]^-$, $[Ln_2(TPP)_2(Pc)]^-/[Ln_2(TPP)_2(Pc)]]^{2-}$), along with oxidations associated with thiomethyl groups. On the other hand, a previous study[207] reported that electron donating/withdrawing substituents on the porphyrin cause the shift of those peak positions accordingly. The first oxidation potential of **3-Tb** and **3-Y** is lower than that of $Ln_2(Pc)(TClPP)_2$ or $Eu_2(Pc)(TPP)_2$ (the abbreviations are explained below), suggesting that electron donating substituents on the phthalocyanine macrocycle are also lowering the redox potentials of the complexes. The potential difference between the first oxidation and the first reduction process, $\Delta E°_{1/2}$ (oxd.1-red.1), is an important value for sandwich porphyrinato-phthalocyaninato complexes since they involve the HOMO and the LUMO of the molecule, respectively. The energy difference between these two redox processes corresponds to the electrochemical molecular band gap. When band gaps were compared (Table 4.1) based on literature values of different bis(porphyrinato)phthalocyaninato dinuclear rare-earth(III) molecules, the difference appeared according to the electron-donating ability of -SMe substituents such as it can be significantly reduced. Thus, the ligand design strategy utilized in this work has effectively stabilized the desired redox pair and is controlled by tailoring redox states.

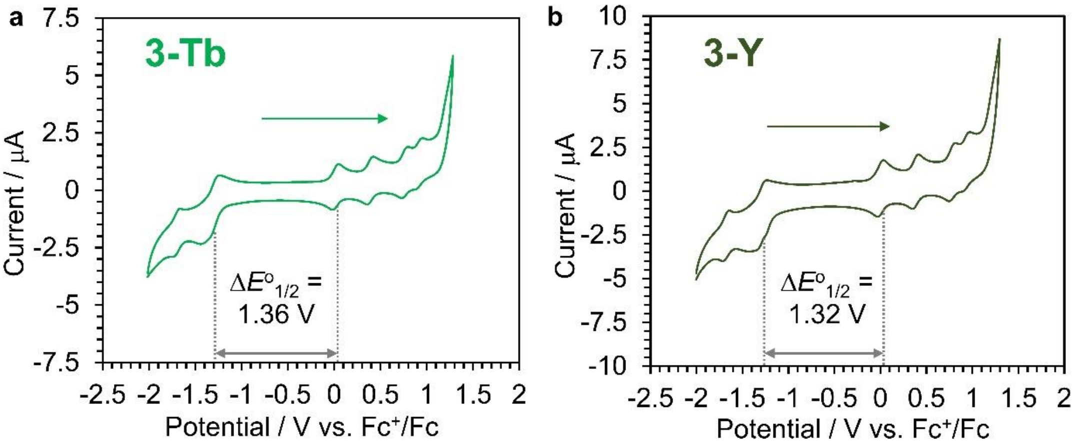

Figure 4.10. Cyclic voltammogram of **3-Tb** (a) and **3-Y** (b) at a scan rate of 100 mVs^{-1}. The arrow represents the direction of the scan.

Table 4.1. Comparison of the redox peak positions of **3-Tb** and **3-Y** with literature values. The values are shown in the unit of V vs. Fc^+/Fc.

	4th Ox.	3rd Ox.	2nd Ox.	1st Ox.	1st Red.	2nd Red.	$\Delta E°_{1/2}$[c]
3-Tb	0.94	0.78	0.40	0.04	-1.33	-1.68	1.36
3-Y	0.95	0.79	0.39	0.01	-1.31	-1.67	1.32
$Y_2(Pc)(TClPP)_2$[a]	1.23	1.01	0.63	0.25	-1.14	-1.61	1.39
$Eu_2(Pc)(TClPP)_2$[a]	1.22	1.00	0.67	0.32	-1.13	-1.64	1.45
$Eu_2(Pc)(TClPP)_2$[b]	1.12	0.86	0.54	0.17	-1.28	-1.77	1.45
$Eu_2(Pc)(TPP)_2$[b]	1.09	0.80	0.45	0.07	-1.35	-1.80	1.42
$Eu_2(Pc)(T^tBuPP)_2$[b]	1.00	0.72	0.39	0.00	-1.43	-1.87	1.43
$Eu_2(Pc)(TOMePP)_2$[b]	0.84	0.63	0.31	0.01	-1.38	-1.76	1.39

a. From ref. 11.[204] TClPP represents 5,1015,20-tetrakis(4-chlorophenyl)porphyrin. b. From ref. 12.[207] TPP represents 5,1015,20-tetraphenylporphyrin, T^tBuPP represents 5,1015,20-tetrakis(4-tButhyl)porphyrin, TOMePP represents 5,1015,20-tetrakis(4-methoxyphenyl)porphyrin, respectively. Both of the literature values were given in V vs. SCE, which was converted into V vs. Fc^+/Fc by using the conversion equation $E°_{1/2}(Fc^+/Fc)$ = +0.400 V vs. SCE.[208] c. Calculated by $\Delta E^{o}_{1/2} = 1st\ Ox. - 1st\ Red.$.

Conversion to cationic radical (4-Ln)

Encouraged by the result of cyclic voltammetry of **3-Tb** and **3-Y**, oxidation of them was attempted to obtain cationic radicals (**4-Tb** and **4-Y**, respectively). **3-Tb** or **3-Y** was mixed with an equimolar amount of phenoxathiine hexachloroantimonate(V) - $(Phen)^+SbCl_6$ - in chloroform (Figure 4.11). The reaction mixture immediately turned from green to brown. The resulting solution was transferred into test tubes placed in a hexane bath, allowing for the slow diffusion of hexane and yielding needle-like crystals of **4-Tb** or **4-Y**, suitable for single-crystal XRD analysis (*vide infra*).

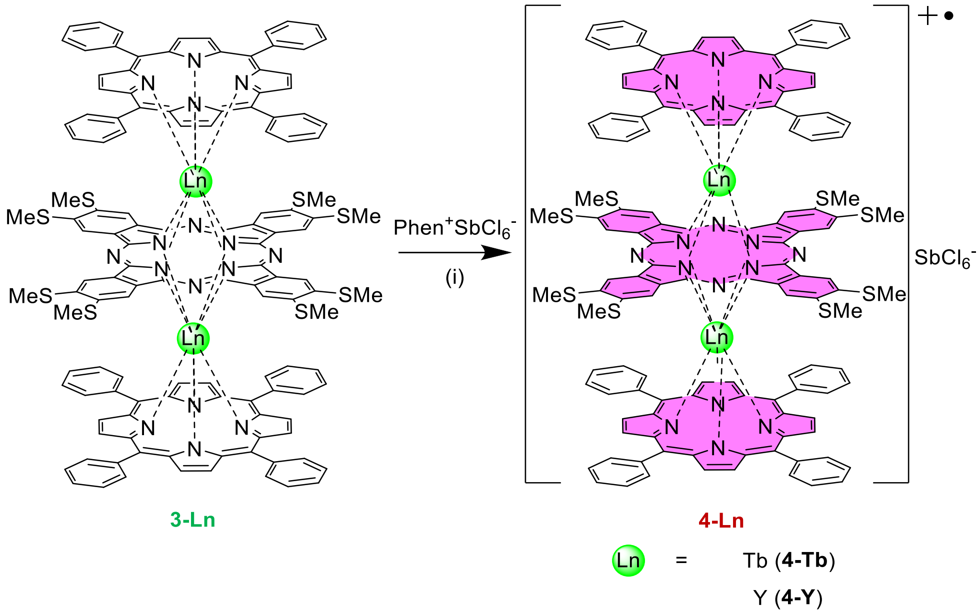

Figure 4.11. Reaction scheme for the preparation of **4-Ln**. (i) at room temperature, under an inert atmosphere, 30 minutes.

UV-vis-NIR absorption spectroscopy of 4-Ln, and stability test

The electronic absorption spectra for all compounds, taken in $CHCl_3$ solution are illustrated in Figure 4.12. The UV-vis/NIR absorption spectra of the neutral (**3-Tb** and **3-Y)** and one-electron oxidized forms (**4-Tb** and **4-Y**) differ significantly. Notable differences include a stronger peak at λ = 330 nm, the disappearance of peaks at λ = 380 and 1025 nm; a blue shift of the peak at λ = 420 nm; the broadening and red-shift of the peak at λ = 500 nm; and the appearance of the peaks at λ = 700 nm and the broad one in λ = 1250-2250 nm. Previous reports have shown similar phenomena via spectroelectrochemical techniques, where one-electron oxidation of Tb_2Pc_3 complex causes a significant change in its electronic absorption.[140,149,194,197,209] More importantly, the broad peak in the NIR range was typically observed in tetrapyrrolic sandwich compounds with π radicals: monocationic Tb_2Pc_3, $[TbPc_2]^0$ and corrole-bearing dinuclear complex (Ln_2Pc_2Cor).[140,149,194,197,209] In the case of $LnPc_2$, two bands are observed in the NIR range: the high-energy band is related to the radical part and attributed to the SOMO-LUMO transition, while the lower-energy band is assigned to an intramolecular charge transfer (CTI), both of which are the fingerprints of the presence of a delocalized organic radical.[149,210] Overall, the change of the spectrum indicates the formation of the monocationic radical, which was further proven by crystal structure and EPR study (*vide infra*).

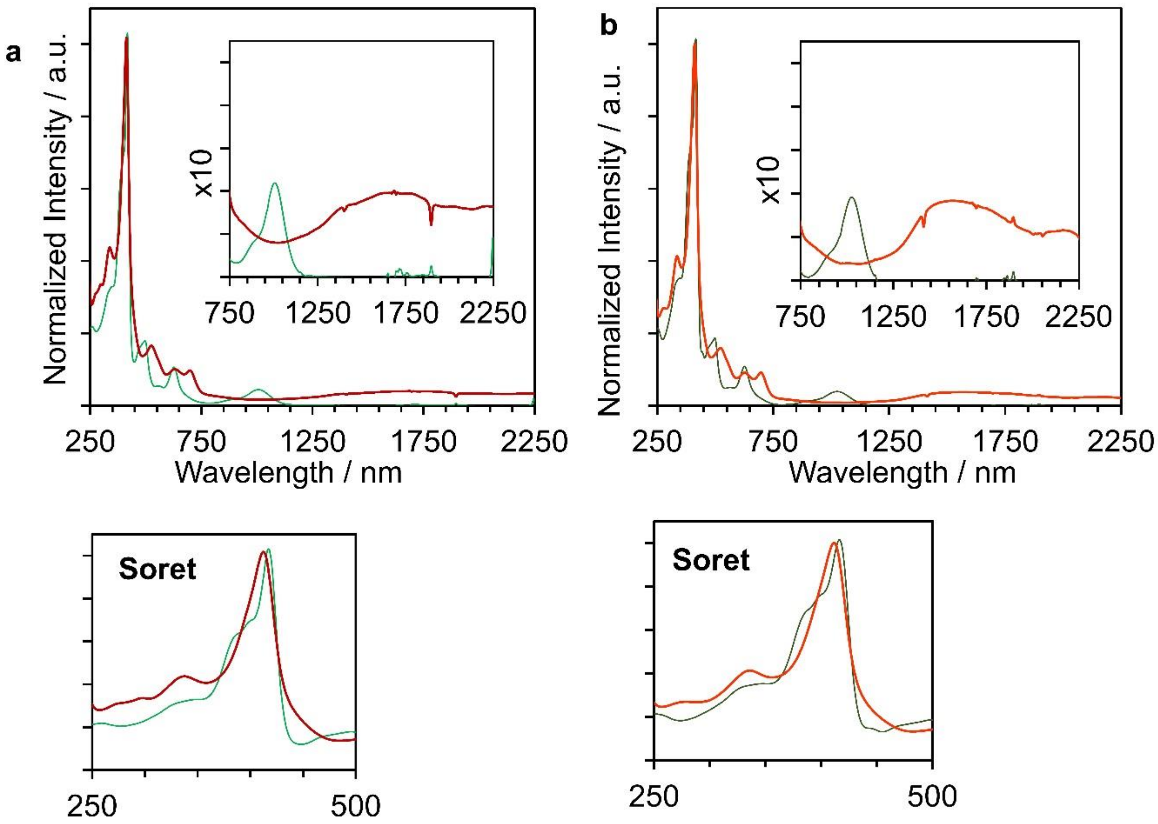

Figure 4.12. Comparison of normalized UV-vis-absorption spectra of (a) **3-Tb** (green) and **4-Tb** (maroon) / (b) **3-Y** (olive) and **4-Y** (orange). The near-infrared region is shown as an insert and Soret band at 350 and 400 nm is shown below.

Furthermore, the sample used for UV spectroscopy was kept under ambient condition at room temperature and the UV-vis abs. spectra were measured after 3 days and 7 days (Figure 4.13). Importantly, spectra observed after 3 days and 7 days remained unchanged, which proves the air stability of the compound under ambient conditions.

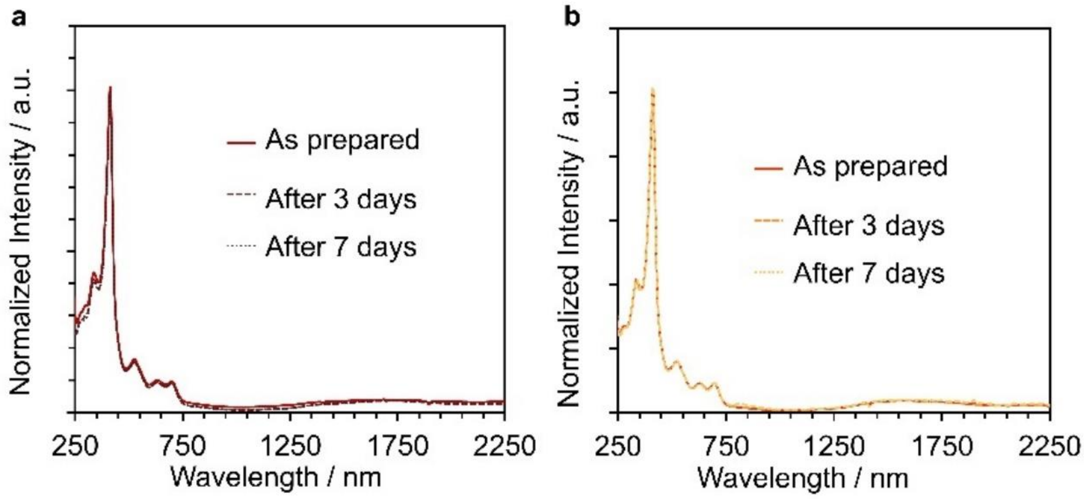

Figure 4.13. Time dependence of UV-vis-NIR spectra of **4-Tb** (a) and **4-Y** (b).

IR spectroscopy and ESI spectrometry of 4-Tb and 4-Y

IR spectra of **4-Tb** and **4-Y** are similar to those of **3-Tb** and **3-Y**, except for broadened peak in 3000 – 3500 cm^{-1} attributed to O-H vibration, probably due to the condensation of water in air caused by the cold sample. The presence of the $SbCl_6^-$ anion is proven by single-crystal XRD (*vide infra*). ESI-MS of **4-Tb** and **4-Y** show two sets of peaks, whose isotopic pattern matches with z = 1 and z = 2, respectively.

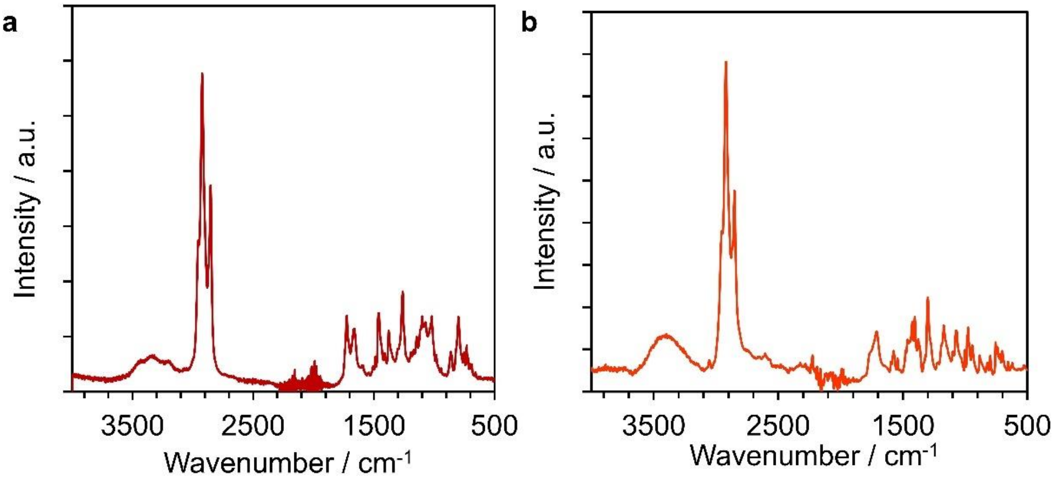

Figure 4.14. IR-spectrum of **4-Tb** (a) and **4-Y** (b).

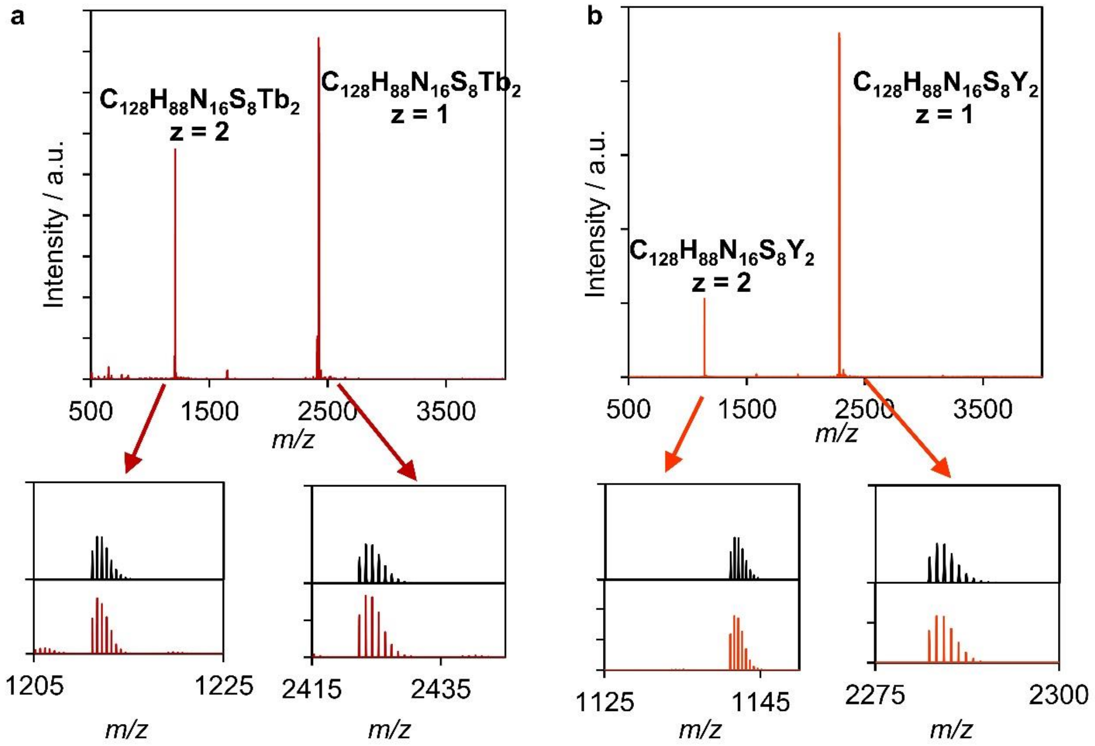

Figure 4.15. ESI-ToF MS spectrum of **4-Tb** (a) and **4-Y** (b). At the bottom of each spectrum, the expanded spectra and corresponding simulated spectra were illustrated.

4.2.2. Crystallographic analyses of 3-Tb, 3-Y, 4-Tb, and 4-Y

The crystals of **3-Tb**, **3-Y**, **4-Tb**, and **4-Y** were obtained as mentioned above, and their solid-state structures were determined by single-crystal XRD analysis (Figure 4.16, 4.17). For all of them, the structure with a symmetrical [Por]Ln[Pc]Ln[Por] configuration was confirmed. The structures of **4-Tb**, and **4-Y** included hexachloroantimonate(V) in a one-to-one ratio with the complex. Considering charge balance, **4-Ln** complexes were revealed to be organic radicals, which was further proven by EPR technique (*vide infra*). Since molecular symmetry has a great impact on magnetic property[143], crystal parameters of **3-Tb**, **3-Y**, **4-Tb**, and **4-Y**, and TbPc(TPP)$_2$ were compared in detail. First, the isostructural character of terbium and yttrium analogues (**3-Tb** and **3-Y**, **4-Tb** and **4-Y**, respectively) was confirmed by similar values for various crystal parameters and crystal packing indexes (Table 4.2, 5.4). Second, the coordination geometry of the lanthanide centers are compared, where all of those local symmetries are described best as cuboid /square prism (Table 5.3).[143] In addition, some crystal parameters were selected to quantitatively compare the differences in geometry. (Table 4.2). Comparing **4-Ln** to **3-Ln**, some differences can be observed, such as the elongation of the Ln-Ln distance, the contraction of the Por-Pc distance, and a smaller twisting angle for both Tb and Y. Finally, the intermolecular distances in the crystal packing structure were closely investigated. The intermolecular Tb ··· Tb distances were estimated to be 13.113 / 14.173 / 15.967 / 15.951 Å and 12.709 / 18.855 /15.761 / 15.929 Å for for **3-Tb, 4-Tb** respectively (Figure S10). Overall, the similar structure of **3-Ln** and **4-Ln** and their isolated character were utilized to understand their magnetic property (see discussion section).

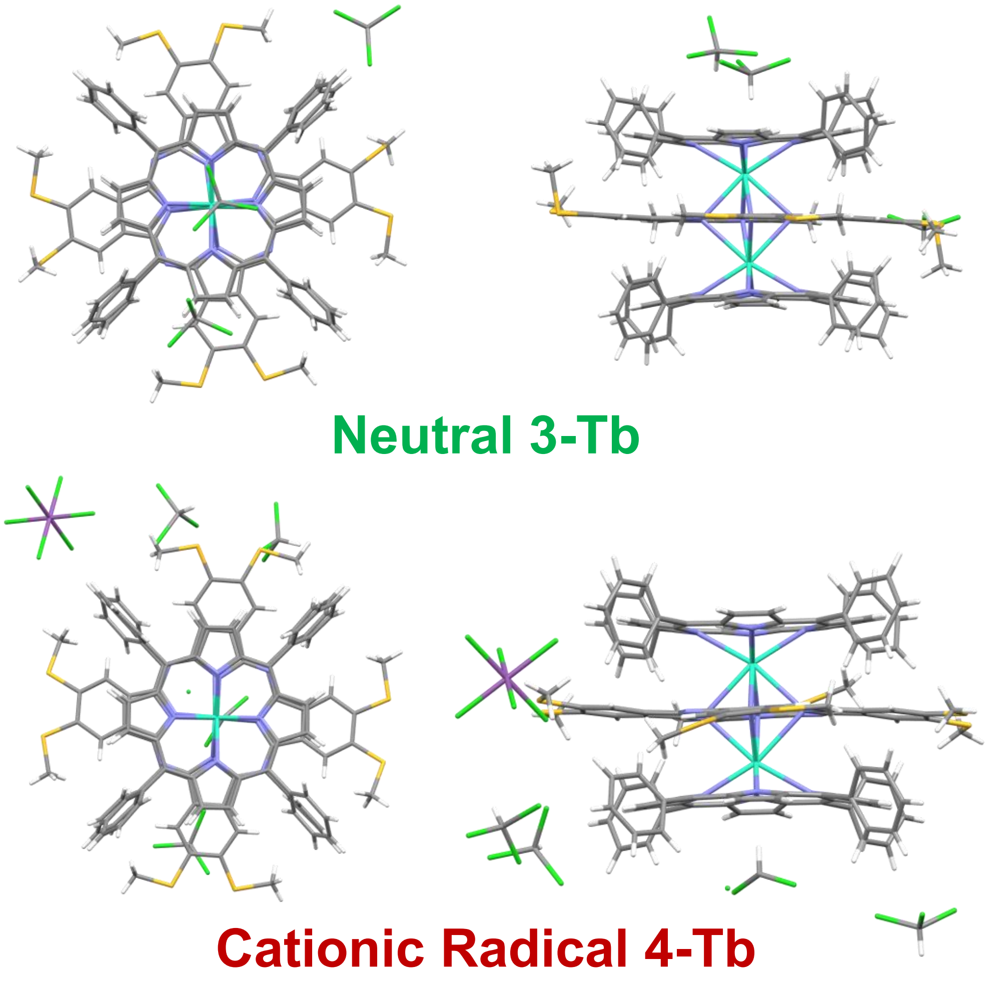

Figure 4.16. Crystal structure of **3-Tb** (top) and **4-Tb** (bottom) represented in stick model. For both of them, top view is shown on the left, while side view is shown on the right. Hydrogen, carbon, nitrogen, sulfur, terbium, chlorine, antimony are shown in white, grey, violet, yellow, turquoise, green, and purple, respectively.

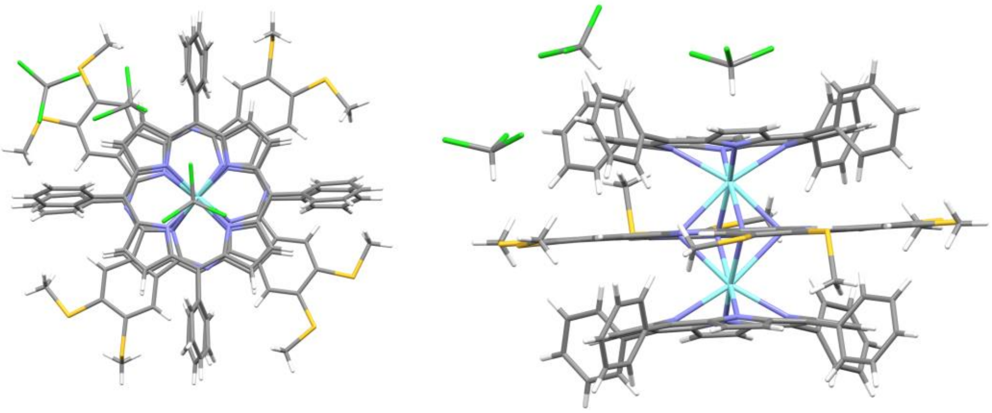

Neutral 3-Y

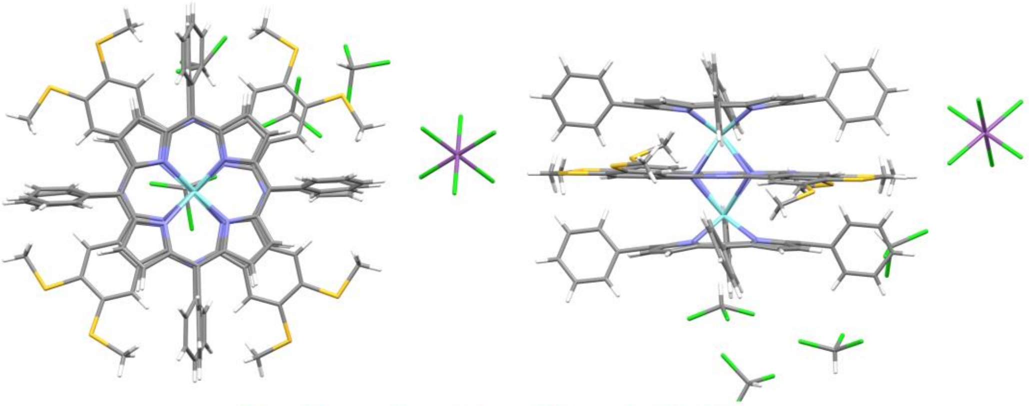

Cationic Radical 4-Y

Figure 4.17. Crystal structure of **3-Y** (top) and **4-Y** (bottom) represented in stick model. For both of them, top view is shown on the left, while side view is shown on the right. Hydrogen, carbon, nitrogen, sulfur, yttrium, chlorine, antimony are shown in white, grey, violet, yellow, turquoise, green, and purple, respectively.

Table 4. 2. Selected crystal parameters for **3-Tb**, **4-Tb**, **3-Y**, **4-Y**, and $Tb_2Pc(TPP)_2$.

Compound	Ln-Ln / Å	Por-Pc / Å	Por-Ln / Å	Ln-Pc / Å	Twisting Angle / °
3-Tb	3.74	3.11	1.24	1.87	7.61
4-Tb	3.75	3.09	1.21	1.88	4.16
3-Y	3.72	3.07	1.21	1.86	7.55
4-Y	3.73	3.05	1.19	1.86	4.17
$Tb_2Pc(TPP)_2$[a]	3.72	3.10	1.24	1.86	3.90

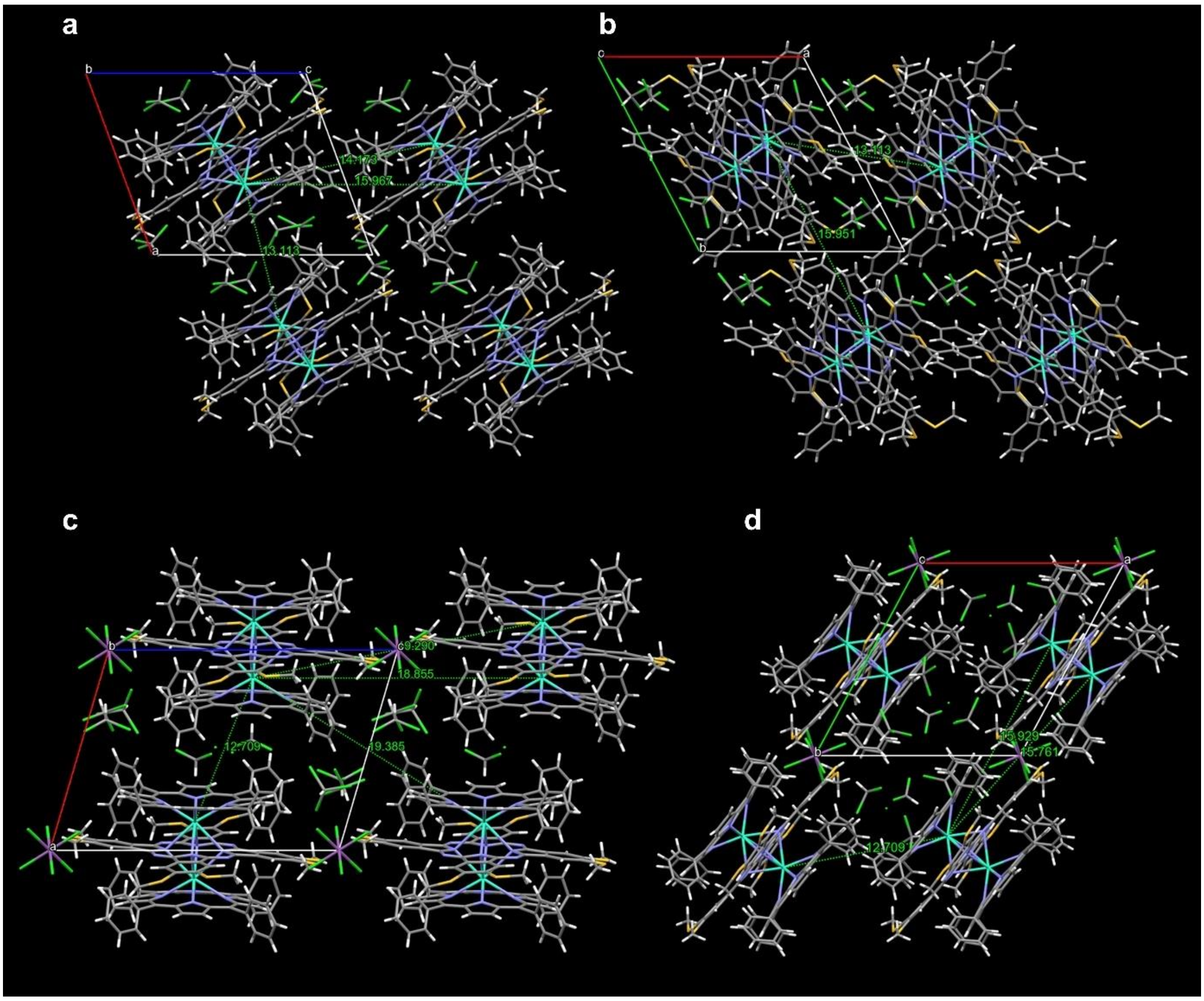

Figure 4.18. The views of the crystal packing in **3-Tb** along the b (a) and c (b) crystallographic axes. The views of the crystal packing in **4-Tb** along the b (c) and c (d) crystallographic axes. An arbitrary view that allows for the reflectance of relevant distances and interactions (see text).

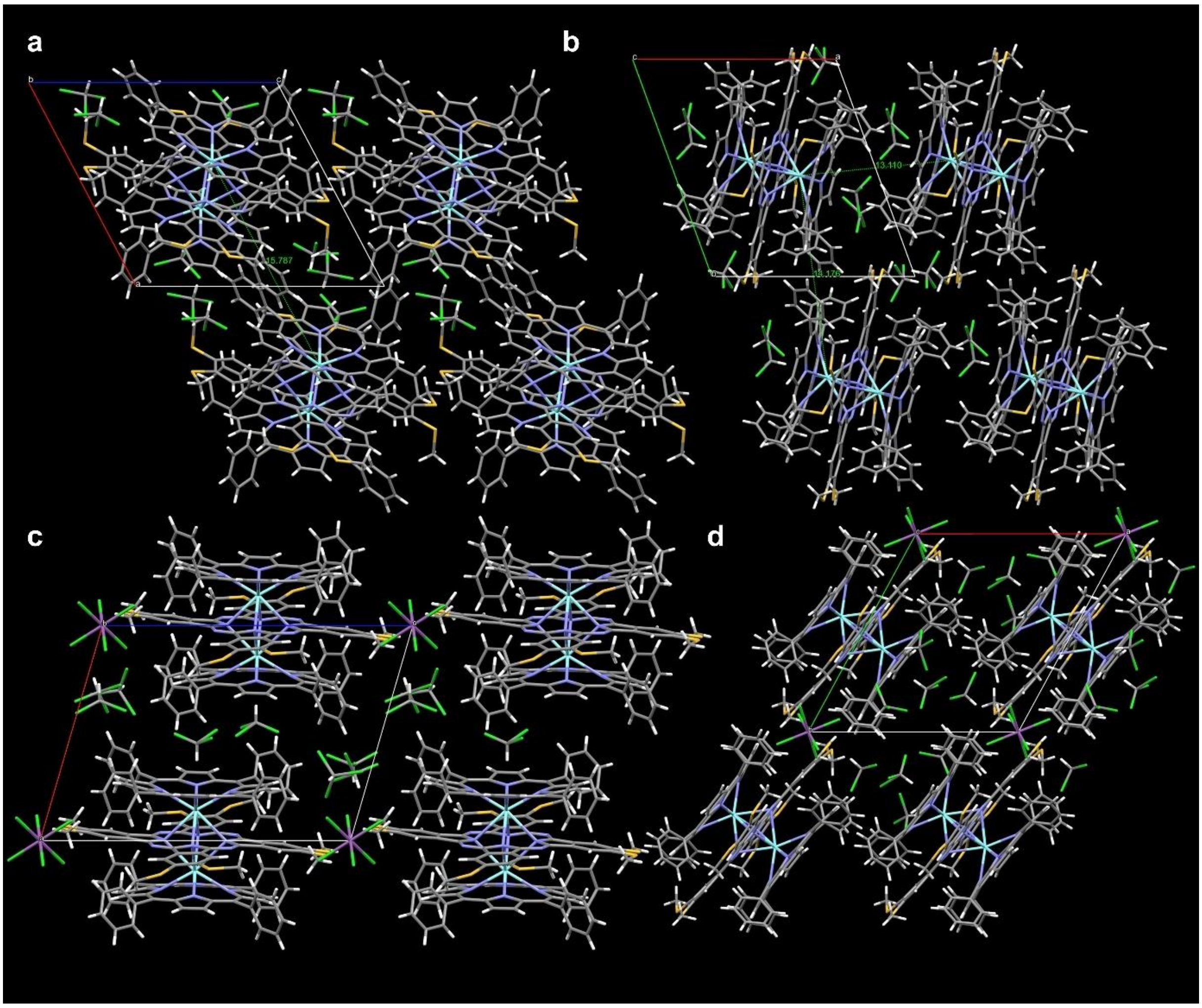

Figure 4.19. The views of the crystal packing in **3-Y** along the b (a) and c (b) crystallographic axes. The views of the crystal packing in **4-Y** along the b (c) and c (d) crystallographic axes. An arbitrary view that allows for the reflectance of relevant distances and interactions (see text).

4.2.3. EPR study

Before the EPR study, DFT calculation was conducted on the obtained structure of **4-Y**, without structural optimization. The spin density is fully delocalized over the Pc and Por ligands (Figure 4.20), which is similar to that of previously reported YPc_2 and YPcPor.[57]

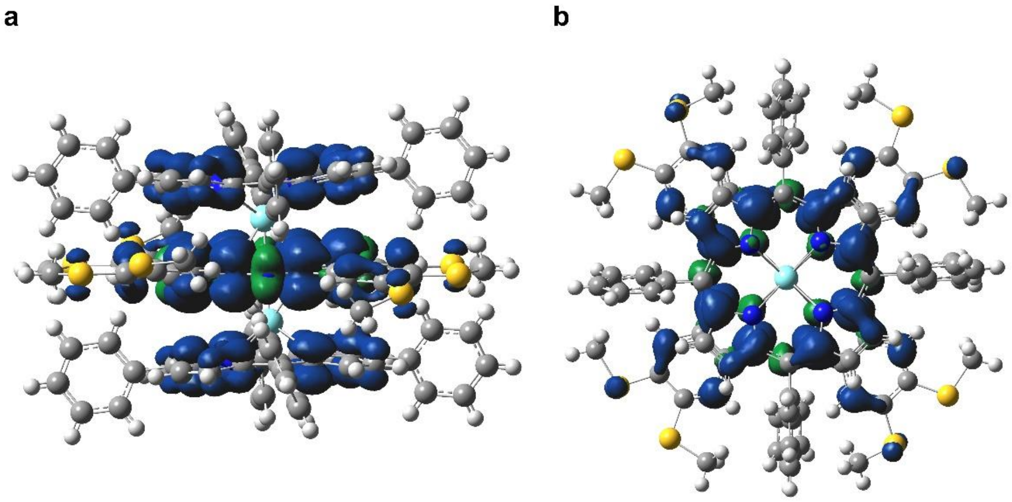

Figure 4.20. Spin distribution of **4-Y** from side (a) and top (b) calculated from DFT. The calculation was performed using the crystal structure without optimization.

To prove the presence of the radical, a CW-EPR measurement was performed on the frozen-solution of **4-Y** at 92 K (Figure 4.21 a). It exhibited a simple resonance centered around g = 2.0023. Fits to a simple isotropic absorption yielded best-fit parameters: g = 2.00237(7), σ_G = 0.25(1) mT_{pp}, σ_L = 0.14(1) mT_{pp}. The lack of hyperfine splitting is attributed to the low spin density on nitrogen atoms, likewise YPc_2 and YPcPor. The MW power dependence of the integrated intensity of EPR signal was investigated (Figure 4.21 b). In agreement with related systems $[Y(Pc)_2]^{\cdot}$ and $[Y(Pc)(Por)]^{\cdot}$, the detected radical exhibited easy saturation, typical of long T_1 times.

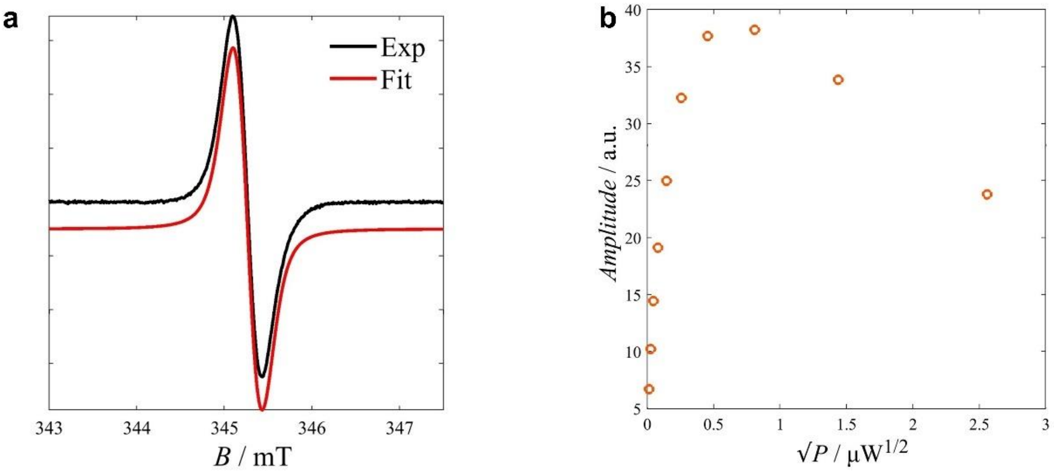

Figure 4.21. (a) CW-EPR spectrum (black) and its fitting (red). Experimental parameters: f_{MW} = 9.67742 GHz, $\Delta B_{1(pp)}$ = 0.1 mT, P_{MW} = 0.207 μW. (b) Integrated intensity as a function of MW power.

4.2.4. Magnetic property

CASSCF calculation

Before the magnetic study, CAS-SCF calculations were performed to predict the magnetic properties of **3-Tb** and **4-Tb**. For the calculation of both of them, modified crystal structures were used where phenyl groups on porphyrins were converted to methyl groups, and one of two terbium centers was converted to yttrium. First, a CASSCF (8, 7) calculation on **3-Tb** was performed considering all possible spin configurations S = 3, 2, 1, 0 with the maximum number of CI roots (**3-Tb** (full)). SOC was included with RASSI, and the magnetic properties were obtained using the SINGLE_ANISO routine. The thirteen m_J states in $J = 6$ are shown in Figure A1, which were characterized by a doubly-degenerated ground state which is well isolated from a doubly degenerated first excited state (~200 cm^{-1}). Two ground states are in a one-to-one mixture of |±6>, which hampers **3-Tb** to be a zero-field SMM (*vide infra*) (Table A1). This is due to the ligand field Hamiltonian, $\widehat{H}_{LF} = \Sigma B_k^q O_k^q$ (O_k^q are the Steven's operators) having non-negligible values of $B_k^{q\neq 0}$, which affects transverse anisotropy (Table A2).[143] The direction of the magnetic z axis was obtained for terbium, which is almost parallel to the axis of the molecule but slightly tilted (Figure A2). Next, the calculation on **4-Tb** was carried out. The approach of ref.[211,212] was taken, where a 9 in 8 CASSCF calculation was performed using only S = 7/2 and 5/2 and only the seven lowest CI roots for each state. This describes the situation where a Tb(III) ion is coupled (anti-)ferromagnetically to a radical, preventing electron transfer between the Tb ion and the ligand. The calculated states were shown in Figures 4.22 and A5, featuring 13 doubly-degenerate states, similar to the 13 states of **3-Tb**, with the ground states energetically separated from the first excited states. Note that with this method, the exchange coupling $J_{\text{Ln-Rad}}$ is inherently included. To estimate this value quantitatively, CASSCF calculation was performed on the same structure as **4-Tb**, but with one fewer electron (**4-Tb** dication). It gave an energy diagram similar to **3-Tb** or **4-Tb**, characterized by a pseudo-degenerated ground state (Figure 4.22, 5.4). Subsequently, by using the PHI program[213], the effect of exchange coupling on the energy diagram was estimated (Figure 4.22). The energy diagram from CASSCF was best reproduced when considering $J_{\text{Ln-Rad}} = -2.67\ cm^{-1}$ or 2.73 cm^{-1} (Figure 4.22). Furthermore, the satisfactory fit confirms that **4-Tb** can be treated as the sum of the radical and the **4-Tb** dication.

To prove the validity of the method used for **4-Tb** and **4-Tb** dication, a similar calculation on **3-Tb** was performed, using only 7 CI roots and only the highest spin state (**3-Tb** simplified). The comparison between the full and simplified calculation is shown in Figure 5.4, showing very similar results. Therefore, for consistency, the result from simplified calculation was used for further discussion.

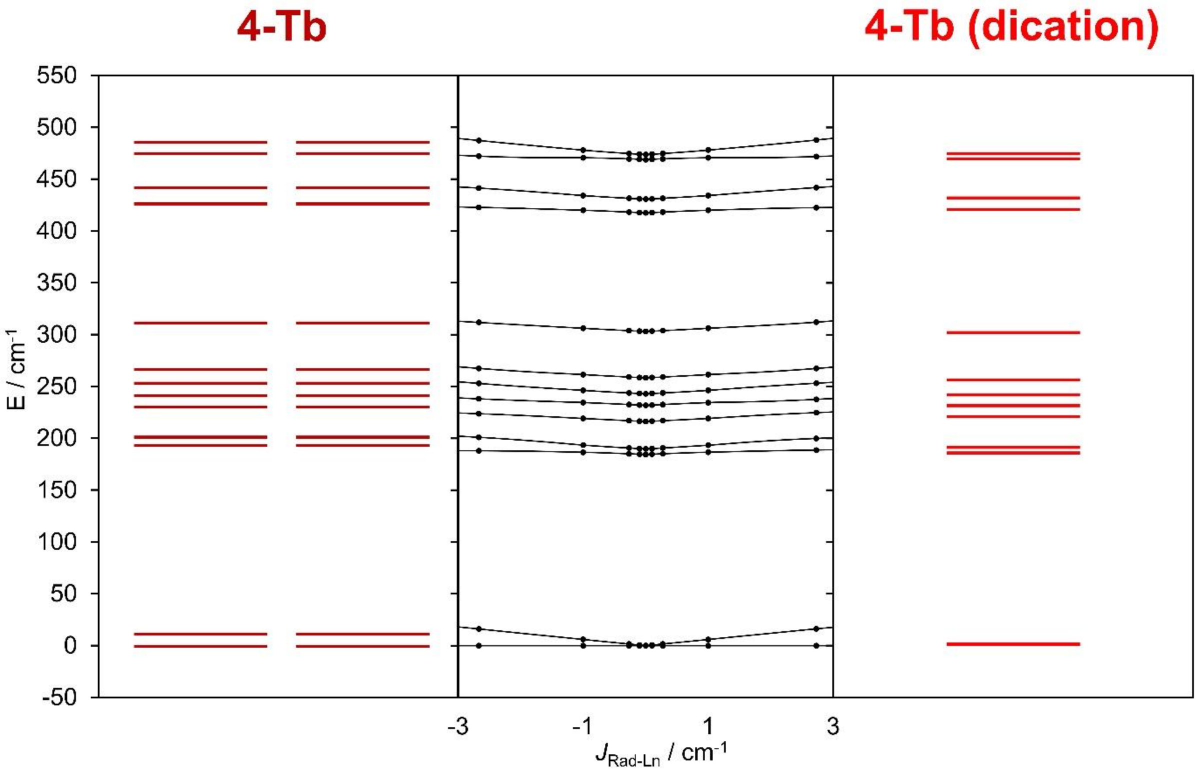

Figure 4.22. Calculated energy diagrams for **4-Tb** (left) and dication of **4-Tb** (right). The middle represent $J_{\text{Ln-Rad}}$ dependence of the energy diagram of **4-Tb** simulated using the PHI program[213].

Static magnetic property

In order to study the static magnetic behavior of **3-Tb** and **4-Tb**, DC magnetic susceptibility was measured on both of them in the temperature range from 300 K to 2 K under a DC field of 0.1 T (Figure 4.23 a,b). The value of χ_{m}T of **3-Tb** at 300 K was 24.9 $\text{cm}^3{\cdot}\text{K}{\cdot}\text{mol}^{-1}$, which is in good agreement with the value expected for two Tb^{3+} ions (23.6 $\text{cm}^3{\cdot}\text{K}{\cdot}\text{mol}^{-1}$)[95]. Upon cooling, χ_{m}T showed a slow decrease followed by an abrupt increase around 23 K, suggesting ferromagnetic coupling between two Tb^{III} ions. On the other hand, the χ_{m}T value of **4-Tb** at 300 K was 24.9 $\text{cm}^3{\cdot}\text{K}{\cdot}\text{mol}^{-1}$, which is also close to the expected value for two Tb^{3+} ions and one radical (24.0 $\text{cm}^3{\cdot}\text{K}{\cdot}\text{mol}^{-1}$). Likewise, the χ_{m}T of **3-Tb**, that of **4-Tb** also showed slow decrease upon cooling and abrupt increase at 28 K. Comparing the two plots, the one of **4-Tb** showed a slightly larger drop in the value of χ_{m}T with cooling, as well as larger rise in the low temperature regime, indicating enhanced $J_{\text{Ln-Ln}}$. In addition, magnetization versus field (*M*(*H*)) was measured on **3-Tb** and **4-Tb** in the field range of 0 – 7 T at 2, 3, 4, 5, 6, 7, 8, and 9 K (Figure 4.23 c,d). The $\chi_{\text{m}}T(T)$ and *M*(*H*) data were fitted simultaneously employing the crystal filed parameters obtained from CASSCF. For **3-Tb**, a variable single isotropic exchange gave satisfactory fitting, resulting in $J_{\text{Ln-Ln}} = 0.039\ \text{cm}^{-1}$. It is notable that $J_{\text{Ln-Ln}}$ is of the same magnitude as that of previously reported Tb_2Pc_3, Dy_2Pc_3 or $\text{Tb}_2\text{PcTPP}_2$ (0.097 cm^{-1}, 0.2 cm^{-1}

and 0.012 cm^{-1}, respectively).[138,184,214] On the other hand, for **4-Tb**, two variable single isotropic exchanges, $J_{Ln\text{-}Ln}$ and $J_{Ln\text{-}Rad}$ (Figure 4.23 b inset), were considered to give a satisfactory fitting with the parameters: $J_{Ln\text{-}Ln} = 0.025$ cm^{-1} and $J_{Ln\text{-}Rad} = –0.45$ cm^{-1}. While $J_{Ln\text{-}Ln}$ of **4-Tb** is similar to that of **3-Tb**, $J_{Ln\text{-}Rad}$ of **4-Tb** is in the same order of that of $TbPc_2$ and $GdPc_2$ ($J_{Ln\text{-}Rad} = –0.15$ cm^{-1} and 0.2 cm^{-1}, respectively) [179,215].

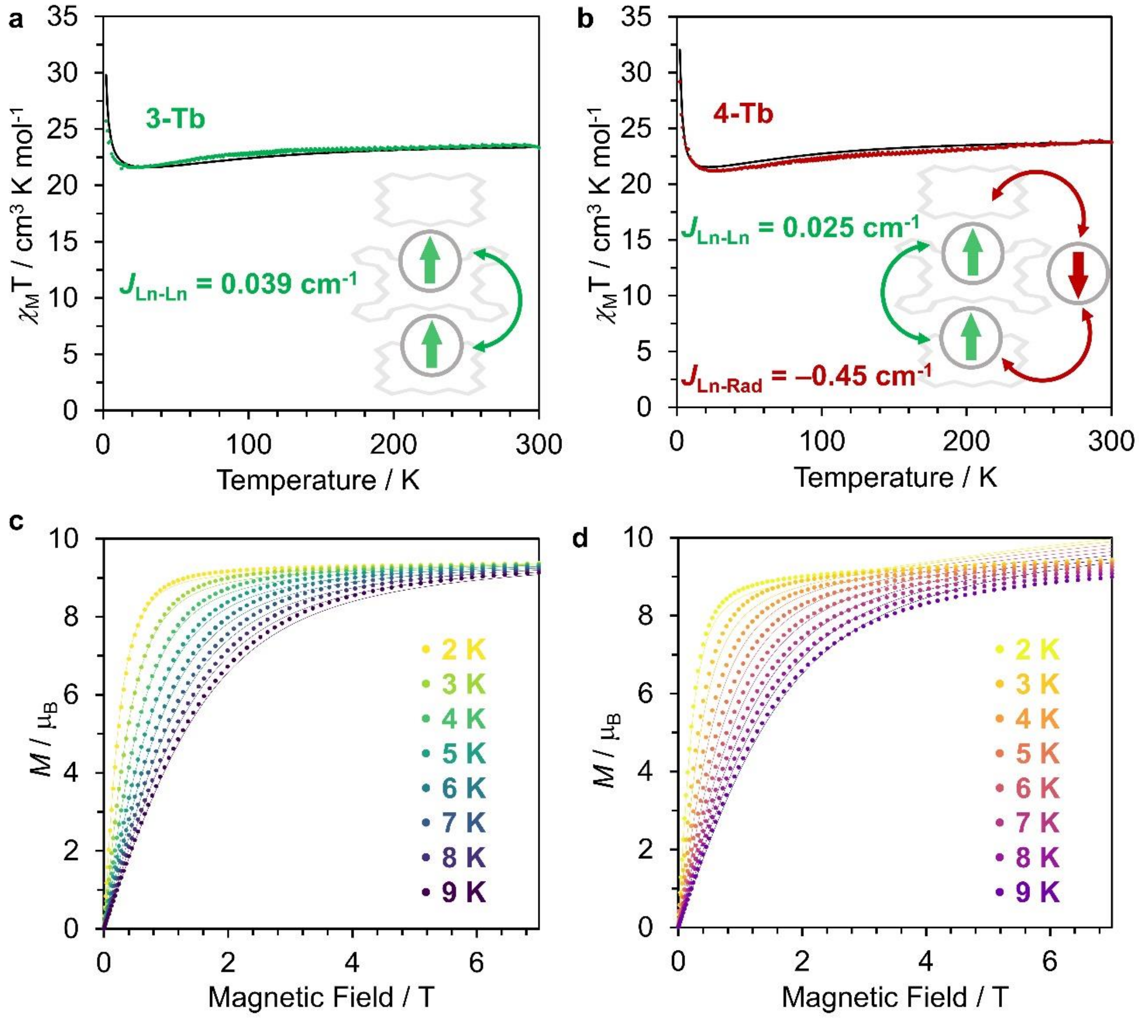

Figure 4.23. (a,b) Temperature dependence of $\chi_M T$ of **3-Tb** (a) and **4-Tb** (b). Circles in green and maroon represent the experimental data, while the black solid lines represent their fitting. (c,d) Magnetization versus field plots of **3-Tb** (c) and **4-Tb** (d). The solid lines represent their fitting. The color represents the measured temperature, as shown in the inset.

Dynamic magnetic property

AC magnetometry was performed on both **3-Tb** and **4-Tb** to investigate their dynamic magnetic properties. Initially, the field-dependence of χ_m” versus frequency plots at 2 K were investigated to decide the optimal field (Figure 4.24). The maximum was observed out of the measurement range (1-1000 Hz) in **3-Tb** (Figure 4.24 a). This was further verified through χ_m” versus frequency measurements of **3-Tb** at zero field, where the maximum was not observed in the scan window within the temperature range (Figure 4.25 a). Increasing the field, the peak was shifted to lower frequencies, which suggests that **3-Tb** is a field-induced SMM. The optimal field of 1500 Oe was decided based on the signal strength and frequency. Overall, the dynamic magnetic behavior of **3-Tb** is comparable to that of Tb_2PcTPP_2.[143] On the other hand, in the case of **4-Tb**, $\chi_M''(\nu)$ shows a peak even at zero field, revealing its zero-field SMM character (Figure 4.24d). As the field increases, the peak shifts to a higher frequency, suggesting the optimal field is zero. The substantial difference in the behaviors of **3-Tb** and **4-Tb** evidenced that the radical significantly affects the magnetic properties.

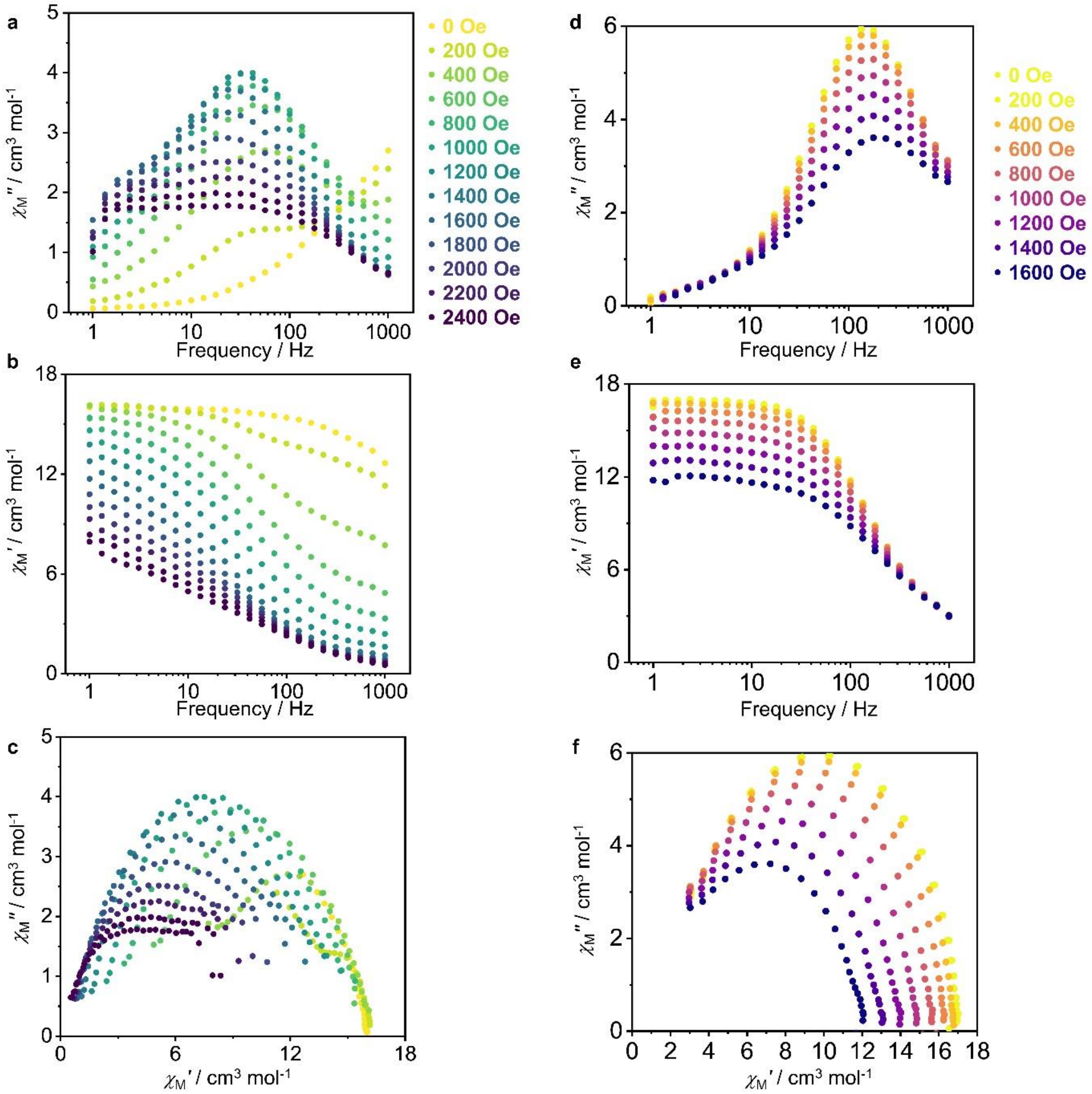

Figure 4. 24. Field-dependence of χ_M'' versus frequency (a), χ_M' versus frequency (b), and χ_M'' versus χ_M' (c) plots of **3-Tb**. Field-dependence of χ_M'' versus frequency (d), χ_M' versus frequency (e), and χ_M'' versus χ_M' (f) plots of **4-Tb**.

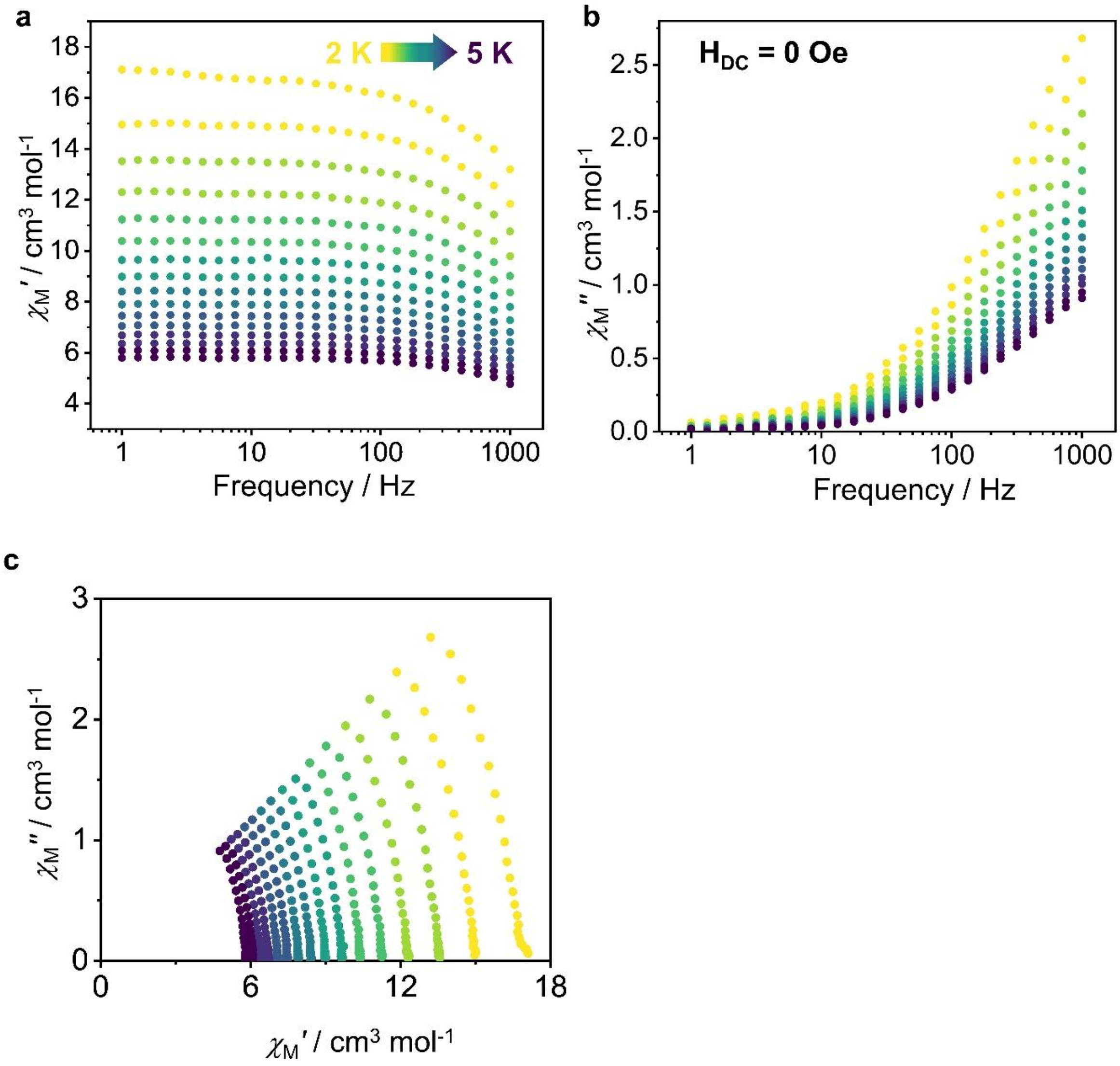

Figure 4. 25. Temperature-dependence of χ_M' versus frequency (a), χ_M'' versus frequency (b), χ_M' versus χ_M'' (c) of **3-Tb** measured at zero-field.

Afterward, the temperature-dependence of χ_m' and χ_m'' versus frequency was measured at 1500 Oe for **3-Tb** and zero-field for **4-Tb** (Figure 4.26). For **3-Tb**, the maximum in χ_m'' vs. T appeared around 10 Hz at 2 K, which showed a gradual shift to higher frequency upon heating and was observed up to 11 K. On the other hand, for **4-Tb**, the maximum was already around 100 Hz at 2 K, and was observable up to 3.95 K.

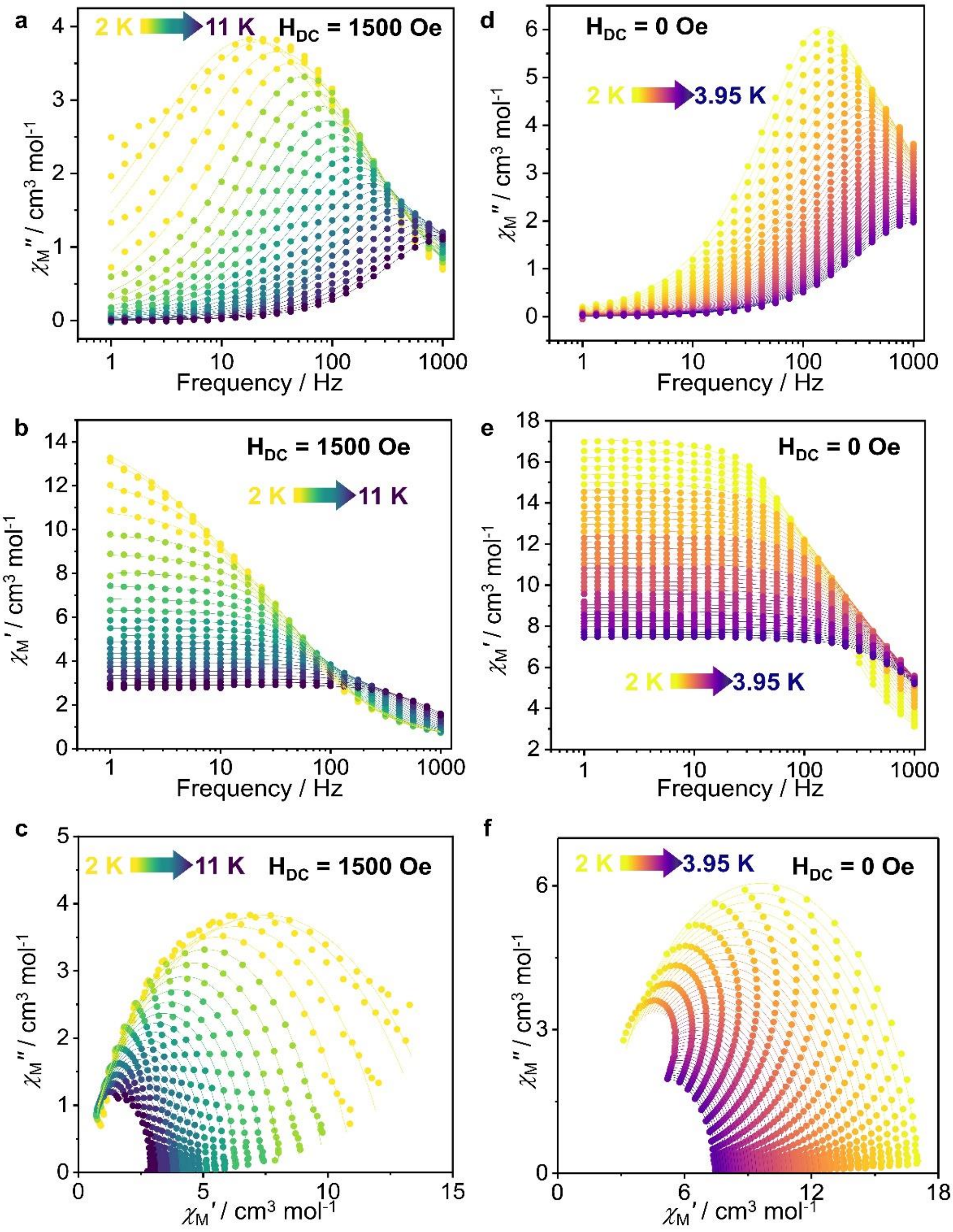

Figure 4. 26. Temperature-dependence of χ_M' versus frequency (a), χ_M'' versus frequency (b), χ_M' versus χ_M'' (c) of **3-Tb** measured at H_{DC} = 1500 Oe. Temperature-dependence of χ_M' versus frequency (d), χ_M' versus frequency (e), χ_M' versus χ_M'' (f) of **4-Tb** measured at zero DC field.

The obtained results were fitted with a generalized Debye model using CC-FIT2[181,182]. Figure 4.27 represents the relaxation time (τ in log scale) versus temperature (inverse) plot. The plot of **3-Tb** was fitted by using a combination of Orbach process and Raman process using the following equation:

$$\tau^{-1} = \tau_0^{-1} \exp\left(-\frac{U_{eff}}{T}\right) + CT^n \tag{4.1}$$

where the first term stands for the Orbach process, while the second represents the Raman process. It yielded the following parameters: $\tau_0 = (7.56 \pm 0.26) \times 10^{-6}$ s, $U_{eff} = 43.65 \pm 0.64$ K, $C = 40.75 \pm 2.01$ s^{-1}, $n = 1.71 \pm 0.03$. On the other hand, the plot of **4-Tb** was fitted with the Orbach process using the following equation:

$$\tau^{-1} = \tau_0^{-1} \exp\left(-\frac{U_{eff}}{T}\right) \tag{4.2}$$

It yielded the following parameters: $U_{eff} = 7.33 \pm 0.12$ K, $\tau_0 = (2.32 \pm 0.09) \times 10^{-5}$. Note that the plots show a slightly convex downward trend, which is attributed to the error (Figure 5.13).

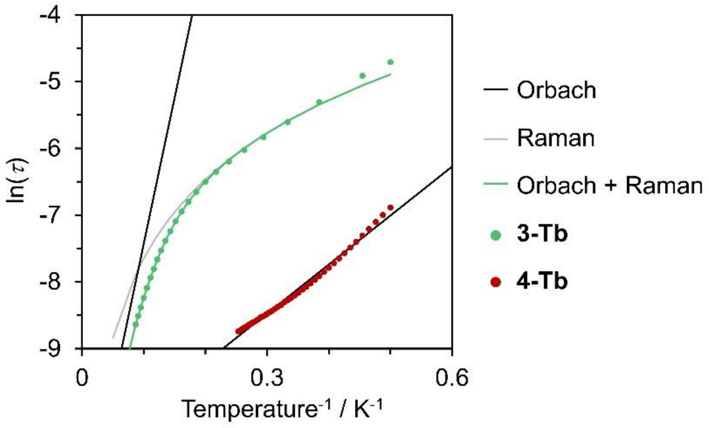

Figure 4.27. Relaxation time (ln(τ)) versus temperature (T^{-1}) plot of **3-Tb** and **4-Tb** (circles in green and maroon, respectively). The solid lines represent each process: Orbach $\tau^{-1} = \tau_0^{-1} exp\left(\frac{-U_{eff}}{T}\right)$ (black), Raman $\tau^{-1} = CT^n$ (grey), Orbach + Raman $\tau^{-1} = \tau_0^{-1} exp\left(\frac{-U_{eff}}{T}\right) + CT^n$ (green). The best-fit parameters are described in the manuscript.

To understand the magnetic property of **3-Tb**, a Zeeman diagram was simulated utilizing the crystal field parameters from CASSCF and the exchange coupling obtained in the fitting of static magnetic measurements (Figure 4.28). Under zero field, the doubly-degenerate ground states are an equal mixture of $|\pm 6, \pm 6\rangle$, a configuration commonly found in non-Kramers systems (Table 4.3). When a magnetic field is applied, the degenerate state undergoes Zeeman splitting, leading to the emergence of SMM behavior as fast tunnelling between the degenerate states is quenched. It is notable that although this Zeeman diagram explains the magnetic behavior well qualitatively, it doesn't match quantitatively, which was also true for the previously studied Tb_2PcTPP_2.[193]

In contrast, the doubly-degenerate ground states of **4-Tb** consist solely of $|+6,+6,-1/2\rangle$ or $|-6,-6,+1/2\rangle$, which is reasonably explained by the fact that **4-Tb** is a Kramers system (Table 4.3). The first excited states include $|+6,-6,+1/2\rangle$ and so on, characterized by antiferromagnetic coupling between the Tb centers. Remarkably, the energy gap between the ground states and the excited states (= 3.6 cm^{-1}) is in good agreement to the energy barrier U_{eff} of **4-Tb** (= 7.33 K = 5.09 cm^{-1}).

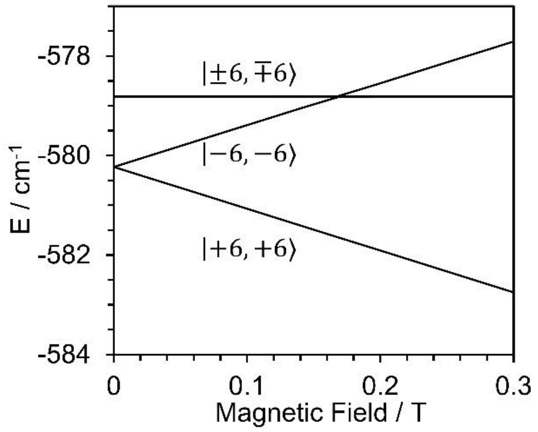

Figure 4.28. Zeeman diagram of **3-Tb**.

Table 4.3. Energy states and wavefunction composition of **3-Tb** and **4-Tb**.

	3-Tb		**4-Tb**	
state	ΔE(cm^{-1})	Wavefunction composition	ΔE(cm^{-1})	Wavefunction composition
1	0	50%|+6, +6⟩, 50%|-6, -6⟩	0	99.1%|+6, +6,-1/2⟩, 0.9%|-6, -6,+1/2⟩
2	0	50%|+6, +6⟩, 50%|-6, -6⟩	0	99.1%|-6, -6,+1/2⟩, 0.9%|+6, +6,-1/2⟩
3	1.42	50%|+6, -6⟩, 50%|-6, +6⟩	3.60	50%|+6, -6,-1/2⟩, 50%|-6,+6,-1/2⟩
4	1.42	50%|+6, -6⟩, 50%|-6, +6⟩	3.60	50%|-6, +6,+1/2⟩, 50%|+6,-6,+1/2⟩
5			3.60	2.3%|+6, -6,-1/2⟩, 47.6%|+6, -6,+1/2⟩, 2.3%|-6,+6,-1/2⟩, 47.6%|-6,+6,+1/2⟩
6			3.60	2.3%|+6, -6,+1/2⟩, 47,6%|+6, -6,-1/2⟩, 2.3%|-6,+6,+1/2⟩, 47.6%|-6,+6,-1/2⟩
7			5.41	100%|-6, -6,-1/2⟩
8			5.41	100%|+6, +6,+1/2⟩

4.3. Discussion and conclusion

Bis(porphyrinato)phthalocyaninato dinuclear rare-earth(III) molecules with thiomethyl functional groups were designed. One of the primary design objectives is to enhance bonding with gold electrodes. Due to the robust Au-S bond, thiol derivatives are widely used in molecular spintronics.[216–219] The designed molecules incorporate thiomethyl groups solely on the middle phthalocyanine ligands, allowing for selective junction configuration. In this regard, the molecules studied here are more suitable for spin transport than previously used Tb_2Pc_3. Future transport measurement will reveal its potential as a nuclear spin qudit with enhanced Hilbert space.

The neutral forms of the designed molecules, **3-Tb** and **3-Y**, were synthesized first. The synthesis route employed here is an optimized method for preparing lanthanide heteroleptic symmetrical [Por]Ln[Pc]Ln[Por] complexes (**3-Tb** and **3-Y)** by utilizing in situ-generated unstable intermediates to ensure regiospecific formation of the target complexes through selective interactions driven by electronic and charge density distributions. Both **3-Tb** and **3-Y** were characterized using UV-vis-NIR, IR spectroscopies, HR ESI-MS, and ^{1}H- and ^{13}C-NMR (only with **3-Y**). Cyclic voltammetry measurements on **3-Tb** and **3-Y** revealed their lowered oxidation potential compared to those of bis(porphyrinato)phthalocyaninato dinuclear rare-earth(III) derivatives, which proved the other design aim; redox state tuning by the introduction of electron donating groups.

3-Tb and **3-Y** were then converted into the corresponding cationic radicals (**4-Tb** and **4-Y**, respectively) by the addition of an equimolar amount of oxidation reagent (phenoxathiine hexachloroantimonate (V)). **4-Tb** and **4-Y** were characterized using UV-vis-NIR, IR spectroscopies, and HR ESI-MS. The UV-vis-NIR spectra of **4-Tb** and **4-Y** remained unchanged for over a week at room temperature in air, revealing their air stability. The presence of a radical was confirmed by EPR on **4-Y**. The amplitude got saturated quickly against increased MW power, indicating its long spin-lattice relaxation time(T_1). In the field of molecular electron-spin QIP, organic radicals have attracted increased attention because their small spin-orbital coupling tends to give long T_1.[53] Attempts have been made to use $[YPc_2]^0$ as an electron-spin qubit.[57,144] The result presented here may offer **4-Y** as a new platform of electron-spin qubit. Further pulsed EPR studies on **4-Y** are needed.

Single crystal XRD analysis of **3-Tb**, **3-Y**, **4-Tb**, and **4-Y** confirmed their symmetrical [Por]Ln[Pc]Ln[Por] configuration. Their mono-cationic character was confirmed by the 1:1 ratio of the complex to $SbCl_6^-$ in the lattice of **4-Ln**. To understand the magnetic property, some parameters were highlighted. First, **4-Tb** exhibited the elongation of the Tb-Tb distance in 0.01 Å, the contraction of the Por-Pc distance in 0.02 Å, and a smaller twisting angle in 3.45°. Previously, Horii *et al.*[140] revealed that upon two-electron oxidation ($[Tb_2Pc_3]^{0/2+}$), crystal parameters in Tb_2Pc_3 changed significantly, including the contraction of the Tb-Tb distance in 0.08 Å, the contraction of the Por-Pc distance in 0.07 Å, and a smaller twisting angle in 12.4°. They performed a CASSCF study and concluded that the contraction of Tb-Tb induced the decrease in the energy barrier U_{eff} (from 279 $\mathrm{cm^{-1}}$ to 217 $\mathrm{cm^{-1}}$). Considering the subtle difference in the crystal parameters, the effect of the crystal field on the difference in the energy barriers between **3-Tb** and **4-Tb** is expected to be limited. On the other hand, the nearest intermolecular Tb ··· Tb distance was 13.1 Å for **3-Tb** while 12.7 Å for **4-Tb**. Similar to the previously reported $Tb_2Pc(TPP)_2$,[143] it can be inferred that they are sufficiently distant from each other, allowing to disregard the intermolecular Tb ··· Tb magnetic interaction. Furthermore, the phenyl groups perpendicular to the porphyrin plane and the lattice solvents make intermolecular distanbce isolated (Figure 4.18 d, 4.19 d), suggesting that the intermolecular radical ··· radical magnetic interaction is also negligible.

The magnetic properties of **3-Tb** and **4-Tb** were investigated using CASSCF calculations and bulk magnetometry. The $\chi_{\mathrm{m}}T(T)$ and $M(H)$ plots showed different behavior between **3-Tb** and **4-Tb**. The fitting of **3-Tb** was performed using Steven's coefficients obtained in CASSCF, giving isotropic exchange coupling of $J_{\mathrm{Ln\text{-}Ln}} = 0.039\ \mathrm{cm^{-1}}$ for **3-Tb**. On the other hand, the fitting was performed for **4-Tb** using the result of CASSCF of the dication of **4-Tb**, yielding $J_{\mathrm{Ln\text{-}Ln}} = 0.025\ \mathrm{cm^{-1}}$ and $J_{\mathrm{Ln\text{-}Rad}} = –0.45\ \mathrm{cm^{-1}}$. The dynamic magnetic properties of **3-Tb** and **4-Tb** differ significantly. The field-dependence of χ_{m}'' versus frequency plots revealed that **3-Tb** was a field-induced SMM while **4-Tb** was a zero-field SMM. In addition, the temperature-dependence of the χ_{m}'' versus frequency plots and their fitting was performed on **3-Tb** and **4-Tb**. That of **3-Tb** was fitted with the combination of Orbach and Raman processes. The plot of **3-Tb** resembles to that of $Tb_2Pc(TPP)_2$, where the value of U_{eff} is also similar ($U_{eff} = 43.65 \pm 0.64$ K for **3-Tb** while $U_{\mathrm{eff}} = 25.9$ - 34.6 K for $Tb_2Pc(TPP)_2$). On the other hand, the plot of **4-Tb** was fitted solely with Orbach process to give $U_{eff} = 7.33 \pm 0.12$ K. Overall, **3-Tb** and **4-Tb** showed a significant difference in magnetic properties, represented by the switch from field-induced SMM behavior of **3-Tb** to zero-field SMM behavior of **4-Tb**. As mentioned in the introduction part, varieties of radical-bridged dinuclear lanthanide SMMs have been investigated for the improvement of SMM properties. The key distinction between them and **4-Tb** lies in the fact that those studies are aiming to disperse the spin distribution of radicals, reaching into the deeply buried 4f orbitals of Ln centers.[105] Contrary to that, as EPR studies revealed, **4-Tb** have radical spin density solely on the ligands. As a consequence, $J_{\mathrm{Ln\text{-}Rad}} = –0.45\ \mathrm{cm^{-1}}$ of **4-Tb** is much smaller than that of other reported examples, for instance, $J_{\mathrm{Ln\text{-}Rad}} = –10\ \mathrm{cm^{-1}}$ for $[(Cp^*{}_2Gd)_2(\mu\text{-bpym}^{\cdot})]^{+}$.[116] In terms of weak exchange coupling, **4-Tb** is better compared to the $[TbPc_2]^0$ species. As explained in Section 1.4, the superior SMM properties of $[TbPc_2]^0$ over $[TbPc_2]^-$ are attributed to the difference in the ligand field associated with the structural difference, as well as the suppression of QTM via the exchange-bias.[106,141,173] As discussed above, the difference of the LF in **3-Tb** and **4-Tb** are negligible; instead, the Exchange-bias and the Kramers/Non-Kramers switch are likely the main contributing factors.

In summary, to achieve better bonding to gold electrodes and lower oxidation potential, bis(porphyrinato)phthalocyaninato dinuclear rare-earth(III) molecules were designed, which were functionalized with thiomethyl group solely on Pc rings. The development of these molecules led to several key outcomes:

1. The target molecule (**3-Ln**) was synthesized and characterized , with cyclic voltammetry confirming lowered oxidation potential
2. **3-Ln** was converted into a monoradical (**4-Ln**) , demonstrating air stability for over a week.
3. EPR analysis on **4-Y** confirmed the presence of a π radical, highlighting its potential as an electron spin qubit.
4. Bulk magnetometry on **3-Tb** and **4-Tb** revealed a transition from a field-induced SMM (**3-Tb**) to a zero-field SMM (**4-Tb**).

Those findings open avenues for future studies on organic radical-based electron spin qubits and enhancement of SMM properties. Among all, the study of nuclear spin qudits is of primary interest. The results revealed the radical is weakly coupled to both terbium ions equally. In addition, the thiomethyl group’s strong bonding affinity with gold makes **3-Tb** promising for spin transport measurements.

Conclusive Remark

This thesis aimed at the investigation of the effect of an additional radical on the properties of bis(phthalocyaninato) lanthanide(III) and bis(phthalocyaninato)porphyritnato bis-lanthanide(III) complexes. To this end, three systems were thoroughly investigated, as explained in Chapter 2, 3, and 4.

Chapter 2 described a diradical based on $[YPc_2]^0$ incorporated with an isoindoline-based nitroxide radical. Because of the long spin-lattice relaxation time T_1 of $[YPc_2]^0$, this study was initiated for the purpose of the construction of a CNOT gate. The isoindoline-based nitroxide radical was chosen for its structural rigidity and stability against reaction temperature. The diradical **1** was synthesized and characterized with various techniques, including UV-vis-NIR absorption spectroscopy, IR spectroscopy, ESI-mass spectrometry, and cyclic voltammetry. The CW-EPR spectrum of a fluid solution sample was fitted to give the spin Hamiltonian parameters, such as asymmetric g values (g_{NO} = 2.0060, g_{pc} = 2.0023), hyperfine couplings ($A_{N\text{-}NO}$ = 40.74 MHz, $A_{H\text{-}NO}$ = 0.67 MHz), and an exchange coupling $|J|$ = 0.014 cm^{-1}. On the other hand, the CW-EPR spectrum of the frozen solution didn't give satisfactory fitting due to inapplicability of the point dipole model. The pulsed EPR spectra (FSED) differed significantly from CW-EPR, attributed to two factors: independent relaxation of the two spins and intermultiplet transition. The former was excluded through a combination of saturation recovery, echo-decay, and Laplace transformation of FSED spectra. Both of them revealed unique T_1 and T_m, and anisotropy, similar to the nitroxide radical. This behavior is well explained by the sequential mechanism where faster relaxing species (nitroxide radical) accelerate the relaxation of slower relaxing species ($[YPc_2]^0$ radical). The FSED measurements at varying amplitudes revealed peak shifts, with spin nutation at different fields showing three oscillations: one is associated with ^{1}H enveloped and the others are Rabi oscillations. The ratio of the magnitude of these oscillations is close to $\sqrt{2}$, which is expected to be attributed to S = 1 and S = ½. The gap is attributed to intramultiplet (singlet-triplet transition), and it gives dipolar coupling D = 53.7 MHz. The similar J and A create a closely-packed spin ladder, which makes **2** challenging to apply as a CNOT gate. On the other hand, the capability to arbitrarily control two transitions makes it well-suited for qutrit applications.

Chapter 3 examined the terbium analogue of compound **1** (**2**) to examine its effects on SMM properties and its potential as a molecular qubit. Compound **2** was characterized using the same techniques as **1**, confirming both radicals remained intact. DC magnetometry validated the magnetic purity of **2**, and three parameters necessary to discuss SMM properties, U_{eff}, T_B and H_c, were obtained from hysteresis loop measurement and AC susceptibility with fitting analysis. The blocking temperature was discussed from both hysteresis and AC measurements, showing that **2** is comparable with other $[TbPc_2]^0$ derivatives. H_c was zero even at 2K, unlike for the $[TbPc_2]^0$ dimer. AC susceptibility and fitting revealed its nature of relaxation which was mainly dominated by Orbach and Raman processes. U_{eff} was 677 K, which is in the range of $[TbPc_2]^0$. Overall, **2** was characterized with unchanged magnetic properties from $[TbPc_2]^0$. As an outlook, the potential of **2** as a molecular qubit was discussed. The situation where two radicals and SMM behavior coexist in one molecule is analogous to the qubit gate system studied by STM-EPR, hence **2** would be an intriguing target of STM EPR studies.

Chapter 4 described a radical in bis(porphyrinato)phthalocyaninato dinuclear rare-earth(III) complexes (**4-Ln**). The goal was to introduce the function of a π radical in this inherently radical-free structure. The thiomethyl group was chosen for its good connection to gold electrodes and electron-donating properties. Initially, the neutral form (**3-Ln**) was synthesized and characterized with various spectroscopic techniques. Cyclic voltammetry of **3-Ln** revealed their narrower HOMO-LUMO gaps than those of other bis(porphyrinato)phthalocyaninato dinuclear rare-earth(III) derivatives. Encouraged by this result, **3-Ln** was converted into cationic radicals (**4-Ln**) by mixing with an equimolar amount of oxidation reagent. **4-Ln** was characterized by UV-vis-NIR abs. spectroscopy, IR spectroscopy, and ESI-mass spectrometry. UV-vis-NIR spectra remained unchanged for one week in air at room temperature, suggesting their air stability. CW-EPR spectra for **4-Y** displayed a signal at g = 2.002, confirming the radical's presence. The EPR signal intensity saturated quickly with increased MW power, indicating a long spin-lattice relaxation time. Each sample yielded crystals suitable for sc-XRD analysis, which revealed the isostructural character of **3-Tb** and **3-Y**, and **4-Tb** and **4-Y**, respectively. The fittings of DC susceptibility and M(H) measurements gave the exchange interactions quantitatively: $J_{\text{Ln-Ln}}$ = 0.039 cm^{-1} for **3-Tb**, while $J_{\text{Ln-Ln}}$ = 0.025 cm^{-1} and $J_{\text{Ln-Rad}}$ = –0.45 cm^{-1} for **4-Tb**. AC susceptibility measurements revealed the switch from a field-induced SMM (**3-Tb**) to a zero-field SMM (**4-Tb**). Ab initio calculation indicated that this was due to the exchange-bias and/or the shift from a non-Kramers system to a Kramers system. This study represents the first bulk magnetic study of radical-bearing dinuclear complexes with porphyrin or phthalocyanine ligands, offering valuable insights for fields such as radical-based electron-spin qubits and radical-bridged dinuclear lanthanide SMMs. Notably, the potential application as nuclear-spin qudits is promising.

These thorough bulk-phase studies have highlighted the function of additional radicals, represented by the potential of $[\text{YPc}_2]^0$ based diradicals for use as either a CNOT gate or qutrit, or the switchable magnetic property with and without a radical in bis(porphyrinato)phthalocyaninato dinuclear rare-earth(III) complexes. They will also lead future single-molecule studies. As described in Chapter 3, **2** has a potential to be the first molecular Heinrich's qubit. This will liberate molecular design from the limited varieties of g values, and make it possible to construct higher quantum logic gates, such as CCNOT gates. Currently, the deposition of **2** with electrospray is under investigation. On the other hand, the good connection between Au-S and the understanding on $J_{\text{Ln-Rad}}$ makes **3-Tb** advantageous against Tb_2Pc_3. Therefore, it is promising as a new material for nuclear spin qudits. Spin-transport measurements on this molecule are planned. In the end, the results of this thesis will lead to future studies, paving a new way for QIP.

Chapter 5. Experimental Details

5.1. Experimental Section for Chapter 2

As explained in Chapter 2, the contents in this section are based on the published paper: "J. Komeda, A. K. Boudalis, N. Montenegro-Pohlhammer, C. Antheaume, A. Mizuno, P. Turek, M. Ruben. Selective Transition Enhancement in a G-Engineered Diradical. *Chem. Eur. J.* **2024**, *202400420*. https://doi.org/10.1002/chem.202400420." The figures and tables represented in this section are reproduced from the original paper under the terms of the CC BY-NC-ND 4.0 license (https://creativecommons.org/licenses/by-nc-nd/4.0/).

5.1.1. Materials and Methods

All reagents and solvents were of commercial grade and were used without further purification unless otherwise stated. Tetra-*n*-butylammonium hexafluorophosphate ($n\mathrm{Bu_4NPF_6}$) was purchased from Sigma–Aldrich and recrystallized from hot ethanol, then dried in vacuo. Bis(phthalocyaninato)yttrium(III) complex (**1**) was synthesized following the literature method.[90]

FTIR spectra were measured with an ATR detector by using Nicolet iS50 FT-IR spectrometer Thermo Fischer. UV-Visible-NIR spectra were taken on a Cary 500 Scan UV-Vis-NIR Spectrophotometer. TD-DFT calculations were performed using the Gaussian 16 Revision C.02 program package.[220] ^{1}H-NMR spectra were obtained using Bruker Avance 500 MHz NMR spectrometer. Specific conditions are described in the relevant sections.

ESI-MS (KIT) was observed using MicroTOF-Q II Bruker. ESI-HRMS (ISIS) was measured using Orbitrap Exactive Plus with Extend Mass Range: Source HESI II from ThermoFicher. The samples that didn't require separation or additional sample preparation were therefore placed in a syringe and pushed at a defined flow rate of 12 μL min^{-1} by a syringe pump through transfer tubing directly to the ESI source.

Cyclic voltammetry (CV) was performed using Gamry Interface 1010 E electrochemical analyzers at room temperature (25 °C). Cyclic voltammograms were measured in a 0.1 M $n\mathrm{Bu_4NPF_6}$ solution of $\mathrm{CH_2Cl_2}$ as a supporting electrolyte solution with scan rates of 100 mVs^{-1} with the concentration of 0.5 mM for nitroxide-functionalized $\mathrm{YPc_2}$ (**1**) and $[\mathrm{NO}\ ]^{\cdot}$dibromobenzene (**SM3**), and as a saturated solution (less than 0.5 mM) for $[\mathrm{YPc_2}]^0$. The solutions were bubbled with argon flow for more than 10 minutes before the measurements, and kept under argon atmosphere during the measurements. A glassy carbon electrode with a radius of 3 mm, a Pt wire, and an $\mathrm{Ag^+/Ag}$ reference electrode (10 mM $\mathrm{AgNO_3}$ in 0.1 M $n\mathrm{Bu_4NClO_4/CH_3CN}$) was used as a working electrode, a counter electrode, and a reference electrode, respectively. The $\mathrm{Fc^+/Fc}$ redox couple was used as an internal standard.

5.1.2. Synthesis

All the syntheses were performed under inert atmosphere, unless otherwise stated. Each compounds were synthesized in the following procedure.

Synthesis of SM1

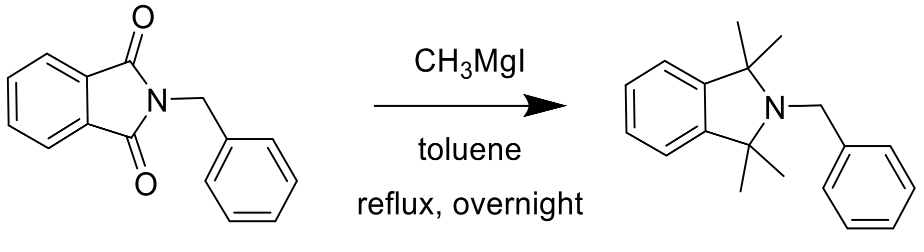

SM1

SM1 was synthesized according to the previous report with a small modification.[150] In a three-neck flask connected to a condenser with a magnetic stirrer, 200 mL of a solution of CH_3MgI in diethyl ether (0.400 mol) was added, which was dried into vacuo. In a separate Schlenk flask, 24.1 g of 2,3-Dihydro-1,1,3,3-tetramethyl-2-(phenylmethyl)-1*H*-isoindole (0.102 mol) was added and dissolved into 250 mL of toluene. This solution was transferred to the three-neck flask via cannular, and the mixture was heated to reflux and stirred for 16 hours. After cooling down to room temperature, the reaction mixture was filtered through Celite. The obtained solution was condensed, then re-diluted with hexane, followed by silica-gel column chromatography (eluent: hexane 100%) to yield white crystalline powder (8.1 g, yield: 30.0%).

^{1}H-NMR ($CDCl_3$, 500 MHz, δ in ppm): δ = 1.30 (s, 2H), 3.99 (s, 2H), 7.11-7.16 (m, 2H), 7.18-7.30 (m, 5H), 7.44-7.48 (m, 2H). ^{13}C-NMR ($CDCl_3$, 500 MHz, δ in ppm): δ = 28.4, 46.2, 65.2, 121.3, 126.4, 126.7, 127.9, 128.3, 143.5, 147.9.

Synthesis of SM2

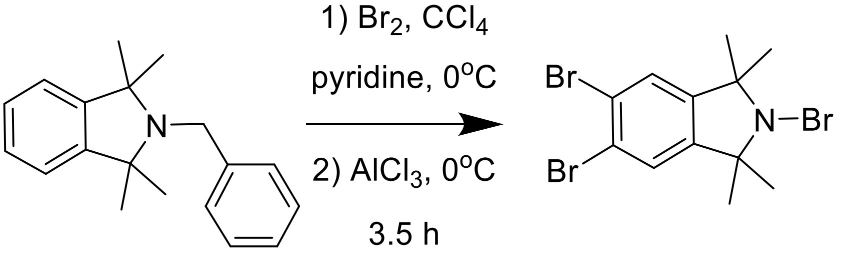

SM1 **SM2**

SM2 was synthesized following the reported method with some modifications.[151] In a three-neck flask with a magnetic stirrer equipped with NaOH aqueous solution trap, 2.50 g of **SM1** (9.51 mmol), 50 mL of CCl_4, and 280 μL of pyridine were added and stirred vigorously. The solution was cooled to 0°C for 1 hour, and 7.5 mL of bromine was added dropwise. After 20 minutes, 8.04 g (60.0 mmol) of anhydrous $AlCl_3$ was added to the solution. The mixture was stirred for 3.5 hours, and then basified with an aqueous solution of KOH. The mixture was extracted with DCM, and then washed with water, followed by drying over Na_2SO_4. After drying into vacuo, the crude mixture was purified with silica-gel column chromatography (eluent: hexane/ethyl acetate/acetic acid = 96/3/1) to yield a yellowish crystalline powder (2.83 g, yield: 72%).

^{1}H-NMR ($CDCl_3$, 500 MHz, δ in ppm): δ = 1.45 (s, 12H), 7.42 (s, 2H). ^{13}C-NMR ($CDCl_3$, 500 MHz, δ in ppm): δ = 28.0, 69.5, 123.2, 127.1, 145.4.

Synthesis of SM3

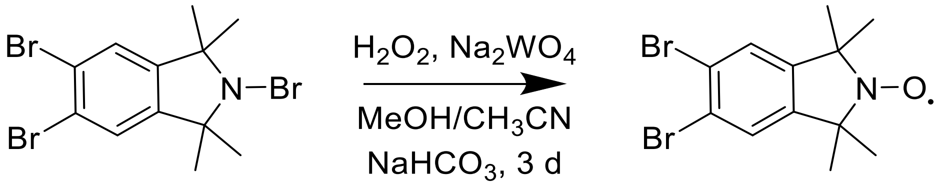

SM2 **SM3**

SM3 was synthesized similarly to the previous report.[151] 5.65 g of **SM2** (16.2 mmol) was dissolved into a mixed solvent of methanol (350 mL) and acetonitrile (11 μL). To the solution, 2.12 g of $NaHCO_3$ (25.2 mmol), 895 mg of $Na_2WO_4{\cdot}2H_2O$ (2.70 mmol), and 18 mL of H_2O_2 (160 mmol) were added, and the mixture was stirred vigorously for 2 days. Afterwards, the reaction was quenched with water, and extracted with DCM. The DCM solution was washed with brine and then dried into vacuo to yield a yellowish crystal (2.10 g, yield: 19 %).

HRMS (ESI-Tof) calcd. (%) for $C_{12}H_{14}Br_2NO$: 347.9417, found: 347.9544.

Synthesis of [NO]$^{\cdot}$PN

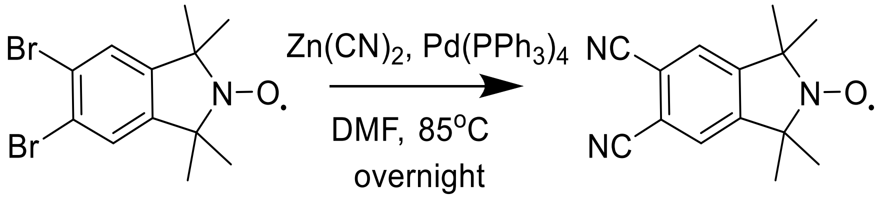

SM3 **[NO]$^{\cdot}$ PN**

The synthesis of **[NO]$^{\cdot}$PN** was conducted according to the previous reports with slight modifications.[146] Prior to the use, the glasswares used here were dried in an oven at 120°C to remove water. 8 mL of anhydrous DMF was degassed in a freeze-pump-thaw cycle, which was repeated three times. To a Schlenck flask with a stirring bar filled with argon, 526 mg of **SM3** (1.50 mmol), 1.72 g of $Zn(CN)_2$ (14.7 mmol), and 1.68 g of $Pd(PPh_3)_4$ (1.45 mmol) were introduced, which were subsequently dissolved into 8 mL of DMF. The mixture was heated up to 85°C and stirred vigorously for 2.5 days. Afterwards, the reaction was cooled down to room temperature, and quenched by the addition of 40 mL of aqueous solution of NH_3 (8%). The mixture was extracted with DCM and washed with NH_3 aq. After drying under vacuo, the crude was purified by silica-gel column chromatography (eluent: hexane/ethyl acetate = 7/3) to yield yellow powder (189 mg, yield: 52.5%). IR spectrum of $[NO]^{\cdot}PN$ is shown in Chapter 2 manuscript.

Synthesis of YPcOAc

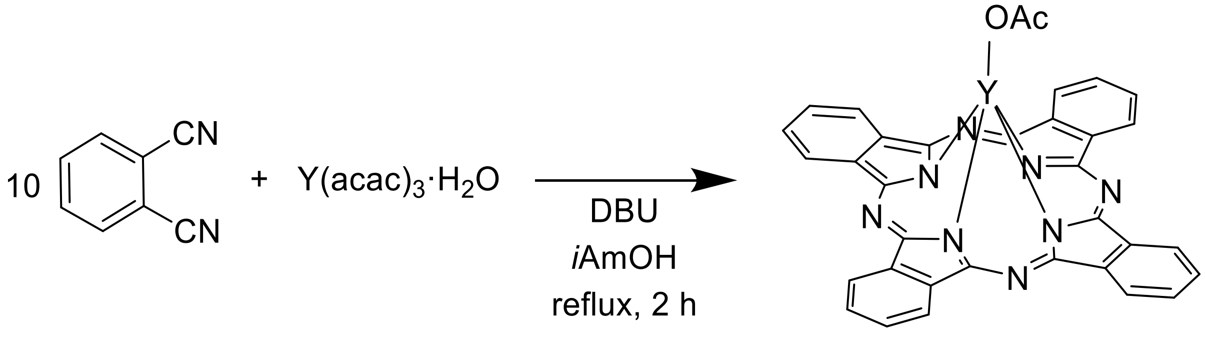

YPcOAc

YPcOAc was synthesized in a similar way as the previously reported method.[152] Under an argon atmosphere, phthalonitrile (816 mg, 6.38 mmol), yttrium(III) acetate (266 mg, 0..689 mmol) were dissolved into 15 mL of 1-hexanol. After adding 0.9 mL of 1,8-Diazabicyclo[5.4.0]undec-7-ene, the solution was heated to reflux, stirring vigorously for 2 h. The reaction mixture was dried *in vacuo*, and purified with silica gel column chromatography. The first fraction was eluted with 100% $CHCl_3$, mainly composed of $[YPc_2]^0$. After removing $[YPc_2]^0$, the fraction consisting of YPcOAc was eluted with $CHCl_3$ containing 5% of CH_3OH. The solvent was removed in vacuo to give a blue solid of YPcOAc (280 mg, yield: 10%).

Synthesis of 1

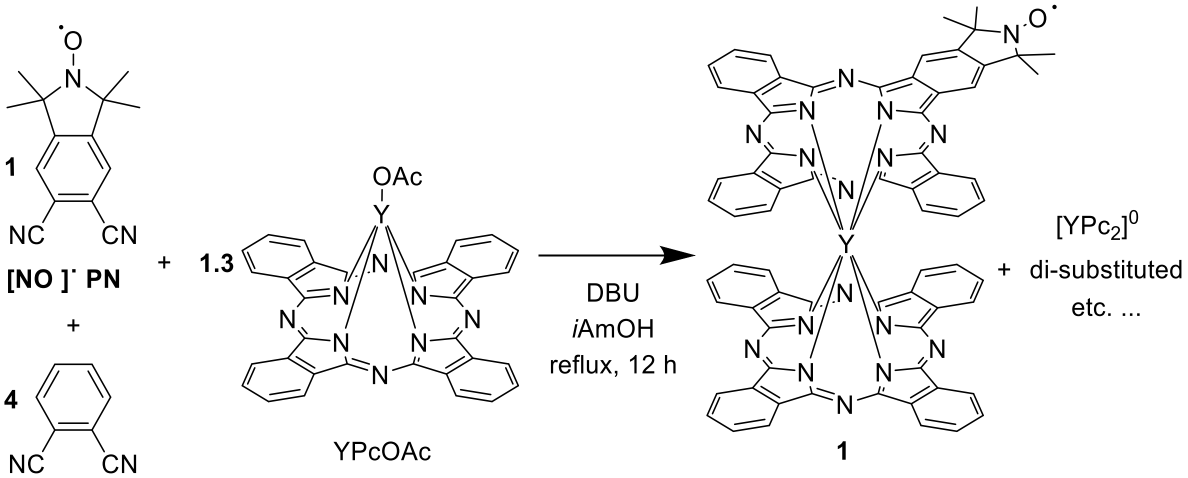

[NO]˙PN (54 mg, 0.228 mmol), phthalonitrile (116 mg, 0.91 mmol), and YPcOAc (209 mg, 0.30 mmol) were dissolved into 9 mL of isoamyl alcohol. After adding 1.65 μL of 1,8-Diazabicyclo[5.4.0]undec-7-ene, the mixture was heated to reflux, stirring vigorously for 12 h. The reaction mixture was dried in vacuo, and purified with repeated silica gel column chromatography (eluent; $CHCl_3$ with 1% of Et_3N). The obtained material was further purified by reprecipitation in $CHCl_3$/MeOH to yield a dark green powder of **2** (45 mg, 16%). Note that crystallization of **2** was attempted by slow evaporation in CH_2Cl_2, $CHCl_3$, or by slow diffusion in $CHCl_3$/Hexane, CH_2Cl_2/Hexane, $CHCl_3$/MeOH, CH_2Cl_2/MeOH, toluene/MeOH, toluene/Acetonitrile, $C_2H_4Cl_2$/Heptane, $C_2H_4Cl_2$/MeOH, in all of which crystal was not obtained. The detail of the characterization was described in Chapter 2 manuscript. HRMS(ESI): calcd (%) for $C_{70}H_{42}N_{17}OY$: 1225.2811, found 1225.2701.

5.1.3. Computational Studies

Magnetic properties

The Spin Hamiltonian (SH) is a particular case of effective Hamiltonian, used to study the interaction between any kind of spin carrier. In this model, all orbital coordinates are removed and replaced by only spin coordinates. For two magnetic centres in the absence of an external magnetic field it can be written as:

$$\hat{H} = -J\hat{S}_1 \cdot \hat{S}_2 + D\sum_{i=1,2}\left[\hat{S}_{i,z}^2 - \frac{1}{3}S(S+1)\right] + E\sum_{i=1,2}\left[\hat{S}_{i,x}^2 - \hat{S}_{i,y}^2\right] \tag{5.1}$$

Where $\hat{S}_i$ are the local spin operators, J is the isotropic coupling constant, D and E are the single-ion axial and rhombic zero-field splitting parameters, respectively, and S is the global spin of the system. In most cases the first term is dominant, and the remaining is included as perturbations, in this case, the SH is reduced to:

$$\hat{H} = -J\hat{S}_1 \cdot \hat{S}_2 \tag{5.2}$$

also known as the ‘‘Heisenberg–Dirac–Van-Vleck Spin-Hamiltonian” (HDVV). The energy of each state with total spin S is given by:

$$E(S) = -\frac{J}{2}[S(S+1) - S_1(S_1+1) - S_2(S_2+1)] \tag{5.3}$$

where the energy between adjacent spin levels can be expressed as:

$$E(S-1) - E(S) = JS \tag{5.4}$$

and J can be computed as:

$$J = \frac{E(S-1) - E(S)}{S} \tag{5.5}$$

All density functional theory (DFT) and wave function WFT based (WFT) calculations were performed by using the ORCA software package[221], employing a def2-TZVP basis set[222] to represent all the atoms in the structure.

Density functional theory (DFT) calculations

By means of the DFT, the isotropic coupling constant *J* was calculated for the **1** complex using the Broken Symmetry (BS) method introduced by Noodleman[223], using the B3LYP hybrid exchange correlation (XC) functional[224]. The orbitals used for the High Spin (HS) state were obtained from SCF optimization of the S = 1, M_S = 1 unrestricted determinant. The BS determinant is constructed by taking the HS determinant as a reference and flipping the spin density localized on the inner 16 C atoms (Figure S8 c,d), followed by the corresponding SCF energy optimization. The magnitude of the coupling constant *J* is then calculated in terms of the energy $E_{HS,BS}$ and the spin expectations value $\langle S^2 \rangle_{HS,BS}$ of this two determinants, using the expression proposed by Yamaguchi *et al.*[225]:

$$J = \frac{2(E_{BS} - E_{HS})}{\langle S^2 \rangle_{HS} - \langle S^2 \rangle_{BS}} \tag{5.6}$$

Wave function based (WFT) calculations

The exact energy and wave functions of each spin state on both complexes were determined through the state average complete active space self-consistent field (SA-CASSCF) methodology.[226] To consider the effects of dynamic correlation, the N-Electron Valence State Perturbation Theory (NEVPT2) method[227] was employed in subsequent calculations using the converged SA-CASSCF wavefunction as the reference. In all WFT-based calculations, the resolution of the identity approximation (RI)[228] was adopted.

Geometry Optimizations

The molecular structure of **1** was optimized through the DFT methodology, utilizing the Perdew–Burke–Ernzerhof (PBE) exchange-correlation. Dispersion interactions were treated with the DFT-D3 atom-pairwise correction[229,230]. Optimized molecular coordinates are shown Appendix:

5.1.4. EPR studies

Materials and methods

All EPR spectra were recorded from $CD_2Cl_2/CDCl_3$ 4:1 solutions.

Room-temperature fluid solution EPR spectra from 0.05 mM solutions were recorded on a Bruker ESP300 spectrometer using a Bruker 4102ST rectangular cavity operating in the TE_{102} mode. The solutions were deoxygenated under an argon stream, transferred to 100 μL glass capillaries (Hirschmann) and sealed from both ends with sealing wax.

Frozen solution experiments were carried out on 0.1 mM solutions. The solutions were deoxygenated with freeze-pump-thaw cycles, and flame-sealed under a helium atmosphere in the EPR tubes. CW EPR spectra on the X-band were collected on a Bruker ELEXSYS E580 spectrometer, fitted with an upgraded ESP1010 microwave bridge, a 1 kW TWT amplifier and a Bruker ER4118X-MD-5W dielectric resonator. Based on previous calibration, the maximum B_1 (0 dB attenuation) is 1.1 mT. Q-band CW spectra were recorded on an EMXplus spectrometer fitted with an EMX premiumQ microwave bridge and an ER5106QTW microwave resonator operating in the TE_{012} mode and controlled by the Bruker Xenon software. The magnetic field was applied by a Bruker BE25 electromagnet using a Bruker ER082(155/45)Z power supply. In both cases, for low-temperature experiments the resonators were fitted in Oxford CF935 dynamic continuous flow cryostats and the temperature was regulated with Oxford servocontrols (Mercury iTC and ITC503, respectively).

Pulsed EPR spectra were collected on the above mentioned ELEXSYS spectrometer. FSED spectra were detected by monitoring the integrated intensity of the Hahn echo ($\pi/2$–τ–π–τ–echo) under varying fields. Hahn echo decay traces were obtained as a function of the incremented interpulse delay τ_{incr} ($\pi/2$–τ_{incr}–π–τ_{incr}–echo). Phasing cycling schemes $(x)x$ (2-step) and $x[x]$ (4-step) proposed by Stoll[162] were found not to afford any particular improvement and no phase cycling was used for FSED and echo decay experiments. Echos were symmetrically integrated around the peak maximum, starting around 25% of the maximum intensity. For the 16/32 ns echos, this meant a 120-150 ns width.

T_1 times were measured with saturation recovery sequences, preceded by a picket-fence train of 27 π pulses separated by 100 ns to saturate the magnetization, before a regular Hahn echo. Transient nutation experiments were carried out by applying nutation pulses of incremented duration t_{nut} and by monitoring the intensity of a Hahn echo (detection block) as a function of t_{nut}. The Hahn echo sequence was applied after a long decoherence time used to remove off-resonance coherences (t_{nut}-t_{dec}-$\pi/2$–τ–π–τ–echo). For the experiments, the delays were chosen so that $t_{\mathrm{dec}} >> t_{\mathrm{nut}}$, typically 8 μs. For all experiments, the delay between two nutation sequences (shot repetition time) was larger than $5T_1$. Damping times τ_R of the Rabi oscillations were determined by fits to the time-domain data to an exponentially damped periodic function.

Fourier transforms in all cases were carried out after applying a baseline correction, zero filling, and apodization to a Hamming function.

5.2. Experimental Section for Chapter 3

5.2.1. General Information

The quality of the reagent, as well as the laboratory equipment (FTIR spectrometer, UV-vis-NIR spectrometer, and potentiostat) here is the same as in Chapter 2, see Section 5.1.1. Cyclic voltammograms of **2** were measured in the same condition as Chapter 2. ESI-MS was observed using MicroTOF-Q II Brucker.

The sample for SQUID experiment was prepared by putting 13.6 mg of **2** in 36.9 mg of gelatine capsule together with 74.5 mg of eicosane, which was inserted into a straw. DC magnetic susceptibility and magnetic hysteresis were measured by using Quantum Design MPMS®3 magnetometers. DC data was collected in the temperature range 2 – 300 K under an applied DC magnetic field (H) of 1000 Oe, and corrected for diamagnetic contributions from eicosane and sample holder employing Pascal's constants.[8] Magnetization versus field was performed in the scanning rate of 25 Oe/s. AC data was collected using MPMS- XL SQUID. An oscillating magnetic field of 3.5 Oe and frequencies between 1 and 1.5 kHz were employed. Fitting of Cole-Cole plot was done employing the generalized Debye model by using CC-Fit2[181,182],

5.2.2. Synthesis

[NO]˙ PN was synthesized according to the method presented in Section 5.1 and the original paper[144].

Synthesis of TbPcOAc

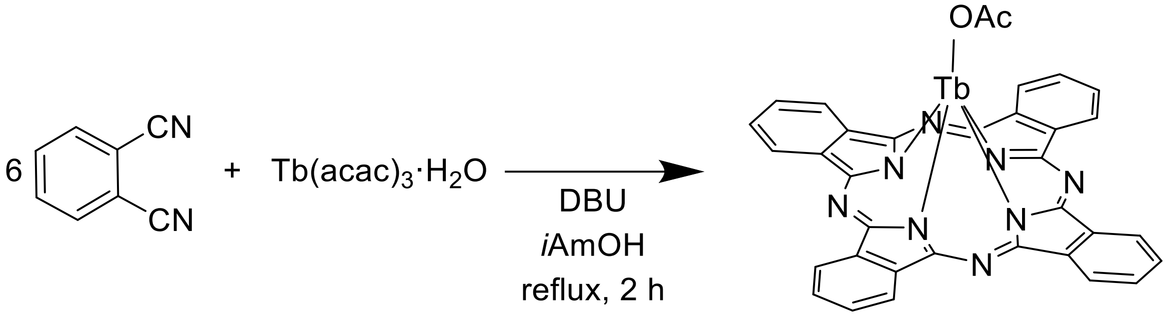

TbPcOAc

TbPcOAc was synthesized in a similar way as the previously reported method.[152] Under Ar atmosphere, phthalonitrile (825 mg, 6.44 mmol), yttrium(III) acetate (504 mg, 1.11 mmol) were dissolved into 15 mL of 1-hexanol. After adding 0.9 mL of 1,8-Diazabicyclo[5.4.0]undec-7-ene, the solution was heated to reflux, stirring vigorously for 2 h. The reaction mixture was dried *in vacuo*, and purified with silica gel column chromatography. The first fraction was eluted with 100% $CHCl_3$, mainly composed of $[TbPc_2]^0$. After removing $[TbPc_2]^0$, the fraction consisting of TbPcOAc was eluted with $CHCl_3$ containing 5% of CH_3OH. The solvent was removed in vacuo to give a blue solid of TbPcOAc (280 mg, 36.8%).

Synthesis of 2

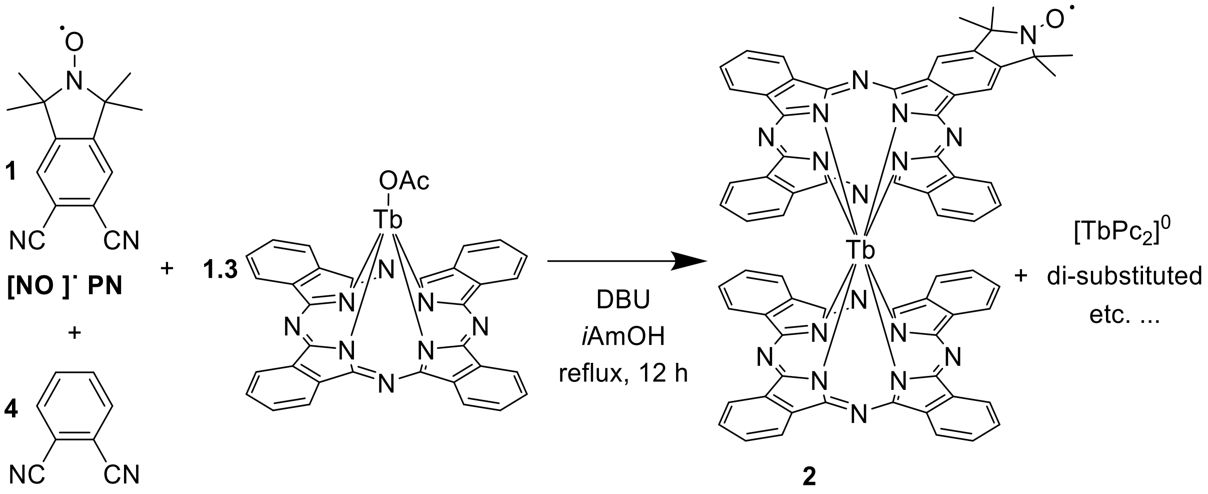

Compound **2** was synthesized in the similar way as **1**.[144] [NO]˙ PN (43.3 mg, 0.180 mmol), phthalonitrile (103 mg, 0.80 mmol), and TbPcOAc (211 mg, 0.275 mmol) was dissolved into 9 mL of isoamyl alcohol. After adding 1.65 μL of 1,8-Diazabicyclo[5.4.0]undec-7-ene, the mixture was heated to reflux, stirring vigorously for 12 h. The reaction mixture was dried in vacuo, and purified with repeated silica gel column chromatography (eluent; $CHCl_3$ / toluene mixture in the ratio of 9 to 1 with the addition of 0.5% of acetone). The obtained material was further purified by reprecipitation in $CHCl_3$/MeOH to yield a dark green powder of **1** (18.7 mg, 8.0%). Note that recrystallization was attempted with **2** in CH_2Cl_2/MeOH, CH_2Cl_2/hexane, both of them resulted in green powder.

HRMS(ESI): calcd (%) for $C_{70}H_{42}N_{17}OTb$: 1295.3032, found 1295.2538.

5.2.3. Magnetometry

Table 5. 1. Best fit parameters to a generalized Debye model for AC susceptibility measured on **2**.

Temp. / K	τ / s	χ_S / cm^{3}mol^{-1}	χ_T / cm^{3}mol^{-1}	α
2.50	1.23E-01	1.69E-01	6.71E+00	4.47E-01
3.00	9.60E-02	1.42E-01	5.21E+00	4.45E-01
3.50	7.96E-02	1.33E-01	4.25E+00	4.41E-01
4.00	6.61E-02	1.18E-01	3.56E+00	4.33E-01
5.00	4.97E-02	9.89E-02	2.69E+00	4.20E-01
5.50	4.66E-02	9.43E-02	2.42E+00	4.22E-01
6.00	4.07E-02	8.19E-02	2.16E+00	4.11E-01
6.50	3.83E-02	8.18E-02	1.98E+00	4.11E-01
7.00	3.52E-02	7.51E-02	1.82E+00	4.07E-01
7.50	3.37E-02	7.42E-02	1.70E+00	4.11E-01
8.00	3.12E-02	6.81E-02	1.57E+00	4.08E-01
9.00	2.27E-02	5.32E-02	1.14E+00	3.87E-01
10.00	1.99E-02	5.05E-02	1.00E+00	3.68E-01
11.51	1.77E-02	4.13E-02	9.07E-01	3.76E-01
12.56	1.60E-02	3.90E-02	8.28E-01	3.40E-01
14.16	1.48E-02	3.58E-02	7.65E-01	3.46E-01
15.00	1.24E-02	3.12E-02	6.37E-01	3.41E-01
17.00	1.12E-02	3.00E-02	5.58E-01	3.36E-01
20.00	9.28E-03	2.18E-02	4.62E-01	3.07E-01
25.00	8.12E-03	2.02E-02	3.70E-01	3.11E-01
30.00	6.41E-03	1.35E-02	3.11E-01	3.37E-01
35.00	5.68E-03	1.43E-02	2.60E-01	2.65E-01
36.00	5.29E-03	1.50E-02	2.54E-01	2.56E-01
37.00	4.44E-03	1.81E-02	2.42E-01	2.02E-01

38.00	3.77E-03	1.25E-02	2.41E-01	2.54E-01
39.00	3.80E-03	1.40E-02	2.29E-01	1.74E-01
40.00	2.30E-03	1.44E-02	2.25E-01	2.04E-01
41.00	2.22E-03	1.76E-02	2.14E-01	6.33E-02
42.00	1.75E-03	1.42E-02	2.09E-01	1.00E-01
43.00	1.23E-03	1.69E-02	2.05E-01	4.30E-02
44.00	8.23E-04	1.57E-02	1.99E-01	3.50E-02
45.00	6.38E-04	7.50E-03	1.96E-01	1.15E-01
46.00	4.56E-04	9.62E-20	1.90E-01	1.78E-01
47.00	3.11E-04	1.02E-02	1.87E-01	5.21E-02
48.00	2.25E-04	9.98E-03	1.82E-01	4.45E-02
49.00	1.72E-04	1.99E-02	1.85E-01	8.76E-03
50.00	1.24E-04	1.85E-02	1.78E-01	1.59E-02

5.3. Experimental Section of Chapter 4

5.3.1. General Information

The quality of the reagents and the spectroscopic equipment is the same as described in section 5.1.1, unless otherwise stated. ESI-ToF mass-spectra were measured using either a MicroTOF-Q II Brucker or a Orbitrap Exploris 240 from Thermo Fischer.

Cyclic voltammograms were measured in a 0.1 M $n\mathrm{Bu_4NPF_6}$ solution of CH_2Cl_2 as the supporting electrolyte, with scan rates of 100mV/s and a sample concentration of 0.5 mM. The solutions were saturated with argon for more than 10 minutes before the measurements, and kept under argon atmosphere during the measurements. A glassy carbon electrode with a radius of 3 mm, a Pt wire, and an Ag^+/Ag reference electrode (10 mM $AgNO_3$ in 0.1 M $n\mathrm{Bu_4NClO_4}/CH_3CN$) were used as working, counter and reference electrodes, respectively. The Fc^+/Fc redox couple was used as an internal standard.

DFT calculations were carried out using the Gaussian 16 Revision C.02 program package.[220] The calculations on **3-Y** and **4-Y** were carried out on the structure from scXRD, while the calculation of Y_2PcPor_2 was performed on the reported structure (CCDC 989974). For **3-Y** and Y_2PcPor_2, due to the calculation power, two terbium atoms were converted into yttrium atoms.

Single crystal X-ray diffraction data of compound 1 were collected on a STOE STADI VARI diffractometer with monochromated Ga Kα (1.34143 Å) radiation at 180 K. Using Olex2[231], the structures were solved with the ShelXT[232] structure solution program using Intrinsic Phasing and refined with the ShelXL[233] refinement package using Least Squares minimization. Refinement was performed with anisotropic temperature factors for all non-hydrogen atoms; hydrogen atoms were calculated on idealized positions. Crystal data and details of data collection and structure refinement are given in Table 5.3. Crystallographic data for compounds **3-Tb**, **4-Tb**, **3-Y**, **4-Y** reported in this thesis have been deposited with the Cambridge Crystallographic Data Centre as supplementary information no. CCDC-2384846, 2384847, 2384848, 2384849, respectively. Copies of the data can be obtained free of charge from https://www.ccdc.cam.ac.uk/structures/.

EPR experiments were carried out on frozen $CD_2Cl_2/CDCl_3$ 4:1 solutions (0.1 mM). The solution was deoxygenated with freeze-pump-thaw cycles, and flame-sealed in the EPR tube under a helium atmosphere. X-band CW EPR spectra were recorded on an Elexsys E580 spectrometer equipped with a 4118X-MD5 resonator (Bruker Biospin GmbH) and a CF935 continuous flow cryostat controlled by a Mercury ITC (Oxford Instruments).

The CASSCF calculation of **3-Tb** and **4-Tb** was performed using OpenMolcas[234]. The calculation was carried out employing the modified crystal structures where phenyl groups on porphyrin were converted to methyl groups, and one of two terbium centers was converted to yttrium. The models were constructed based on the structures of them obtained from the single crystal X-ray structure, without any further geometry optimization. The basis sets from ANO-RCC library17-19 were employed with VTZP quality for Tb^{III} ion, VDZP quality for N atoms directly bound to the Tb^{III} ion, and VDZ quality for all remaining atoms was employed, using the second-order DKH transformation.[235]

For the magnetometry, polycrystalline samples of **3-Tb** and **4-Tb** were suspended in eicosane to prevent torquing and placed into a gelatin capsule, which was then inserted into a straw. DC magnetic susceptibility and magnetization versus field were measured by using a Quantum Design MPMS®3 magnetometer. The data of DC susceptibility was collected in the temperature range 2 – 300 K under an applied DC magnetic field (H) of 1000 Oe, and corrected for the diamagnetism of the sample holder, eicosane, and sample itself. Magnetization versus field was measured in a range of 0 – 7 T using the option "stable at each field". On the other hand, AC data was collected using a MPMS- XL SQUID magnetometer. An oscillating magnetic field of 3.5 Oe and frequencies between 1 and 1000 Hz were employed. Fitting of Cole-Cole plot was acquired employing generalized Debye model by using CC-Fit2.[181,182]

5.3.2. Synthesis

Synthesis of 2SMe-PN

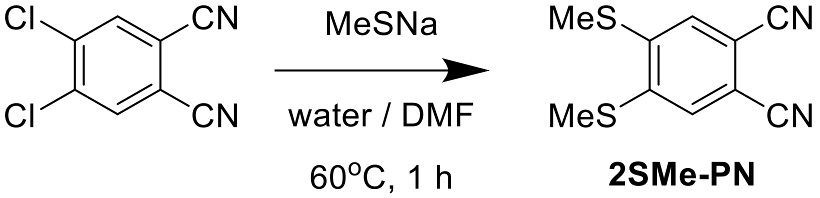

To a solution of 4,5-dichlorophthalonitrile (528 mg, 2.68 mmol) in 12 mL of DMF, 2.4 mL of an aqueous solution of sodium methanethiolate (402 mg) was added dropwise. The mixture was then heated to 60 °C and stirred for 1 hour before being cooled down to room temperature. A white precipitate formed upon the addition of 15 mL of water, and the mixture was stirred for 30 minutes. The precipitate was collected by filtration and washed with water, yielding 403 mg of white powder (yield: 68.2%).

^{1}H-NMR (400 MHz, $CDCl_3$, δ in ppm) δ = 7.40 (s, 2H, aromatic), 2.62 (s, 6H, $-SCH_3$). ^{13}C-NMR (400 MHz, $CDCl_3$, δ in ppm) δ = 144.33, 126.92, 115.62, 111.25, 15.46. Assignments are shown in Figure 5.1.

Synthesis of $[\mathbf{TbPc_2(SMe)_{16}}]^0$

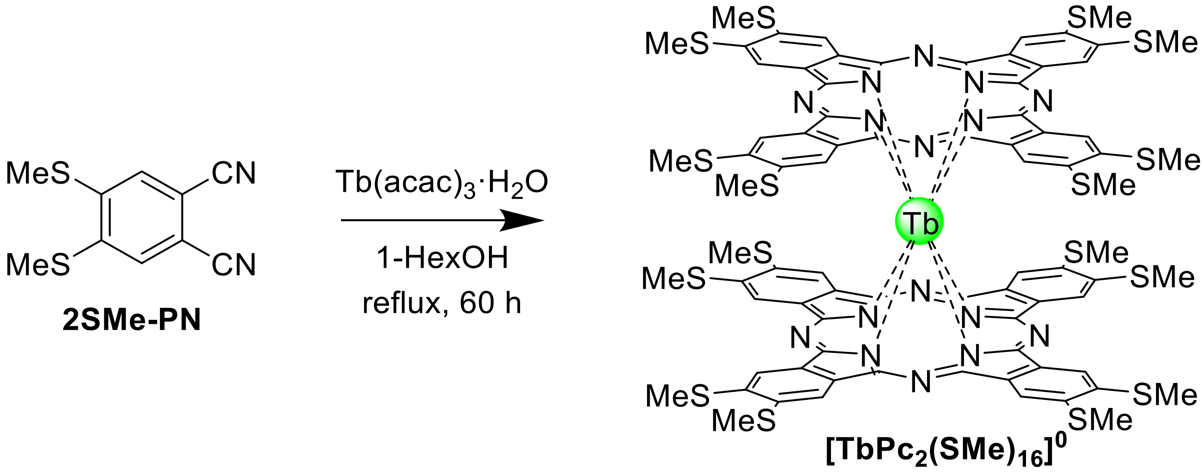

$[TbPc_2(SMe)_{16}]^0$ was synthesized in a similar way, as reported before.[90,215] **2SMe-PN** (890 mg, 4.05 mmol), terbium(III) acetylacetonate monohydrate (211 mg, 0.462 mmol) were dissolved into 20 mL of 1–hexanol. After adding 0.382 mL of 1,8–diazabicyclo[5.4.0]undec–7-ene,the mixture was heated to reflux and stirred vigorously for 60 hours. The reaction mixture was then cooled to room temperature, and 100 mL of methanol was added. The precipitate was collected by filtration, redissolved in chloroform, and purified by silica gel column chromatography (eluent; chloroform 100%). The dark grey fraction was collected and reprecipitated in chloroform/hexane to yield black powder of 16SMe-TbPc2 (386 mg, 34.4%).The characterization data (UV-Vis-NIR,IR ans ESI MS spectra) was shown in section 2.2., which is also true for the following compounds unless otherwise stated.

HRMS (ESI): calcd(%) for $C_{88}H_{72}N_8S_{16}Tb$ 1921.0257, found 1921.4053

Synthesis of $[\mathbf{YPc_2(SMe)_{16}}]^0$

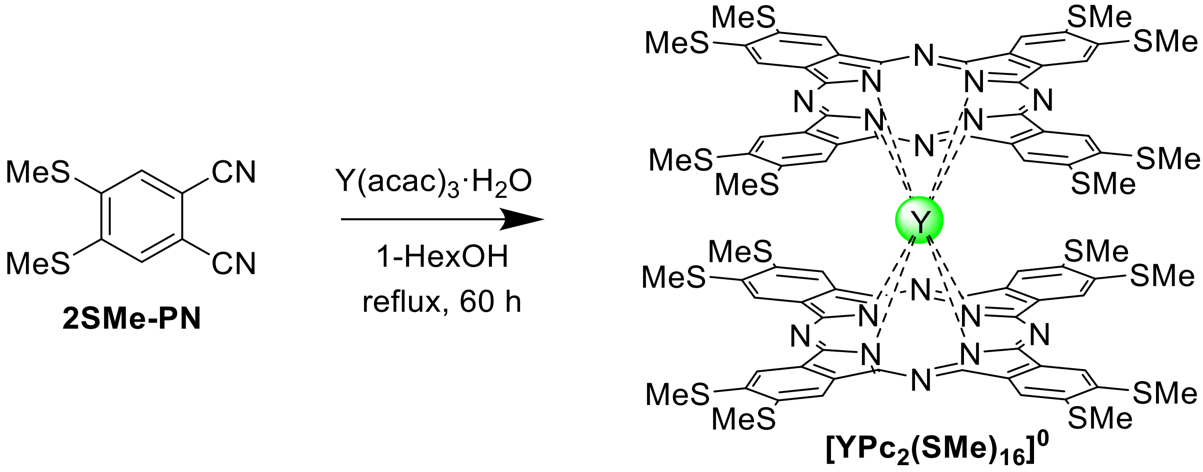

In the same manner as **$[TbPc_2(SMe)_{16}]^0$**, **$[YPc_2(SMe)_{16}]^0$** was obtained from 210 mg (0.956mmol) of **2SMe-PN**, 48 mg (0.124 mmol) of yttrium(III) acetylacetonate monohydrate, and 100 μL of 1,8–diazabicyclo[5.4.0]undec–7-ene in 4 mL of 1-hexanol.

Yield: 52.4 mg, 20.8%. HRMS (ESI-ToF): calcd(%) for $C_{88}H_{72}N_8S_{16}Y$ 1851.0084, found 1850.8882

Synthesis of 3-Tb

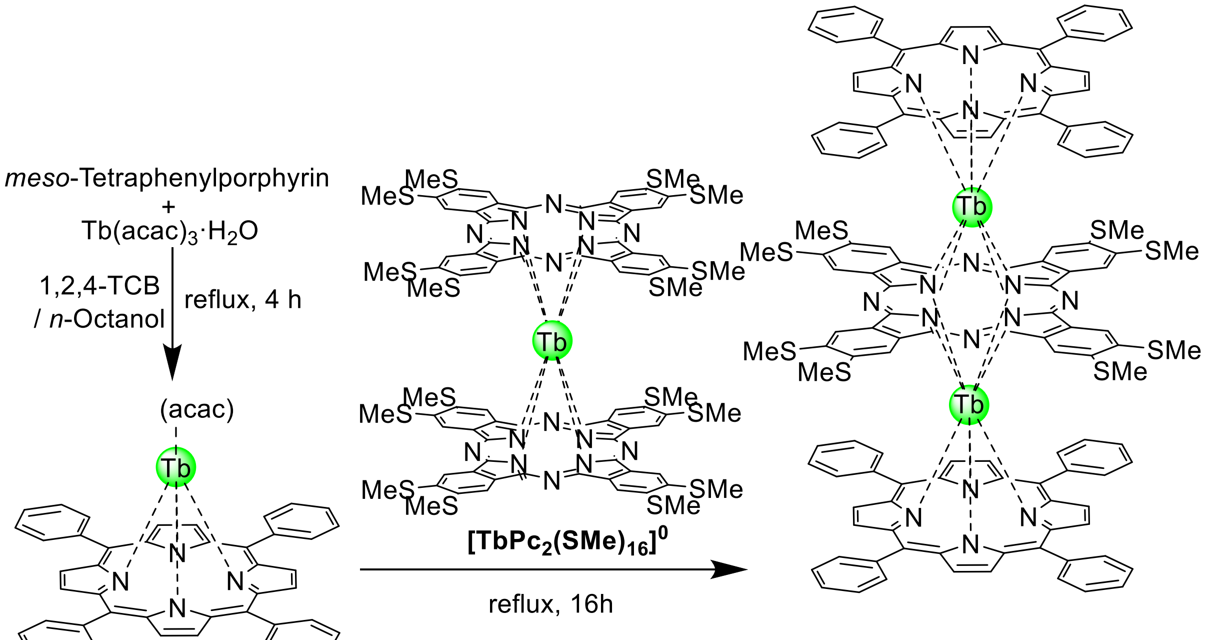

3-Tb

62.7 mg (0.102 mmol) of 5,10,15,20-tetraphenylporphin (TPP) and 52.0 mg (0.100 mmol) of terbium(III) acetylacetonate monohydrate were dissolved into the mixture of of 1,2,4-trichlorobenzene and 1-octanol (2 mL/2 mL), and the mixture was heated up to reflux, stirred vigorously for 4 h. The reaction mixture was cooled down to room temperature, and 52.0 mg (0.0250 mmol) of **$[TbPc_2(SMe)_{16}]^0$** was added to it. The reaction mixture was heated to reflux and stirred vigorously for 4 hours. . Upon cooling to room temperature, the mixture was combined with methanol to precipitate the product. The precipitate was collected by filtration, redissolved in a minimum amount of chloroform, and purified by silica gel column chromatography. Initially, a mixture of chloroform and hexane in a 2:1 ratio was used as the eluent until the pink fraction was fully collected, after which the eluent was switched to 100% chloroform. The olive-colored fraction was collected and recrystallized in chloroform/hexane, yielding 9.32 mg of the target compound (15%).

HRMS (ESI-ToF): calcd (%) for $C_{128}H_{88}N_{16}S_8Tb_2$ 2423.3650, found 2423.3721.

Synthesis of 3-Y

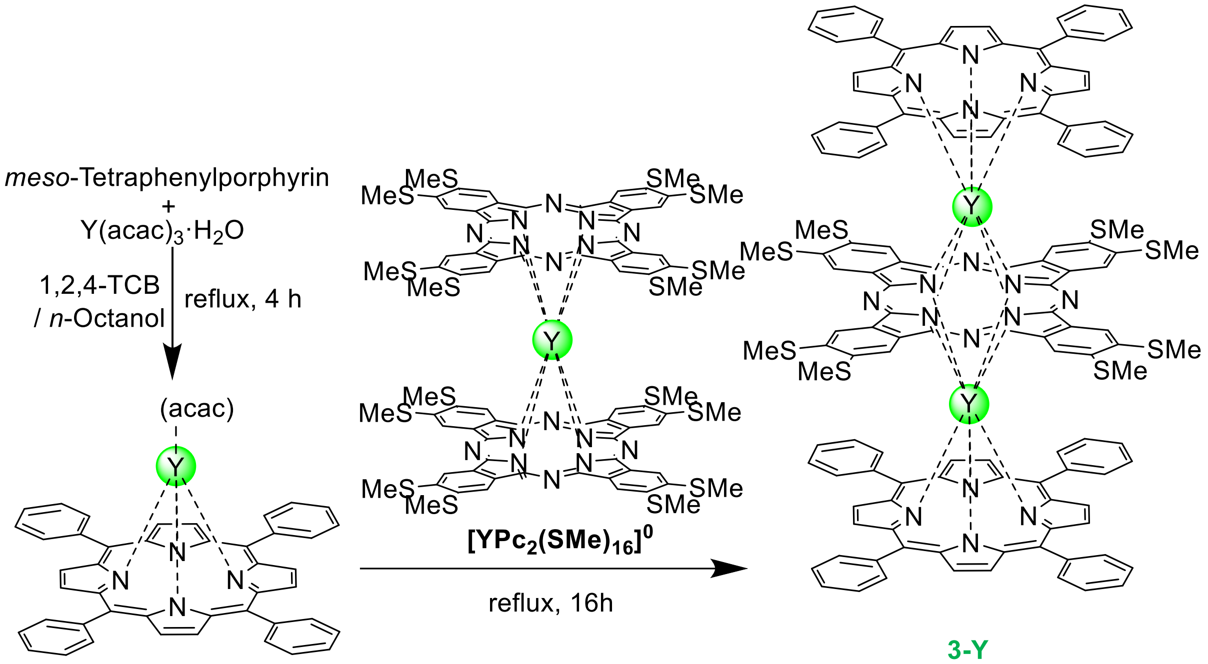

3-Y

In the same manner as **3-Tb**, **3-Y** was obtained from 61.8 mg (0.100 mmol) of TPP, 51.6 mg (0.118 mmol) of yttrium(III) acetylacetonate monohydrate, 52.3 mg (0.028 mmol) of **[YPc$_2$(SMe)$_{16}$]^0**, and 2 mL/2 mL mixed-solvent of 1,2,4-trichlorobenzene and 1-octanol.

Yield: 9.80 mg, 15%. HRMS (ESI): calcd(%) for $C_{128}H_{88}N_{16}S_8Y_2$ 2283.3261, found 2283.3229. ^{1}H-NMR (400 MHz, CDCl$_3$, δ in ppm) δ = 9.18 (s, 8H, Pc), 8.71 (quasi d, *J* = 6.8 Hz, 8H, o_{endo}), 7.99 (quasi t, *J* = 8.0 Hz, 8H, m_{endo}), 7.56 (quasi t, *J* = 7.8 Hz, *p*), 7.29 (s, 16 H, Por β), 7.00 (quasi t, *J* = 8.0 Hz, 8H, m_{exo}), 6.10 (quasi d, *J* = 6.8 Hz, 8H, o_{exo}), 3.12 (s, 24H, –SCH_3).). ^{13}C-NMR (400 MHz, CDCl$_3$, δ in ppm) δ = 156.36, 150.01, 142.64, 141.52, 134.46, 132.06, 128.25, 127.09, 126.11, 125.95, 120.95, 120.66, 17.25. Assignments are shown in Chapter 2 manuscript.

Synthesis of Phenoxathiin hexachloroantimlonate(V) (Phen$^+$SbCl$_6^-$)

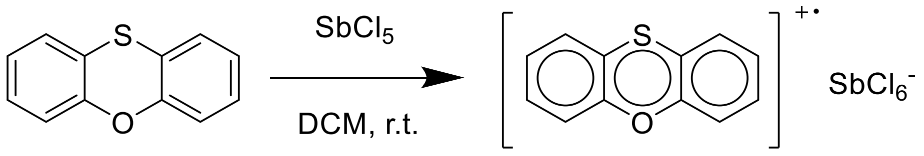

Phen$^+$SbCl$^-$

The synthesis was carried out following the reported procedure.[236] Dichloromethane used in this process was saturated with argon for more than one hour prior to use. To a solution of phenoxathiine (102 mg, 0.51 mmol) in dichloromethane, a solution of SbCl$_5$ (145 mg, 0.48 mmol) in dichloromethane was added dropwise. The reaction mixture turned immediately blue-violet. It was cooled in an ice bath and after 15 min a microcrystalline precipitate formed. The remaining dichloromethane was removed by decantation, and the precipitate was washed twice with fresh dichloromethane. The obtained material was dried in vacuo, and used without further characterization It was stored in a freezer at -25 °C under argon atmosphere

Synthesis of 4-Tb

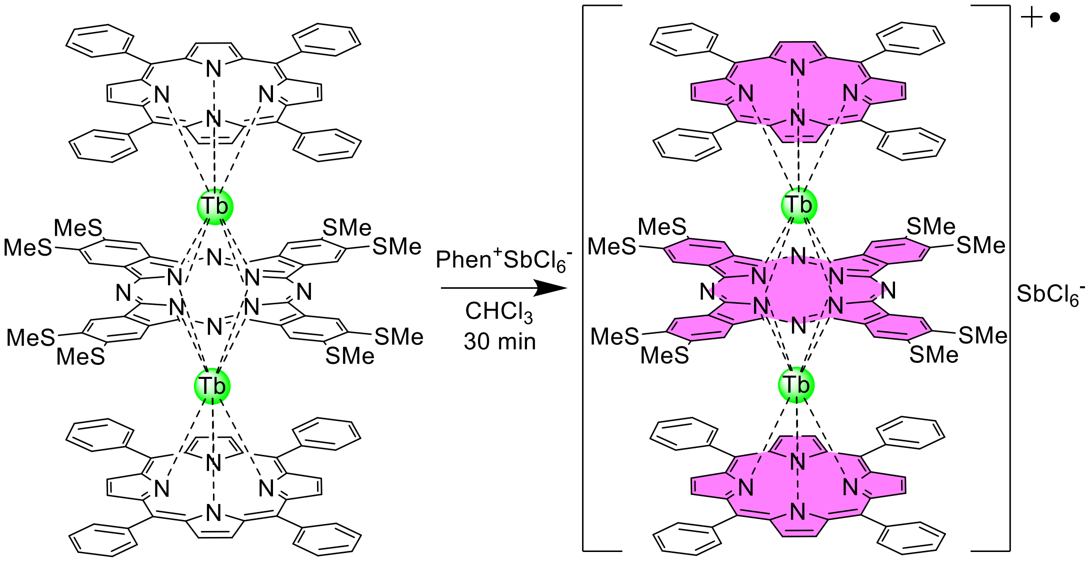

3-Tb **4-Tb**

Chloroform and hexane used in this procedure were saturated with argon for two hours before use. 2.87 mg of Phen$^+$SbCl$_6^-$ (0.00536 mmol) and 13.0 mg of **3-Tb** (0.00536 mmol) were dissolved in 10 mL of chloroform and stirred vigorously for 30 min. The reaction mixture was filtered through cotton and immediately subjected for crystallization in the hexane bath under argon atmosphere. Crystallization was conducted in a fridge at 5 °C, yielding black needles (6.32 mg, 42.6%).

HRMS (ESI-ToF): calcd(%) for $C_{128}H_{88}N_{16}S_8Tb_2$ 2423.3650, found 2423.3648.

Synthesis of 4-Y

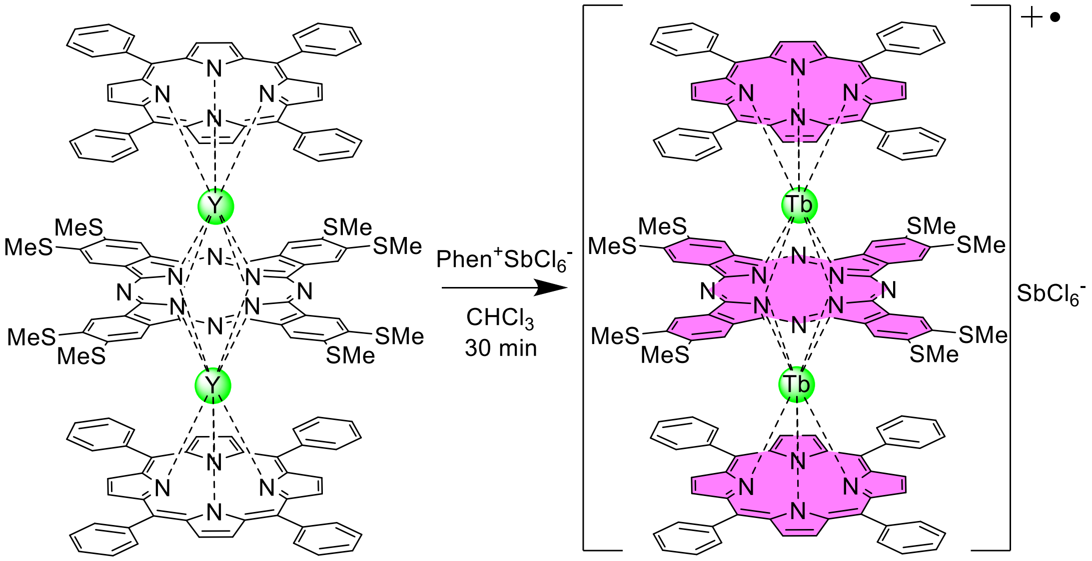

3-Y **4-Y**

In the same manner as **4-Tb**, **4-Y** was obtained from 2.33 mg (0.00436 mmol) of Phen$^+$SbCl$_6^-$, 9.80 mg (0.00429 mmol) of **3-Y**, to yield black needles (4.50 mg, 40.0%).

HRMS (ESI-ToS): calcd.(%) for $C_{128}H_{88}N_{16}S_8Y_2$ 2283.3261, found 2283.3187.

5.3.3. Characterization

Characterization of 2SMe-PN

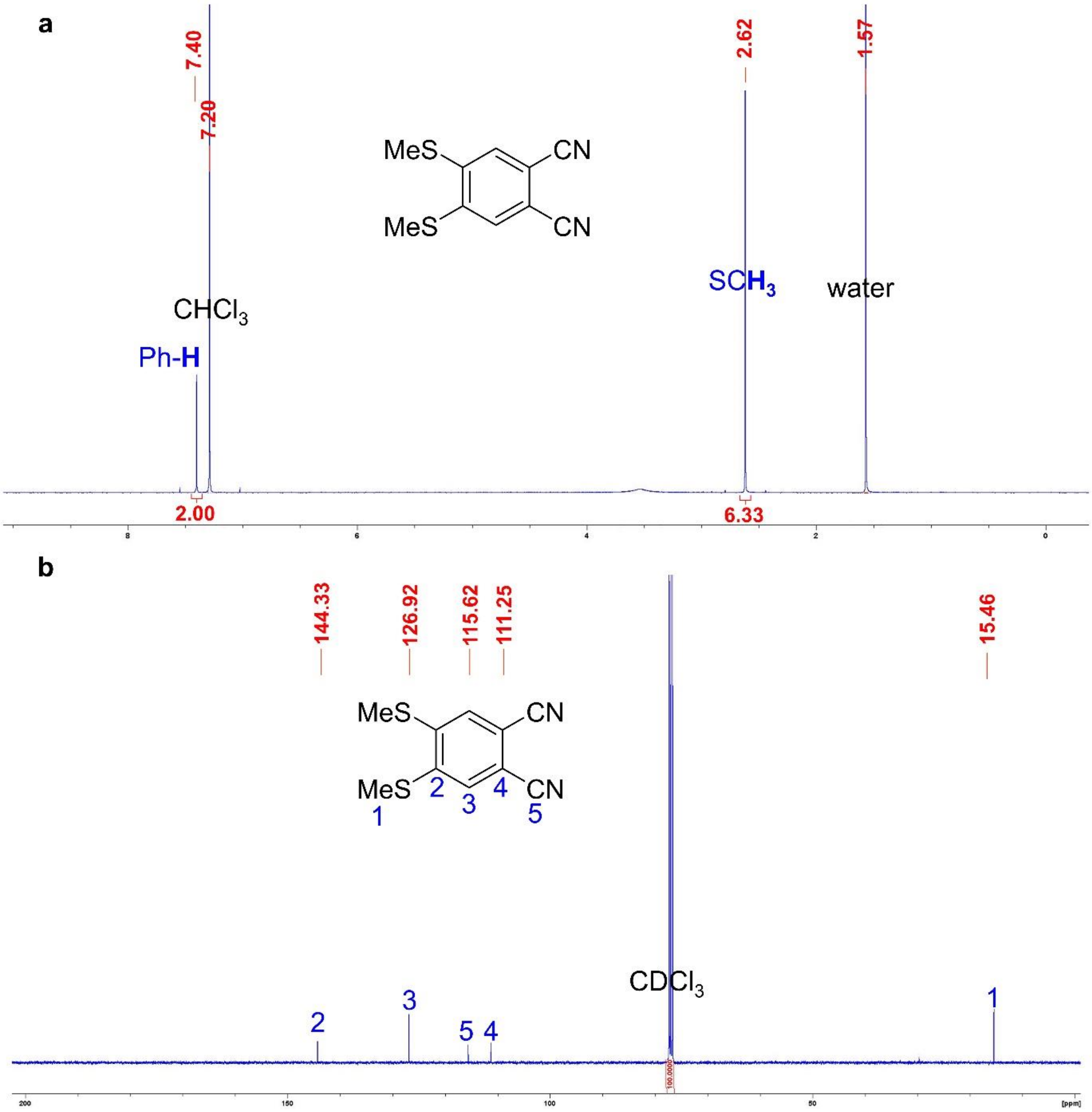

Figure 5.1. ^{1}H-NMR (a) and ^{13}C-NMR (b) spectra of **2SMe-PN**.

DFT calculation

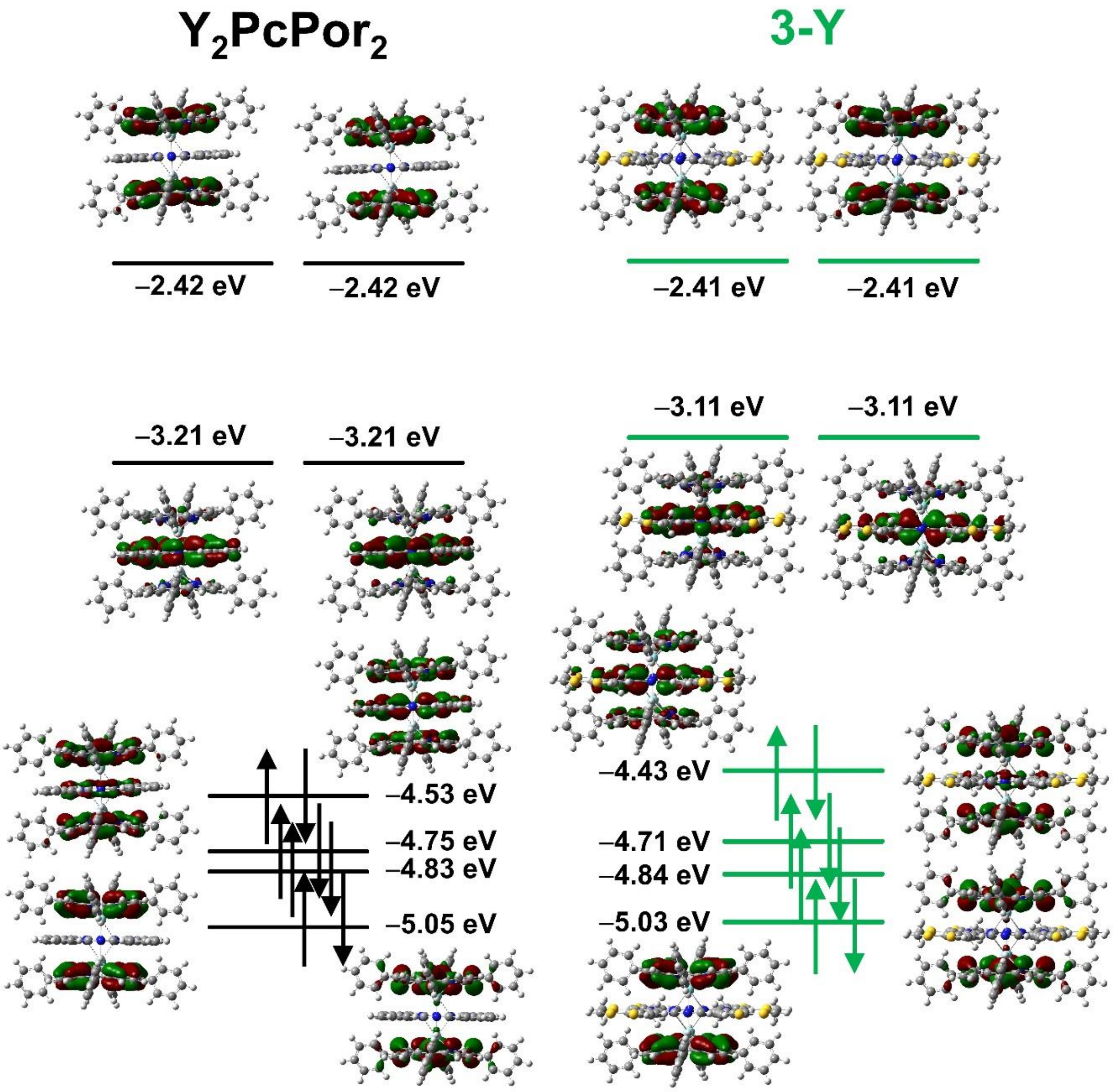

Figure 5.2. Molecular orbitals of Y_2PcPor_2 (left) and **3-Y** (right). The isocounter value is 0.02 for both of them.

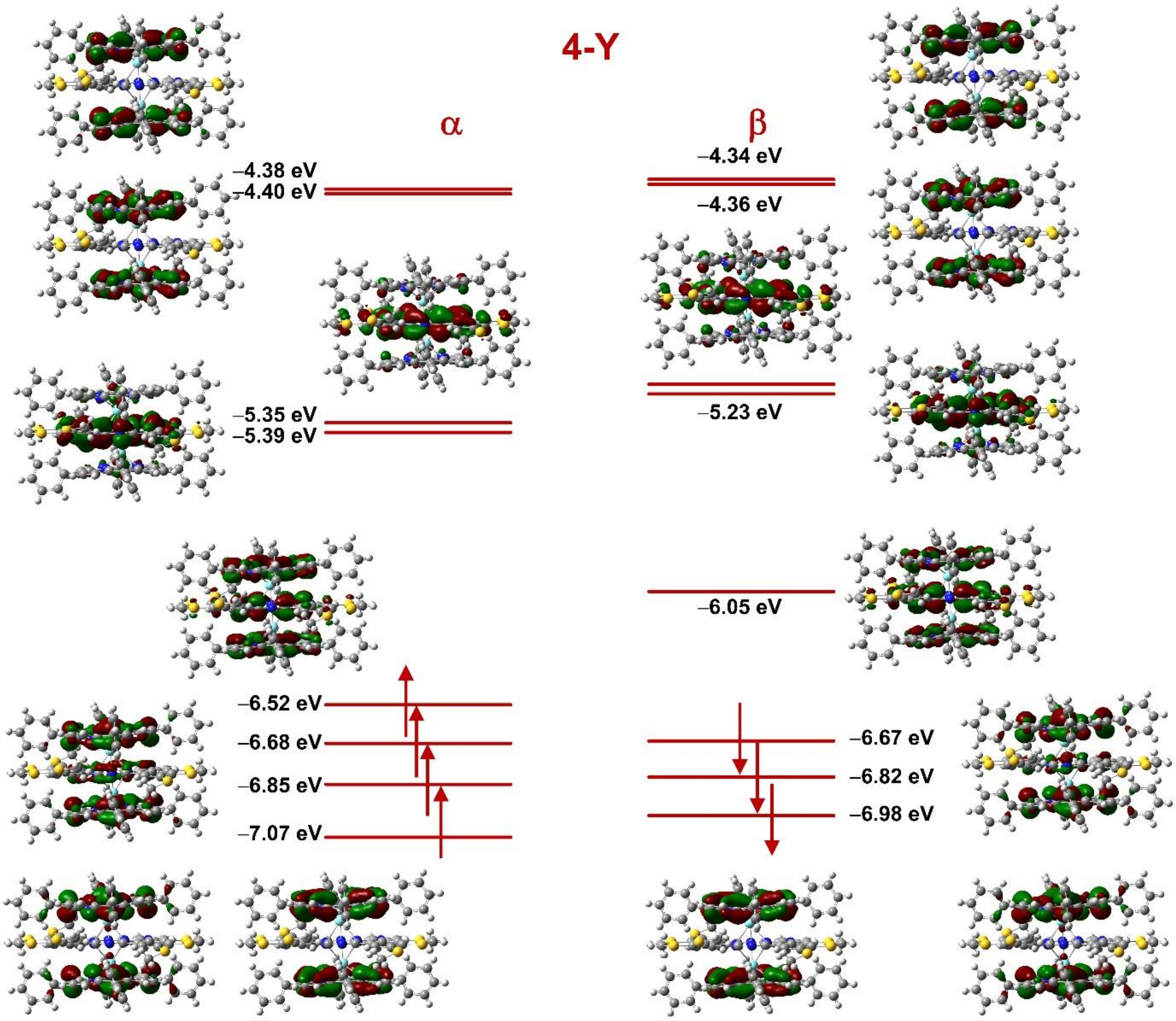

Figure 5.3. Molecular orbitals of **4-Y**.The isocounter value is 0.02 for both of them.

Structural Study

Table 5. 2. Continuous shaped measures (CShM) for **3-** and **4-Ln**, as well as $Tb_2Pc(TPP)_2$.

Compound	**3-Tb**	**3-Y**	**4-Tb**	**4-Y**	Tb_2PcPor_2[a]
OP-8	36.7	36.9	36.6	36.9	36.8
HPY-8	27.7	27.7	28.9	28.8	29.0
HBPY-8	8.91	8.86	8.82	8.76	8.88
CU-8	0.781	0.736	0.593	0.549	0.532
SAPR-8	8.82	8.74	10.10	10.00	10.17
TDD-8	6.35	6.29	7.23	7.15	7.31
JGBF-8	17.5	17.5	17.8	17.8	18.1
JETBPY-8	25.0	25.0	25.3	25.2	25.4
JBTPR-8	10.9	10.8	12.0	11.9	12.2
BTPR-8	10.0	9.9	11.1	11.0	11.3
JSD-8	12.5	12.4	13.4	13.3	13.6
TT-8	1.71	1.67	1.45	1.43	1.48
ETBPY-8	23.3	23.3	23.4	23.3	23.5

a. from ref.[143]

OP-8 = (D_{8h}) Octagon HPY-8 = (C_{7v}) Heptagonal pyramid HBPY-8 = (D_{6h}) Hexagonal bipyramid CU-8 = (O_h) Cube SAPR-8 = (D_{4d}) Square antiprism TDD-8 = (D_{2d}) Triangular dodecahedron JGBF-8 = (D_{2d}) Johnson gyrobifastigium J26 JETBPY-8 = (D_{3h}) Johnson elongated triangular bipyramid J14 JBTPR-8 = (C_{2v}) Biaugmented trigonal prism J50 BTPR-8 = (C_{2v}) Biaugmented trigonal prism JSD-8 = (D_{2d}) Snub diphenoid J84 TT-8 = (T_d) Triakis tetrahedron ETBPY-8 = (D_{3h}) Elongated trigonal bipyramid

Table 5. 3. Crystal packing parameters of **3-Tb**, **4-Tb**, **3-Y**, and **4-Y**.

	3-Tb	**3-Y**	**4-Tb**	**4-Y**
Empirical formula	$C_{134}H_{94}Cl_{18}N_{16}S_8Tb_2$	$C_{134}H_{94}Cl_{18}N_{16}S_8Y_2$	$C_{138}H_{98}Cl_{36}N_{16}S_8SbTb_2$	$C_{138}H_{98}Cl_{36}N_{16}S_8SbY_2$
Formula weight	3140.67	3000.65	3952.59	3812.57
Temperature/K	180	180	180	180
Crystal system	triclinic	triclinic	triclinic	triclinic
Space group	P-1	P-1	P-1	P-1
a/Å	15.8139(3)	15.7874(3)	15.3741(3)	15.3486(3)
b/Å	15.9511(3)	15.9637(3)	15.9288(3)	15.9879(3)
c/Å	15.9670(3)	15.9986(3)	18.8546(4)	18.8341(4)
α/°	83.8340(10)	83.7740(10)	90.180(2)	90.040(2)
β/°	69.3450(10)	61.8820(10)	104.359(2)	104.252(2)
γ/°	62.1490(10)	69.4520(10)	117.331(2)	117.5390(10)
Volume/Å^3	3324.19(11)	3322.00(11)	3936.85(15)	3936.52(14)
Z	1	1	1	1
ρ_{calc}g/cm^3	1.569	1.5	1.667	1.608
μ/mm^{-1}	8.869	4.025	10.224	6.172
F(000)	1574	1522	1959	1907
Crystal size/mm^3	0.15 × 0.11 × 0.08	0.12 × 0.1 × 0.03	0.15 × 0.04 × 0.03	0.12 × 0.1 × 0.03
Radiation	Ga Kα (λ = 1.34143)	GaKα (λ = 1.34143)	Ga Kα (λ = 1.34143)	Ga Kα (λ = 1.34143)
2Θ range for data collection/°	5.858 to 124.988	5.462 to 128.972	5.484 to 115.002	5.816 to 128.658
Index ranges	$-20 \le h \le 18$, $-20 \le k \le 6$, $-21 \le l \le 20$	$-12 \le h \le 21$, $-19 \le k \le 21$, $-21 \le l \le 20$	$-17 \le h \le 19$, $-19 \le k \le 9$, $-23 \le l \le 23$	$-20 \le h \le 13$, $-21 \le k \le 21$, $-24 \le l \le 25$

Reflections collected	58979	50537	39606	64867
Independent reflections	15800 [R_{int} = 0.0268, R_{sigma} = 0.0287]	16084 [R_{int} = 0.0228, R_{sigma} = 0.0266]	16006 [R_{int} = 0.0331, R_{sigma} = 0.0342]	19206 [R_{int} = 0.0306, R_{sigma} = 0.0334]
Data/restraints/parameters	15800/0/806	16084/0/806	16006/0/870	19206/0/875
Goodness-of-fit on F^2	1.067	1.057	1.058	1.075
Final R indexes [I>=2σ (I)]	R_1 = 0.0424, wR_2 = 0.1206	R_1 = 0.0629, wR_2 = 0.1874	R_1 = 0.0699, wR_2 = 0.1982	R_1 = 0.0751, wR_2 = 0.2313
Final R indexes [all data]	R_1 = 0.0469, wR_2 = 0.1231	R_1 = 0.0727, wR_2 = 0.1963	R_1 = 0.0788, wR_2 = 0.2076	R_1 = 0.0921, wR_2 = 0.2471
Largest diff. peak/hole / e Å^{-3}	3.23/-2.01	3.67/-2.00	1.82/-1.48	3.09/-1.58

Comparison of the result of CASSCF

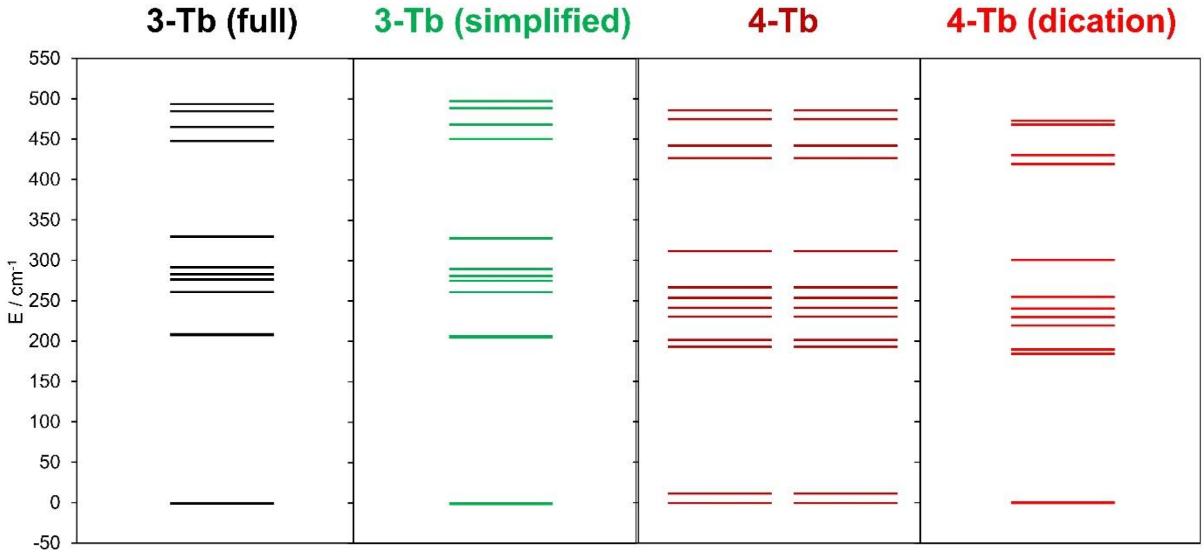

Figure 5. 4. Comparison of the energy states of **3-Tb** (full) (black), **3-Tb** (simplified) (green), **4-Tb** (maroon), and **4-Tb** dication (red).

5.5. Magnetometry

Table 5. 4. Best fit parameters to a generalized Debye model for AC susceptibility measured on **3-Tb** at DC field of 1500 Oe.

Temp. / K	τ / s	$\tau_{\mathrm{ln\_err\_up}}$ / s	$\tau_{\mathrm{ln\_err\_lw}}$ / s	τ_{err} / s	χ_S / cm^3 mol^{-1}	χ_{S_err} / cm^3 mol^{-1}	χ_T / cm^3 mol^{-1}	χ_{T_err} / cm^3 mol^{-1}	α	α_{err}
2.00	9.01E-03	6.07E-02	1.34E-03	3.67E-04	2.55E-17	1.38E-01	1.50E+01	1.98E-01	3.98E-01	1.34E-02
2.20	7.35E-03	4.44E-02	1.22E-03	2.39E-04	2.13E-14	1.16E-01	1.43E+01	1.46E-01	3.78E-01	1.14E-02
2.60	4.95E-03	2.27E-02	1.08E-03	1.18E-04	1.05E-01	8.76E-02	1.25E+01	8.68E-02	3.22E-01	9.42E-03
3.00	3.67E-03	1.32E-02	1.02E-03	5.87E-05	2.42E-01	5.78E-02	1.10E+01	4.84E-02	2.67E-01	6.96E-03

3.40	2.93E-03	9.04E-03	9.48E-04	3.02E-05	3.22E-01	3.61E-02	9.90E+00	2.68E-02	2.28E-01	4.77E-03
3.80	2.42E-03	6.66E-03	8.80E-04	1.20E-05	3.80E-01	1.66E-02	8.94E+00	1.13E-02	1.98E-01	2.40E-03
4.20	2.03E-03	5.08E-03	8.15E-04	1.29E-05	4.20E-01	2.04E-02	8.10E+00	1.27E-02	1.73E-01	3.19E-03
4.60	1.75E-03	4.20E-03	7.26E-04	8.02E-06	4.17E-01	1.41E-02	7.45E+00	8.10E-03	1.63E-01	2.32E-03
5.00	1.50E-03	3.46E-03	6.51E-04	8.95E-06	4.21E-01	1.76E-02	6.87E+00	9.82E-03	1.52E-01	3.08E-03
5.40	1.29E-03	2.86E-03	5.83E-04	8.41E-06	4.27E-01	1.85E-02	6.35E+00	9.04E-03	1.41E-01	3.35E-03
5.80	1.11E-03	2.38E-03	5.21E-04	8.72E-06	4.29E-01	2.15E-02	5.90E+00	9.69E-03	1.31E-01	4.06E-03
6.20	9.61E-04	1.99E-03	4.64E-04	8.16E-06	4.29E-01	2.25E-02	5.51E+00	9.33E-03	1.23E-01	4.39E-03
6.60	8.30E-04	1.67E-03	4.12E-04	7.47E-06	4.34E-01	2.33E-02	5.17E+00	9.21E-03	1.16E-01	4.69E-03
7.00	7.17E-04	1.42E-03	3.63E-04	5.93E-06	4.27E-01	2.07E-02	4.87E+00	7.15E-03	1.11E-01	4.21E-03
7.40	6.21E-04	1.20E-03	3.21E-04	5.69E-06	4.30E-01	2.23E-02	4.60E+00	6.98E-03	1.05E-01	4.60E-03
7.80	5.38E-04	1.01E-03	2.87E-04	5.24E-06	4.33E-01	2.31E-02	4.35E+00	6.53E-03	9.70E-02	4.82E-03
8.20	4.70E-04	8.61E-04	2.57E-04	4.08E-06	4.50E-01	2.00E-02	4.13E+00	5.10E-03	9.12E-02	4.20E-03
8.60	4.08E-04	7.34E-04	2.27E-04	3.86E-06	4.37E-01	2.12E-02	3.93E+00	4.83E-03	8.69E-02	4.43E-03
9.00	3.57E-04	6.33E-04	2.02E-04	3.66E-06	4.38E-01	2.23E-02	3.75E+00	4.66E-03	8.30E-02	4.63E-03
9.50	3.06E-04	5.24E-04	1.79E-04	3.08E-06	4.62E-01	2.09E-02	3.54E+00	3.68E-03	7.42E-02	4.33E-03

10.00	2.64E-04	4.28E-04	1.63E-04	4.50E-06	4.84E-01	3.41E-02	3.35E+00	5.55E-03	6.21E-02	7.14E-03
10.50	2.29E-04	3.67E-04	1.43E-04	2.94E-06	4.94E-01	2.44E-02	3.19E+00	3.28E-03	5.93E-02	4.97E-03
11.00	2.01E-04	3.14E-04	1.29E-04	2.60E-06	5.23E-01	2.33E-02	3.04E+00	2.87E-03	5.37E-02	4.75E-03
11.50	1.78E-04	2.68E-04	1.17E-04	2.56E-06	5.43E-01	2.47E-02	2.91E+00	2.51E-03	4.69E-02	4.93E-03

Table 5. 5. Best fit parameters to a generalized Debye model for AC susceptibility measured on **4-Tb** at zero DC field.

Temp. / K	τ / s	$\tau_{\text{ln\_err\_up}}$ / s	$\tau_{\text{ln\_err\_lw}}$ / s	τ_{err} / s	χ_S / cm^3 mol^{-1}	χ_{S_err} / cm^3 mol^{-1}	χ_T / cm^3 mol^{-1}	χ_{T_err} / cm^3 mol^{-1}	α	α_{err}
2.00	1.02E-03	2.20E-03	4.73E-04	9.26E-06	2.15E+00	6.91E-02	1.71E+01	2.95E-02	1.34E-01	4.62E-03
2.05	9.15E-04	2.00E-03	4.19E-04	8.98E-06	2.13E+00	7.40E-02	1.67E+01	2.93E-02	1.37E-01	4.90E-03
2.10	8.23E-04	1.82E-03	3.72E-04	8.86E-06	2.11E+00	8.03E-02	1.63E+01	2.96E-02	1.40E-01	5.25E-03
2.15	7.41E-04	1.65E-03	3.32E-04	8.88E-06	2.11E+00	8.80E-02	1.58E+01	3.01E-02	1.43E-01	5.70E-03
2.20	6.71E-04	1.51E-03	2.98E-04	8.92E-06	2.11E+00	9.59E-02	1.54E+01	3.05E-02	1.46E-01	6.15E-03
2.25	6.11E-04	1.39E-03	2.69E-04	8.94E-06	2.14E+00	1.04E-01	1.50E+01	3.07E-02	1.47E-01	6.60E-03
2.30	5.61E-04	1.28E-03	2.45E-04	8.61E-06	2.18E+00	1.06E-01	1.47E+01	2.94E-02	1.49E-01	6.75E-03
2.35	5.16E-04	1.19E-03	2.24E-04	8.59E-06	2.20E+00	1.13E-01	1.43E+01	2.92E-02	1.51E-01	7.11E-03

2.40	4.78E-04	1.10E-03	2.08E-04	8.42E-06	2.25E+00	1.16E-01	1.40E+01	2.83E-02	1.51E-01	7.36E-03
2.45	4.45E-04	1.02E-03	1.94E-04	8.31E-06	2.30E+00	1.20E-01	1.36E+01	2.76E-02	1.50E-01	7.62E-03
2.50	4.14E-04	9.51E-04	1.81E-04	8.08E-06	2.35E+00	1.22E-01	1.33E+01	2.63E-02	1.50E-01	7.75E-03
2.55	3.89E-04	8.92E-04	1.70E-04	7.84E-06	2.42E+00	1.23E-01	1.30E+01	2.50E-02	1.50E-01	7.83E-03
2.60	3.66E-04	8.36E-04	1.60E-04	7.58E-06	2.47E+00	1.22E-01	1.27E+01	2.37E-02	1.49E-01	7.88E-03
2.65	3.46E-04	7.85E-04	1.53E-04	7.44E-06	2.53E+00	1.24E-01	1.24E+01	2.28E-02	1.47E-01	8.04E-03
2.70	3.29E-04	7.40E-04	1.46E-04	7.22E-06	2.59E+00	1.23E-01	1.21E+01	2.15E-02	1.45E-01	8.07E-03
2.75	3.12E-04	7.00E-04	1.39E-04	7.03E-06	2.63E+00	1.23E-01	1.18E+01	2.05E-02	1.44E-01	8.12E-03
2.80	2.99E-04	6.62E-04	1.35E-04	6.79E-06	2.69E+00	1.20E-01	1.16E+01	1.93E-02	1.41E-01	8.09E-03
2.85	2.86E-04	6.32E-04	1.29E-04	6.45E-06	2.73E+00	1.16E-01	1.13E+01	1.78E-02	1.40E-01	7.89E-03
2.90	2.75E-04	6.00E-04	1.26E-04	6.25E-06	2.78E+00	1.14E-01	1.11E+01	1.68E-02	1.37E-01	7.87E-03
2.95	2.65E-04	5.73E-04	1.22E-04	6.01E-06	2.82E+00	1.11E-01	1.08E+01	1.58E-02	1.35E-01	7.76E-03
3.00	2.55E-04	5.46E-04	1.19E-04	5.87E-06	2.86E+00	1.09E-01	1.06E+01	1.50E-02	1.32E-01	7.78E-03
3.05	2.47E-04	5.26E-04	1.16E-04	5.57E-06	2.91E+00	1.03E-01	1.04E+01	1.38E-02	1.30E-01	7.53E-03
3.10	2.38E-04	5.02E-04	1.12E-04	5.46E-06	2.88E+00	1.03E-01	1.02E+01	1.32E-02	1.28E-01	7.55E-03
3.15	2.32E-04	4.84E-04	1.11E-04	5.34E-06	2.94E+00	1.01E-01	9.99E+00	1.25E-02	1.26E-01	7.53E-03

3.20	2.24E-04	4.65E-04	1.08E-04	5.06E-06	2.94E+00	9.63E-02	9.79E+00	1.16E-02	1.23E-01	7.29E-03
3.25	2.18E-04	4.45E-04	1.06E-04	5.02E-06	2.96E+00	9.60E-02	9.59E+00	1.12E-02	1.20E-01	7.40E-03
3.30	2.12E-04	4.29E-04	1.05E-04	4.94E-06	2.98E+00	9.46E-02	9.41E+00	1.11E-02	1.17E-01	7.46E-03
3.35	2.06E-04	4.15E-04	1.02E-04	4.76E-06	2.98E+00	9.14E-02	9.23E+00	1.00E-02	1.16E-01	7.25E-03
3.40	2.01E-04	4.02E-04	1.01E-04	4.47E-06	2.99E+00	8.58E-02	9.06E+00	9.17E-03	1.14E-01	6.91E-03
3.45	1.98E-04	3.91E-04	9.99E-05	4.46E-06	3.02E+00	8.48E-02	8.89E+00	8.89E-03	1.11E-01	7.01E-03
3.50	1.91E-04	3.76E-04	9.75E-05	4.56E-06	2.99E+00	8.77E-02	8.73E+00	8.87E-03	1.09E-01	7.28E-03
3.55	1.87E-04	3.66E-04	9.58E-05	4.39E-06	2.98E+00	8.43E-02	8.57E+00	8.30E-03	1.08E-01	7.09E-03
3.60	1.83E-04	3.54E-04	9.50E-05	4.18E-06	2.98E+00	8.02E-02	8.42E+00	7.71E-03	1.05E-01	6.86E-03
3.65	1.80E-04	3.43E-04	9.46E-05	4.21E-06	2.99E+00	8.06E-02	8.27E+00	7.59E-03	1.01E-01	7.03E-03
3.70	1.77E-04	3.32E-04	9.40E-05	4.16E-06	2.99E+00	7.95E-02	8.12E+00	7.32E-03	9.77E-02	7.05E-03
3.75	1.72E-04	3.26E-04	9.06E-05	4.17E-06	2.96E+00	8.00E-02	7.99E+00	7.12E-03	1.00E-01	7.10E-03
3.80	1.69E-04	3.17E-04	9.05E-05	4.09E-06	2.97E+00	7.79E-02	7.86E+00	6.80E-03	9.67E-02	7.06E-03
3.85	1.66E-04	3.09E-04	8.89E-05	4.23E-06	2.94E+00	8.06E-02	7.73E+00	6.86E-03	9.58E-02	7.36E-03
3.90	1.62E-04	3.01E-04	8.74E-05	3.92E-06	2.93E+00	7.47E-02	7.60E+00	6.18E-03	9.46E-02	6.89E-03
3.95	1.60E-04	2.94E-04	8.68E-05	4.13E-06	2.92E+00	7.82E-02	7.48E+00	6.35E-03	9.27E-02	7.34E-03

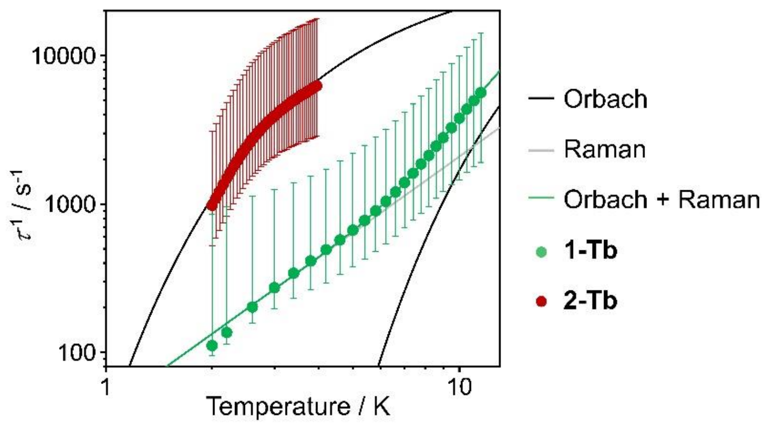

Figure 5. 5. Relaxation time (τ^{-1}) versus temperature (in log scale) plot of **3-Tb** and **4-Tb** (circles in green and maroon, respectively). The solid lines represent each process: Orbach $\tau^{-1} = \tau_0^{-1} exp\left(\frac{-U_{eff}}{T}\right)$ (black), Raman $\tau^{-1} = CT^{n}$ (grey), Orbach + Raman $\tau^{-1} = \tau_0^{-1} exp\left(\frac{-U_{eff}}{T}\right) + CT^{n}$ (green). The best-fit parameters are described in the manuscript. Error bars are calculated from the log-normalized (ln) distribution.[181]

Bibliography

(1) Khanna, R. *Dignity in a Digital Age: Making Tech Work for All of Us*; Simon and Schuster, 2022.

(2) C. E. Shannon. A Mathematical Theory of Communication. *Bell Syst. Tech. J.* **1948**, *27* (3), 379–423. https://doi.org/10.1016/s0016-0032(23)90506-5.

(3) Moore, G. E. Cramming More Components onto Integrated Circuits. *Electronics* **2004**, *38* (8), 114.

(4) Ronse, K. Patterning Infrastructure Development for Advanced EUV Lithography: Continuing Dimensional Scaling Through EUV Lithography to Support Moore's Law. *IEEE Electron Devices Mag.* **2024**, *2* (1), 35–44. https://doi.org/10.1109/med.2023.3336276.

(5) Waldrop, M. M. More Than Moore. *Nature* **2016**, *530* (7589), 144–147. https://doi.org/10.1038/530144a.

(6) Leiserson, C. E.; Thompson, N. C.; Emer, J. S.; Kuszmaul, B. C.; Lampson, B. W.; Sanchez, D.; Schardl, T. B. There's Plenty of Room at the Top: What Will Drive Computer Performance after Moore's Law? *Science* **2020**, *368* (6495). https://doi.org/10.1126/science.aam9744.

(7) Reig, C.; Cardoso, S.; Chandra, S. *Giant Magnetoresistance (GMR) Sensors*; Springer, 2013.

(8) Feynman, R. P. Simulating Physics with Computers. **1982**, *21*, 467–488.

(9) DiVincenzo, D. P. The Physical Implementation of Quantum Computation. *Fortschritte der Phys.* **2000**, *48* (9–11), 771–783. https://doi.org/10.1002/1521-3978(200009)48:9/11<771::AID-PROP771>3.0.CO;2-E.

(10) Ladd, T. D.; Jelezko, F.; Laflamme, R.; Nakamura, Y.; Monroe, C.; O'Brien, J. L. Quantum Computers. *Nature* **2010**, *464* (7285), 45–53. https://doi.org/10.1038/nature08812.

(11) Niemczyk, T.; Deppe, F.; Huebl, H.; Menzel, E. P.; Hocke, F.; Schwarz, M. J.; Zueco, D.; Hümmer, T.; Solano, E.; Marx, A.; Gross, R. Circuit Quantum Electrodynamics in the Ultrastrong-Coupling Regime. *Nat. Phys.* **2010**, *6* (October), 2–6. https://doi.org/10.1038/nphys1730.

(12) Acharya, R.; Aleiner, I.; Allen, R.; Andersen, T. I.; Ansmann, M.; Arute, F.; Arya, K.; Asfaw, A.; Atalaya, J.; Babbush, R.; Bacon, D.; Bardin, J. C.; Basso, J.; Bengtsson, A.; Boixo, S.; Bortoli, G.; Bourassa, A.; Bovaird, J.; Brill, L.; Broughton, M.; Buckley, B. B.; Buell, D. A.; Burger, T.; Burkett, B.; Bushnell, N.; Chen, Y.; Chen, Z.; Chiaro, B.; Cogan, J.; Collins, R.; Conner, P.; Courtney, W.; Crook, A. L.; Curtin, B.; Debroy, D. M.; Del Toro Barba, A.; Demura, S.; Dunsworth, A.; Eppens, D.; Erickson, C.; Faoro, L.; Farhi, E.; Fatemi, R.; Flores Burgos, L.; Forati, E.; Fowler, A. G.; Foxen, B.; Giang, W.; Gidney, C.; Gilboa, D.; Giustina, M.; Grajales Dau, A.; Gross, J. A.; Habegger, S.;

Hamilton, M. C.; Harrigan, M. P.; Harrington, S. D.; Higgott, O.; Hilton, J.; Hoffmann, M.; Hong, S.; Huang, T.; Huff, A.; Huggins, W. J.; Ioffe, L. B.; Isakov, S. V.; Iveland, J.; Jeffrey, E.; Jiang, Z.; Jones, C.; Juhas, P.; Kafri, D.; Kechedzhi, K.; Kelly, J.; Khattar, T.; Khezri, M.; Kieferová, M.; Kim, S.; Kitaev, A.; Klimov, P. V.; Klots, A. R.; Korotkov, A. N.; Kostritsa, F.; Kreikebaum, J. M.; Landhuis, D.; Laptev, P.; Lau, K. M.; Laws, L.; Lee, J.; Lee, K.; Lester, B. J.; Lill, A.; Liu, W.; Locharla, A.; Lucero, E.; Malone, F. D.; Marshall, J.; Martin, O.; McClean, J. R.; McCourt, T.; McEwen, M.; Megrant, A.; Meurer Costa, B.; Mi, X.; Miao, K. C.; Mohseni, M.; Montazeri, S.; Morvan, A.; Mount, E.; Mruczkiewicz, W.; Naaman, O.; Neeley, M.; Neill, C.; Nersisyan, A.; Neven, H.; Newman, M.; Ng, J. H.; Nguyen, A.; Nguyen, M.; Niu, M. Y.; O'Brien, T. E.; Opremcak, A.; Platt, J.; Petukhov, A.; Potter, R.; Pryadko, L. P.; Quintana, C.; Roushan, P.; Rubin, N. C.; Saei, N.; Sank, D.; Sankaragomathi, K.; Satzinger, K. J.; Schurkus, H. F.; Schuster, C.; Shearn, M. J.; Shorter, A.; Shvarts, V.; Skruzny, J.; Smelyanskiy, V.; Smith, W. C.; Sterling, G.; Strain, D.; Szalay, M.; Torres, A.; Vidal, G.; Villalonga, B.; Vollgraff Heidweiller, C.; White, T.; Xing, C.; Yao, Z. J.; Yeh, P.; Yoo, J.; Young, G.; Zalcman, A.; Zhang, Y.; Zhu, N. Suppressing Quantum Errors by Scaling a Surface Code Logical Qubit. *Nature* **2023**, *614* (7949), 676–681. https://doi.org/10.1038/s41586-022-05434-1.

(13) Bruzewicz, C. D.; Chiaverini, J.; Mcconnell, R.; Sage, J. M. Trapped-Ion Quantum Computing : Progress and Challenges. **2019**. https://doi.org/10.1063/1.5088164.

(14) Ryan-Anderson, C.; Bohnet, J. G.; Lee, K.; Gresh, D.; Hankin, A.; Gaebler, J. P.; Francois, D.; Chernoguzov, A.; Lucchetti, D.; Brown, N. C.; Gatterman, T. M.; Halit, S. K.; Gilmore, K.; Gerber, J. A.; Neyenhuis, B.; Hayes, D.; Stutz, R. P. Realization of Real-Time Fault-Tolerant Quantum Error Correction. *Phys. Rev. X* **2021**, *11* (4), 41058. https://doi.org/10.1103/PhysRevX.11.041058.

(15) Saffman, M. Quantum Computing with Atomic Qubits and Rydberg Interactions : Progress and Challenges. **2016**.

(16) Bluvstein, D.; Evered, S. J.; Geim, A. A.; Li, S. H.; Zhou, H.; Manovitz, T.; Ebadi, S.; Cain, M.; Kalinowski, M.; Hangleiter, D.; Ataides, J. P. B.; Maskara, N.; Cong, I.; Gao, X.; Rodriguez, P. S.; Karolyshyn, T.; Semeghini, G.; Gullans, M. J.; Greiner, M.; Vuletić, V.; Lukin, M. D. Logical Quantum Processor Based on Reconfigurable Atom Arrays. *Nature* **2023**, *626* (February). https://doi.org/10.1038/s41586-023-06927-3.

(17) Emanuele Pelucchi, Giorgos Fagas, Igor Aharonovich, Dirk Englund, Eden Figueroa, Qihuang Gong, Hübel Hannes, Jin Liu, Chao-Yang Lu, Nobuyuki Matsuda, Jian-Wei Pan, Florian Schreck, Fabio Sciarrino, Christine Silberhorn, J. W. & K. D. J. The Potential and Global Outlook of Integrated Photonics for Quantum Technologies. *Nat. Rev. Phys.* **2022**, *4* (March), 194–208. https://doi.org/10.1038/s42254-021-00398-z.

(18) Luis, F.; Hill, S.; Coronado, E. Molecular Spins for Quantum Computation. *Nat. Chem.* **2019**, *11* (April), 301–309. https://doi.org/10.1038/s41557-019-0232-y.

(19) Wasielewski, M. R.; Forbes, M. D. E.; Frank, N. L.; Kowalski, K.; Scholes, G. D.; Yuen-Zhou, J.; Baldo, M. A.; Freedman, D. E.; Goldsmith, R. H.; Goodson, T.; Kirk, M. L.; McCusker, J. K.; Ogilvie, J. P.; Shultz, D. A.; Stoll, S.; Whaley, K. B. Exploiting Chemistry and Molecular Systems for Quantum Information Science. *Nat. Rev. Chem.* **2020**, *4* (9), 490–504. https://doi.org/10.1038/s41570-020-0200-5.

(20) Atzori, M.; Sessoli, R. The Second Quantum Revolution: Role and Challenges of

Molecular Chemistry. *Journal of the American Chemical Society*. 2019, pp 11339–11352. https://doi.org/10.1021/jacs.9b00984.

(21) Moreno-Pineda, E.; Martins, D. O. T. A.; Tuna, F. *Molecules as Qubits, Qudits and Quantum Gates*; 2021; Vol. 27. https://doi.org/10.1039/9781839162534-00146.

(22) Sakurai, J. J.; Napolitano, J. *Modern Quantum Mechanics*, Third Edit.; Cambridge University Press: Cambridge, United Kingdom, 1967.

(23) La Pierre, R. *Introduction to Quantum Computing*; Springer, 2021. https://doi.org/10.1002/9781119905172.ch1.

(24) Gerlach, W.; Stern, O. Der Experimentelle Nachweis Der Richtungsquantelung Im Magnetfeld. *Zeitsschrift für Phisik* **1922**, *9*, 349–352.

(25) Fan, X.; Myers, T. G.; Sukra, B. A. D.; Gabrielse, G. Measurement of the Electron Magnetic Moment. *Phys. Rev. Lett.* **2023**, *130* (7), 71801. https://doi.org/10.1103/PhysRevLett.130.071801.

(26) Schweiger, A. Pulsed Electron Spin Resonance Spectroscopy: Basic Principles, Techniques, and Examples of Applications [New Analytical Methods (43)]. *Angew. Chemie Int. Ed. English* **1991**, *30* (3), 265–292. https://doi.org/10.1002/anie.199102651.

(27) Schweiger, A.; Jeschke, G. *Principles of Pulse Electron Paramagnetic Resonance*; Oxford university press, 2001. https://doi.org/10.1093/oso/9780198506348.001.0001.

(28) Price, W. S. *Spin Dynamics: Basics of Nuclear Magnetic Resonance, 2nd Edition.*; 2009; Vol. 34A. https://doi.org/10.1002/cmr.a.20130.

(29) Eaton, S. S.; Eaton, G. R. *Relaxation Mechanisms*; John Wiley & Sons, 2018.

(30) Eaton, S. S.; Eaton, G. R. Relaxation Times of Organic Radicals and Transition Metal Ions. *Distance Meas. Biol. Syst. by EPR* **2000**, 29–154.

(31) Troiani, F.; Ghirri, A.; Affronte, M.; Carretta, S.; Santini, P.; Amoretti, G.; Piligkos, S.; Timco, G.; Winpenny, R. E. P. Molecular Engineering of Antiferromagnetic Rings for Quantum Computation. *Phys. Rev. Lett.* **2005**, *94* (20), 1–4. https://doi.org/10.1103/PhysRevLett.94.207208.

(32) Ardavan, A.; Rival, O.; Morton, J. J. L.; Blundell, S. J.; Tyryshkin, A. M.; Timco, G. A.; Winpenny, R. E. P. Will Spin-Relaxation Times in Molecular Magnets Permit Quantum Information Processing? *Phys. Rev. Lett.* **2007**, *98* (5), 1–4. https://doi.org/10.1103/PhysRevLett.98.057201.

(33) Zadrozny, J. M.; Niklas, J.; Poluektov, O. G.; Freedman, D. E. Millisecond Coherence Time in a Tunable Molecular Electronic Spin Qubit. *ACS Cent. Sci.* **2015**, *1* (9), 488–492. https://doi.org/10.1021/acscentsci.5b00338.

(34) Warner, M.; Din, S.; Tupitsyn, I. S.; Morley, G. W.; Stoneham, A. M.; Gardener, J. A.; Wu, Z.; Fisher, A. J.; Heutz, S.; Kay, C. W. M.; Aeppli, G. Potential for Spin-Based Information Processing in a Thin-Film Molecular Semiconductor. *Nature* **2013**, *503* (7477), 504–508. https://doi.org/10.1038/nature12597.

(35) Atzori, M.; Tesi, L.; Morra, E.; Chiesa, M.; Sorace, L.; Sessoli, R. Room-Temperature Quantum Coherence and Rabi Oscillations in Vanadyl Phthalocyanine: Toward Multifunctional Molecular Spin Qubits. *J. Am. Chem. Soc.* **2016**, *138* (7), 2154–2157. https://doi.org/10.1021/jacs.5b13408.

(36) Bader, K.; Dengler, D.; Lenz, S.; Endeward, B.; Jiang, S. Da; Neugebauer, P.; Van Slageren, J. Room Temperature Quantum Coherence in a Potential Molecular Qubit. *Nat. Commun.* **2014**, *5* (May), 1–5. https://doi.org/10.1038/ncomms6304.

(37) Wedge, C. J.; Timco, G. A.; Spielberg, E. T.; George, R. E.; Tuna, F.; Rigby, S.; McInnes, E. J. L.; Winpenny, R. E. P.; Blundell, S. J.; Ardavan, A. Chemical Engineering of Molecular Qubits. *Phys. Rev. Lett.* **2012**, *108* (10), 1–5. https://doi.org/10.1103/PhysRevLett.108.107204.

(38) Lunghi, A.; Sanvito, S. The Limit of Spin Lifetime in Solid-State Electronic Spins. *J. Phys. Chem. Lett.* **2020**, *11* (15), 6273–6278. https://doi.org/10.1021/acs.jpclett.0c01681.

(39) Lunghi, A. Toward Exact Predictions of Spin-Phonon Relaxation Times: An Ab Initio Implementation of Open Quantum Systems Theory. *Sci. Adv.* **2022**, *8* (31), 1–10. https://doi.org/10.1126/sciadv.abn7880.

(40) Rajasree, S. S.; Li, X.; Deria, P. Physical Properties of Porphyrin-Based Crystalline Metal–organic Frameworks. *Commun. Chem.* **2021**, *4* (1), 1–14. https://doi.org/10.1038/s42004-021-00484-4.

(41) Zadrozny, J. M.; Gallagher, A. T.; Harris, T. D.; Freedman, D. E. A Porous Array of Clock Qubits. *J. Am. Chem. Soc.* **2017**, *139* (20), 7089–7094. https://doi.org/10.1021/jacs.7b03123.

(42) Yamabayashi, T.; Atzori, M.; Tesi, L.; Cosquer, G.; Santanni, F.; Boulon, M. E.; Morra, E.; Benci, S.; Torre, R.; Chiesa, M.; Sorace, L.; Sessoli, R.; Yamashita, M. Scaling Up Electronic Spin Qubits into a Three-Dimensional Metal-Organic Framework. *J. Am. Chem. Soc.* **2018**, *140* (38), 12090–12101. https://doi.org/10.1021/jacs.8b06733.

(43) Yu, C. J.; Krzyaniak, M. D.; Fataftah, M. S.; Wasielewski, M. R.; Freedman, D. E. A Concentrated Array of Copper Porphyrin Candidate Qubits. *Chem. Sci.* **2019**, *10* (6), 1702–1708. https://doi.org/10.1039/c8sc04435j.

(44) Aguilà, D.; Barrios, L. A.; Velasco, V.; Roubeau, O.; Repollés, A.; Alonso, P. J.; Sesé, J.; Teat, S. J.; Luis, F.; Aromí, G. Heterodimetallic [LnLn’] Lanthanide Complexes: Toward a Chemical Design of Two-Qubit Molecular Spin Quantum Gates. *J. Am. Chem. Soc.* **2014**, *136* (40), 14215–14222. https://doi.org/10.1021/ja507809w.

(45) Ranieri, D.; Santanni, F.; Privitera, A.; Albino, A.; Salvadori, E.; Chiesa, M.; Totti, F.; Sorace, L.; Sessoli, R. An Exchange Coupled Meso-Meso Linked Vanadyl Porphyrin Dimer for Quantum Information Processing. *Chem. Sci.* **2022**, *14* (1), 61–69. https://doi.org/10.1039/d2sc04969d.

(46) Ranieri, D.; Privitera, A.; Santanni, F.; Urbanska, K.; Strachan, G. J.; Twamley, B.; Salvadori, E.; Liao, Y. K.; Chiesa, M.; Senge, M. O.; Totti, F.; Sorace, L.; Sessoli, R. A Heterometallic Porphyrin Dimer as a Potential Quantum Gate: Magneto-Structural Correlations and Spin Coherence Properties. *Angew. Chemie - Int. Ed.* **2023**, *62* (48).

https://doi.org/10.1002/anie.202312936.

(47) Vitorica-yrezabal, J.; Tuna, F.; Timco, G. A.; Mcinnes, E. J. L.; Carretta, S.; Santini, P.; Winpenny, R. E. P. A Modular Design of Molecular Qubits to Implement Universal Quantum Gates Jesu´s. *Nat. Commun.* **2016**, *7*, 11377. https://doi.org/10.1038/ncomms11377.

(48) M. Gomberg. AN INSTANCE OF TRIVALENT CARBON: TRIPHENYLMETHYL. *J. Am. Chem. Soc.* **1900**, *22* (11), 757–771.

(49) *Stable Radicals: Fundamentals and Applied Aspects of Odd-Electron Compounds*; Hicks, R. G., Ed.; John Wiley & Son, 2010. https://doi.org/10.1002/9780470666975.ch5.

(50) Mizuno, A.; Matsuoka, R.; Mibu, T.; Kusamoto, T. Luminescent Radicals. *Chem. Rev.* **2024**, *124* (3), 1034–1121. https://doi.org/10.1021/acs.chemrev.3c00613.

(51) Chen, Z. X.; Li, Y.; Huang, F. Persistent and Stable Organic Radicals: Design, Synthesis, and Applications. *Chem*. 2021, pp 288–332. https://doi.org/10.1016/j.chempr.2020.09.024.

(52) Kubo, T.; Abe, M. Introduction: Persistent and Stable Organic Radicals. *Chem. Rev.* **2024**, *124* (8), 4541–4542. https://doi.org/10.1021/acs.chemrev.3c00893.

(53) Zhou, A.; Sun, Z.; Sun, L.; Zhou, A.; Sun, Z.; Sun, L. Stable Organic Radical Qubits and Their Applications in Quantum Information Science Stable Organic Radical Qubits and Their Applications in Quantum Information Science. *Innov.* **2024**, *5* (5), 100662. https://doi.org/10.1016/j.xinn.2024.100662.

(54) Chen, J. S.; Trerayapiwat, K. J.; Sun, L.; Krzyaniak, M. D.; Wasielewski, M. R.; Rajh, T.; Sharifzadeh, S.; Ma, X. Long-Lived Electronic Spin Qubits in Single-Walled Carbon Nanotubes. *Nat. Commun.* **2023**, *14* (1), 1–8. https://doi.org/10.1038/s41467-023-36031-z.

(55) Slota, M.; Keerthi, A.; Myers, W. K.; Tretyakov, E.; Baumgarten, M.; Ardavan, A.; Sadeghi, H.; Lambert, C. J.; Narita, A.; Müllen, K.; Bogani, L. Magnetic Edge States and Coherent Manipulation of Graphene Nanoribbons. *Nature*. 2018, p E31. https://doi.org/10.1038/s41586-018-0297-6.

(56) Lombardi, F.; Lodi, A.; Ma, J.; Liu, J.; Slota, M.; Narita, A.; Myers, W. K.; Müllen, K.; Feng, X.; Bogani, L. Quantum Units from the Topological Engineering of Molecular Graphenoids. *Science* **2019**, *366* (6469), 1107–1110. https://doi.org/10.1126/science.aay7203.

(57) Suryadevara, N.; Boudalis, A. K.; Olivares Peña, J. E.; Moreno-Pineda, E.; Fediai, A.; Wenzel, W.; Turek, P.; Ruben, M. Molecular-Engineered Biradicals Based on the YIII-Phthalocyanine Platform. *J. Am. Chem. Soc.* **2023**, *145* (4), 2461–2472. https://doi.org/10.1021/jacs.2c11760.

(58) Piao, Y.; Meany, B.; Powell, L. R.; Valley, N.; Kwon, H.; Schatz, G. C.; Wang, Y. Brightening of Carbon Nanotube Photoluminescence through the Incorporation of Sp 3 Defects. *Nat. Chem.* **2013**, *5* (10), 840–845. https://doi.org/10.1038/nchem.1711.

(59) Lohmann, S. H.; Trerayapiwat, K. J.; Niklas, J.; Poluektov, O. G.; Sharifzadeh, S.; Ma, X. Sp3-Functionalization of Single-Walled Carbon Nanotubes Creates Localized Spins. *ACS Nano* **2020**, *14* (12), 17675–17682. https://doi.org/10.1021/acsnano.0c08782.

(60) Boudalis, A. K.; Olivares-Peña, J. E.; Moreno-Pineda, E.; Fediai, A.; Wenzel, W.; Turek, P.; Ruben, M. Room-Temperature Spin Nutations in a Magnetically Condensed Phase of [Y(Pc)2]•. *Chem. Commun.* **2021**, *57* (87), 11505–11508. https://doi.org/10.1039/d1cc05491k.

(61) Branzoli, F.; Carretta, P.; Filibian, M.; Klyatskaya, S.; Ruben, M. Low-Energy Spin Dynamics in the [YPc2]0 S=12 Antiferromagnetic Chain. *Phys. Rev. B - Condens. Matter Mater. Phys.* **2011**, *83* (17), 1–5. https://doi.org/10.1103/PhysRevB.83.174419.

(62) Tesi, L.; Stemmler, F.; Winkler, M.; Liu, S. S. Y.; Das, S.; Sun, X.; Zharnikov, M.; Ludwigs, S.; van Slageren, J. Modular Approach to Creating Functionalized Surface Arrays of Molecular Qubits. *Adv. Mater.* **2023**, *35* (10). https://doi.org/10.1002/adma.202208998.

(63) Hou, L.; Zhang, Y. S.; Zhang, Y.; Jiang, S. Da; Wang, M. Tunable Quantum Coherence of Luminescent Molecular Spins Organized via Block Copolymer Self-Assembly. *Adv. Quantum Technol.* **2024**, *2400064*, 1–9. https://doi.org/10.1002/qute.202400064.

(64) Oanta, A. K.; Collins, K. A.; Evans, A. M.; Pratik, S. M.; Hall, L. A.; Strauss, M. J.; Marder, S. R.; D'Alessandro, D. M.; Rajh, T.; Freedman, D. E.; Li, H.; Brédas, J. L.; Sun, L.; Dichtel, W. R. Electronic Spin Qubit Candidates Arrayed within Layered Two-Dimensional Polymers. *J. Am. Chem. Soc.* **2023**, *145* (1), 689–696. https://doi.org/10.1021/jacs.2c11784.

(65) Orihashi, K.; Yamauchi, A.; Fujiwara, S.; Asada, M.; Nakamura, T.; Ka-Ho Hui, J.; Kimizuka, N.; Tateishi, K.; Uesaka, T.; Yanai, N. Spin-Polarized Radicals with Extremely Long Spin-Lattice Relaxation Time at Room Temperature in a Metal-Organic Framework. *J. Am. Chem. Soc.* **2023**, *145* (50), 27650–27656. https://doi.org/10.1021/jacs.3c09563.

(66) Nakazawa, S.; Nishida, S.; Ise, T.; Yoshino, T.; Mori, N.; Rahimi, R. D.; Sato, K.; Morita, Y.; Toyota, K.; Shiomi, D.; Kitagawa, M.; Hara, H.; Carl, P.; Höfer, P.; Takui, T. A Synthetic Two-Spin Quantum Bit: G-Engineered Exchange-Coupled Biradical Designed for Controlled-NOT Gate Operations. *Angew. Chemie - Int. Ed.* **2012**, *51* (39), 9860–9864. https://doi.org/10.1002/anie.201204489.

(67) Little, E. J.; Mrozek, J.; Rogers, C. J.; Liu, J.; McInnes, E. J. L.; Bowen, A. M.; Ardavan, A.; Winpenny, R. E. P. Title: Experimental Realisation of Multi-Qubit Gates Using Electron Paramagnetic Resonance. *Nat. Commun.* **2023**, *14* (1), 1–37. https://doi.org/10.1038/s41467-023-42169-7.

(68) Schäfter, D.; Wischnat, J.; Tesi, L.; De Sousa, J. A.; Little, E.; McGuire, J.; Mas-Torrent, M.; Rovira, C.; Veciana, J.; Tuna, F.; Crivillers, N.; van Slageren, J. Molecular One- and Two-Qubit Systems with Very Long Coherence Times. *Adv. Mater.* **2023**, *35* (38), 1–11. https://doi.org/10.1002/adma.202302114.

(69) Nelson, J. N.; Zhang, J.; Zhou, J.; Rugg, B. K.; Krzyaniak, M. D.; Wasielewski, M. R. CNOT Gate Operation on a Photogenerated Molecular Electron Spin-Qubit Pair. *J.*

Chem. Phys. **2020**, *152* (1). https://doi.org/10.1063/1.5128132.

(70) Teki, Y. Excited-State Dynamics of Non-Luminescent and Luminescent π-Radicals. *Chem. Eur. J.* **2020**, *26* (5), 980–996. https://doi.org/10.1002/chem.201903444.

(71) Quintes, T.; Mayländer, M.; Richert, S. Properties and Applications of Photoexcited Chromophore–Radical Systems. *Nat. Rev. Chem.* **2023**, *7* (2), 75–90. https://doi.org/10.1038/s41570-022-00453-y.

(72) Mayländer, M.; Chen, S.; Lorenzo, E. R.; Wasielewski, M. R.; Richert, S. Exploring Photogenerated Molecular Quartet States as Spin Qubits and Qudits. *J. Am. Chem. Soc.* **2021**, *143* (18), 7050–7058. https://doi.org/10.1021/jacs.1c01620.

(73) Mayländer, M.; Nolden, O.; Franz, M.; Chen, S.; Bancroft, L.; Qiu, Y.; Wasielewski, M. R.; Gilch, P.; Richert, S. Accessing the Triplet State of Perylenediimide by Radical-Enhanced Intersystem Crossing. *Chem. Sci.* **2022**, *13* (22), 6732–6743. https://doi.org/10.1039/d2sc01899c.

(74) Mayländer, M.; Thielert, P.; Quintes, T.; Vargas Jentzsch, A.; Richert, S. Room Temperature Electron Spin Coherence in Photogenerated Molecular Spin Qubit Candidates. *J. Am. Chem. Soc.* **2023**, *145* (25), 14064–14069. https://doi.org/10.1021/jacs.3c04021.

(75) Kobr, L.; Gardner, D. M.; Smeigh, A. L.; Dyar, S. M.; Karlen, S. D.; Carmieli, R.; Wasielewski, M. R. Fast Photodriven Electron Spin Coherence Transfer: A Quantum Gate Based on a Spin Exchange J-Jump. *J. Am. Chem. Soc.* **2012**, *134* (30), 12430–12433. https://doi.org/10.1021/ja305650x.

(76) Qiu, Y.; Eckvahl, H. J.; Equbal, A.; Krzyaniak, M. D.; Wasielewski, M. R. Enhancing Coherence Times of Chromophore-Radical Molecular Qubits and Qudits by Rational Design. *J. Am. Chem. Soc.* **2023**, *145* (47), 25903–25909. https://doi.org/10.1021/jacs.3c10772.

(77) Gorgon, S.; Lv, K.; Grüne, J.; Drummond, B. H.; Myers, W. K.; Londi, G.; Ricci, G.; Valverde, D.; Tonnelé, C.; Murto, P.; Romanov, A. S.; Casanova, D.; Dyakonov, V.; Sperlich, A.; Beljonne, D.; Olivier, Y.; Li, F.; Friend, R. H.; Evans, E. W. Reversible Spin-Optical Interface in Luminescent Organic Radicals. *Nature* **2023**, *620* (7974), 538–544. https://doi.org/10.1038/s41586-023-06222-1.

(78) Ai, X.; Evans, E. W.; Dong, S.; Gillett, A. J.; Guo, H.; Chen, Y.; Hele, T. J. H.; Friend, R. H.; Li, F. Efficient Radical-Based Light-Emitting Diodes with Doublet Emission. *Nature* **2018**, *563* (7732), 536–540. https://doi.org/10.1038/s41586-018-0695-9.

(79) Minyung Lee, Ok-Keun Song, Jung-Chul Seo, D. K. Low-Lying Electronically Excited States of C6o and C7o and Measurement of Their Picosecond Transient Absorption in Solution. *Chem. Phys. Lett.* **1992**, *196* (3), 325–329.

(80) Wang, Y. X.; Liu, Z.; Fang, Y. H.; Zhou, S.; Jiang, S. Da; Gao, S. Coherent Manipulation and Quantum Phase Interference in a Fullerene-Based Electron Triplet Molecular Qutrit. *npj Quantum Inf.* **2021**, *7* (1). https://doi.org/10.1038/s41534-021-00362-w.

(81) Tykwinski, R. R.; Guldi, D. M. Singlet Fission. *ChemPhotoChem*. 2021, p 392.

https://doi.org/10.1002/cptc.202100053.

(82) Wilson, M. W. B.; Rao, A.; Ehrler, B.; Friend, R. H. Singlet Exciton Fission in Polycrystalline Pentacene: From Photophysics toward Devices. *Accounts of Chemical Research*. 2013, pp 1330–1338. https://doi.org/10.1021/ar300345h.

(83) Yamauchi, A.; Tanaka, K.; Fuki, M.; Fujiwara, S.; Kimizuka, N.; Ryu, T.; Saigo, M.; Onda, K.; Kusumoto, R.; Ueno, N.; Sato, H.; Kobori, Y.; Miyata, K.; Yanai, N. Room-Temperature Quantum Coherence of Entangled Multiexcitons in a Metal-Organic Framework. *Sci. Adv.* **2024**, *10* (1), 1–12. https://doi.org/10.1126/sciadv.adi3147.

(84) Matsuoka, R.; Mizuno, A.; Mibu, T.; Kusamoto, T. Luminescence of Doublet Molecular Systems. *Coord. Chem. Rev.* **2022**, *467*, 214616. https://doi.org/10.1016/j.ccr.2022.214616.

(85) Daintith, J. *A Dictionary of Physical Sciences*; Springer, 1976.

(86) Gatteschi, D.; Sessoli, R.; Villain, J. *Molecular Nanomagnets*; Oxford university press, 2006.

(87) Zabala-Lekuona, A.; Seco, J. M.; Colacio, E. Single-Molecule Magnets: From Mn12-Ac to Dysprosium Metallocenes, a Travel in Time. *Coord. Chem. Rev.* **2021**, *441*, 213984. https://doi.org/10.1016/j.ccr.2021.213984.

(88) Novak, M. A.; Sessoli, R.; Gatteschi, D.; Caneschi, A. Magnetic Bistability in a Metal-Ion Cluster. *Nature* **1993**, *365* (365), 141–143.

(89) Ishikawa, N.; Sugita, M.; Ishikawa, T.; Koshihara, S.; Kaizu, Y. Lanthanide Double-Decker Complexes Functioning as Magnets at the Single-Molecular Level. *J. Am. Chem. Soc.* **2003**, 8694–8695.

(90) Katoh, K.; Yoshida, Y.; Yamashita, M.; Miyasaka, H.; Breedlove, B. K.; Kajiwara, T.; Takaishi, S.; Ishikawa, N.; Isshiki, H.; Yan, F. Z.; Komeda, T.; Yamagishi, M.; Takeya, J. Direct Observation of Lanthanide(III)-Phthalocyanine Molecules on Au(111) by Using Scanning Tunneling Microscopy and Scanning Tunneling Spectroscopy and Thin-Film Field-Effect Transistor Properties of Tb(III)- and Dy(III)-Phthalocyanine Molecules. *J. Am. Chem. Soc.* **2009**, *131* (29), 9967–9976. https://doi.org/10.1021/ja902349t.

(91) Martynov, A. G.; Horii, Y.; Katoh, K.; Bian, Y.; Jiang, J.; Yamashita, M.; Gorbunova, Y. G. Rare-Earth Based Tetrapyrrolic Sandwiches: Chemistry, Materials and Applications. *Chem. Soc. Rev.* **2022**, *51* (22), 9262–9339. https://doi.org/10.1039/d2cs00559j.

(92) Marin, R.; Brunet, G.; Murugesu, M. Shining New Light on Multifunctional Lanthanide Single-Molecule Magnets. *Angew. Chemie - Int. Ed.* **2021**, *60* (4), 1728–1746. https://doi.org/10.1002/anie.201910299.

(93) Buchner, M.; Höfler, K.; Henne, B.; Ney, V.; Ney, A. Tutorial: Basic Principles, Limits of Detection, and Pitfalls of Highly Sensitive SQUID Magnetometry for Nanomagnetism and Spintronics. *J. Appl. Phys.* **2018**, *124* (16). https://doi.org/10.1063/1.5045299.

(94) Mugiraneza, S.; Hallas, A. M. Tutorial: A Beginner's Guide to Interpreting Magnetic Susceptibility Data with the Curie-Weiss Law. *Commun. Phys.* **2022**, *5* (1). https://doi.org/10.1038/s42005-022-00853-y.

(95) Benelli, C.; Gatteschi, D. Magnetism of Lanthanides in Molecular Materials with Transition-Metal Ions and Organic Radicals. *Chem. Rev.* **2002**, *102* (6), 2369–2387. https://doi.org/10.1021/cr010303r.

(96) Abragam, A Bleaney, B. *Electron Paramagnetic Resonance of Transition Ions*; 2015; Vol. 1542.

(97) Vieru, V.; Gómez-Coca, S.; Ruiz, E.; Chibotaru, L. Increasing the Magnetic Blocking Temperature of Single-Molecule Magnets. *Angew. Chemie Int. Ed.* **2023**, *202303146*. https://doi.org/10.1002/anie.202303146.

(98) Goodwin, C. A. P. To High-Temperature Lanthanide Single Molecule Magnets. **2020**, 14320–14337. https://doi.org/10.1039/d0dt01904f.

(99) Duan, Y.; Rosaleny, L. E.; Coutinho, J. T.; Giménez-santamarina, S.; Scheie, A.; Baldoví, J. J.; Cardona-serra, S.; Gaita-ariño, A. Data-Driven Design of Molecular Nanomagnets. *Nat. Commun.* **2022**, No. July, 1–11. https://doi.org/10.1038/s41467-022-35336-9.

(100) Rinehart, J. D.; Long, J. R. Exploiting Single-Ion Anisotropy in the Design of f-Element Single-Molecule Magnets. *Chem. Sci.* **2011**, *2* (11), 2078–2085. https://doi.org/10.1039/c1sc00513h.

(101) Giansiracusa, M. J.; Kostopoulos, A. K.; Collison, D.; Winpenny, R. E. P.; Chilton, N. F. Correlating Blocking Temperatures with Relaxation Mechanisms in Monometallic Single-Molecule Magnets with High Energy Barriers (: U Eff > 600 K). *Chem. Commun.* **2019**, *55* (49), 7025–7028. https://doi.org/10.1039/c9cc02421b.

(102) Woodru, D. N.; Winpenny, R. E. P.; Lay, R. A. Lanthanide Single-Molecule Magnets. *Chem. Rev.* **2013**, *113*, 5110–5148.

(103) Guo, F. S.; Day, B. M.; Chen, Y. C.; Tong, M. L.; Mansikkamäki, A.; Layfield, R. A. Magnetic Hysteresis up to 80 Kelvin in a Dysprosium Metallocene Single-Molecule Magnet. *Science* **2018**, *362* (6421), 1400–1403. https://doi.org/10.1126/science.aav0652.

(104) Demir, S.; Jeon, I. R.; Long, J. R.; Harris, T. D. Radical Ligand-Containing Single-Molecule Magnets. *Coord. Chem. Rev.* **2015**, *289–290* (1), 149–176. https://doi.org/10.1016/j.ccr.2014.10.012.

(105) Li, H. D.; Wu, S. G.; Tong, M. L. Lanthanide-Radical Single-Molecule Magnets: Current Status and Future Challenges. *Chem. Commun.* **2023**. https://doi.org/10.1039/d2cc07042a.

(106) Ishikawa, N.; Sugita, M.; Tanaka, N.; Ishikawa, T.; Koshihara, S. Y.; Kaizu, Y. Upward Temperature Shift of the Intrinsic Phase Lag of the Magnetization of Bis(Phthalocyaninato)Terbium by Ligand Oxidation Creating an S = 1/2 Spin. *Inorg. Chem.* **2004**, *43* (18), 5498–5500. https://doi.org/10.1021/ic049348b.

(107) Ishikawa, N.; Mizuno, Y.; Takamatsu, S.; Ishikawa, T.; Koshihara, S. Effects of

Chemically Induced Contraction of a Coordination Polyhedron on the Dynamical Magnetism of Bis (Phthalocyaninato) Disprosium , a Single-4f-Ionic Single-Molecule Magnet with a Kramers Ground State. *Inorg. Chem.* **2008**, *47* (22), 10217–10219.

(108) Ishikawa, N.; Ohno, O.; Kaizu, Y.; Kobayashi, H. Localized Orbital Study on the Electronic Structure of Phthalocyanine Dimers. *J. Phys. Chem.* **1992**, *96* (22), 8832–8839. https://doi.org/10.1021/j100201a028.

(109) Naoto Ishikawa, Osamu Ohno, and Y. K. Electronic States of Bis(Phthalocyaninato)Lutetium Radical and Its Related Compounds: The Application of Localized Orbital Basis Set to Open-Shell Phthalocyanine Dimers. *J. Phys. Chem.* **1993**, *97*, 1004–1010.

(110) Hu, P.; Wang, X.; Ma, Y.; Wang, Q.; Li, L.; Liao, D. A New Family of Ln-Radical Chains (Ln = Nd, Sm, Gd, Tb and Dy): Synthesis, Structure, and Magnetic Properties. *Dalt. Trans.* **2014**, *43* (5), 2234–2243. https://doi.org/10.1039/c3dt52959b.

(111) Rinehart, J. D.; Fang, M.; Evans, W. J.; Long, J. R. Strong Exchange and Magnetic Blocking in N23-- Radical-Bridged Lanthanide Complexes. *Nat. Chem.* **2011**, *3* (7), 538–542. https://doi.org/10.1038/nchem.1063.

(112) Vieru, V.; Iwahara, N.; Ungur, L.; Chibotaru, L. F. Giant Exchange Interaction in Mixed Lanthanides. *Sci. Rep.* **2016**, *6*, 1–8. https://doi.org/10.1038/srep24046.

(113) Liu, F.; Spree, L.; Krylov, D. S.; Velkos, G.; Avdoshenko, S. M.; Popov, A. A. Single-Electron Lanthanide-Lanthanide Bonds Inside Fullerenes toward Robust Redox-Active Molecular Magnets. *Acc. Chem. Res.* **2019**, *52* (10), 2981–2993. https://doi.org/10.1021/acs.accounts.9b00373.

(114) Rinehart, J. D.; Fang, M.; Evans, W. J.; Long, J. R. A N23- Radical-Bridged Terbium Complex Exhibiting Magnetic Hysteresis at 14 K. *J. Am. Chem. Soc.* **2011**, *133* (36), 14236–14239. https://doi.org/10.1021/ja206286h.

(115) Demir, S.; Gonzalez, M. I.; Darago, L. E.; Evans, W. J.; Long, J. R. Giant Coercivity and High Magnetic Blocking Temperatures for N23- Radical-Bridged Dilanthanide Complexes upon Ligand Dissociation /639/638/263/406 /639/638/911 /639/638/298/920 Article. *Nat. Commun.* **2017**, *8* (1), 1–9. https://doi.org/10.1038/s41467-017-01553-w.

(116) Demir, S.; Zadrozny, J. M.; Nippe, M.; Long, J. R. Exchange Coupling and Magnetic Blocking in Bipyrimidyl Radical-Bridged Dilanthanide Complexes. *J. Am. Chem. Soc.* **2012**, *134* (45), 18546–18549. https://doi.org/10.1021/ja308945d.

(117) Gould, C. A.; Mu, E.; Vieru, V.; Darago, L. E.; Chakarawet, K.; Gonzalez, M. I.; Demir, S.; Long, J. R. Substituent Effects on Exchange Coupling and Magnetic Relaxation in 2,2′-Bipyrimidine Radical-Bridged Dilanthanide Complexes. *J. Am. Chem. Soc.* **2020**, *142* (50), 21197–21209. https://doi.org/10.1021/jacs.0c10612.

(118) Gould, C. A.; McClain, K. R.; Reta, D.; Kragskow, J. G. C.; Marchiori, D. A.; Lachman, E.; Choi, E. S.; Analytis, J. G.; Britt, R. D.; Chilton, N. F.; Harvey, B. G.; Long, J. R. Ultrahard Magnetism from Mixed-Valence Dilanthanide Complexes with Metal-Metal Bonding. *Science* **2022**, *375* (6577), 198–202. https://doi.org/10.1126/science.abl5470.

(119) Morita, T.; Damjanović, M.; Katoh, K.; Kitagawa, Y.; Yasuda, N.; Lan, Y.; Wernsdorfer, W.; Breedlove, B. K.; Enders, M.; Yamashita, M. Comparison of the Magnetic Anisotropy and Spin Relaxation Phenomenon of Dinuclear Terbium(III) Phthalocyaninato Single-Molecule Magnets Using the Geometric Spin Arrangement. *J. Am. Chem. Soc.* **2018**, *140* (8), 2995–3007. https://doi.org/10.1021/jacs.7b12667.

(120) Thomas, L.; Lionti, F.; Ballou, R.; Gatteschi, D.; Sessoli, R.; Barbara, B. Macroscopic Quantum Tunnelling of Magnetization in a Single Crystal of Nanomagnets. *Nature* **1996**, *383* (6596), 145–147. https://doi.org/10.1038/383145a0.

(121) Leuenberger, M. N.; Loss, D. Quantum Computing in Molecularmagnets. *Nature* **2001**, *410* (April), 789–793.

(122) Hill, S.; Edwards, R. S.; Aliaga-Alcalde, N.; Christou, G. Quantum Coherence in an Exchange-Couped Dimer of Single-Molecule Magnets. *Science* **2003**, *302* (5647), 1015–1018. https://doi.org/10.1126/science.1090082.

(123) Ishikawa, N.; Sugita, M.; Wernsdorfer, W. Quantum Tunneling of Magnetization in Lanthanide Single-Molecule Magnets: Bis(Phthalocyaninato)Terbium and Bis(Phthalocyaninato)Dysprosium Anions. *Angew. Chemie - Int. Ed.* **2005**, *44* (19), 2931–2935. https://doi.org/10.1002/anie.200462638.

(124) Moreno-Pineda, E.; Damjanović, M.; Fuhr, O.; Wernsdorfer, W.; Ruben, M. Nuclear Spin Isomers: Engineering a Et4N[DyPc2] Spin Qudit. *Angew. Chemie - Int. Ed.* **2017**, *56* (33), 9915–9919. https://doi.org/10.1002/anie.201706181.

(125) Maurer, P. C.; Kucsko, G.; Latta, C.; Jiang, L.; Yao, N. Y.; Bennett, S. D.; Pastawski, F.; Hunger, D.; Chisholm, N.; Markham, M.; Twitchen, D. J.; Ignacio Cirac, J.; Lukin, M. D. Room-Temperature Quantum Bit Memory Exceeding One Second. *Science* **2012**, *336* (June), 1283–1286.

(126) Vincent, R.; Klyatskaya, S.; Ruben, M.; Wernsdorfer, W.; Balestro, F. Electronic Read-out of a Single Nuclear Spin Using a Molecular Spin Transistor. *Nature* **2012**, *488* (7411), 357–360. https://doi.org/10.1038/nature11341.

(127) Thiele, S.; Balestro, F.; Ballou, R.; Klyatskaya, S.; Ruben, M.; Wernsdorfer, W. Electrically Driven Nuclear Spin Resonance in Single-Molecule Magnets. *Science* **2014**, *344* (6188), 1135–1138. https://doi.org/10.1126/science.1249802.

(128) Godfrin, C.; Ferhat, A.; Ballou, R.; Klyatskaya, S.; Ruben, M.; Wernsdorfer, W.; Balestro, F. Operating Quantum States in Single Magnetic Molecules: Implementation of Grover's Quantum Algorithm. *Phys. Rev. Lett.* **2017**, *119* (18), 1–5. https://doi.org/10.1103/PhysRevLett.119.187702.

(129) Godfrin, C.; Thiele, S.; Ferhat, A.; Klyatskaya, S.; Ruben, M.; Wernsdorfer, W.; Balestro, F. Electrical Read-Out of a Single Spin Using an Exchange-Coupled Quantum Dot. *ACS Nano* **2017**, *11* (4), 3984–3989. https://doi.org/10.1021/acsnano.7b00451.

(130) Janković, D.; Hartmann, J. G.; Ruben, M.; Hervieux, P. A. Noisy Qudit vs Multiple Qubits: Conditions on Gate Efficiency for Enhancing Fidelity. *npj Quantum Inf.* **2024**, *10* (1), 1–10. https://doi.org/10.1038/s41534-024-00829-6.

(131) Chiesa, A.; Roca, S.; Chicco, S.; De Ory, M. C.; Gómez-León, A.; Gomez, A.; Zueco, D.; Luis, F.; Carretta, S. Blueprint for a Molecular-Spin Quantum Processor. *Phys. Rev. Appl.* **2023**, *19* (6), 1. https://doi.org/10.1103/PhysRevApplied.19.064060.

(132) Mezzadri, M.; Chiesa, A.; Lepori, L.; Carretta, S. Fault-Tolerant Computing with Single-Qudit Encoding in a Molecular Spin. *Mater. Horizons* **2024**, 25–28. https://doi.org/10.1039/d4mh00454j.

(133) Vitali, L.; Fabris, S.; Conte, A. M.; Brink, S.; Ruben, M.; Baroni, S.; Kern, K. Electronic Structure of Surface-Supported Bis(Phthalocyaninato) Terbium(Lll) Single Molecular Magnets. *Nano Lett.* **2008**, *8* (10), 3364–3368. https://doi.org/10.1021/nl801869b.

(134) Gómez-Segura, J.; Díez-Pérez, I.; Ishikawa, N.; Nakano, M.; Veciana, J.; Ruiz-Molina, D. 2-D Self-Assembly of the Bis(Phthalocyaninato)Terbium(III) Single-Molecule Magnet Studied by Scanning Tunnelling Microscopy. *Chem. Commun.* **2006**, No. 27, 2866–2868. https://doi.org/10.1039/b606276h.

(135) Zhang, Y. F.; Isshiki, H.; Katoh, K.; Yoshida, Y.; Yamashita, M.; Miyasaka, H.; Breedlove, B. K.; Kajiwara, T.; Takaishi, S.; Komeda, T. Low-Temperature Scanning Tunneling Microscopy Investigation of Bis(Phthalocyaninato)Yttrium Growth on Au(111): From Individual Molecules to Two-Dimensional Domains. *J. Phys. Chem. C* **2009**, *113* (22), 9826–9830. https://doi.org/10.1021/jp902410q.

(136) Komeda, T.; Isshiki, H.; Liu, J.; Zhang, Y. F.; Lorente, N.; Katoh, K.; Breedlove, B. K.; Yamashita, M. Observation and Electric Current Control of a Local Spin in a Single-Molecule Magnet. *Nat. Commun.* **2011**, *2* (1). https://doi.org/10.1038/ncomms1210.

(137) Frauhammer, T.; Chen, H.; Balashov, T.; Derenbach, G.; Klyatskaya, S.; Moreno-Pineda, E.; Ruben, M.; Wulfhekel, W. Indirect Spin-Readout of Rare-Earth-Based Single-Molecule Magnet with Scanning Tunneling Microscopy. *Phys. Rev. Lett.* **2021**, *127* (12), 123201. https://doi.org/10.1103/PhysRevLett.127.123201.

(138) Moreno-Pineda, E.; Klyatskaya, S.; Du, P.; Damjanović, M.; Taran, G.; Wernsdorfer, W.; Ruben, M. Observation of Cooperative Electronic Quantum Tunneling: Increasing Accessible Nuclear States in a Molecular Qudit. *Inorg. Chem.* **2018**, *57* (16), 9873–9879. https://doi.org/10.1021/acs.inorgchem.8b00823.

(139) Biard, H.; Moreno-Pineda, E.; Ruben, M.; Bonet, E.; Wernsdorfer, W.; Balestro, F. Increasing the Hilbert Space Dimension Using a Single Coupled Molecular Spin. *Nat. Commun.* **2021**, *12* (1), 1–8. https://doi.org/10.1038/s41467-021-24693-6.

(140) Horii, Y.; Damjanović, M.; Ajayakumar, M. R.; Katoh, K.; Kitagawa, Y.; Chibotaru, L.; Ungur, L.; Mas-Torrent, M.; Wernsdorfer, W.; Breedlove, B. K.; Enders, M.; Veciana, J.; Yamashita, M. Highly Oxidized States of Phthalocyaninato Terbium(III) Multiple-Decker Complexes Showing Structural Deformations, Biradical Properties and Decreases in Magnetic Anisotropy. *Chem. Eur. J.* **2020**, *26* (39), 8621–8630. https://doi.org/10.1002/chem.202001365.

(141) Gonidec, M.; Davies, E. S.; McMaster, J.; Amabilino, D. B.; Veciana, J. Probing the Magnetic Properties of Three Interconvertible Redox States of a Single-Molecule Magnet with Magnetic Circular Dichroism Spectroscopy. *J. Am. Chem. Soc.* **2010**, *132* (6), 1756–1757. https://doi.org/10.1021/ja9095895.

(142) Ishikawa, N.; Otsuka, S.; Kaizu, Y. The Effect of the F-f Interaction on the Dynamic Magnetism of a Coupled 4f8 System in a Dinuclear Terbium Complex with Phthalocyanines. *Angew. Chemie - Int. Ed.* **2005**, *44* (5), 731–733. https://doi.org/10.1002/anie.200461546.

(143) Katoh, K.; Breedlove, B. K.; Yamashita, M. Symmetry of Octa-Coordination Environment Has a Substantial Influence on Dinuclear TbIII Triple-Decker Single-Molecule Magnets. *Chem. Sci.* **2016**, *7* (7), 4329–4340. https://doi.org/10.1039/c5sc04669f.

(144) Komeda, J.; Boudalis, A. K.; Montenegro-Pohlhammer, N.; Antheaume, C.; Mizuno, A.; Turek, P.; Ruben, M. Selective Transition Enhancement in a G-Engineered Diradical. *Chem. Eur. J.* **2024**, *202400420*. https://doi.org/10.1002/chem.202400420.

(145) Volkov, M. Y.; Salikhov, K. M. Pulse Protocols for Quantum Computing with Electron Spins as Qubits. *Appl. Magn. Reson.* **2011**, *41* (2–4), 145–154. https://doi.org/10.1007/s00723-011-0297-2.

(146) Barrett, A. G. M.; Hanson, G. R.; White, A. J. P.; Williams, D. J.; Micallef, A. S. Synthesis of Nitroxide-Functionalized Phthalocyanines. *Tetrahedron* **2007**, *63* (24), 5244–5250. https://doi.org/10.1016/j.tet.2007.03.170.

(147) Ishikawa, N.; Kaizu, Y. Cation- and Solvent-Induced Formation of Supramolecular Structures Composed of Crown-Ether Substituted Double-Decker Phthalocyanine Radicals. *J. Phys. Chem. A* **2000**, *104* (44), 10009–10016. https://doi.org/10.1021/jp002109z.

(148) Sheng, N.; Li, R.; Choi, C. F.; Su, W.; Ng, D. K. P.; Cui, X.; Yoshida, K.; Kobayashi, N.; Jiang, J. Heteroleptic Bis(Phthalocyaninato) Europium(III) Complexes Fused with Different Numbers of 15-Crown-5 Moieties. Synthesis, Spectroscopy, Electrochemistry, and Supramolecular Structure. *Inorg. Chem.* **2006**, *45* (9), 3794–3802. https://doi.org/10.1021/ic0600937.

(149) Pushkarev, V. E.; Tomilova, L. G.; Nemykin, V. N. Historic Overview and New Developments in Synthetic Methods for Preparation of the Rare-Earth Tetrapyrrolic Complexes. *Coord. Chem. Rev.* **2016**, *319*, 110–179. https://doi.org/10.1016/j.ccr.2016.04.005.

(150) Chan, K. S.; Mak, K. W.; Tse, M. K.; Yeung, S. K.; Li, B. Z.; Chan, Y. W. Reactions of Nitroxides with Metalloporphyrin Alkyls Bearing Beta Hydrogens: Aliphatic Carbon-Carbon Bond Activation by Metal Centered Radicals. *J. Organomet. Chem.* **2008**, *693* (3), 399–407. https://doi.org/10.1016/j.jorganchem.2007.11.009.

(151) Micallef, A. S.; Bott, R. C.; Bottle, S. E.; Smith, G.; White, J. M.; Matsuda, K.; Iwamura, H. Brominated Isoindolines: Precursors to Functionalised Nitroxides. *J. Chem. Soc. Perkin Trans. 2* **1999**, No. 1, 65–71. https://doi.org/10.1039/a806884d.

(152) Horii, Y.; Kishiue, S.; Damjanović, M.; Katoh, K.; Breedlove, B. K.; Enders, M.; Yamashita, M. Supramolecular Approach for Enhancing Single-Molecule Magnet Properties of Terbium(III)-Phthalocyaninato Double-Decker Complexes with Crown Moieties. *Chem. Eur. J.* **2018**, *24* (17), 4320–4327. https://doi.org/10.1002/chem.201705378.

(153) Ruiz, E. Exchange Coupling Constants Using Density Functional Theory: The M0X Suite. *Chem. Phys. Lett.* **2008**, *460* (1–3), 336–338. https://doi.org/10.1016/j.cplett.2008.05.073.

(154) Rivero, P.; Moreira, I. D. P. R.; Illas, F.; Scuseria, G. E. Reliability of Range-Separated Hybrid Functionals for Describing Magnetic Coupling in Molecular Systems. *J. Chem. Phys.* **2008**, *129* (18). https://doi.org/10.1063/1.3006419.

(155) Malrieu, J. P.; Caballol, R.; Calzado, C. J.; De Graaf, C.; Guihéry, N. Magnetic Interactions in Molecules and Highly Correlated Materials: Physical Content, Analytical Derivation, and Rigorous Extraction of Magnetic Hamiltonians. *Chem. Rev.* **2014**, *114* (1), 429–492. https://doi.org/10.1021/cr300500z.

(156) Valero, R.; Costa, R.; De P. R. Moreira, I.; Truhlar, D. G.; Illas, F. Performance of the M06 Family of Exchange-Correlation Functionals for Predicting Magnetic Coupling in Organic and Inorganic Molecules. *J. Chem. Phys.* **2008**, *128* (11). https://doi.org/10.1063/1.2838987.

(157) Blinco, J. P.; Hodgson, J. L.; Morrow, B. J.; Walker, J. R.; Will, G. D.; Coote, M. L.; Bottle, S. E. Experimental and Theoretical Studies of the Redox Potentials of Cyclic Nitroxides. *J. Org. Chem.* **2008**, *73* (17), 6763–6771. https://doi.org/10.1021/jo801099w.

(158) Zhu, P.; Lu, F.; Pan, N.; Arnold, D. P.; Zhang, S.; Jiang, J. Comparative Electrochemical Study of Unsubstituted and Substituted Bis(Phthalocyaninato) Rare Earth(III) Complexes. *Eur. J. Inorg. Chem.* **2004**, No. 3, 510–517. https://doi.org/10.1002/ejic.200300509.

(159) Bolton, R.; Gillies, D. G.; Sutcliffe, L. H.; Wu, X. An EPR and NMR Study of Some Tetramethylisoindolin-2-Yloxyl Free Radicals. *J. Chem. Soc. Perkin Trans. 2* **1993**, No. 11, 2049–2052. https://doi.org/10.1039/p29930002049.

(160) Eaton, G. R.; Eaton, S. S. *Resolved Electron-Electron Spin-Spin Splittings in EPR Spectra*; Springer, 1989.

(161) Eaton, S. S.; DuBois, D. L.; Eaton, G. R. Metal-Nitroxyl Interactions VI. Analysis of EPR Spectra of Spin-Labeled Copper Complexes. *J. Magn. Reson.* **1978**, *32* (2), 251–263. https://doi.org/10.1016/0022-2364(78)90209-3.

(162) Eaton, S. S.; Woodcock, L. B.; Eaton, G. R. Continuous Wave Electron Paramagnetic Resonance of Nitroxide Biradicals in Fluid Solution. *Concepts Magn. Reson. Part A Bridg. Educ. Res.* **2018**, *47A* (2). https://doi.org/10.1002/cmr.a.21426.

(163) Moore, W.; Yao, R.; Liu, Y.; Eaton, S. S.; Eaton, G. R. Spin-Spin Interaction and Relaxation in Two Trityl-Nitroxide Diradicals. *J. Magn. Reson.* **2021**, *332*, 107078. https://doi.org/10.1016/j.jmr.2021.107078.

(164) Wilson, R.; Kivelson, D. ESR Linewidths in Solution. IV. Experimental Studies of Anisotropie and Spin-Rotational Effects in Copper Complexes. *J. Chem. Phys.* **1966**, *44* (12), 4445–4452. https://doi.org/10.1063/1.1726659.

(165) Drago, R. S. *Physical Methods for Chemists*, 2nd ed.; Saunders: Philadelphia, 1992.

(166) Lupulescu, A.; Kotecha, M.; Frydman, L. Relaxation-Assisted Separation of Chemical Sites in NMR Spectroscopy of Static Solids. *J. Am. Chem. Soc.* **2003**, *125* (11), 3376–3383. https://doi.org/10.1021/ja021173m.

(167) Cernescu, A.; Maly, T.; Prisner, T. F. 2D-REFINE Spectroscopy: Separation of Overlapping Hyperfine Spectra. *J. Magn. Reson.* **2008**, *192* (1), 78–84. https://doi.org/10.1016/j.jmr.2008.02.018.

(168) Du, J. L.; Eaton, G. R.; Eaton, S. S. Temperature, Orientation, and Solvent Dependence of Electron Spin-Lattice Relaxation Rates for Nitroxyl Radicals in Glassy Solvents and Doped Solids. *J. Magn. Reson. Ser. A* **1995**, *115* (2), 213–221. https://doi.org/10.1006/jmra.1995.1169.

(169) Eaton, S. S.; Eaton, G. R. Impact of Electron-Electron Spin-Spin Coupling on Electron-Spin Turning Angle in a Spin-Labeled Copper(II) Complex. *J. Magn. Reson. Ser. A* **1995**, *117* (1), 62–66. https://doi.org/10.1006/jmra.1995.9972.

(170) Astashkin, A. V; Schweiger, A. Electron-Spin Transient Nutation: A New Approach to Simplify the Interpretation of ESR Spectra. *Chem. Phys. Lett.* **1990**, *174* (6), 595–602. https://doi.org/10.1016/0009-2614(90)85493-V.

(171) Matsuoka, H.; Sato, K.; Shiomi, D.; Takui, T. 2-D Electron Spin Transient Nutation Spectroscopy of Lanthanoid Ion Eu2+(8S7/2) in a CaF2 Single Crystal on the Basis of FT-Pulsed Electron Spin Resonance Spectroscopy: Transition Moment Spectroscopy. *Appl. Magn. Reson.* **2003**, *23*, 517–538. https://doi.org/10.1007/BF03166639.

(172) Ayabe, K.; Sato, K.; Nishida, S.; Ise, T.; Nakazawa, S.; Sugisaki, K.; Morita, Y.; Toyota, K.; Shiomi, D.; Kitagawa, M.; Takui, T. Pulsed Electron Spin Nutation Spectroscopy of Weakly Exchange-Coupled Biradicals: A General Theoretical Approach and Determination of the Spin Dipolar Interaction. *Phys. Chem. Chem. Phys.* **2012**, *14* (25), 9137–9148. https://doi.org/10.1039/c2cp40778g.

(173) Gonidec, M.; Krivokapic, I.; Vidal-Gancedo, J.; Davies, E. . tephan; McMaster, J.; Gorun, S. M.; Veciana, J. Highly Reduced Double-Decker Single-Molecule Magnets Exhibiting Slow Magnetic Relaxation. *Inorg. Chem.* **2013**, *52*, 4464–4471.

(174) Chen, Y.; Ma, F.; Chen, X.; Dong, B.; Wang, K.; Jiang, S.; Wang, C.; Chen, X.; Qi, D.; Sun, H.; Wang, B.; Gao, S.; Jiang, J. A New Bis(Phthalocyaninato) Terbium Single-Ion Magnet with an Overall Excellent Magnetic Performance. *Inorg. Chem.* **2017**, *56* (22), 13889–13896. https://doi.org/10.1021/acs.inorgchem.7b02010.

(175) Wang, Y.; Chen, Y.; Bui, H. T.; Wolf, C.; Haze, M.; Mier, C.; Kim, J.; Choi, D.-J.; Lutz, C. P.; Bae, Y.; Phark, S.; Heinrich, A. J. An Atomic-Scale Multi-Qubit Platform. *Science* **2023**, *382* (C), 87–92. https://doi.org/10.1126/science.ade5050.

(176) Zhang, X.; Wolf, C.; Wang, Y.; Aubin, H.; Bilgeri, T.; Willke, P.; Heinrich, A. J.; Choi, T. Electron Spin Resonance of Single Iron Phthalocyanine Molecules and Role of Their Non-Localized Spins in Magnetic Interactions. *Nat. Chem.* **2022**, *14* (1), 59–65. https://doi.org/10.1038/s41557-021-00827-7.

(177) Willke, P.; Bilgeri, T.; Zhang, X.; Wang, Y.; Wolf, C.; Aubin, H.; Heinrich, A.; Choi, T. Coherent Spin Control of Single Molecules on a Surface. *ACS Nano* **2021**, *15* (11),

17959–17965. https://doi.org/10.1021/acsnano.1c06394.

(178) Kawaguchi, R.; Hashimoto, K.; Kakudate, T.; Katoh, K.; Yamashita, M.; Komeda, T. Spatially Resolving Electron Spin Resonance of π-Radical in Single-Molecule Magnet. *Nano Lett.* **2023**, *23* (1), 213–219. https://doi.org/10.1021/acs.nanolett.2c04049.

(179) Komijani, D.; Ghirri, A.; Bonizzoni, C.; Klyatskaya, S.; Moreno-Pineda, E.; Ruben, M.; Soncini, A.; Affronte, M.; Hill, S. Radical-Lanthanide Ferromagnetic Interaction in a T BIII Bis-Phthalocyaninato Complex. *Phys. Rev. Mater.* **2018**, *2* (2), 1–9. https://doi.org/10.1103/PhysRevMaterials.2.024405.

(180) Yamabayashi, T.; Katoh, K.; Breedlove, B. K.; Yamashita, M. Molecular Orientation of a Terbium(III)-Phthalocyaninato Double-Decker Complex for Effective Suppression of Quantum Tunneling of the Magnetization. *Molecules* **2017**, *22* (6), 1–11. https://doi.org/10.3390/molecules22060999.

(181) Reta, D.; Chilton, N. F. Uncertainty Estimates for Magnetic Relaxation Times and Magnetic Relaxation Parameters. *Phys. Chem. Chem. Phys.* **2019**, *21* (42), 23567–23575. https://doi.org/10.1039/c9cp04301b.

(182) Blackmore, W. J. A.; Gransbury, G. K.; Evans, P.; Kragskow, J. G. C.; Mills, D. P.; Chilton, N. F. Characterisation of Magnetic Relaxation on Extremely Long Timescales. *Phys. Chem. Chem. Phys.* **2023**, *25* (25), 16735–16744. https://doi.org/10.1039/d3cp01278f.

(183) Chen, Y.; Liu, C.; Ma, F.; Qi, D.; Liu, Q.; Sun, H. L.; Jiang, J. Fabricating Bis(Phthalocyaninato) Terbium SIM into Tetrakis(Phthalocyaninato) Terbium SMM with Enhanced Performance through Sodium Coordination. *Chem. Eur. J.* **2018**, *24* (32), 8066–8070. https://doi.org/10.1002/chem.201800408.

(184) Horii, Y.; Kishiue, S.; Damjanović, M.; Katoh, K.; Breedlove, B. K.; Enders, M.; Yamashita, M. Supramolecular Approach for Enhancing Single-Molecule Magnet Properties of Terbium(III)-Phthalocyaninato Double-Decker Complexes with Crown Moieties. *Chem. Eur. J.* **2018**, *24* (17), 4320–4327. https://doi.org/10.1002/chem.201705378.

(185) Mannini, M.; Bertani, F.; Tudisco, C.; Malavolti, L.; Poggini, L.; Misztal, K.; Menozzi, D.; Motta, A.; Otero, E.; Ohresser, P.; Sainctavit, P.; Condorelli, G. G.; Dalcanale, E.; Sessoli, R. Magnetic Behaviour of TbPc 2 Single-Molecule Magnets Chemically Grafted on Silicon Surface. *Nat. Commun.* **2014**, *5*, 6–13. https://doi.org/10.1038/ncomms5582.

(186) Ganivet, C. R.; Ballesteros, B.; De La Torre, G.; Clemente-Juan, J. M.; Coronado, E.; Torres, T. Influence of Peripheral Substitution on the Magnetic Behavior of Single-Ion Magnets Based on Homo- and Heteroleptic TbIII Bis(Phthalocyaninate). *Chem. Eur. J.* **2013**, *19* (4), 1457–1465. https://doi.org/10.1002/chem.201202600.

(187) Barhoumi, R.; Amokrane, A.; Klyatskaya, S.; Boero, M.; Ruben, M.; Bucher, J. Screening the 4f-Electron Spin of TbPc2 Single-Molecule Magnets on Metal Substrates by Ligand Channeling. *Nanoscale* **2019**, *11*, 21167–21179. https://doi.org/10.1039/c9nr05873g.

(188) Ran, W.; Walz, A.; Stoiber, K.; Knecht, P.; Xu, H.; Papageorgiou, A. C.; Huettig, A.;

Cortizo-lacalle, D.; Mora-fuentes, J. P.; Mateo-alonso, A.; Schlichting, H.; Reichert, J.; Barth, J. V. Depositing Molecular Graphene Nanoribbons on Ag (111) by Electrospray Controlled Ion Beam Deposition : Self-Assembly and On-Surface Transformations. *Angew. Chemie (International Ed. English)* **2022**, *61*, e202111816. https://doi.org/10.1002/anie.202111816.

(189) Moreno-Pineda, E.; Godfrin, C.; Balestro, F.; Wernsdorfer, W.; Ruben, M. Molecular Spin Qudits for Quantum Algorithms. *Chem. Soc. Rev.* **2018**, *47* (2), 501–513. https://doi.org/10.1039/c5cs00933b.

(190) Thiele, S.; Balestro, F.; Ballou, R.; Klyatskaya, S.; Ruben, M.; Wernsdorfer, W. Supplementary Materials for Electrically Driven Nuclear Spin Resonance in Single-Molecule Magnets. *Science* **2014**, *344* (6188), 1135–1138. https://doi.org/10.1126/science.1249802.

(191) Wernsdorfer, W.; Ruben, M. Synthetic Hilbert Space Engineering of Molecular Qudits: Isotopologue Chemistry. *Adv. Mater.* **2019**, *31* (26). https://doi.org/10.1002/adma.201806687.

(192) Horii, Y.; Katoh, K.; Cosquer, G.; Breedlove, B. K.; Yamashita, M. Weak DyIII-DyIII Interactions in DyIII-Phthalocyaninato Multiple-Decker Single-Molecule Magnets Effectively Suppress Magnetic Relaxation. *Inorg. Chem.* **2016**, *55* (22), 11782–11790. https://doi.org/10.1021/acs.inorgchem.6b01870.

(193) Katoh, K.; Yasuda, N.; Damjanović, M.; Wernsdorfer, W.; Breedlove, B. K.; Yamashita, M. Manipulation of the Coordination Geometry along the C4 Rotation Axis in a Dinuclear Tb3+ Triple-Decker Complex via a Supramolecular Approach. *Chem. Eur. J.* **2020**, *26* (21), 4805–4815. https://doi.org/10.1002/chem.201905400.

(194) Martynov, A. G.; Polovkova, M. A.; Gorbunova, Y. G.; Tsivadze, A. Y. Redox-Triggered Switching of Conformational State in Triple-Decker Lanthanide Phthalocyaninates. *Molecules* **2022**, *27* (19). https://doi.org/10.3390/molecules27196498.

(195) Xia, H. N.; Minamitani, E.; Žitko, R.; Liu, Z. Y.; Liao, X.; Cai, M.; Ling, Z. H.; Zhang, W. H.; Klyatskaya, S.; Ruben, M.; Fu, Y. S. Spin-Orbital Yu-Shiba-Rusinov States in Single Kondo Molecular Magnet. *Nat. Commun.* **2022**, *13* (1), 1–7. https://doi.org/10.1038/s41467-022-34187-8.

(196) Liao, X.; Minamitani, E.; Xie, T.; Yang, L.; Zhang, W.; Klyatskaya, S.; Ruben, M.; Fu, Y. S. Altering Spin Distribution of Tb2Pc3 via Molecular Chirality Manipulation. *J. Am. Chem. Soc.* **2024**, *146* (9), 5901–5907. https://doi.org/10.1021/jacs.3c11882.

(197) Lu, G.; Li, J.; Yan, S.; Zhu, W.; Ou, Z.; Kadish, K. M. Synthesis and Characterization of Rare Earth Corrole-Phthalocyanine Heteroleptic Triple-Decker Complexes. *Inorg. Chem.* **2015**, *54* (12), 5795–5805. https://doi.org/10.1021/acs.inorgchem.5b00477.

(198) Lu, G.; He, C.; Fang, Y.; Wang, L.; Zhu, W. Construction of Mixed Corrole-Phthalocyanine Europium Triple-Decker Complexes Involving: Meso -Substituted Trans -A2B-Corrole. *New J. Chem.* **2018**, *42* (4), 2498–2503. https://doi.org/10.1039/c7nj04446a.

(199) Lu, G.; He, C.; Wang, K.; Sun, J.; Qi, D.; Gong, L.; Wang, C.; Ou, Z.; Yan, S.; Zeng, S.; Zhu, W. Dysprosium Heteroleptic Corrole-Phthalocyanine Triple-Decker Complexes: Synthesis, Crystal Structure, and Electrochemical and Magnetic Properties. *Inorg. Chem.* **2017**, *56* (19), 11503–11512. https://doi.org/10.1021/acs.inorgchem.7b01060.

(200) NAITO, R.; OHTA, K.; SHIRAI, H. Discotic Liquid Crystals of Transition Metal Complexes: 28. Temperature-Dependent Electronic Spectra and X-Ray Structural Analysis of Discotic Liquid Crystalline Bis(Octakisdodecyloxyphthalocyaninato)Lutetium(III) Complex. *J. Porphyr. Phthalocyanines* **2001**, *05* (01), 44–50. https://doi.org/10.1002/1099-1409(200101)5:1<44::aid-jpp295>3.0.co;2-u.

(201) Gellini, C.; Moroni, L.; Muniz-Miranda, M. High Overtones of the C-H Stretching Vibrations in Anisole and Thioanisole. *J. Phys. Chem. A* **2002**, *106* (46), 10999–11007. https://doi.org/10.1021/jp020691g.

(202) Birin, K. P.; Gorbunova, Y. G.; Tsivadze, A. Y. Efficient Scrambling-Free Synthesis of Heteroleptic Terbium Triple-Decker (Porphyrinato)(Crown-Phthalocyaninates). *Dalt. Trans.* **2012**, *41* (32), 9672–9681. https://doi.org/10.1039/c2dt30841j.

(203) Birin, K. P.; Gorbunova, Y. G.; Yu. Tsivadze, A. Novel One-Pot Regioselective Route towards Heteroleptic Lanthanide (Phthalocyaninato)(Porphyrinato) Triple-Decker Complexes. *J. Porphyr. Phthalocyanines* **2009**, *13* (2), 283–290. https://doi.org/10.1142/S1088424609000358.

(204) Sun, X.; Li, R.; Wang, D.; Dou, J.; Zhu, P.; Lu, F.; Ma, C.; Choi, C. F.; Cheng, D. Y. Y.; Ng, D. K. P.; Kobayashi, N.; Jiang, J. Synthesis and Characterization of Mixed Phthalocyaninato and Meso-Tetrakis(4-Chlorophenyl)Porphyrinato Triple-Decker Complexes - Revealing the Origin of Their Electronic Absorptions. *Eur. J. Inorg. Chem.* **2004**, No. 19, 3806–3813. https://doi.org/10.1002/ejic.200400289.

(205) Muranaka, A.; Matsumoto, Y.; Uchiyama, M.; Jiang, J.; Bian, Y.; Ceulemans, A.; Kobayashi, N. Definitive Assignments of the Visible-near-IR Bands of Porphyrin-Naphthalocyanine Rare-Earth Sandwich Double- and Triple-Decker Compounds by Magnetic Circular Dichroism Spectroscopy. *Inorg. Chem.* **2005**, *44* (11), 3818–3826. https://doi.org/10.1021/ic0502325.

(206) Lu, F.; Bao, M.; Ma, C.; Zhang, X.; Arnold, D. P.; Jiang, J. Infrared Spectra of Phthalocyanine and Naphthalocyanine in Sandwich-Type (Na)Phthalocyaninato and Porphyrinato Rare Earth Complexes. Part 3. The Effects of Substituents and Molecular Symmetry on the Infrared Characteristics of Phthalocyanine in Bis(Phthal. *Spectrochim. Acta - Part A Mol. Biomol. Spectrosc.* **2003**, *59* (14), 3273–3286. https://doi.org/10.1016/S1386-1425(03)00158-6.

(207) Jiang, J.; Liu, W.; Law, W. F.; Ng, D. K. P. Heteroleptic Triple-Decker (Phthalocyaninato)-(Porphyrinato) Europium (III) Complexes: Synthesis and Electrochemical Study. *Inorganica Chim. Acta* **1998**, *268* (1), 49–53. https://doi.org/10.1016/S0020-1693(97)05718-6.

(208) Peloquin, D. M.; Dewitt, D. R.; Patel, S. S.; Merkert, J. W.; Donovan-Merkert, B. T.; Schmedake, T. A. Spectroelectrochemistry of Tris(Bipyridyl)Silicon(IV): Ligand Localized Reductions with Potential Electrochromic Applications. *Dalt. Trans.* **2015**, *44*

(43), 18723–18726. https://doi.org/10.1039/c5dt03548a.

(209) Gasyna, Z.; Schatz, P. N.; Boyle, M. E. Analysis of the Intervalence Band in Lutetium Bis(Phthalocyanine): The System Is Delocalized. *J. Phys. Chem.* **1995**, *99* (25), 10159–10165. https://doi.org/10.1021/j100025a016.

(210) Klar, D.; Candini, A.; Joly, L.; Klyatskaya, S.; Krumme, B.; Ohresser, P.; Kappler, J. P.; Ruben, M.; Wende, H. Hysteretic Behaviour in a Vacuum Deposited Submonolayer of Single Ion Magnets. *Dalt. Trans.* **2014**, *43* (28), 10686–10689. https://doi.org/10.1039/c4dt01005a.

(211) Wysocki, A. L.; Park, K. Nature of Hyperfine Interactions in TbPc2 Single-Molecule Magnets: Multiconfigurational Ab Initio Study. *Inorg. Chem.* **2020**, *59* (5), 2771–2780. https://doi.org/10.1021/acs.inorgchem.9b03136.

(212) Pederson, R.; Wysocki, A. L.; Mayhall, N.; Park, K. Multireference Ab Initio Studies of Magnetic Properties of Terbium-Based Single-Molecule Magnets. *J. Phys. Chem. A* **2019**, *123* (32), 6996–7006. https://doi.org/10.1021/acs.jpca.9b03708.

(213) Chilton, N. F.; Anderson, R. P.; Turner, L. D.; Soncini, A.; Murray, K. S. PHI : A Powerful New Program for the Analysis of Anisotropic Monomeric and Exchange-Coupled Polynuclear d - and f -Block Complexes. **2013**. https://doi.org/10.1002/jcc.23234.

(214) Katoh, K.; Aizawa, Y.; Morita, T.; Breedlove, B. K.; Yamashita, M. Elucidation of Dual Magnetic Relaxation Processes in Dinuclear Dysprosium(III) Phthalocyaninato Triple-Decker Single-Molecule Magnets Depending on the Octacoordination Geometry. *Chem. Eur. J.* **2017**, *23* (61), 15377–15386. https://doi.org/10.1002/chem.201703014.

(215) Gürek, A. G.; Basova, T.; Luneau, D.; Lebrun, C.; Kol'tsov, E.; Hassan, A. K.; Ahsen, V. Synthesis , Structure , and Spectroscopic and Magnetic Properties of Mesomorphic Octakis (Hexylthio) -Substituted Phthalocyanine Rare-Earth Metal Sandwich Complexes. *Inorg. Chem.* **2006**, *45* (4), 1667–1676.

(216) Bogani, L.; Wernsdorfer, W. Molecular Spintronics Using Single-Molecule Magnets. *Nat. Mater.* **2008**, *7*, 179–186.

(217) Wagner, S.; Kisslinger, F.; Ballmann, S.; Schramm, F.; Chandrasekar, R.; Bodenstein, T.; Fuhr, O.; Secker, D.; Fink, K.; Ruben, M.; Weber, H. B. Switching of a Coupled Spin Pair in a Single-Molecule Junction. *Nat. Nanotechnol.* **2013**, *8* (8), 575–579. https://doi.org/10.1038/nnano.2013.133.

(218) Heersche, H. B.; De Groot, Z.; Folk, J. A.; Van Der Zant, H. S. J.; Romeike, C.; Wegewijs, M. R.; Zobbi, L.; Barreca, D.; Tondello, E.; Cornia, A. Electron Transport through Single Mn12 Molecular Magnets. *Phys. Rev. Lett.* **2006**, *96* (20), 1–4. https://doi.org/10.1103/PhysRevLett.96.206801.

(219) Parks, J. J.; Champagne, A. R.; Costi, T. A.; Shum, W. W.; Pasupathy, A. N.; Neuscamman, E.; Flores-Torres, S.; Cornaglia, P. S.; Aligia, A. A.; Balseiro, C. A.; Chan, G. K. L.; Abruña, H. D.; Ralph, D. C. Mechanical Control of Spin States in Sp. *Science* **2010**, *328* (5984), 1370–1373.

(220) Frisch, M. J.; Trucks, G. W.; Schlegel, H. B.; Scuseria, G. E.; Robb, M. a.; Cheeseman, J. R.; Scalmani, G.; Barone, V.; Petersson, G. a.; Nakatsuji, H.; Li, X.; Caricato, M.; Marenich, a. V.; Bloino, J.; Janesko, B. G.; Gomperts, R.; Mennucci, B.; Hratchian, H. P.; Ortiz, J. V.; Izmaylov, a. F.; Sonnenberg, J. L.; Williams; Ding, F.; Lipparini, F.; Egidi, F.; Goings, J.; Peng, B.; Petrone, A.; Henderson, T.; Ranasinghe, D.; Zakrzewski, V. G.; Gao, J.; Rega, N.; Zheng, G.; Liang, W.; Hada, M.; Ehara, M.; Toyota, K.; Fukuda, R.; Hasegawa, J.; Ishida, M.; Nakajima, T.; Honda, Y.; Kitao, O.; Nakai, H.; Vreven, T.; Throssell, K.; Montgomery Jr., J. a.; Peralta, J. E.; Ogliaro, F.; Bearpark, M. J.; Heyd, J. J.; Brothers, E. N.; Kudin, K. N.; Staroverov, V. N.; Keith, T. a.; Kobayashi, R.; Normand, J.; Raghavachari, K.; Rendell, a. P.; Burant, J. C.; Iyengar, S. S.; Tomasi, J.; Cossi, M.; Millam, J. M.; Klene, M.; Adamo, C.; Cammi, R.; Ochterski, J. W.; Martin, R. L.; Morokuma, K.; Farkas, O.; Foresman, J. B.; Fox, D. J. G16_C02. 2016, p Gaussian 16, Revision C.02, Gaussian, Inc., Wallin.

(221) Neese, F. The ORCA Program System. *Wiley Interdiscip. Rev. Comput. Mol. Sci.* **2012**, *2* (1), 73–78. https://doi.org/10.1002/wcms.81.

(222) Weigend, F.; Ahlrichs, R. Balanced Basis Sets of Split Valence, Triple Zeta Valence and Quadruple Zeta Valence Quality for H to Rn: Design and Assessment of Accuracy. *Phys. Chem. Chem. Phys.* **2005**, *7* (18), 3297–3305. https://doi.org/10.1039/b508541a.

(223) Noodleman, L. Valence Bond Description of Antiferromagnetic Coupling in Transition Metal Dimers. *J. Chem. Phys.* **1981**, *74* (10), 5737–5743. https://doi.org/10.1063/1.440939.

(224) Becke, A. D. Density-Functional Thermochemistry. III. The Role of Exact Exchange. *J. Chem. Phys.* **1993**, *98* (September), 5648–5652.

(225) Soda, T.; Kitagawa, Y.; Onishi, T.; Takano, Y.; Shigeta, Y.; Nagao, H.; Yoshioka, Y.; Yamaguchi, K. Ab Initio Computations of Effective Exchange Integrals for H – H , H – He – H and Mn 2 O 2 Complex : Comparison of Broken-Symmetry Approaches. *Chem. Phys. Lett.* **2000**, *319* (2000), 223–230. https://doi.org/10.1016/S0009-2614(00)00166-4.

(226) Roos, B. O.; Taylor, P. R.; Sigbahn, P. E. M. A Complete Active Space SCF Method (CASSCF) Using a Density Matrix Formulated Super-CI Approach. *Chem. Phys.* **1980**, *48*, 157–173. https://doi.org/10.1007/b11437.

(227) Angeli, C.; Cimiraglia, R.; Malrieu, J. P. N-Electron Valence State Perturbation Theory: A Fast Implementation of the Strongly Contracted Variant. *Chem. Phys. Lett.* **2001**, *350* (3–4), 297–305. https://doi.org/10.1016/S0009-2614(01)01303-3.

(228) Neese, F. An Improvement of the Resolution of the Identity. *J. Comput. Chem.* **2003**, *24* (14), 1740–1747. https://doi.org/10.1002/jcc.10318.

(229) Grimme, S.; Ehrlich, S.; Goerigk, L. Effect of the Damping Function in Dispersion Corrected Density Functional Theory. *J. Comput. Chem.* **2011**, *32* (7), 1457–1465. https://doi.org/10.1002/jcc.

(230) Grimme, S.; Antony, J.; Ehrlich, S.; Krieg, H. A Consistent and Accurate Ab Initio Parametrization of Density Functional Dispersion Correction (DFT-D) for the 94 Elements H-Pu. *J. Chem. Phys.* **2010**, *132* (15). https://doi.org/10.1063/1.3382344.

(231) Dolomanov, O. V.; Bourhis, L. J.; Gildea, R. J.; Howard, J. A. K.; Puschmann, H. OLEX2: A Complete Structure Solution, Refinement and Analysis Program. *J. Appl. Crystallogr.* **2009**, *42* (2), 339–341. https://doi.org/10.1107/S0021889808042726.

(232) Sheldrick, G. M. SHELXT - Integrated Space-Group and Crystal-Structure Determination. *Acta Crystallogr. Sect. A Found. Crystallogr.* **2015**, *71* (1), 3–8. https://doi.org/10.1107/S2053273314026370.

(233) Sheldrick, G. M. Crystal Structure Refinement with SHELXL. *Acta Crystallogr. Sect. C Struct. Chem.* **2015**, *71* (Md), 3–8. https://doi.org/10.1107/S2053229614024218.

(234) Aquilante, F.; Autschbach, J.; Baiardi, A.; Battaglia, S.; Borin, V. A.; Chibotaru, L. F.; Conti, I.; De Vico, L.; Delcey, M.; Galván, I. F.; Ferré, N.; Freitag, L.; Garavelli, M.; Gong, X.; Knecht, S.; Larsson, E. D.; Lindh, R.; Lundberg, M.; Malmqvist, P. Å.; Nenov, A.; Norell, J.; Odelius, M.; Olivucci, M.; Pedersen, T. B.; Pedraza-González, L.; Phung, Q. M.; Pierloot, K.; Reiher, M.; Schapiro, I.; Segarra-Martí, J.; Segatta, F.; Seijo, L.; Sen, S.; Sergentu, D. C.; Stein, C. J.; Ungur, L.; Vacher, M.; Valentini, A.; Veryazov, V. Modern Quantum Chemistry with [Open]Molcas. *J. Chem. Phys.* **2020**, *152* (21). https://doi.org/10.1063/5.0004835.

(235) Peng, D.; Hirao, K. An Arbitrary Order Douglas-Kroll Method with Polynomial Cost. *J. Chem. Phys.* **2009**, *130* (4). https://doi.org/10.1063/1.3068310.

(236) Gans, P.; Marchon, J. C.; Buisson, G.; Duée, E.; Erler, B. S.; Scholz, W. F.; Reed, C. A. High-Valent Iron Porphyrins: Synthesis, X-Ray Structures, π-Cation Radical Formulation, and Notable Magnetic Properties of Chloro(Meso-Tetraphenylporphinato)Iron(III) Hexachloroantimonate and Bis(Perchlorato)(Meso-Tetraphenylporphinato)Iron(III). *J. Am. Chem. Soc.* **1986**, *108* (6), 1223–1234. https://doi.org/10.1021/ja00266a017.

Appendix

Optimized molecular coordinate of compound 1.

131

Coordinates from ORCA-job OPT

Y	-0.05489329174555	-0.01077272691496	-0.04406663853921
N	-0.09088901309241	-2.02371643963649	-1.39562372065467
N	1.87771546274282	-0.02142854577682	-1.51374456908611
N	-0.11327181512337	1.96226635808325	-1.45546433065161
N	-2.09250063875639	-0.04097112639824	-1.35132391738914
N	-1.39170868759248	-1.40756086087349	1.41644122386965
N	-1.40833861368056	1.41203518334745	1.37519229788988
N	1.40343829179851	1.42533753929870	1.26354251041916
N	1.42050467986402	-1.38869605683390	1.30746170238764
C	1.02156200735185	-2.80363140114105	-1.60001102300582
N	2.29382949389525	-2.41109476905970	-1.67062119002179
C	2.67373709283340	-1.13347473298367	-1.64547623196204
C	4.07238237774824	-0.71930373705632	-1.79148338363317
C	5.26229602617787	-1.44119497987579	-1.81879873221440
H	5.25349158941986	-2.53218342254331	-1.78233589953908
C	5.24487700820195	1.42796612017447	-1.86204335416331
H	5.22208442233200	2.51934792674307	-1.85862906898735
C	4.06409989647642	0.69263774071759	-1.81275085254534
C	2.66087755391725	1.09496438935227	-1.67967901662512

N	2.26668289798670	2.36677567135478	-1.74504774707469
C	0.99017525189061	2.74721007540149	-1.68728678723636
C	0.56638577307790	4.13316732812897	-1.91170841089728
C	1.27546400589008	5.31295458440438	-2.11875307836498
H	2.36587716068739	5.30707787159470	-2.15164029673092
C	0.54094965805257	6.49510323480379	-2.26314732413566
H	1.06485911240851	7.44010128110459	-2.41560932678693
C	-0.86289980528071	6.48873780818673	-2.21409507417229
H	-1.40473841606759	7.42896368162980	-2.32892990358696
C	-1.57504162981751	5.30013721990670	-2.01896653581743
H	-2.66503258912941	5.28452654281256	-1.97557404595227
C	-0.84286507392060	4.12679911026709	-1.86227309088955
C	-1.23731418500716	2.73664120390840	-1.61011608787385
N	-2.51094153111488	2.34225039811339	-1.59500732688585
C	-2.88978123290568	1.06687379590936	-1.51025088130743
C	-4.28914692016279	0.64709030150772	-1.64279625583447
C	-5.47966915993835	1.35967796325046	-1.75357075719773
H	-5.47481373644918	2.45053685165359	-1.76668808256306
C	-6.66983891137893	0.62792451013665	-1.82828322437560
H	-7.62256372840040	1.15470700269944	-1.90350184168088
C	-6.66189450252349	-0.77656476995148	-1.80632710758827
H	-7.60856544800603	-1.31624864315328	-1.86460936723487
C	-5.46347861584314	-1.49200991907977	-1.70880456320900
H	-5.44618861853930	-2.58263259205515	-1.68771384931987
C	-4.28120259548787	-0.76278858916400	-1.62060979567769

C	-2.87732326439736	-1.16226387988096	-1.47488040866417
N	-2.48411372432742	-2.43539587105241	-1.51857424697881
C	-1.20607612970771	-2.81571678465818	-1.52192825610768
C	-0.79578375873559	-4.20925067619788	-1.72630090947551
C	-1.51406411139184	-5.39608006762692	-1.83943952893704
H	-2.60411428308673	-5.39198796186756	-1.79521108373613
C	-0.78807370004195	-6.58253531644744	-1.99176253931718
H	-1.31898507896392	-7.53259806384868	-2.07160136786824
C	0.61574005854052	-6.57448052904897	-2.04108675180054
H	1.15061955303510	-7.51830327980111	-2.15880422735734
C	1.33631976683825	-5.37940075881188	-1.94000191716859
H	2.42662521369032	-5.36196160591358	-1.97262324503775
C	0.61348606033402	-4.20119540198166	-1.77624054483990
C	-2.72588834407071	-1.17779362419183	1.65299303311354
N	-3.35757544174435	-0.00480877565769	1.70475427055064
C	-2.74044974644139	1.17355255039612	1.61507023954427
C	-3.43315040532052	2.44745056167074	1.83591268866239
C	-4.76932157420213	2.76574417645330	2.06184615766444
H	-5.52707562062743	1.98230675570936	2.10621687425107
C	-5.09817909668631	4.11713318017336	2.21292330860890
C	-4.11232409369780	5.11576155098877	2.15350987715778
C	-2.76756891007853	4.79371544065785	1.94049795841785
H	-1.99462568081199	5.56184032079493	1.89254551671445
C	-2.44341210427205	3.45000220570036	1.77597970625335
C	-1.17498233508035	2.75934392825216	1.51930495561246

N	-0.00338759575492	3.39447480818332	1.49149231765908
C	1.17283539989868	2.77233442295326	1.40655579462486
C	2.45415662638678	3.47934434742368	1.51602275609600
C	2.78284610689396	4.83006346113678	1.59631770586987
H	2.00293349713923	5.59266060196525	1.60631702360775
C	4.14018171841716	5.16679035859286	1.64159871696728
C	5.13623394700204	4.17649838810326	1.62340383914267
C	4.80500279790851	2.81897026805716	1.55932624330155
H	5.57119312687592	2.04313127654957	1.54287335569554
C	3.45459843892398	2.48543797091332	1.49748991267275
C	2.75568842674051	1.20276577806779	1.37205604504492
N	3.39182675941333	0.03205466781965	1.40369851521423
C	2.77005361297456	-1.14683710233608	1.40698571107186
C	3.48468236345740	-2.41676823262581	1.56745775758311
C	4.83908033843632	-2.73166159426072	1.63686267946139
H	5.59538691629922	-1.94714970166380	1.59692479165694
C	5.18710499969679	-4.08264358500442	1.73962823956676
C	4.20325363360182	-5.08415238947452	1.78698342421473
C	2.84184811127437	-4.76557035064682	1.73354871273846
H	2.07127598123178	-5.53702948510496	1.76565613662913
C	2.49653676213538	-3.42186635517617	1.61557854680085
C	1.20651124576003	-2.73392011931798	1.48853945595462
N	0.03813164741681	-3.36755398946469	1.59441753809313
C	-1.14116079697622	-2.74622647951086	1.60464877012329
C	-2.39973256808034	-3.44350773810141	1.88933439287235

C	-2.70556911487228	-4.78458985850827	2.10254704873753
H	-1.92264005928612	-5.54365269290390	2.07800889452681
C	-4.04495372489504	-5.11612568363479	2.33373034117162
C	-5.04324025844631	-4.12855830027506	2.36333084867621
H	-6.07796566800779	-4.42210669635614	2.54750407014641
C	-4.73263860947812	-2.77925647946758	2.16313853517398
H	-5.50024943043946	-2.00452205148931	2.18445746341899
C	-3.40178776100439	-2.45203956410696	1.91937139389307
H	6.24023571630936	-4.36617080036867	1.78438746554836
H	4.50955574535619	-6.12847444541897	1.86712668744384
H	4.43356568476583	6.21670615305434	1.69202263966353
H	6.18573559095144	4.47410711503597	1.66045970337056
H	-6.13758451792084	4.40358372825237	2.38132704683239
H	-4.40350528143482	6.16023585264462	2.27666290758799
H	-4.32207873313470	-6.15916512261425	2.49535670537632
C	6.43853421929950	0.70454455572468	-1.86589629503432
C	6.44710729709428	-0.70349169099317	-1.84482732125475
C	7.85174894653357	-1.25016731984585	-1.81710658975226
N	8.64376984290916	0.01455972869285	-1.83530459569069
C	7.83608648189497	1.26932346690150	-1.85350185071776
O	9.91298218809489	0.02293018818825	-1.80582939645010
C	8.16089712911059	-2.02980030489365	-0.52957114267984
C	8.17552088933568	2.07745427812060	-3.11394137373490
C	8.20117381041504	-2.08883877970108	-3.05467293331894
C	8.13508173545882	2.08828283992831	-0.58813196059024

H	9.27893584699444	-2.30057290978026	-3.05786359803623
H	7.94165808110746	-1.55092848594560	-3.97638040174128
H	7.65138047336477	-3.03918459651486	-3.03826746898335
H	7.92534526976606	1.50989190261569	-4.02030320553508
H	9.20466963004878	2.33524996581296	-0.55674141572161
H	9.25001379120225	2.30487094797914	-3.12202359511322
H	7.55108464163923	3.01853645920381	-0.59083484882854
H	7.87671012920879	1.51706226776050	0.31426989050860
H	9.23278839242148	-2.26585680416021	-0.49278866203844
H	7.58550834063083	-2.96502483743448	-0.50585095907289
H	7.89833233612431	-1.43567270071618	0.35671443023667
H	7.61186509926704	3.01964779333182	-3.12453324809798

CASSCF calculation of compound 3-Ln, 4-Ln

CASSCF calculation of 3-Tb with all spin configuration and maximum number of CI roots (full)

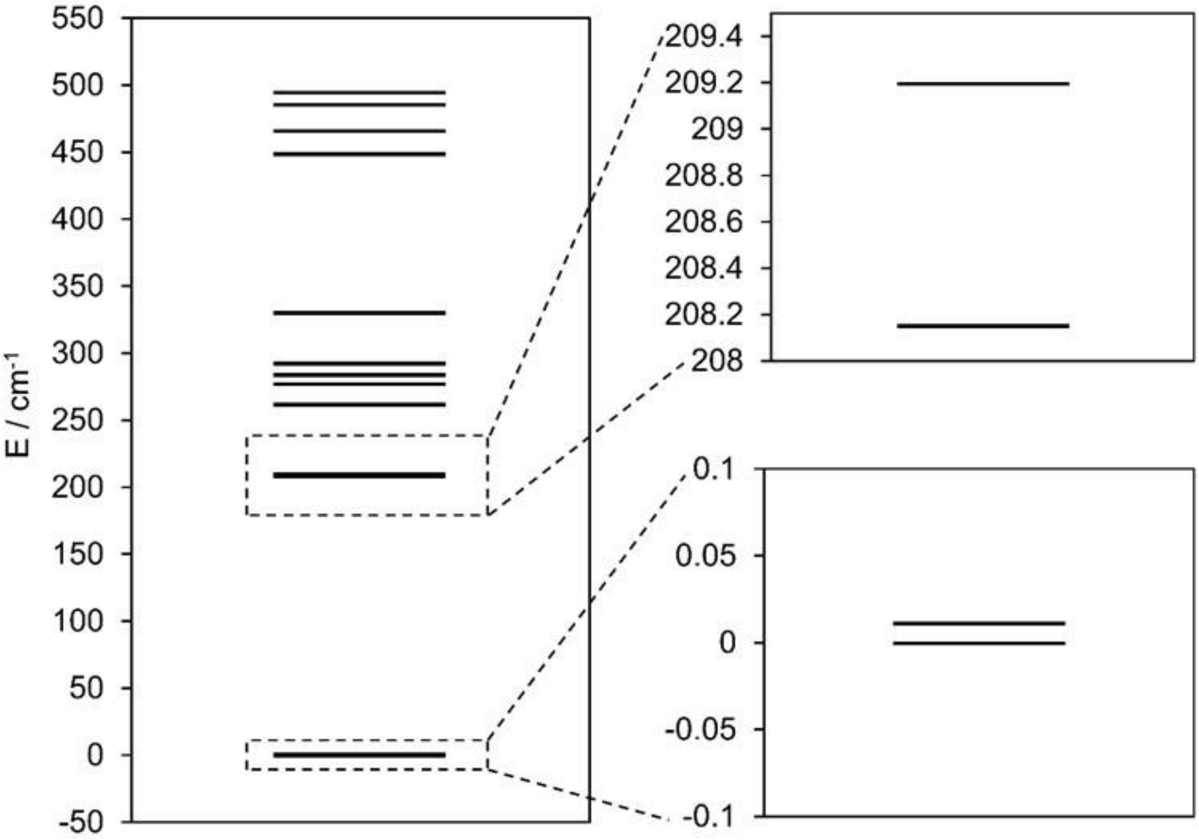

Figure A1. Energy diagram of LF states of **3-Tb** calculated from CASSCF (full).

Table A1. The list of LF states, and the composition of |m$_J$> of **3-Tb** (full). Note that ± m$_J$ contributes equally.

	|m$_J$>						
Energy / cm^{-1}	|±6>	|±5>	|±4>	|±3>	|±2>	|±1>	|0>
0	100	0	0	0	0	0	0
0.01125529	100	0	0	0	0	0	0
208.147524	0	92.6	0.2	1.8	0.2	5.4	0
209.190426	0	94	0.2	1	0.6	4.2	0.1
261.290841	0	0.2	59.4	1.6	2.6	0.4	35.8
276.969683	0	0.2	2.2	10.8	78.4	7.6	1
283.435118	0	5.8	4.2	41.4	14	34.6	0.1
291.864336	0	6	0.6	48	3.6	41.6	0.1
329.636072	0	0	95.8	2.2	0.8	1.4	0
448.590346	0	0	35.4	0	5.6	0	59
465.82547	0	0.6	0.2	48.4	0	50.8	0.1
485.726663	0	0.8	0	45.2	0	54	0
494.029557	0	0	1.8	0	94.2	0	3.7

Table A2. Calculated LF parameters of **3-Tb** with SOC (full).

k	q	B(k,q)
2	-2	-7.06E-03
2	-1	-1.41E-01
2	0	-3.44E+00
2	1	2.87E-01
2	2	3.05E-01
4	-4	-5.95E-02
4	-3	-4.65E-04
4	-2	8.80E-05
4	-1	1.55E-03
4	0	-1.05E-02
4	1	-4.37E-03
4	2	-1.30E-03
4	3	-2.38E-02
4	4	8.25E-02
6	-6	-5.36E-06
6	-5	1.20E-04
6	-4	4.42E-04
6	-3	-3.27E-05
6	-2	-3.62E-06
6	-1	4.39E-06
6	0	1.49E-06
6	1	-8.82E-06
6	2	1.76E-06
6	3	8.02E-05
6	4	-5.22E-04

6	5	-3.88E-05
6	6	1.45E-05

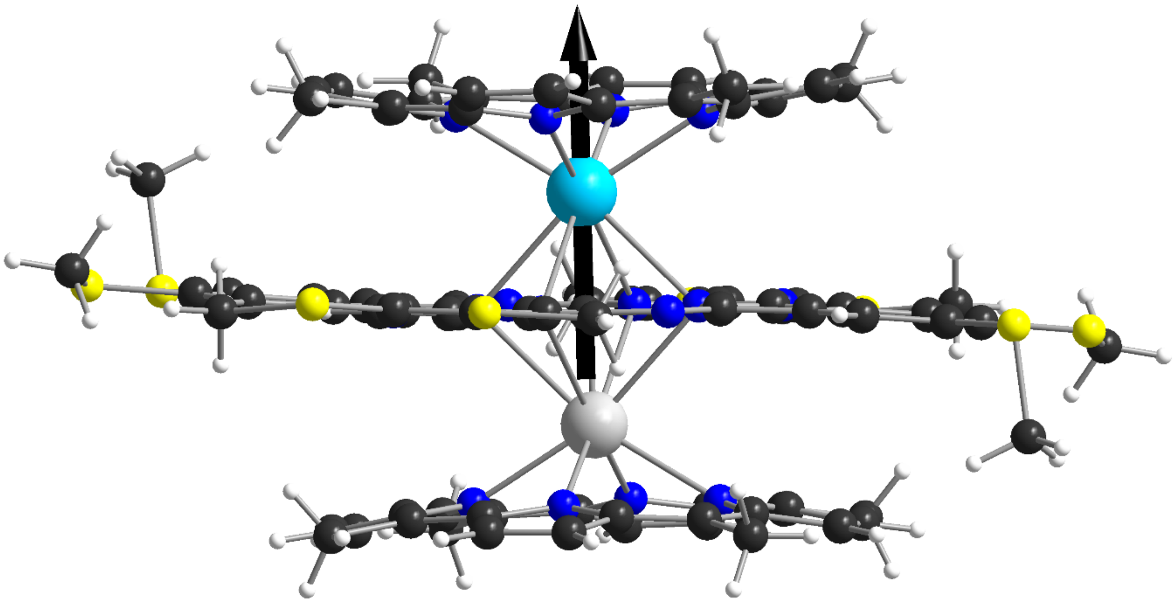

Figure A2. The modified molecular structure used for CASSCF calculation of **3-Tb**. Hydrogen, carbon, nitrogen, sulfur, terbium, and yttrium, are shown in white, black, blue, yellow, cyan, and grey, respectively. The black arrow represents the orientation of the principal magnetic axes obtained in full calculation.

CASSCF calculation of 3-Tb (simplified)

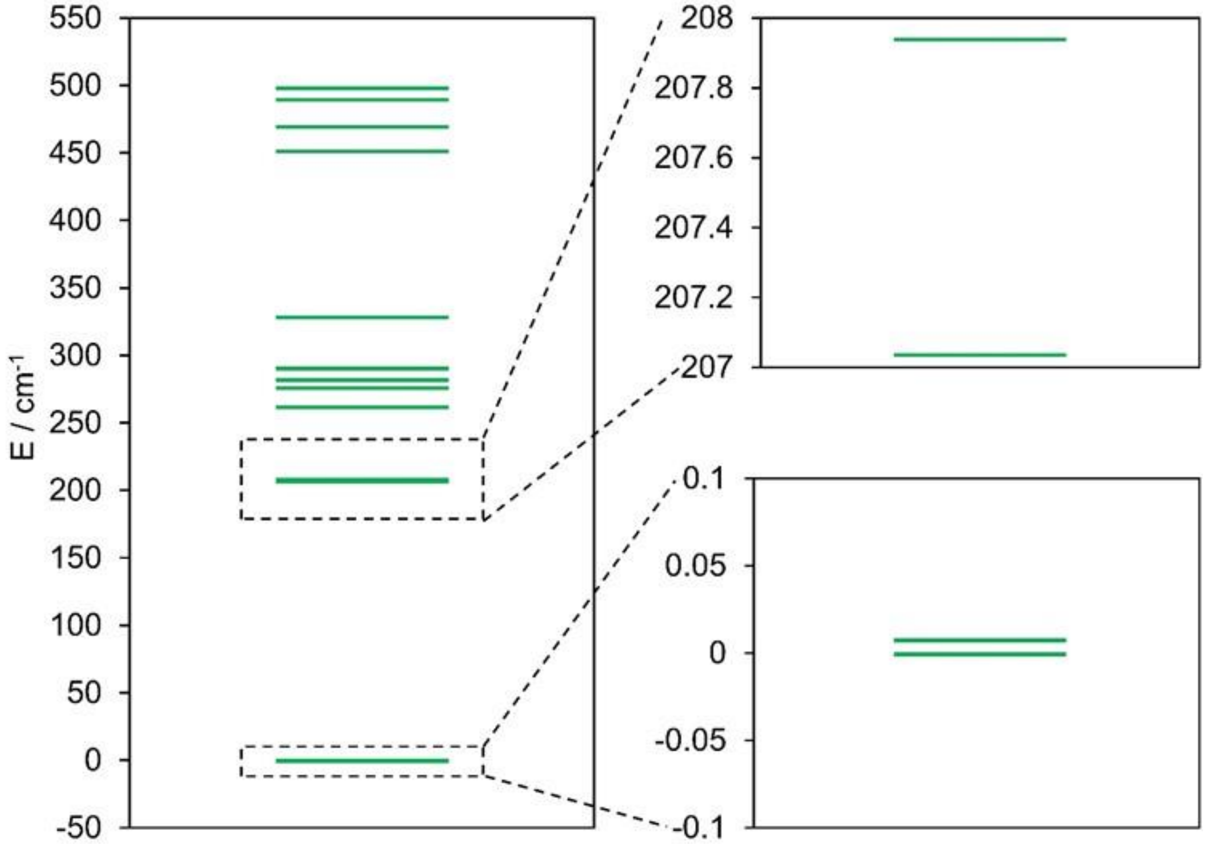

Figure A3. Energy diagram of LF states of **3-Tb** calculated from CASSCF (simplified).

Table A3. The list of LF states, and the composition of |m$_J$> of **3-Tb**. ± m$_J$ contributes equally (simplified).

	|m$_J$>						
Energy / cm^{-1}	|±6>	|±5>	|±4>	|±3>	|±2>	|±1>	|0>
0	100	0	0	0	0	0	0
0.007551779	100	0	0	0	0	0	0
207.0376833	0	93.4	0.2	1.6	0.2	4.8	0.1
207.9433113	0	94.6	0.2	0.8	0.6	3.6	0.1
262.0152671	0	0.2	59.2	1.8	3.4	0.4	35.1
276.2419447	0	0.2	2.6	10.6	77.8	7.6	1.2
282.4736027	0	5	4.2	41.8	14	34.8	0.2
290.8385185	0	5.2	0.8	48.6	3.6	41.6	0.2
328.7645976	0	0	95.8	2.2	0.6	1.4	0
451.6330675	0	0	35	0	5.4	0	59.6
469.3936295	0	0.6	0.2	47.8	0	51.4	0.1
489.4265554	0	0.6	0	44.8	0	54.4	0
498.193512	0	0	1.8	0	94.4	0	3.6

Table A4. Calculated ligand field parameters of **3-Tb** (simplified).

k	q	B(k,q)
2	-2	-6.77E-03
2	-1	-1.54E-01
2	0	-3.47E+00
2	1	3.04E-01
2	2	3.04E-01
4	-4	-6.09E-02
4	-3	-4.79E-04
4	-2	8.08E-05
4	-1	1.39E-03
4	0	-1.03E-02
4	1	-4.12E-03
4	2	-1.39E-03
4	3	-2.35E-02
4	4	8.32E-02
6	-6	-6.64E-06
6	-5	1.16E-04
6	-4	4.74E-04
6	-3	-3.37E-05
6	-2	-4.21E-06
6	-1	6.27E-06
6	0	2.46E-06

6	1	-1.11E-05
6	2	2.83E-06
6	3	7.90E-05
6	4	-5.50E-04
6	5	-3.60E-05
6	6	1.67E-05

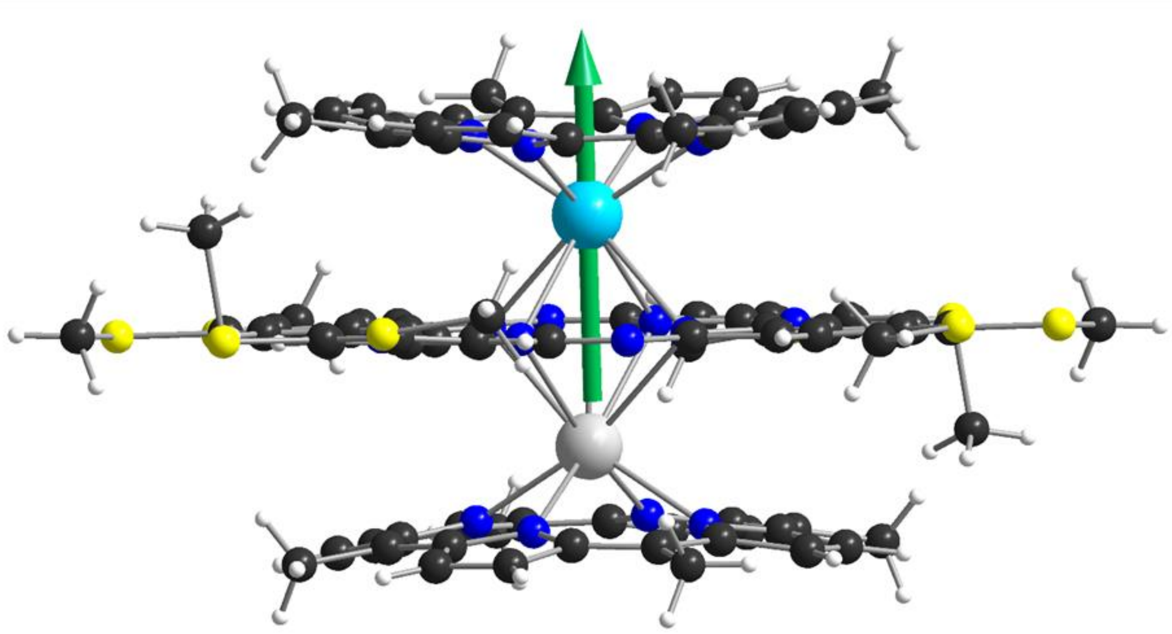

Figure A4. The modified molecular structure used for CASSCF calculation of **3-Tb**. Hydrogen, carbon, nitrogen, sulfur, terbium, and yttrium, are shown in white, black, blue, yellow, cyan, and grey, respectively. The green arrow represents the orientation of the principal magnetic axes obtained in the simplified calculation.

CASSCF calculation of 4-Tb

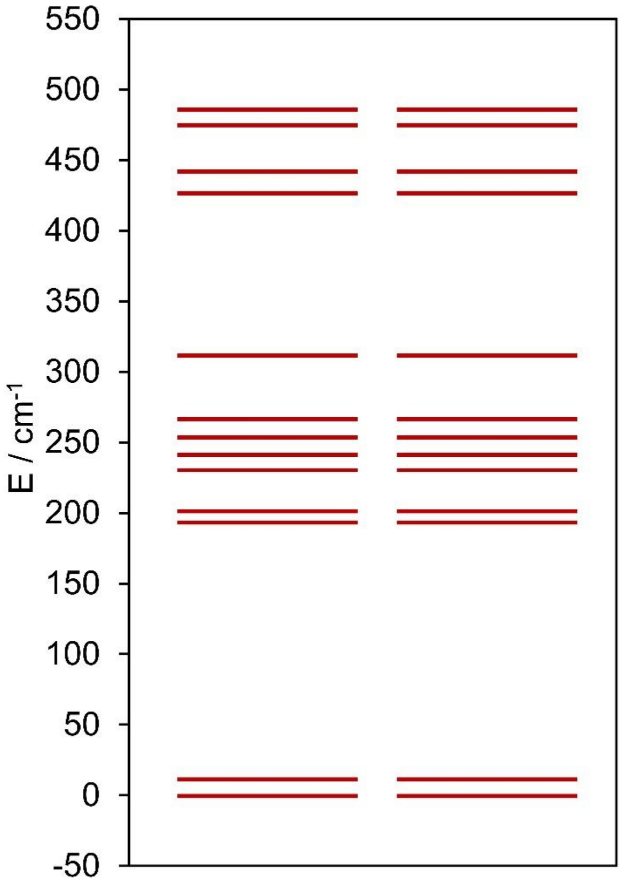

Figure A5. Energy diagram of LF states of **4-Tb** calculated from CASSCF.

Table A5. Calculated ligand field parameters of **4-Tb**.

k	q	B(k,q)
2	-2	4.71E-03
2	-1	7.35E-03
2	0	-2.54E+00
2	1	7.72E-03
2	2	2.56E-02
4	-4	-4.19E-03
4	-3	1.51E-03
4	-2	4.75E-04
4	-1	6.95E-04
4	0	-1.25E-03
4	1	-5.75E-04
4	2	4.11E-04
4	3	-6.23E-03
4	4	1.17E-03
6	-6	2.84E-05
6	-5	-1.13E-04
6	-4	2.03E-05
6	-3	7.44E-06
6	-2	-2.44E-05
6	-1	-1.78E-05
6	0	9.88E-05
6	1	1.79E-05
6	2	-2.85E-05

6	3	9.81E-05
6	4	-1.15E-05
6	5	-5.69E-05
6	6	3.79E-06

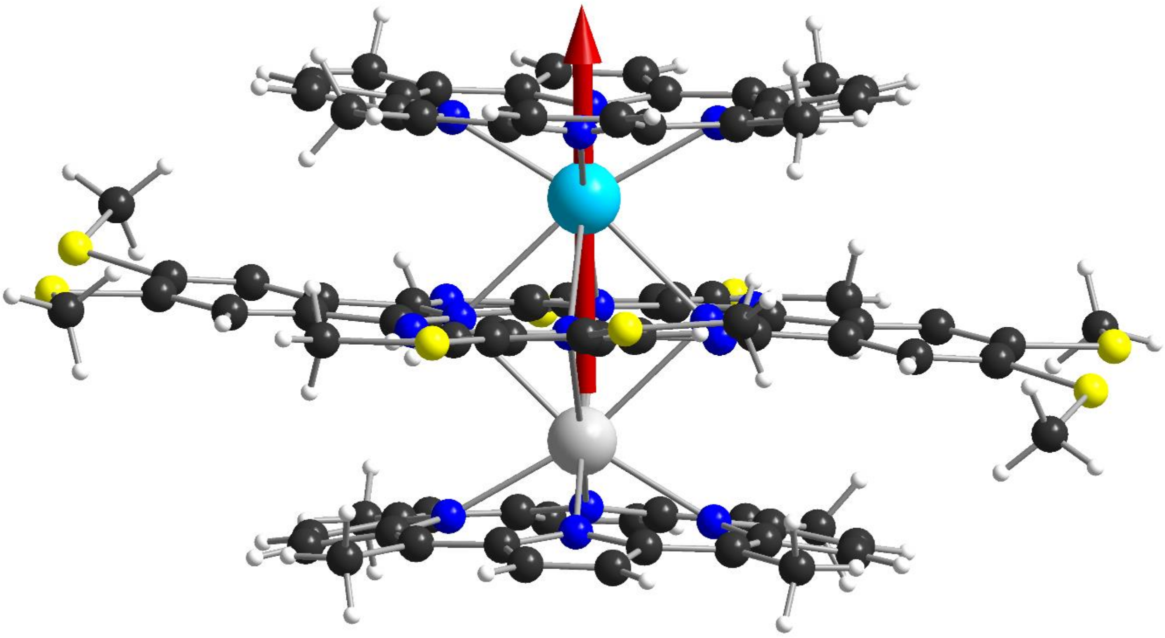

Figure A6. The modified molecular structure used for CASSCF calculation of **4-Tb**. Hydrogen, carbon, nitrogen, sulfur, terbium, and yttrium, are shown in white, black, blue, yellow, cyan, and grey, respectively. The maroon arrow represents the orientation of the principal magnetic axes obtained in the simplified calculation

CASSCF calculation of 4-Tb dication

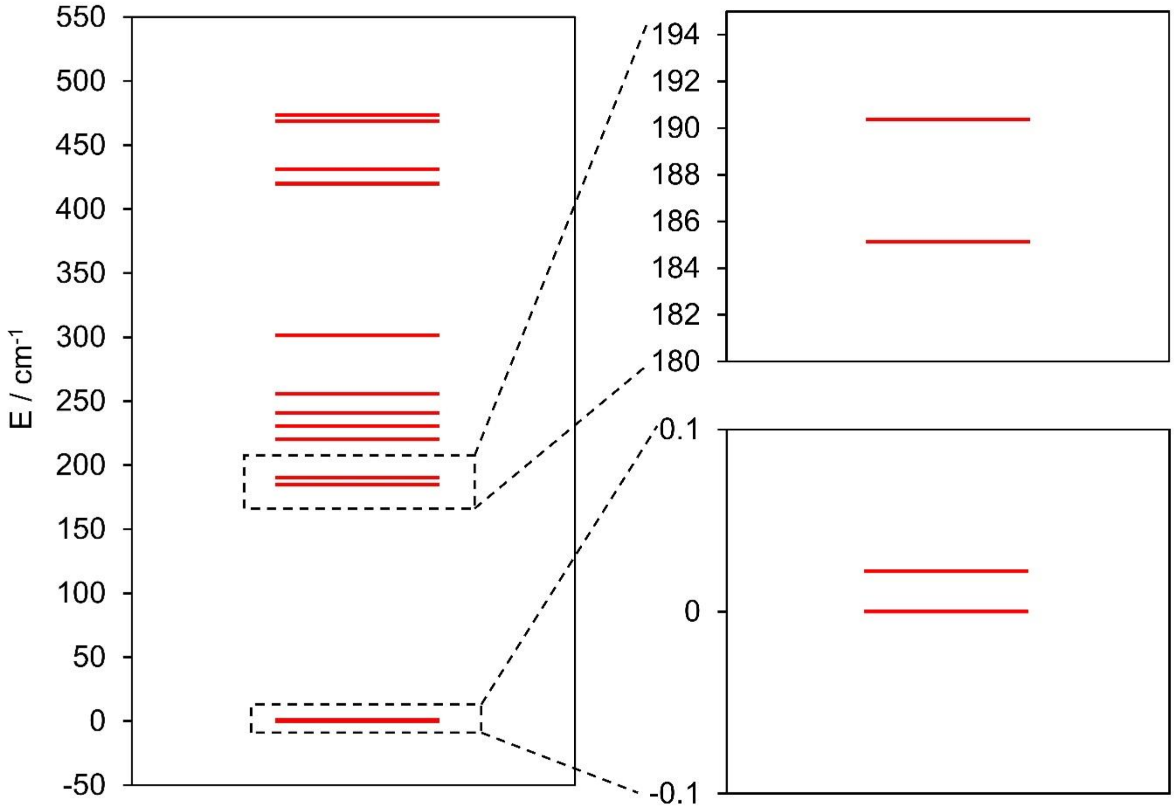

Figure A7. Energy diagram of LF states of the dication of **4-Tb** calculated from CASSCF.

Table A6. The list of LF states of dication of **4-Tb**, and the composition of |m$_J$>. Note that ± m$_J$ contributes equally.

	|m$_J$>						
Energy / cm^{-1}	|±6>	|±5>	|±4>	|±3>	|±2>	|±1>	|0>
0.0000	100	0	0	0	0	0	0
0.0223	100	0	0	0	0	0	0
185.0884	0	81.4	0.4	6	0	12	0.2
190.2869	0	89.4	0.6	2	0.2	7.6	0.2
219.3500	0	0	47.4	2.4	15.4	1.6	33.2
230.5567	0	1.6	5.2	13.8	68.4	8.6	2.4
240.8346	0	10.2	7.4	37.4	12.2	28.4	4.5
255.3489	0	15.6	1.6	42.4	2.4	37.6	0.4
300.9930	0	0	96.2	1	1.6	1.2	0
419.4271	0	0	34.4	0	16.4	0	49
430.7434	0	0.6	0	49.6	0.2	49.6	0
469.0412	0	1.2	0.2	45.2	0	53.4	0
473.3911	0	0	6.4	0.2	83.2	0	10.1

Table A7. Calculated ligand field parameters of dication of **4-Tb**.

k	q	B(k,q)
2	-2	-1.74E-01
2	-1	3.11E-01
2	0	-3.10E+00
2	1	-4.19E-01
2	2	-5.89E-01
4	-4	-4.94E-03
4	-3	8.63E-03
4	-2	6.32E-04
4	-1	-3.21E-03
4	0	-9.82E-03
4	1	4.42E-03
4	2	1.21E-04
4	3	7.80E-03
4	4	1.12E-01
6	-6	-1.51E-05
6	-5	-1.37E-04
6	-4	-5.19E-06
6	-3	-4.39E-05
6	-2	6.97E-06
6	-1	-9.97E-06
6	0	-6.96E-07
6	1	1.19E-05
6	2	8.52E-06

6	3	-4.27E-05
6	4	-7.19E-04
6	5	1.35E-04
6	6	-4.22E-05

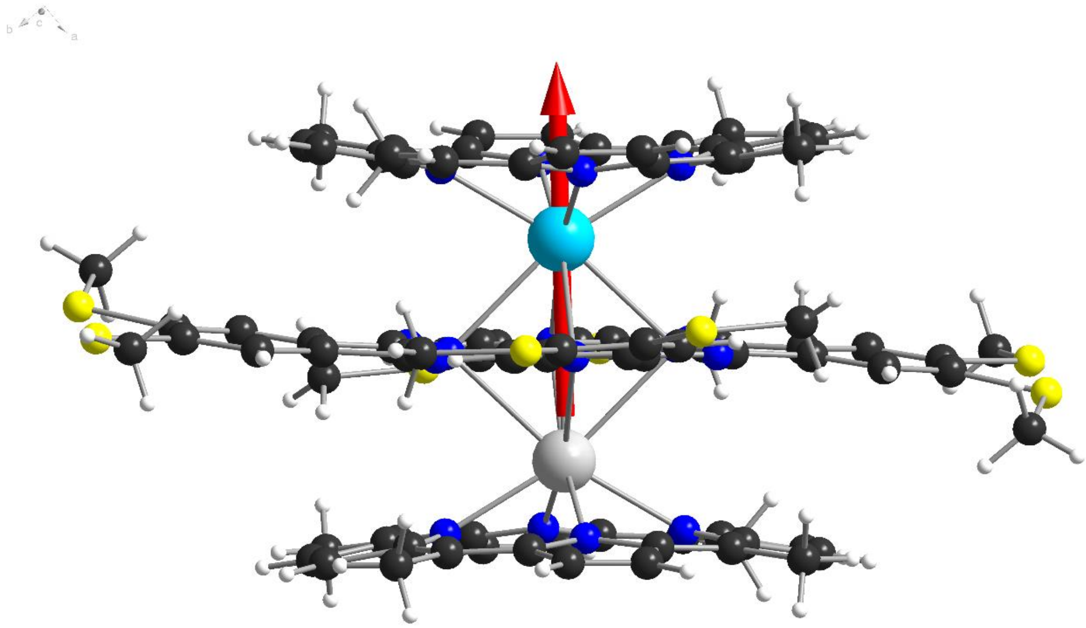

Figure A8. The modified molecular structure used for CASSCF calculation of dication of **4-Tb**. Hydrogen, carbon, nitrogen, sulfur, terbium, and yttrium, are shown in white, black, blue, yellow, cyan, and grey, respectively. The red arrow represents the orientation of the principal magnetic axes obtained in simplified calculation.

Publications

Published

J. Komeda, A. K. Boudalis, N. Montenegro-Pohlhammer, C. Antheaume, A. Mizuno, P. Turek, M. Ruben. Selective Transition Enhancement in a g-Engineered Diradical. *Chem. - A Eur. J.* **2024**, *202400420*. (Chosen as the front cover)

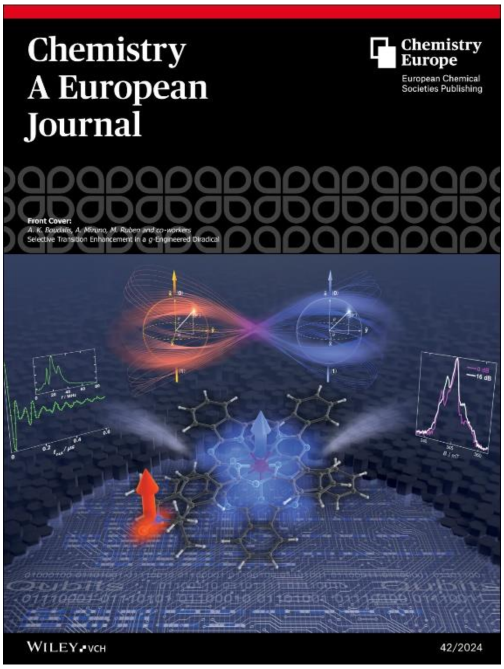

Under preparation

J. Komeda, S. Schlittenhardt, A. Mizuno, E. Moreno-Pineda, C. Yaorong, O. Fuhr, J. Appleton, A. K. Boudalis, S. Klyatskaya, M. Ruben. Stable Radical in Cationic Dinuclear Terbium^{III} Triple-Decker with Switchable Magnetic Property.